Title

Synthesis and Design of Small Molecule-Based Functional Materials: Applications in Lithium-Ion Batteries and Molecular Machines

Permalink

https://escholarship.org/uc/item/6xk2w9xx

Author

Vadehra, Geeta

Publication Date

2016

Peer reviewed|Thesis/dissertation

UNIVERSITY OF CALIFORNIA

Los Angeles

Synthesis and Design of Small Molecule-Based Functional Materials: Applications

in Lithium-Ion Batteries and Molecular Machines

A dissertation submitted in partial satisfaction of the

requirements for the degree Doctor of Philosophy

in Chemistry

by

Geeta Sophie Vadehra

2016

ABSTRACT OF THE DISSERTATION

Synthesis and Design of Small Molecule-Based Functional Materials: Applications in Lithium-
Ion Batteries and Molecular Machines

by

Geeta Sophie Vadehra

Doctor of Philosophy in Chemistry

University of California, Los Angeles 2016

Professor Miguel A. Garcia-Garibay, Chair

Solid-state organic chemistry is a broad topic with a wide variety of materials applications. This dissertation focuses on two very different applications, and should be considered in two separate parts. Part One focuses on the use of organic compounds as electrode materials in lithium ion batteries (Chapters Two and Three) and Part Two focuses on the design of molecular rotors for their applications in molecular machines (Chapters Four and Five).

Part One. The application of organic redox reactions in lithium ion batteries is a relatively unexplored topic. Though first examined in the early 1970s, the field was quickly abandoned in favor of inorganic insertion compounds, which showed more desirable redox potentials and lower solubility in typical organic electrolyte solvents. As such, these metal oxides have

dominated the field ever since. However, while these compounds show impressive performance, they are plagued with unavoidable environmental consequences of their continued use. Organic alternatives provide a useful platform to circumventing this, which has sparked a resurgence of interest in the last decade in addressing the two issues mentioned above.

Chapter Two. The redox potentials demonstrated in organic redox reactions most often fall approximately halfway between those displayed by traditional cathode and anode materials—meaning that applying these to either would cut the cell voltage in half. However, as this is an effect of the electronics of the process, it follows that controlling the electronics would control this. Naphthalene diimides provide an ideal model to explore the effects of probing the electronics of the material based on their low solubility and redox capabilities. In this chapter, the synthesis and characterization of a family of naphthalene diimide derivatives is documented, along with the tunability of the electronics of the redox process based on substituent effects and the subsequent control that can be exhibited on the experimental discharge potentials.

Chapter Three. The motivation for exploring the redox capabilities of organic compounds for electrodes to replace the inorganic insertion compounds that currently dominate the field is largely based on the environmental implications of the current materials. A recent discovery that a furan backbone can be accessed in highly sustainable methods provided an environmentally friendly synthesis of furan dicarbonyl derivatives such that their electrochemical activity could be characterized.

Part Two. Analogous to their macroscopic counterparts, a machine on the molecular scale requires the cooperative movement of its parts. The Garcia-Garibay group has developed the design of the molecular gyroscope, which, like a macroscopic gyroscope, has both stationary and rotating parts. However, incorporation of this motion into the solid requires control not just with

regard to molecular design, but, also with regard to crystal packing. In the context of the molecular gyroscope, this means that in order for the rotating component to rotate, sufficient free volume around it is required.

Chapter Four. While the inability to predict crystal packing remains a major obstacle in the field of crystal engineering, it has been shown that the use of hexamethyl triptycene as the stator portion can allow for an optimal packing arrangement of the rotor molecules. However, closer inspection of the crystal structure revealed that the free volume discussed above, was actually filled by crystallographically defined solvent molecules. Despite this, the system demonstrated impressive rotational dynamics. Given the dynamics of this system in combination with analysis of the crystal structure demonstrated the presence of a correlated motion analogous to a macroscopic "gearing" system. This chapter documents synthetic advances that allow access to this system efficiently such that appreciable quantities of this rotor *and* a variety of its derivatives can be accessed in order to fully characterize their rotation dynamics. Preliminary data showing qualitative evidence of a correlated motion are presented, but studies are still ongoing.

Chapter Five. Inspired by the work discussed in the previous chapter, it followed that while iptycene based stators would often lead to rotors with a tendency to interdigitate, peripheral substitution was a promising strategy to overcome this obstacle. Despite this, traditional strategies of synthesizing these compounds were considerably too long and low yielding to be practical for further study. With this in mind, this chapter documents the development of an efficient, high yielding method for late stage installation of peripheral substitution that can be applied not just to triptycenes, but also to pentiptycenes.

The dissertation of Geeta Sophie Vadehra is approved.

Robin L. Garrell

Bruce S. Dunn

Miguel A. Garcia-Garibay, Committee Chair

University of California, Los Angeles

2016

TABLE OF CONTENTS

List of Schemes

about the molecule as a whole, activation energy is a function of free volume specifically about the rotator. Therefore, while packing coefficient gives a good rough estimate of the trend, it is not a substitution for analysis of the crystal structure.

Figure 2.1. Redox capabilities of naphthalene diimide system demonstrating two connectivities to control different aspects of the system.

Figure 2.2.1. Structure and redox process of naphthalene diimides (NDIs) with different aromatic (X) and imide (R) substituents. Although there is a potential four electron mechanism resulting in the lithiation of the remaining carbonyls, attempts to reach sufficiently low potentials to access this state resulted in irreversible decomposition

Figure 2.3.1. Cyclic voltammograms of NDIs **6-9** measured vs Ag/AgCl in 0.1 M Bu_4NPF_6 in CH_2Cl_2 (Li/Li^+ is -3.237 vs Ag/AgCl).

Figure 2.3.2. Cyclic voltammetry and cyclability of a) compound **6**, b) compound **7**, c) compound **8** and d) compound **9**. The galvanostatic cycling with electrodes prepared with e) compound **6**, f) **8** and g) **9** was carried out between 1 and 4 V vs Li/Li^+. The N,N-Dimethyl NDI **7** in f) was cycled between 1 and 3.5 V in order to avoid an irreversible oxidation above that value.

Figure 2.3.3. Cyclic voltammetry and galvanostatic cyclability of a) and d) compound **10**, b) and e) compound **13**, and c) and f) compound **11**.

Figure 2.3.4. (a.) Discharge capacity vs. cycle number for three of the compounds tested. Cycling data for all compounds studied can be found in the supplementary information. (b.) Solid state reduction potential vs. calculated gas-phase B3LYP/6-311+G(d,p) LUMO energy levels. Numbered solid squares correspond to the NDI studies here and open triangles to heterocyclic anthraquinone analogs reported by Liang *et al*.

Figure 3.3.1.1. a.) Semiconducting polymer in which redox active, dopeable centers are conjugated (b.) Non-conjugated polymer in which redox active centers are separated by a linker. Also referred to as linker model (c.) Non-conjugated polymer in which the redox active centers are attached as pendants to a polymer backbone. Also referred to as pendant model

Figure 3.3.2.1. The polymer bearing a redox active center as a pendant on an alkyl polymer backbone proved too insulating for practical use.

Figure 3.3.2.2. Pendant radical polymers (a.) Insulating alkyl backbone (b.) Ionophoric poly(ethylene oxide) backbone (c.) alkyl backbone with ionophoric side chains.

Figure 3.3.3.1. The expected two electron redox processes and performance of (a.) Di-lithium terephthalate and (b.) Di-lithium *trans-trans-* muconate (c.) 4,4'tolanedicarboxylate.

Figure 3.3.4.1. (a.) Mascal's formation of furan backbone from cellulose (b.) Redox process of furan dicarbonyls can be applied to a variety of different X and Y.

Figure 3.4.2.1. Electrochemistry of furan **5** at 0.1 M $(nBu)_4ClO_4$ in THF at a scan rate of 100mV/sec (a.) compared against the supporting electrolyte and (b.) alone.

Figure 3.4.3.1. Cyclic voltammetry of furan **3** in 2016 coin cell with 1M $LiClO_4$ in 1:1 vol/vol ethylene carbonate : dimethyl carbonate (EC:DMC) electrolyte, using lithium metal as counter electrode at a scan rate of 5 mV/sec with an electrode formulation composition of furan **3** and acetylene black in a 1:1 ratio. *Inset shows control experiment under similar conditions in the absence of furan.*

Figure 4.2.1. (a.) Optimal packing arrangement allows for sufficient free volume around the rotator to allow for unhindered rotation. (b.) Crystal structure and (c.) space-filling model of triptycene based rotor crystallized from m-xylene demonstrates absence of this free volume due

to interdigitation and solvent molecules. (d.) As the triptycene did not provide sufficient bulk to create the desired cavity, the steric bulk was increased. *Adapted from Godinez,* et al

Figure 4.2.2. (a.) Crystallization of the phenyl substituted rotor from m-xylenes still displayed an interdigitated packing arrangement. (b.) Crystallization of the propyl substituted rotor **1**, however, demonstrated desired packing, but with the presences of crystallographically defined bromobenzene in the voids (c.) space-filling model of rotor **1** with solvent molecules removed for clarity demonstrates desirable packing. (d.) Top-down view of rotator and solvent molecules demonstrates a ratchet like arrangement of solvent molecules suggesting a correlation between the motion of the rotator with the rotation of the solvent.

Figure 4.3.1.1. The triptycene model has two main areas of substitution: the peripheral (X) and the bridgehead (Y).

Figure 4.3.2.1. Preliminary **SS** ^{2}H NMR data of a rotor/ bromobenzene-d_4 co-crystal demonstrating temperature dependent rotation.

Figure 5.1.1. Traditional Strategies versus our strategy to access peripherally substituted iptycenes

Figure 5.3.1. ^{1}H NMR of crude reaction mixture of pentiptycene 2 (above) and dimethyl triptycene (below) showing a clean and complete bromination of all eight and six sites, respectively. Key signals for the above include an aromatic singlet at 7.55 ppm, the bridgehead hydrogen at 4.8 ppm, and the four signals of the aliphatic butoxy groups.

Figure 5.3.2. (a) (Left) ORTEP diagram of pentiptycene quinone 5c with ellipsoids shown at 50% probability and (Right) packing interactions between adjacent molecules in the lattice. Benzene molecules shown in red. **(b)** Line structure and space-filling model of pentiptycene

quinone 5e with eight *para*-(triphenylmethyl)-phenyl groups in the periphery of the structure illustrating the power of the method.

List of Tables

List of Abbreviations

A	pre-exponential factor in hertz (solid state NMR)
A	ampere (capacity)
Ar	aryl
BMF	5-(bromomethyl)furfural
ca.	approximately
C_k	packing coefficient
CDCl3	deuterated chloroform
CMF	5-(chloromethyl)furfural
d	doublet (NMR)
d	deuterium
dd	doublet of doublets (NMR)
DFF	2,5-diformylfuran
e^-	electron
e.g.	exempli gratia
E_a	activation energy
et. al.	*et alia*
FDCA	furan dicarboxylic acid
FG	functional group
FTIR	Fourier transformed infrared spectroscopy
g	gram
Hz	hertz
HOMO	highest occupied molecular orbital

h	hour
K	Kelvin
k_{rot}	rate of rotation
kcal	kilocalories
kHz	kilohertz
LCO	$LiCoO_2$
LUMO	lowest unoccupied molecular orbital
m	multiplet
MHz	megahertz
min	minute
mL	milliliter
mol	mole
m.p.	melting point
m/z	mass to charge ratio
NMR	nuclear magnetic resonance
PXRD	powder X-ray diffraction
ppm	parts per million
R	general alkyl group substituent
rt	room temperature
s	singlet (NMR)
T	temperature
THF	tetrahydrofuran
TLC	thin layer chromatography

t	triplet (NMR)
t	time
V	volts
Å	angstrom

Acknowledgements

First and foremost, my family who has always been supportive.

As far as research supervisors go, I could not have imagined being any luckier. Without any of these three, I would not have made it to where I am today.

Firstly, my advisor, Professor Miguel Garcia-Garibay has been incredible in not only helping guide me intellectually towards becoming the scientist I have become, but also in his endless patience with me during times of particular stress. His understanding of me, both as a mentor and as a teacher, have made him my key support system and completely responsible for my ability to achieve my goals.

Professor Bruce Dunn, whom, I had initially imagined would be simply a collaborator, has ended up taking his role as co-advisor very seriously. Despite his own large research group and numerous responsibilities, he, somehow, always managed to make time for me when I asked and give advice and alternative perspectives—which were integral to the success of my multi-disciplinary education—when I needed. He has been a consistently active supporter and advisor throughout my education and I could not be more grateful.

And, finally, Professor John Dayton Tovar, my undergraduate research advisor. His willingness to allow a creative writing major considering a pre-medical track with no chemical knowledge or experience into his lab began my career in the sciences. His support, encouragement and mentorship over that time allowed me to realize my curiosity and, eventually, he was the one to introduce me to Professor Miguel Garcia-Garibay.

VITA

University of California, Los Angeles   2016
     Ph.D., Chemistry (Expected)

Graduate Researcher: University of California, Los Angeles   September 2011-Present
     Advisor: Professor Miguel A. Garcia-Garibay
     Co-Advisor: Professor Bruce Dunn

Organization for Culture and Diversity in Science   January 2011-Present

High School Nanoscience Program   September 2011-2013

NSF IGERT Materials Creation Training Program Traineeship UCLA   2011-2013

NSF IGERT Materials Creation Training Program Bridge Internship UCLA   2010

Johns Hopkins University   2009
     B. A. in Chemistry, Minor in Writing Seminars

Undergraduate Researcher: Johns Hopkins University   June 2007 – May 2010
     Advisor: Professor John D. Tovar

NSF Research Experience for Undergraduates UCLA NANOCER   2008
     Advisor: Professor Miguel A. Garcia Garibay

PUBLICATIONS AND SELECTED PRESENTATIONS

PUBLICATIONS

Vadehra, G. S.; Jiang, X.; Chu, G. M.; Garcia-Garibay, M. A. "A Succinct, High Yielding, Divergent Synthesis of D$_2$h-Symmetric Octakis-Substituted Pentiptycenequinones." *Accepted Pending Revisions.*

Staehle, I.O.; Chung, T.S.; Stopin, A.; **Vadehra, G.S.**; Hsieh, S.I.; Gibson, J. H.; Garcia-Garibay, M.A. "An Approach to Enhance the Safety Culture of an Academic Research Laboratory by Addressing Behavioral Factors" J. Chem. Educ., 2016, **93**, 217-222. **DOI:** 10.1021/acs.jchemed.5b00299.

Vadehra, G. S.; Maloney, R. P.; Garcia-Garibay, M. A.; Dunn, B. "Naphthalene Diimide Based Materials with Adjustable Redox Potentials: Evaluation for Organic Lithium-Ion Batteries." Chem. Mater., 2014, **26**, 7151-7157. **DOI:** 10.1021/cm503800r

Vadehra, G. S.; Wall, B. D.; Diegelmann, S. R.; Tovar, J. D. "On resin dimerization incorporates a diverse array of pi-conjugated functionality within aqueous self-assembling peptide backbone." Chem. Commun., 2010, **46**, 3947-3949. **DOI:** 10.1039/c0cc00301h

PATENTS

J. D. Tovar, S. R. Diegelmann, B. D. Wall, and **G. S. Vadehra**, "Self-assembling peptides bearing organic electronic functionality and applications employing the same," PCT Int. Appl. 2010 (WO 2010115080).

PRESENTATIONS

Facile Synthesis of Substituted Iptycenes (Oral). Geeta S. Vadehra, Xing Jiang, and Miguel A. Garcia-Garibay. *250th ACS National Meeting*, Boston, MA, August 2015.

Naphthalene Diimide Based Materials with Adjustable Redox Potentials for Organic Lithium Ion Batteries (Poster). Geeta S. Vadehra, Ryan P. Maloney, Bruce Dunn and Miguel A. Garcia-Garibay. *249th ACS National Meeting*, Denver, CO, March 2015.

Cultivating a Culture of Safety in an Organic Chemistry Lab at UCLA (Poster). Geeta Vadehra, Ira Staehle, Tim Chung, Patrick J. Commins and Miguel A. Garcia-Garibay. *UC Center for Laboratory Safety: Workshop on Laboratory Safety*, Irvine, CA, April 2014.

Structure-Property Relationships of Naphthalene Diimide Based Organic Electrodes (Oral). Ryan P. Maloney, **Geeta S. Vadehra**, Bruce Dunn and Miguel A. Garcia-Garibay. *224th ECS National Meeting*, San Francisco, CA, October 2013.

Supramolecular Polymer Nanostructures Derived from the Amyloid-Inspired Self-Assembly of Optoelectronic Peptides (Poster). Stephen R. Diegelmann, Brian D. Wall, **Geeta S. Vadehra**, John D. Tovar. *240th ACS National Meeting*, Boston, MA, August 2010.

CHAPTER 1

Introduction:

Design of Small Molecule-Based Functional Materials: Applications

in Lithium-Ion Batteries and Molecular Machines

1.1 Introduction.

Solid-state organic chemistry is a broad topic with a wide variety of both synthetic and materials applications. Its advantages are numerous. From a synthetic perspective, the ability to do a reaction in the solid state means avoiding the use of solvents during the reaction. These solvents, though seemingly innocuous in comparison to some of the other materials used during these processes, become problematic when considered on the industrial scale. Synthetic organic transformations require such a large amount of solvent use between the reaction and the purification that two major pharmaceutical companies have recently estimated that 70-80% of their chemical waste is related to solvents.[1,2] However, the ability to do chemical reactions in the absence of solvent is incredibly difficult due to the restrained molecular motion and kinetic energy in the solid state. It follows that if molecules have limited degrees of freedom or kinetic energy to move, then they cannot react with one another. And, so, despite the obvious advantages of the solid state, doing reactions in this way has remained comparatively unexplored. Aristotle is famously quoted as saying, "*No coopora nisi fluida,*" which translates as "no reaction occurs in the absence of solvent"[3]. Though, today, many processes are known which break this rule—chemically, we have observed topochemical transformations, mechanochemistry, solid-gas reaction, and structurally, simple phase transitions in the absence of solvent[4]—this area still remains largely unexplored.

From the perspective designing materials with a specific function in mind, the lack of motion can be a great advantage. Creating the boundaries inherent to the solid state allows us to assume fixed locations of the atoms, and, subsequently, envision the design of functional

materials. Utilizing crystalline materials allows us to gain structural understanding of the arrangement of these functional materials on the molecular scale through X-ray diffraction techniques.

Over the course of my doctoral research I have had the opportunity to pursue this field from a few different vantage points leading to a diversified dissertation. Though my research has remained under the overarching theme of the design, synthesis and characterization of solid-sate, organic based materials, my work has been aimed at exploiting these materials for two different applications: the application of organic based materials in lithium ion batteries and the design and synthesis of molecular gyroscopes.

1.2. Organic based electrode materials for Lithium-Ion Batteries.

Establishing new means to access cost-efficient and renewable energy has become an area of increasing concern. Energy storage technology promises to enable the potential of renewable energy storage due to its ability to store energy gathered from sun, wind or other sources, and advances in lithium-ion technology have made its application attractive.[5]

The concept of utilizing the redox abilities a metallic element as an electrode material has existed for over a century and lithium's low atomic weight makes it an obvious choice.[5] Its first application—and, commonly accepted, the first lithium ion battery—can be traced back to Gilbert N. Lewis's 1913 demonstration of its electrochemical[6] activity following his similar studies on sodium and potassium.[7] Lewis's model, however, noted the extreme instability of lithium, and, so, it was another 45 years[8]—when Harris and Tobias demonstrated its stability in cyclic ester-based solvents—that the research into the field really began, leading to Jon Goodenough's 1980 study documenting the utility of $LiCoO_2$ (LCO),[9] and, finally, Sony's 1991

commercialization of the first rechargeable lithium ion battery, as we currently know the technology, in mobile phones and camcorders.

1.2.1. Electrode Material Design

Since Sony first commercialized rechargeable lithium ion batteries in the early 1990s, they have achieved great popularity—showing up and dictating the market in the world of small electronics.[10] While these batteries are largely considered an incredibly promising form of energy storage, their current materials and methods of production have become sufficiently environmentally problematic on the industrial scale that researchers have begun to look at alternative materials.[11-14]

The current energy storage mechanism of the lithium ion battery relies on the ability of an electron and lithium cation to be able to be shuttled back and forth between two host structures—the electrodes—which will undergo this process at sufficiently different potentials.[15]
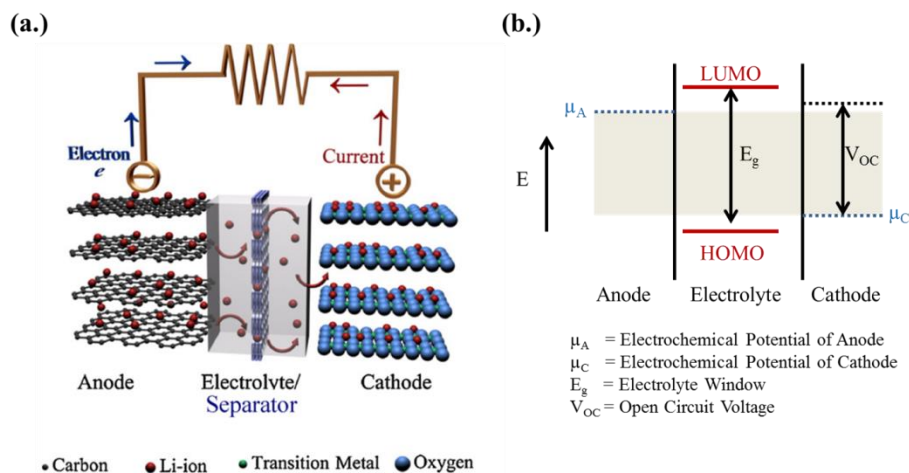
Figure 1.2.1.1. (a.) Illustrative picture of a standard lithium ion cell utilizing the layered, carbonaceous graphite at the negative electrode (anode) and a transition metal oxide at the positive electrode (cathode). *Adapted from Song* et al. *[16]* (b.) Energy level diagram demonstrating the relative energy levels of the negative electrode, positive electrode and electrolyte. Adapted from *ref [15,17]*.

From the consideration of the electron, it is a case of redox chemistry in molecular design—can the material accommodate and transport the electron? From the perspective of the lithium cation,

on the other hand, it becomes a question of supramolecular architecture—can the cation access a site to effectively balance the charge.

The insertion/de-insertion potential of a material is based on the energy of its LUMO. The difference in potentials between the two host structures is the cell voltage. As such, the ideal materials will maximize this value, without exceeding the limits of the rest of the system, e.g. electrolyte stability due to its own HOMO/LUMO, the potential of the Li/Li^+ couple, etc.[17-19] With this *in* mind, current technology requires the use of inorganic insertion metal oxides at the positive electrode, the traditional material being cobalt based, and a carbonaceous material, such as graphite, as the negative electrode.

Numerous metal oxides have been explored as potential electrode material.[18] The cobalt based compound, lithium cobalt oxide (LCO), has become an especially popular positive electrode material owing to its high electronic and ionic conductivity as well as cell voltage—the electrochemical potential occurs at 4.0 V vs Li/Li^+ in comparison to the ~200 mV vs Li/Li^+ displayed by graphite—and impressive cyclability. On the other hand, however, LCO comes with its own set of drawback. While the electrochemical potential of 4.0 V vs Li/Li^+, is considered high, its gravimetric capacity of 140 mAh/g—essentially a measure of the amount of energy storage per unit mass—is comparatively moderate. Furthermore, the environmental implications of its continued use are also troubling. The natural supply of cobalt will dwindle with increased use, and, possibly more troubling, the high temperature processing required to convert the naturally occurring cobalt into its higher potential metal oxide form is energy intensive.[12] Recently, it was estimated that approximately 30% of cobalt produced globally was used in the production of electrode material in lithium ion batteries. Moreover, the production and recycling of it produces large amounts of carbon dioxide.[13]

With this in mind, the scientific community has aimed to explore other technologies to access these electrode materials.

1.2.2. Application of Organic Based materials

Small organic molecules provide an attractive alternative to current inorganic materials because they have the potential ability to address many the concerns the traditional electroactive materials face: organic materials tend to be lighter, cheaper and less toxic than their inorganic counterparts. Furthermore, if we re-visit the mechanism of the electrode materials discussed above, it follows that organic based compounds could show promise from this perspective. There are many known naturally occurring redox processes: our hair is curly due to disulfide bond formation (Figure 1.2.2.1a), the mechanism by which Coenzyme Q can act as an electron shuttle is based on quinone chemistry (Figure 1.2.2.1c), ascorbic acid or vitamin c, is known as an effective preservative based on the redox abilities of its conjugated dicarbonyl moiety, to act as an anti oxidant. Furthermore, while open-shell free radicals are generally considered to be

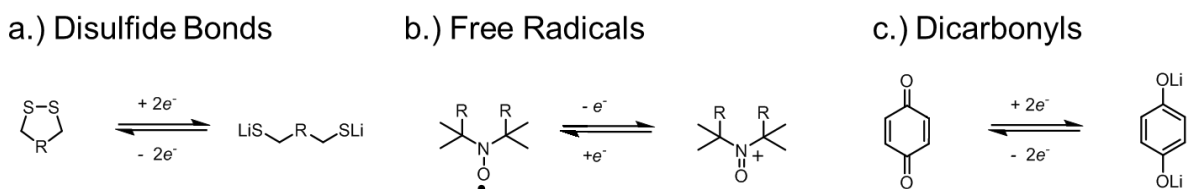**Figure 1.2.2.1.** Most well known small organic molecule based redox processes can be split into three main categories: disulfide bond formation, free radical oxidation and dicarbonyl chemistry

fleeting or unstable species, nitroxyl radicals—the most well known being (2,2,6,6-tetramethylpiperidin-1-yl)oxidanyl, or "TEMPO"—are considered to be bench stable and can under go a one-electron oxidation.[14]

However, generally speaking, while these compounds can potentially address the concerns of their inorganic counterparts, they come with a different set of problems. Firstly, small organic molecules are generally significantly more soluble in non-aqueous electrolytes than their inorganic counterparts, and, under the rigorous electrochemical cycling conditions inherent to this application, dissolution of the active material quickly becomes a problem.[13,14,20] Secondly, the redox potentials of these materials tend to fall in an undesirable region. The electrochemical potential of LCO occurs at 4.0 V vs Li/Li$^+$ in comparison to the ~200 mV vs
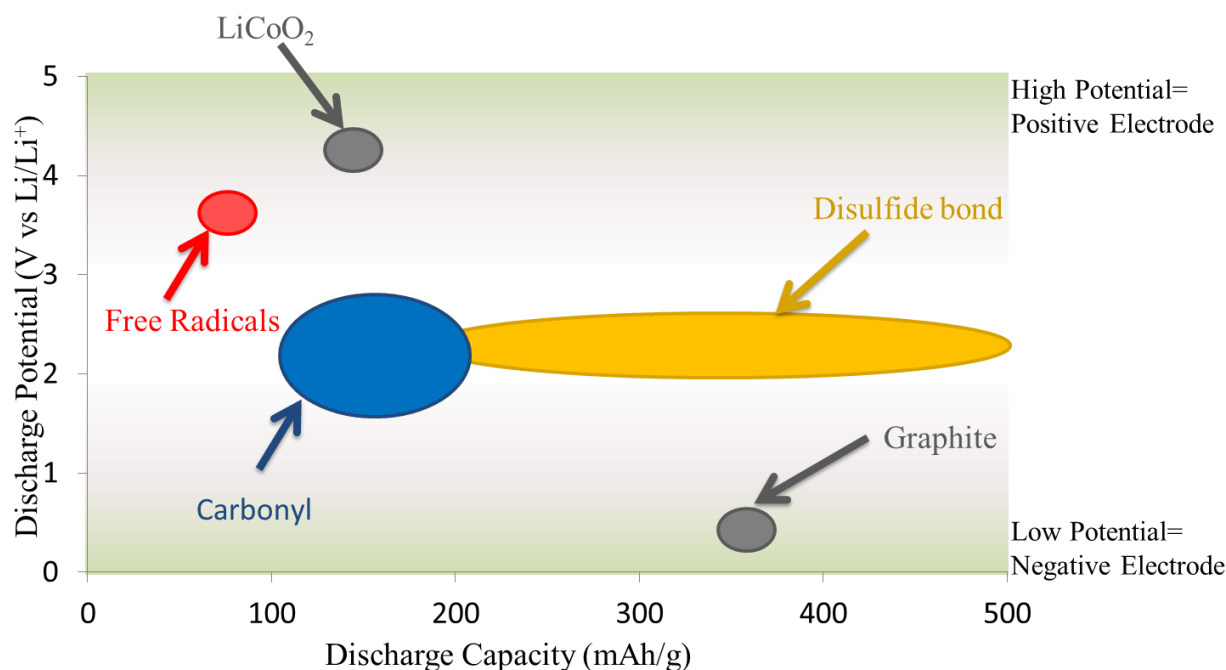
Figure 1.2.2.2. Graphical representation demonstrating the typical potentials and discharge capacities of organic based redox processes in comparison to electrode materials. [14]

Li/Li$^+$ displayed by graphite leading to a cell voltage of ~3.8 V, the redox potentials of most organic based compounds tends to fall in the region of ~2.0 V vs Li/Li$^+$ effectively cutting the cell voltage in half.

With these concerns in mind, although the idea of utilizing the reversible redox process of small organic molecules as positive electrode material has been around since the early 1970s,[21]

research in this area was essentially abandoned in favor of the more efficient progress of inorganic insertion compounds. However, as the limits of research on inorganic insertion compounds seem fast approaching, researchers are attempting to explore other avenues and providing some promising early work taking advantage of known organic redox reactions including quinone chemistry,[22] disulfide bond formation[23] and tolane compounds.[24]

Jean-Marie Tarascon's 2008 communication on rhodizonic acid sparked a resurgence of interest.[22] He initially re-visited this idea by returning to a carefully chosen derivative of the quinone model. The lithiated form of rhodizonic acid can be synthesized from naturally occurring *myo*-inositol in just three steps. The resulting rhodizonate dianion has the ability to take quinone chemistry one step further, undergoing a four electron reduction process in a compound with an extremely low molecular weight, as can be seen in Figure 1.2.2.3a, as well as
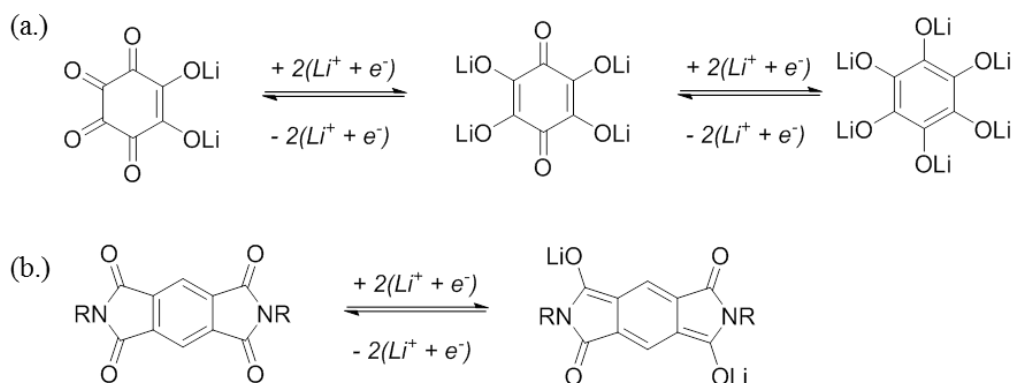

Figure 1.2.2.3. (a.) Redox process of Tarascon' Rhodizonic acid.[Error! Bookmark not defined.] (b.) Redox process of Poizot's Pyromellitic diimide[20]

taking advantage of decreased solubility due to the charged nature of all oxidation states. However, it was found that the cyclability of this compound was extremely low for the four electron process showing a decrease in capacity of more than 50% after just twelve cycles—most likely due to either dissolution of the compound into the electrolyte or break down of the supramolecular architecture. In contrast, Philippe Poizot 2011 study concentrated on addressing this concern by exploring the redox capabilities of a pyromellitic dianion, as can be seen in

8

Figure 1.2.2.3b.[25] This model demonstrated significantly improved cyclability showing almost no decrease in capacity over the 25 cycles shown in this work. The pyromellitic diimide took advantage of two strategies to increase stability: planar aromatic compounds tend to be rigid, therefore decreasing solubility, and charge at all oxidation states. However, while this idea of utilizing charge to increase cyclability was successful—it was noted that the uncharged, protonated diimide suffered dissolution fairly quickly—it also came with its own drawbacks. The synthesis required the use of pyrophoric lithium hydride, followed by thermal treatment to yield the product as a moisture-sensitive compound only stable under inert conditions. Moreover, the increased electron density of the dianion decreased the potential of the start of the reduction process to below 2V in contrast to ca. 2.3V in the uncharged diimide. Although both of these values are significantly below the nearly 4V observed in cobalt models, the increased electron density of the charged dianion strategy proves to worsen this problem. As such, while Tarascon's model most certainly demonstrated, as a proof of concept, the promise of organic redox-active compounds for this application, it suffered from the high solubility so common to these compounds. By contrast, Poizot's study focused on addressing, specifically, this issue, and, in so doing, weakened this material with regards to one of the other major restraints these compounds suffer from.

1.3. Crystalline Molecular Machines

Ever since Richard Feynman's 1959 lecture "There's Plenty of room at the bottom" [26] in the late 1950s, the scientific community has become increasingly interested in the concept of miniaturization and nanotechnology. With this in mind, the design of artificial machines on the molecular scale has gained increasing interest over the past few decades.[27] A machine on the macroscopic level is composed of a set of macroscopic parts that are designed and arranged in

such a way as to work together in order perform a particular function.[28] It follows that by decreasing the size of these parts, we would be able to access smaller and smaller machines, ultimately miniaturizing these parts to the molecular level. However, the translation from macroscopic to molecular is not trivial. Though, seemingly obvious, it is important to note that our ability to design these macroscopic machines is contingent on our ability design, assemble, understand and control the motion of its parts, none of which translate easily to the molecular scale. At this scale, the rules of classical Newtonian physics no longer apply,[29] and, therefore, we no longer possess a similar level of understanding and control. This is not to say that molecular machines do not exist. They are found in many naturally, occurring processes,[29b,30] demonstrating, as is often the case, evolution in nature has a huge head start on scientific research. With that in mind, however, we should be able to design and create molecular machines to perform desired functions as nature has done.

1.3.1. Phases

In order to translate technology to the molecular scale, knowing that these molecules will no longer possess the same physical behaviors as their macroscopic counterpart, it becomes important to evaluate the media. The crystalline phase allows us to achieve fixed atom locations, and obtain structural information as earlier discussed. However, if we want to look at the *motion* of molecules in the *crystalline* phase, we are forced to consider that conventional knowledge would traditionally regard this as a contradiction in terms. The fixed and ordered arrangements
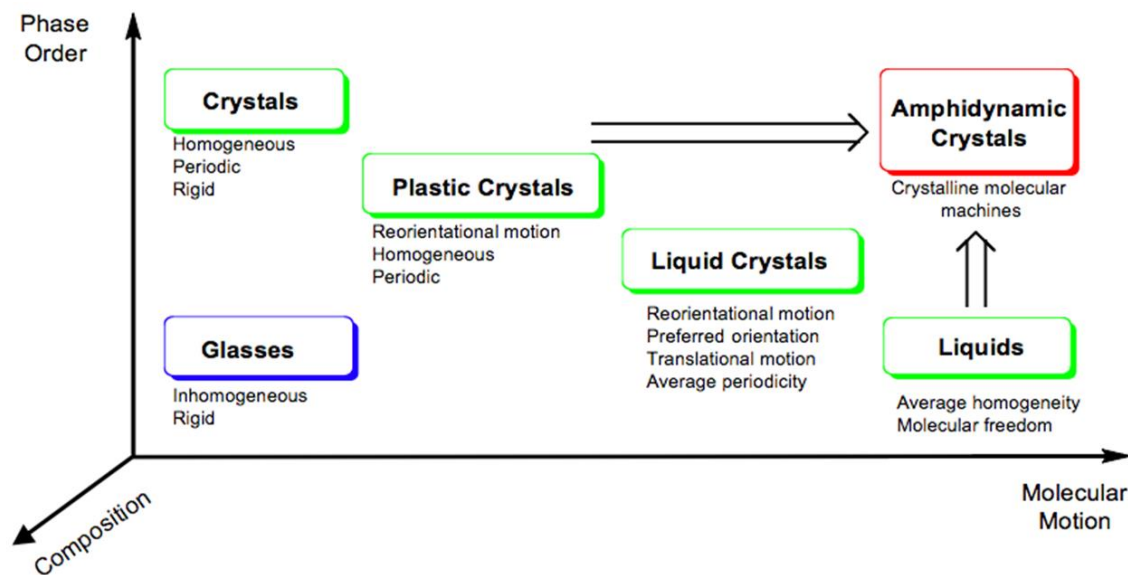
Figure 1.3.1.1. Phase diagram demonstrating relationship between phase and molecular motion. *Adapted from Garcia-Garibay, M.A.*[31]

of atoms that made the crystalline phase so desirable, also dictates a lack of the molecular motion of liquids and gases. As such, it becomes necessary to access a new phase that can combine the advantage of the molecular motion of a liquid with the phase order of a crystal—a phase known as an "amphidynamic" crystal (figure 1.3.1.1)[31].

1.3.2. Molecular Design

Though conceptually attractive, the design of synthesizable, artificial molecular machines is inherently complex. While one can easily envision designing a molecule to resemble the shape of a useful macroscopic object, proving a subsequent functional correlation does not necessarily follow. The breakthrough in this idea came from Mislow and Iwamura's bitriptycene "bevel gear" system (Figure 1.3.2.1), demonstrating two triptycene groups connected via either an ether or methylene linker.[32] As the bond angle of the sp^3 linker—oxygen or methylene—necessarily causes an interdigitated arrangement between the two triptycenes, the shape of the subsequent

molecule resembles that of a macroscopic beveled gear (Figure 1.3.2.1), demonstrating a structural correlation. More importantly, however, the system showed fast and *correlated* motion
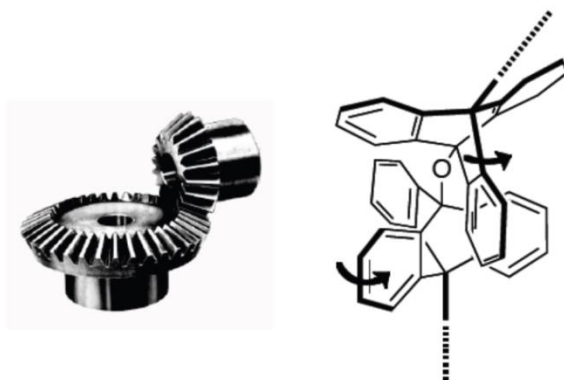

Figure 1.3.2.1. Mislow and Iwamura's beveled gear—here showing the ether connectivity—demonstrating not just structural similarities to its macroscopic counterpart, but subsequent functional behavior rotation. *Adapted from Vogelsberg, et al. [32b].*[32,32,32]

between the two triptycene groups showing a subsequent functional correlation. This study, however, demonstrated this correlation in solution, which allowed the authors to consider the intramolecular interactions of the triptycene without encountering challenges inherent to the solid state.

In order to translate this idea to the solid state, where we can take advantage of fixed atom location, it became necessary to incorporate crystallization into the molecular design. The Garcia-Garibay group has done a great deal of work on this topic concentrating on a model designed to mimic a macroscopic gyroscope—similarly to the above example's design to mimic a bevel gear. The molecules consist of three main parts: the stator, which would remain motionless within the crystal lattice, the axis, which would be "barrierless," and the rotator (Figure 1.3.2.2a,b).[33] The early attempts at this design relied on aromatic stator and rotator portions connected via an alkyne axis. As the barrier to rotation of an alkyne has been calculated
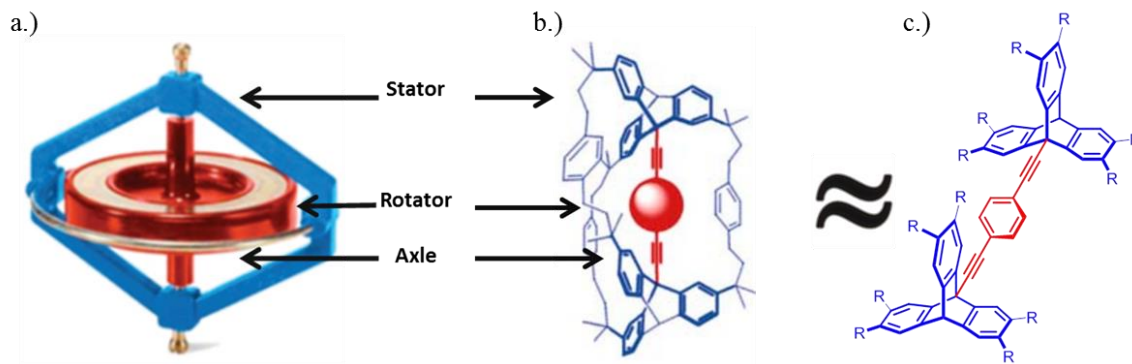
Figure 1.3.2.2. Structural correlation between a (a.) macroscopic gyroscope, (b) molecular gyroscope bridging two stators—"closed" topology—and (c.) with no bridging or "open" topology. *Adapted from Godinez, et al. [34]* [34]

to be negligible,[35] it follows that any barrier to rotation observed by the rotator can be assumed to have supramolecular basis. In other words, as the rotation is not hindered by the molecular design, it can only be slowed as a result of packing. It follows that in an idealized arrangement the packing would allow for sufficient free volume about the rotator to allow for unhindered rotation. Therefore, as a first approximation, it seems reasonable to conclude that increasing the steric bulk of the stator relative to that of the rotator could lead to a subsequent increase in free volume about the rotator. The original work towards this hypothesis came from the synthesis and study of trityl rotor **2** in 2002.[33a] Crystallization of this rotor from benzene yielded a clathrate of $C_k=0.73$ and demonstrating an activation energy of 12.8 kcal/mol[36] . As the trend continues, we see that in the comparable dodecabutylated rotor **4**, the steric bulk of stator is greatly increased, leading to a decreased $C_k=0.68$ and subsequent
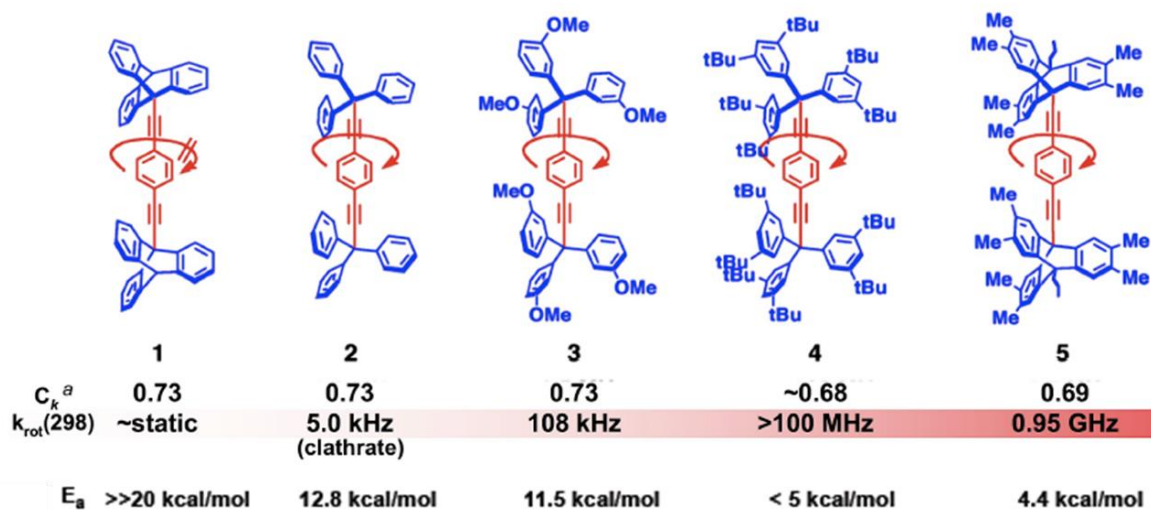
Figure 1.3.3.3. Experimentally determined barrier to rotations of five molecular rotor demonstrating relationship between packing coefficient (C_k) and activation energy of rotation[29b,37] It should be noted that while packing coefficient describes the amount of free volume about the molecule as a whole, activation energy is a function of free volume specifically about the rotator. Therefore, while packing coefficient give a good rough estimate of the trend, it is not a substitution for analysis of the crystal structure.

E_a=<5 kcal/mol. However, as this value does not take into account the local environment of the rotator, deviations from this trend, as in triptycene base rotor **1**, being static despite its similar packing coefficient to that of **2**, demonstrates a need for greater attention to be paid to the effects of molecular design on crystal engineering—a topic to be covered more thoroughly in Chapter 4.

1.4. References

1 GlaxoSmithKlein: (a.) Curzons, A.D.; Jimenez-Gonzalez, C.; Duncan, A.L.; Constable, D.J.C.; Cunningham, V.L. *Int. J. LCA.*, **2007**, *12*, 272. (b.) Jimenez-Gonzalez, C.;Curzons, A.D.; Constable, D.J.C.;Cunningham, V.L. *Int. J. LCA*, **2004**, *9*, 115.

2 Amgen: Ritter, S. K. *C&EN*, **2013**, *15*, 22.

3 Toda, F. *Acc. Chem. Res.*, **1995**, *28*, 480.

4 Desiraju, G. R.. (1987). *Organic Solid State Chemistry*. Amsterdam; Elsevier Science Publishers.

5 (a.) Quian, J.; Henderson, W. A.; Xu, W.; Bhattacharya, P.; Engelhard, M.; Borodin, O.; Zhang, J.-G. *Nat. Commun.*, **2015**, *6*, 6362. (b.) Xu, W.; Wang, J.; Ding, F.; Chen, X.; Nasybulin, E.; Zhang, Y.; Zhang, J.-G. **2014**, *7*, 513. (c.) Takehara, Z.-I. *J. Power Sources*, **1997**, *68*, 82.

6 Lewis, G.N; Keyes, F.G. *J. Am. Chem. Soc.*, **1913**, *35*, 340.

7 (a.) Lewis, G.N; Kraus, C. A. *J. Am. Chem. Soc.*, **1911**, *32*, 1459. (b.) Lewis, G.N; Keyes, F.G. *J. Am. Chem. Soc.*, **1912**, *34*, 119.

8 W. S. Harris, Ph. D. Thesis, UCRL-8381, Univ. California, Berkeley, 1958.

9 Mizushima, K.; Jones, P. C.; Wiseman, P. J., Goodenough, J. B. *Mat. Res. Bul.*, **1980**, *15*, 783.

10 Whittingham, M. S. *Proc. IEEE*, **2012**, *100*, 1518.

11 Xie, J.; Zhang, Q. *J. Mater. Chem. A*, **2016**, *4*, 7091.

12 Dunn, B.; Kamath, H.; Tarascon, J. M. *Science*, **2011**, *334*, 928.

13 Chen, H.; Armand, M.; Demailly, G.; Dolhem, F.; Poizot, P.; Tarascon, J. M. *ChemSusChem* **2008**, *1*, 348.

14 Lian, Y.; Tao, Z.; Chen, J. *Adv. Energy Mater*, **2012**, *2*, 742.

15 Goodenough, J.B.; Park, K-S. . *J. Am. Chem. Soc.*, **2013**, *135*, 1167.

16 Song, M.-K.; Park, S.; Alamgir, F. M.; Cho, J.; Liu, M. *Mat. Sci. Eng. R.*, **2011**, *72*, 203.

17 (a.) Roy, P.; Srivastava, S.K.; *J. Mater. Chem. A.*, **2015**, *3*, 2454.

18 Manthiram, A. *J. Phys. Chem. Lett.*, **2011**, *2*, 176.

19 Goodenough, J.B.; Kim, Y. *J. Power Sources*, **2011**, *196*, 6688.

20 Renault, S.; Geng, J.; Dolhem, F.; Poizot, P. *Chem. Comm.* **2011**, *47,* 2414.

21 Alt, H.; Binder, H.; Kohling, A.; Sandstede, G. *Electrochim.Acta.* **1972**, *17* 873.

22 Chen, H.; Armand, M.; Demailly, G.; Dolhem, F.; Poizot, P.; Tarascon, J. M. *ChemSusChem*, **2008**, *1* 348.

23 Sarukawa, T.; Yamaguchi, S.; Oyama, N. *J. Electro.Soc.* **2010**, *12* 196.

24 Walker, W.; Grudgeon, S.; Vezin, H.; Laruelle, S.; Armand, M.; Wudl, F.; Tarascon, J. M. *J. Mater.Chem.* **2011,** *21* 1615.

25 Renault, S.; Geng, J.; Dolhem, F.; Poizot, P. *Chem. Comm.* **2011**, *47* 2414.

26 (a.) Feynman, R.P. "There's Plenty of Room at the Bottom", *American Physical Society Meeting*. California Institute of Technology. Pasadena, CA. 29 Dec 1959. Oral Presentation. (b.)Feynman, R. P. *Eng. and Sci.*, **1960**, *23*, 22.

27 (a.) Browne, W. R.; Feringa, B. L. *Nat. Nanotechnol.*, **2006**, *1*, 25. (b.) Coskun, A.; Banaszak, M.; Astumian, R.D.; Stoddart, J.F.; Grzybowski, B.A. *Chem. Soc. Rev.*, **2012**, *41*, 19.

28 *Webster's Ninth New Collegiate Dictionary*, Merriam-Webster, Inc., Springfield, MA, 1991.

29 (a.) Karlen, S. D.; Garcia-Garibay, M. A. *Top Curr. C*hem.*,* **2005**, *262*, 179. (b.) Vogelsberg, C. S.; Garcia-Garibay, M. A. *Chem. Soc. Rev.*, **2012**, *41*, 1892.

30 Mavroidis, C.; Dubey, A.; Yarmush, M. L. *Annu. Rev. Biomed. Eng.*, **2004**, *6*, 363.

31 Garcia-Garibay, M. A. *Proc. Natl. Acad. Sci. USA,* **2005,** *102*, 10771.

32 Iwamura, I.; Mislow, K. *Acc. Chem. Res*., **1988**, *21*, 175.

33 (a.) Dominguez, Z.; Dang, H.; Strouse, M. J.; Garcia-Garibay, M. A. *J. Am. Chem. Soc.*, **2002**, *124*, 2398. (b.) Dominguez, Z.; Dang, H.; Strouse, M. J.; Garcia-Garibay, M. A. *J. Am. Chem. Soc.*, **2002**, *124*, 7719. (c.) Godinez, C. E.; Zepeda, G.; Garcia-Garibay, M. A. *J. Am. Chem. Soc.*, **2002**, *124*, 4701. (d.) Dominguez, Z.; Khuong, T-A. V.; Dang, H.; Sanrame, C.; Nuñez, J.; Garcia-Garibay, M. A. *J. Am. Chem. Soc.*, **2003**, *125*, 8827.

34 Godinez, C. E.; Zepeda, G.; Mortko, C.; Dang, H.; Garcia-Garibay, M. A. *J. Org. Chem.*, **2004**, *69*, 1652.

35 (a) Saebo, S.; Almolof, J.; Boggs, J. E.; Stark, J. G. *J. Mol. Struct. (THEOCHEM)*, **1989**, *200*, 361. (b) Sipachev, V. A.; Khaikin, L. S.; Grikina, O. E.; Nikitin, V. S.; Traettberg, M. *J. Mol. Struct*, **2000**, *523*, 1.

36 It should be noted that the solvent free analogue was also characterized, demonstrating an even higher Ck=0.74 and subsequently elevated activation energy of 14.5 kcal/mol.

37 C. S. Vogelsberg, M. A. Garcia-Garibay, Ph. D. Thesis, Univ. California, Los Angeles, 2012.

CHAPTER 2

Naphthalene Diimide Based Materials with Adjustable Redox Potentials:

Evaluation for Organic Lithium-Ion Batteries

2.1. Abstract.

The promising crystallinity and tunable redox capabilities of naphthalene diimides make them attractive candidates as electroactive materials for organic-based lithium-ion batteries. In this study, a family of naphthalene diimide derivates was synthesized and their redox properties explored with the intent of unveiling structures with reduction potentials that are higher than those encountered in previous organic redox processes. Changes in the electronic characteristics of the aryl substituents resulted in materials with discharge potentials that vary from 2.3 to 2.9 V vs. Li/Li+, with discharge capacities as high as 121 mAh/g.
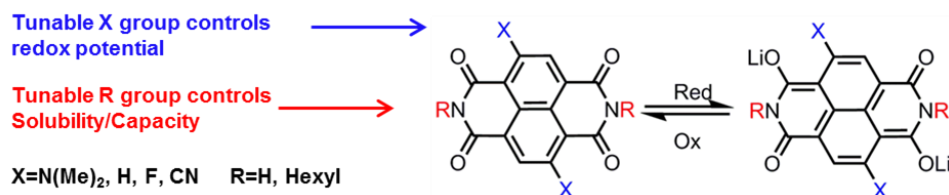

Figure 2.1. Redox capabilities of naphthalene diimide system demonstrating two connectivities to control different aspects of the system.

2.2. Introduction.

Lithium ion batteries have achieved enormous success in the area of energy storage in small electronics due to their impressive energy densities and cyclability.[1,2] These batteries are based on the use of Li intercalation compounds. Li ions are transported between two hos+t structures, a graphite negative electrode that is electrochemically connected by a non-aqueous electrolyte to the positive electrode, commonly a transition metal oxide compound. With an output voltage of ~4 V this process works relatively well, however, the required metal oxides (LCO, $LiNiO_2$, $LiMn_2O_4$) have some drawbacks: they are relatively scarce, heavy, toxic and their production requires expensive high temperature processing.[3] In recent years, there has been growing interest

in creating electroactive organic electrode materials that use natural organic sources as precursors and generally lead to environmentally benign processing.[4]

Many of these concerns can be addressed by taking advantage of organic electrodes based on bulk crystals of suitable redox active compounds. First explored in the early 1970s,[5] organic redox-active compounds tend to be less expensive, less toxic and potentially much lighter than their inorganic counterparts. Their performance, however, has been limited by their inability to reach high redox potentials, and by their tendency to dissolve in non-aqueous electrolytes, which limits their use to a few charge-discharge cycles. Nonetheless, as the limits of inorganic insertion metal oxides are being reached, organic redox materials are being revisited.[6] Recent work has focused on increasing cycling capabilities by decreasing their solubility[6-10] with the use of rigid aromatics[9-10,11] or insoluble salts[6,9]. However, their lithium-insertion potentials are still too low to compete with the nearly 4 V vs Li/Li$^+$ observed with other transition metal oxides. As illustrated in Table 2.2.1, research in organic electrodes thus far has incorporated three main categories of organic redox-active functionalities:[7,12] nitroxyl radicals, disulfides, and conjugated dicarbonyls.

Nitroxyl radicals[13] can be oxidized with potentials of ca. 3.5-3.6 V vs. Li/Li^{+}[13]. The cationic charged state of this mechanism designates it as a "p-type" redox mechanism. This narrow range is determined by its relatively isolated two-atom (N-O$^.$) redox system. Furthermore, having a one-electron redox mechanism results in a more limited energy storage capacity in comparison to the two-electron processes displayed by disulfides[14,15] and conjugated dicarbonyls.[6,8,9,16] In addition, considering that nitroxyls are oxidized in the charging process, their function depends on the insertion of charge-compensating stable anions. The large anions

such as PF_6^- that are common in Li-ion electrolytes cannot be inserted readily into the corresponding material.

The two-electron reduction of disulfides into the corresponding lithium thiolate species, illustrated with derivative **2,** is also not ideal. Disulfides display a relatively low potential,
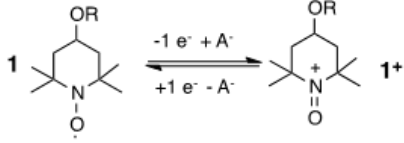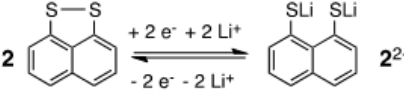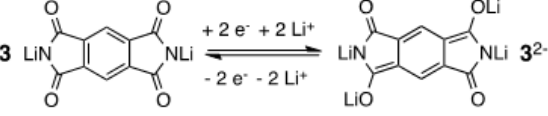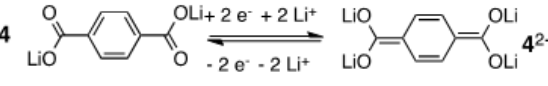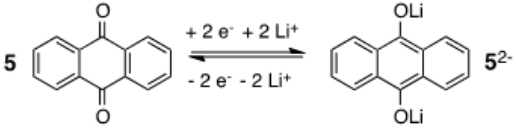
Redox Structure		Category	Discharge Potential (V vs Li/Li^{++})	Redox Type	Theoretical Capacity (mAh/g)	Reference
		Nitroxyl Radical	3.5	p-type	111	13
		Disulfide	1.8	n-type	282	15
		Dicarbonyl	1.7	n-type	235	9
		Dicarbonyl	0.8	n-type	301	18
		Dicarbonyl	2.3	n-type	257	17

Table 2.2.1. Summary of processes typical to each category: disulfide bond, nitroxide radicals and conjugated carbonyls.

typically ranging from 1.8-2.3 V vs. Li/Li,$^{+7}$ and have a redox mechanism that seems not to lend itself to large electronic variations due to the isolated nature of this particular functional group. In contrast, the reduction of conjugated carbonyls into the corresponding dialkoxides seem to have a larger range of molecular design and electronic tunability.[8,16-18] For example, compounds **3**, **4** and **5** in Table 2.2.1 display two-electron redox processes with potentials that cover a range from 0.8 V for dicarboxylate **4** and up to 2.3 V for anthraquinone **5** with a mid-point value of 1.7

V for pyromellitc diimide **3**. These variations demonstrate the relatively large range available for this redox process and the potential for fine-tuning and optimizing the observed potential.

In this chapter, we use a model system, naphthalene diimide (NDI; see Figure 1), to explore the possibility of extending the range of physical properties and redox parameters. We expect that an extended aromatic core as compared to that of pyromellitic diimide **3** should serve the dual purpose of decreasing the solubility of the crystalline material while providing opportunities to modify the LUMO levels of the parent hydrocarbon structure **6** (Figure 2.2.1, X=H) with the help of synthetically accessible substituents. Knowing that a highly desirable low solubility translates into very challenging sample tractability during synthesis and analysis, we decided to analyze two sets of structures with ($R=C_6H_{13}$) and without (R=H) an N-hexyl substituent. In this article we report the synthesis and electrochemical evaluation of compounds with a hydrocarbon aromatic core (X=H), as well compounds with electron donating $X=NMe_2$ (**7** and **11**), and electron withdrawing X=F (**8** and **12**) and X=CN (**9** and **13**) substituents (Figure 1).[19] The decreased electron density of the NDI core was expected to increase the potential of **9** as compared to that of **6** without drastically compromising its capacity.
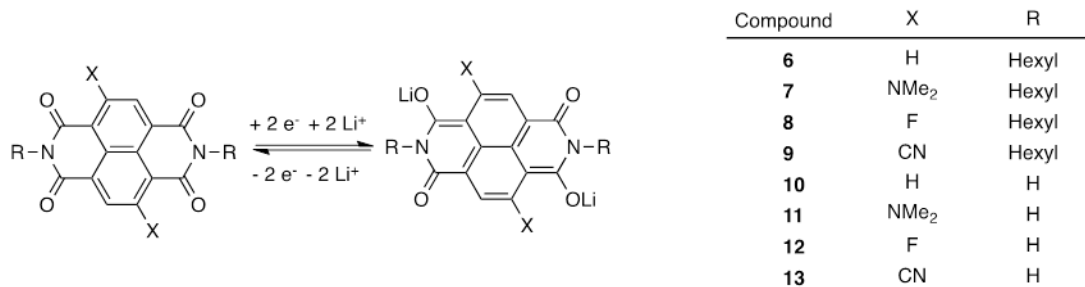

Compound	X	R
6	H	Hexyl
7	NMe$_2$	Hexyl
8	F	Hexyl
9	CN	Hexyl
10	H	H
11	NMe$_2$	H
12	F	H
13	CN	H

Figure 2.2.1. Structure and redox process of naphththalene diimides (NDIs) with different aromatic (X) and imide (R) substituents. Although there is a potential four electron mechanism resulting in the lithiation of the remaining carbonyls, attempts to reach sufficiently low potentials to access this state resulted in irreversible decomposition.[19]
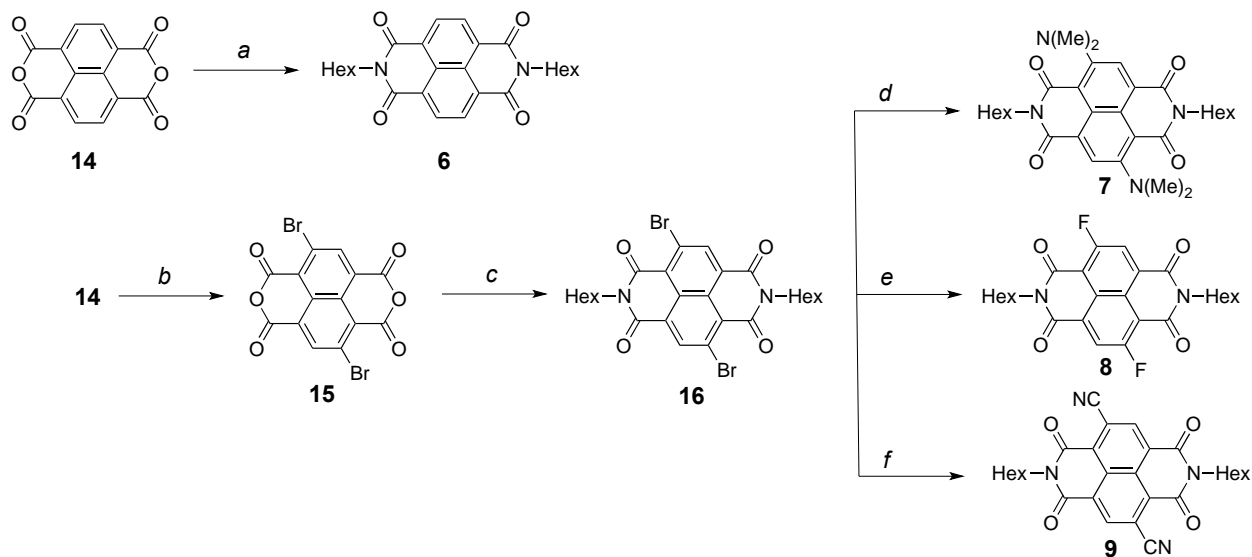
Scheme 2.2.1. (a) Hexylamine, pyridine, 120^{0}C, 83%; (b) Dibromoisocyanuric acid, sulfuric acid, 130^{0}C; (c) Hexylamine, glacial acetic acid, 120^{0}C, 40% over two steps; (d) Dimethylamine, THF, 80^{0}C, 93%; (e) KF, 18-crown-6, 3 Å molecular sieves, sulfolane, 165^{0}C, 53%; (f) CuCN, NMP, 100^{0}C, 87%.

2.3. Results and Discussion

LUMO Energies. As a starting point for this study, and to guide our electrochemical measurements, we looked for qualitative insight into the effects of substituents on the aromatic core of the NDI units. Calculations were carried out using gas phase electronic structure calculations with the B3LYP/6-311+G(d,p) level of theory for both the N-hexyl and the N-H compounds in order to establish the LUMO values versus their neutral states, which are known to correlate directly to redox potentials.[19] As shown in Table 2.3.1, the LUMO levels of N-hexyl compounds **6-9** span an energy range of 1.5 eV from the more electron-rich dimethyl-amino substituted NDI **7**, with a value of -3.0 eV, to the electron-poor cyano substituted NDI **9**, which has a value of -4.5 eV. The unsubstituted core of compound **6** and the fluorine-substituted core of NDI **8** have similar values of -3.7 eV and -3.9 eV, respectively. The larger variation observed with respect to the parent compound in the case of **7** and **9** as compared to **8** confirm a greater effect for resonance effects relative to the inductive effects of the electronegative fluorine atom.

Calculations also showed that removal of the N-hexyl groups in compounds **10**-**13** systematically

shifts the corresponding energies by ca. -0.2 to -0.3 eV, with an increase in the range of values up

to 1.6 eV between **11** (X=NMe$_2$) and **13** (X=CN).

X	R	MW	theoretical capacity (2e) [mA h g^{-1}]	experimental capacity at C/5 rate [mA h g^{-1}][a]	experimental capacity at C/5 rate [# Li]	LUMO [eV][b]	first reducton potential [V vs Li/Li$^+$][c]
H	hexyl	434.5	123	92	1.5	−3.7	2.5
NMe2	hexyl	520.7	103	41	0.8	−3.0	2.3
F	hexyl	470.5	114	45	0.8	−3.9	2.6
CN	hexyl	484.5	111	100	1.8	−4.5	2.8
H	H	266.2	201	121	1.2	−4.0	2.55
NMe2	H	352.3	152	30	0.4	−3.2	2.4
CN	H	316.2	170	34	0.4	−4.8	2.9

Table 2.3.1. Solid State electrochemical properties of NDIs. [a] A C/5 rate is the value needed for the current to reach maximum theoretical capacity to be delivered in 5 h. [b] Gas phase values obtained with the B3LYP/6-311+G(d,p) level of theory. [c] Values obtained using solid state NDI electrodes during the galvanostatic cycling experiments.

Aryl-Substituted N-Hexyl Napthalene Diimides. An experimental evaluation of the effect of aryl

substituents on the reduction potential of the more soluble N-hexyl substituted NDIs **6**-**9** was

carried out both in solution and in a coin cell format. The synthesis of these compounds was

accomplished as illustrated in Scheme 1 starting from naphththalene tetracarboxylic dianhydride

14. Compound **6** was obtained in a single step in 83% yield by reaction of **14** with hexylamine.

Compounds **7**, **8** and **9** were obtained from the N-hexyl-dibromo-naphthalenetetracarboxylic

diimide **16**, which was obtained from readily available dibromo naphthalenetetracarboxylic

dianhydride **15**.

Compound **7** was isolated as a dark blue solid in 93% yield via S$_N$Ar reaction of NDI **16**

with dimethyl amine. The fluorinated NDI **8** could be obtained via the halex process[20] in 53%

yields, and the cyano derivative **9** via copper-mediated coupling.[21] All compounds were

obtained as solids and the purity was established by thinlayer chromatography and NMR

spectroscopy. Cyclic voltammetric analysis of N-Hexyl NDIs **6**-**9** was carried in out at ambient

temperature at a 0.01 mM concentration of active material in 0.1 M tetrabutylammonium

hexafluorophosphate in CH_2Cl_2 (Figure 2). While the result obtained in dilute solution are not representative of the electrochemical behavior of the solid state material in a typical lithium-ion cell, they provide valuable information on the number of redox events and their reversibility or lack thereof. As shown in Figure 2 and in agreement with literature reports with other NDIs, [21,22] each compound exhibits two redox waves characteristic of the two-electron redox process indicated in Figure 1. The first redox wave results in a charge delocalized radical anion, and the second then results in the previously discussed dianion. It is important to point out that all the samples could be reversibly cycled. The effect of the substituent can be seen by the shift of the redox potentials in the figure from the electron donating N,N-dimethyl-aryl substituted NDI **7**, shown at the bottom with the most negative potential vs Ag/AgCl, to the most electron withdrawing cyano-aryl substituted NDI **9**, with least negative potential at the top. It is clear from the figure and Table 2.3.1 that the effects of substituents are greatest on the first reduction potential as the difference between the first and second reduction wave decreases as the aromatic substituents change from electron withdrawing –CN (**9**) and –F (**8**), to the reference compound -H (**6**) to the electron rich –NMe$_2$ (**7**). In the case of NDI **9**, the first reduction of the electron poor aromatic core occurs at a potential of -0.10 V vs Ag/AgCl and the second reduction wave occurs at a more negative potential of -0.64 V. By contrast, the comparatively electron-rich aromatic core of NDI **7** undergoes the first and second reduction waves much closer together, at

E(1/2) V vs Ag/AgCl (vs Li/Li+) in Dichloromethane

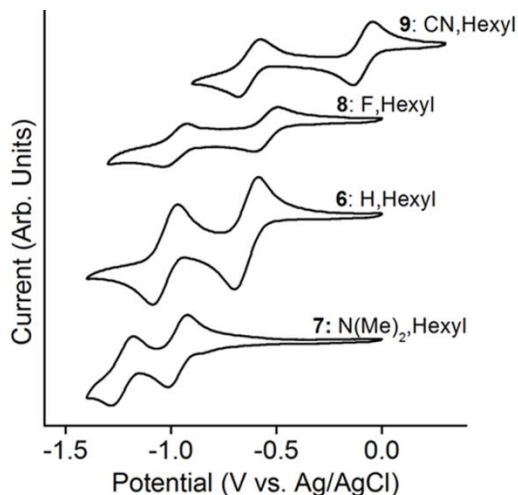|	X/X^-	X^-/X^{-2}	LUMO (eV)
6	-0.64 (2.6)	-1.03 (2.21	-3.7
7	-0.97 (2.27)	-1.23 (2.01)	-3.0
8	-0.55 (2.69)	-0.98 (2.26)	-3.9
9	-0.10 (3.14)	-0.64 (2.6)	-4.5

Figure 2.3.1. Cyclic voltammograms of NDIs **6-9** measured vs Ag/AgCl in 0.1 M Bu$_4$NPF$_6$ in CH$_2$Cl$_2$ (Li/Li$^+$ is -3.237 vs Ag/AgCl).

values of -0.97 V and -1.23 V, with a difference between them that is about half as large as that of the two reduction peaks in **9**.

Having explored the effect of aryl substitution on the redox potential of NDIs **7-9** in solution, we next explored their effect on the potential and capacity in a coin cell format. The four N-Hexyl compounds were characterised both by cyclic voltammetry and galvanostatic cycling. As shown on the left column in Figure 3, the CV curves obtained with the solid electrodes when cycled between 1 and 4 V vs Li/Li$^+$ revealed pronounced differences in shape as compared to those obtained in solution (Figure 2). Only NDI **6** exhibits two clear redox peaks (Figure 3a) while the others have a relatively large shift in the position of the peak and a significant broadening, suggesting kinetic limitations associated with electron and Li$^+$ ion transport in the bulk solid material.

The galvanostatic cycling experiments measure the cell potential during the time that it takes to cycle between two potentials as a function of a constant pre-determined applied current. The current used in these experiments (generally known as the C-rate) was based on the theoretical capacity for a given sample being reached in 5 h; a value commonly referred to as a

C/5 cycling rate (Table 2.3.1). The galvanostatic data plotted in the bottom column in Figure 3 includes representative traces of up to ten cycles for each NDI. The current flowing through the cell was used to calculate the number of Lithium ions per molecule inserted into the material during the charging process (dotted lines), or the number ions released during the discharge (solid lines). On charging, the potential increases rapidly from 1 V to a value that is characteristic of each solid NDI. The potential remains at this value until either there is a new redox event, or until the material reaches the limit of its capacity at a set value of 4V. The discharge cycles (solid lines) start at 4V, rapidly reach the corresponding pleateau(s), and eventually decrease to 1 V. One can appreciate from the galvanostatic cycling measurements that the relationship between aryl substitution and redox potential can be determined with more certainty from the plateau value. First reduction potential values of 2.3, 2.5, 2.6 and 2.8 V vs. Li/Li$^+$ can be determined for compounds **7**, **6**, **8** and **9**, respectively. These values are also included in Table 2.3.1. In agreement with the cyclic voltammetry, only compound **6** (Figure 3e) displays two clear plateaus and all others display only one, despite the two-electron redox mechanism. The initial capacities achieved by compounds **6** (Figures 3e) and **9** (Figures 3h) are determined by the extent of the plateau, and approach the theoretical maximum, with the insertion of two Li$^+$ per NDI. By comparison, compounds **7** (Figures 3f) and **8** (Figures 3g) saturate at about 0.75-1.0 Li$^+$ per NDI. Another significant feature of the galvanostatic cycling data is that the capacity for all N-hexyl compounds decreases with increasing number of cycles, likely due to the partial solubility in the electrolyte. Overall, nitrile **9** has the best initial performance (Figure 3h) with a high potential of 2.8 V vs. Li/Li$^+$, a single flat plateau, and an ability to reach close to 100% of its theoretical capacity (100 mAh g^{-1}).
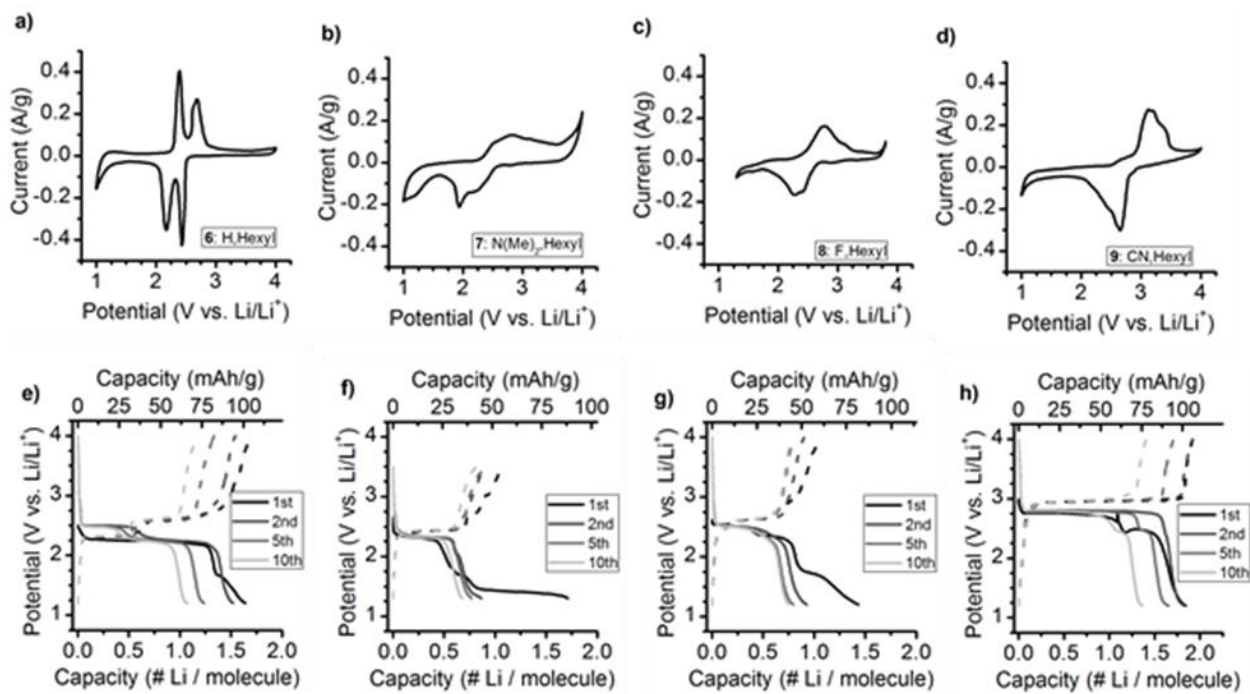
Figure 2.3.2. Cyclic voltammetry and cyclability of a) compound **6**, b) compound **7**, c) compound **8** and d) compound **9**. The galvanostatic cycling with electrodes prepared with e) compound **6**, f) **8** and g) **9** was carried out between 1 and 4 V vs Li/Li+. The N,N-Dimethyl NDI **7** in f) was cycled between 1 and 3.5 V in order to avoid an irreversible oxidation above that value.

Aryl-Substituted N-H Naphthalene Diimides. In a separate series of experiments, we examined the question of whether the loss of capacity as a function of cycle number is determined by the solubility of the N-hexyl compounds. For this study, we decided to evaluate the properties of unsubstituted secondary (N-H) NDIs **10**, **11** and **13**, which are highly insoluble and nearly intractable, but can be obtained by installing a removable protecting group to assist with solubility during the synthesis and purification of all intermediates (Scheme 2). It should be noted that while one may be concerned about the acidity of this proton, previous reports show that for diimides, this proton remains uninvolved.[9,10] Compound **10** was prepared as reported in the literature.[23] The synthesis of NDIs **11** and **13** started with previously prepared dibromo substituted dianhydride **15** to prepare the 2,4-dimethoxybenzyl protected NDI **16a** by reaction

with 2,4-dimethoxybenzyl amine, or the more soluble **16b**, by reaction with 2,4-di-n-butoxybenzyl amine (Scheme 2). The dialkoxybenzyl substituted dibromo intermediates were used to prepare the NDI **11** and **13** by S_NAr reaction with dimethylamine and Rosenmund von Braun reaction with copper cyanide followed by acid catalyzed removal of the 2,4-dialkoxybenzyl group. The use of a di-n-butoxybenzyl protected nitrile **17** for the synthesis of **13**
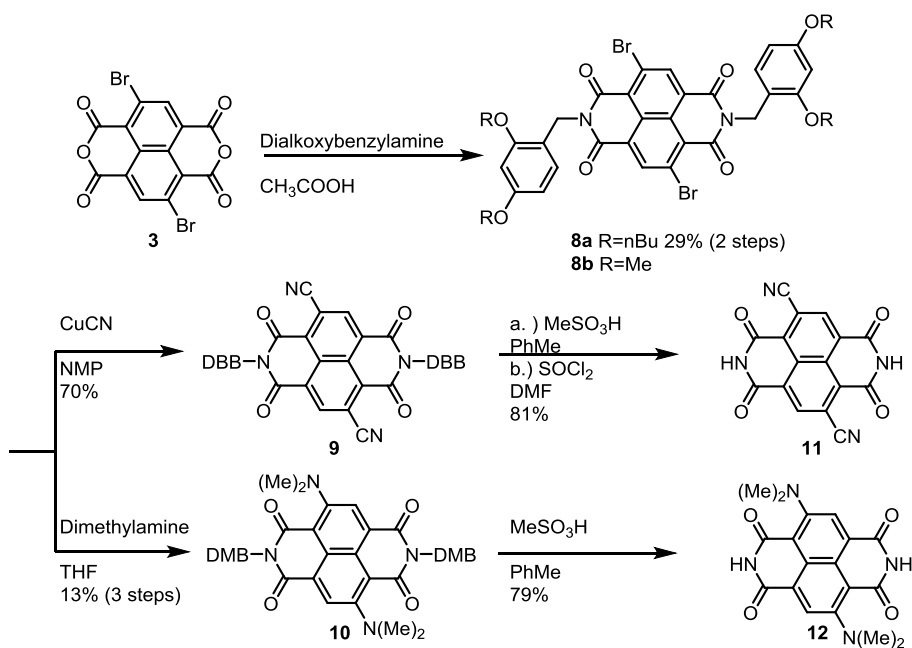
Scheme 2.3.1. (a) Dialkoxybenzyl amine (DAB), acetic acid 120 °C; (b) CuCN, NMP 100 °C, 70%; (c) Dimethylamine, THF, 80 °C, 13% over 3 steps; (d) *i.* MeSO$_3$H, PhMe, 110 °C; *ii.* SOCl$_2$, DMF, 81%; (e) MeSO$_3$H, PhMe, 110 °C, 79%.

was dictated by the low solubility of the dimethoxy analog, which had been suitable in the case of **18**. The required di-*n*-butoxy benzylamine was synthesized as described in the SI section (Scheme SI 1). The desired NDI **11** was obtained as a dark blue solid. It should be noted that acid catalyzed deprotection of **17** was accompanied with hydrolysis. However, the resulting solid could be easily dehydrated with thionyl chloride in dimethylformamide to yield desired NDI **13** as a grey solid.

Solid samples of compounds **10**, **11** and **13** were characterized by both cyclic voltammetry and galvanostatic cycling as shown in Figure 4. As expected, removal of the bulky N-Hexyl group reduces the solubility of the corresponding N-H compound making their handling difficult. The cyclic voltammograms are closely related to those of their N-hexyl counterparts, although compound **11** (Figure 4c) showed only minimal redox activity. A single very broad redox wave was observed for compounds **10** (Figure 4a) and **13** (Figure 4b). Although the theoretical capacity of compounds **10**, **11** and **13** increases in comparison to the N-hexyl series due to their lower molecular weight, the values obtained from the galvanostatic cycling experiments revealed significantly lower Li^+ insertion, with first cycle values of ~ 1.0 Li^+ for **10** (Figure 4a), 0.75 Li^+ for **13** (Figure e) and <0.5 for **11** (figure 4f). Despite the significantly lower solubility of all three NDIs, only the unsubstituted derivative **10** showed better capacity retention during cycling. In general, the N-H compounds have a lower utilization than the N-Hexyl analogs, suggesting that the N-H compounds may have tighter packing arrangements that prevent
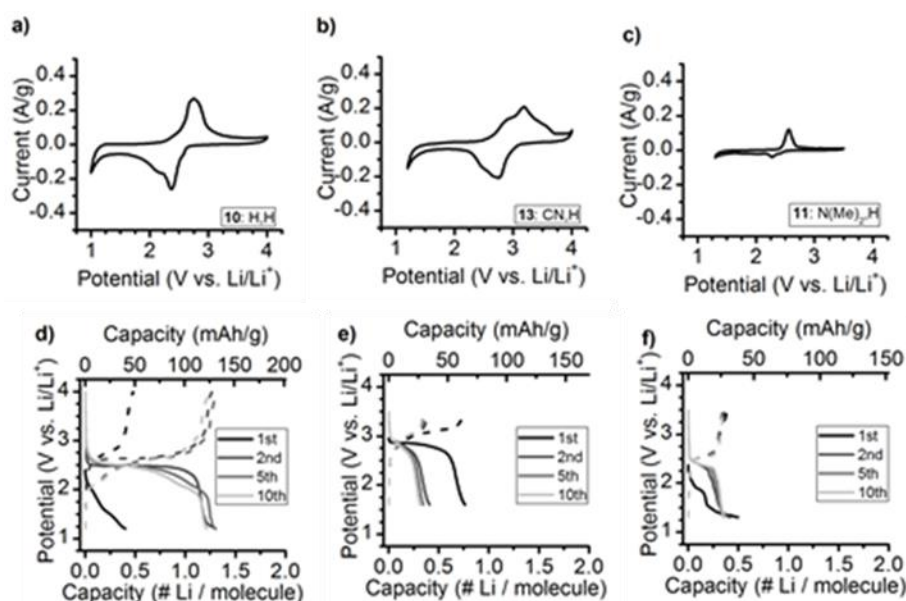
Figure 2.3.3. Cyclic voltammetry and galvanostatic cyclability of a) and d) compound **10**, b) and e) compound **13**, and c) and f) compound **11**.

the intercalation of the Li+ ions.   Another possible explanation is that the N-Hexyl compounds may be cycling in solution rather than in the solid state, but this is confounded by the poor capacity fade of the N-Hexyl compounds and the superior cyclability of the highly insoluble NDI **10**. Figure 5 highlights the cyclability of the three best performing NDIs. The two relatively soluble N-hexyl NDIs **9** (CN) and **6** (H) have the highest initial utilization, but their capacity decreases by ~ 30% over 20 cycles. In contrast, the unsubstituted NDI **10** begins with a lower utilization value but is able to maintain ~ 90% after 20 cycles. While it is possible that conformational degrees of freedom provided by the hexyl chains may help their crystal tolerate the structural changes required for the NDI reduction and initial insertion of the lithium ions, one could also conclude that the higher solubility compromises the integrity of the solid electrodes. Moreover, the much stronger lattice energies of the un-substituted NDI **10** appear to reduce the loss of material but also limit the amount of lithium that can be inserted in the crystal lattice.
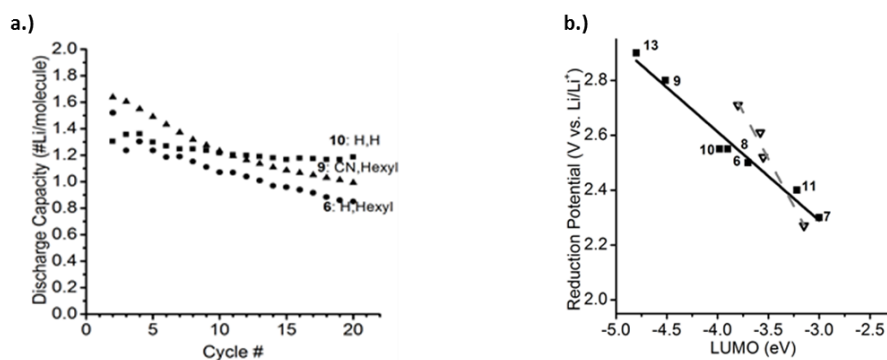
Figure 2.3.4. (a.) Discharge capacity vs. cycle number for three of the compounds tested. Cycling data for all compounds studied can be found in the supplementary information. (b.) Solid state reduction potential vs. calculated gas-phase B3LYP/6-311+G(d,p) LUMO energy levels. Numbered solid squares correspond to the NDI studies here and open triangles to heterocyclic anthraquinone analogs reported by Liang *et al.*[16]

It is worth noting that the experimental reduction potentials for the organic electrodes prepared with NDIs bearing various aromatic substituents have a relatively good correlation with the gas phase electronic structure calculations computed at the B3LYP/6-311+G(d,p) level of

theory. This can be readily appreciated in the calculated LUMO vs. the solid state reduction potential shown in Figure 6, which shows a linear trend. A similar correlation was recently reported by Liang *et al.,*[16] in a study of heterocyclic anthraquinone analogues, which also displayed a linear correlation but with a somewhat steeper slope. While two data sets are clearly too limited to draw conclusions, these results suggest that structural factors within a given compound family may dictate the relationship between the reduction potential in the gas and that in the solid state.

2.4. Conclusions

With a starting potential of 2.55 V vs Li/Li$^+$ and 60% theoretical capacity at C/5 rate, parent naphthalene diimide **10** is both an intriguing material for lithium-ion energy storage and an excellent model system for studying the tailorability of organic electrode materials. The use of N- and aryl-substitution detailed in this article illustrates ways to control cycling performance and redox potential by influencing the solubility and electronic properties of the corresponding materials. The N-hexyl- nitrile-substituted NDI **9** has the highest utilization (90%) and second highest potential (2.8 V vs. Li/Li$^+$) of the compounds studied. This material maintains an appreciable capacity (100 mAh/g) despite a relatively high molecular weight. Furthermore, aryl substitution with CN-, F-, and Me$_2$N- groups allows the redox potential of the NDIs to be tailored between 2.9 and 2.3 V vs Li/Li$^+$ without significantly affecting the solubility or molecular weight. This could be a distinct advantage over standard transition-metal based lithium-ion electrode materials, whose potentials are largely confined to the energy levels of the valence states of the metal. We expect the interest in organic electrode materials such as NDI to increase as their tailorability gains greater recognition.

2.5. Experimental

2.5.1. Sample Preparation

Materials Synthesis. All the naphthalene diimides studied in this work were synthesized by the procedures indicated in Schemes 1 and 2. Their characterization and purity were determined by standard spectroscopic techniques (please see SI).

Electrode preparation. Electrodes were prepared by drop casting a slurry of the electroactive material, acetylene black (Alfa Aesar #39724) conductive additive, and polyvinylidene fluoride (PVDF) binder (Kynar PVDF) onto pre-cut current collectors, which were allowed to dry under ambient conditions. The slurries had a nominal composition of 45:50:5 electroactive material:carbon:PVDF, with the PVDF dissolved in N-methyl pyrrolidone (NMP) prior to addition to the slurry. Enough NMP (Sigma Aldrich #443778) was added to form a paint-like consistency; nominally 800 μL NMP per 100mg of dry material (inclusive of the NMP used to dissolve the PVDF). A volume of 30μL of slurry was pipetted onto each 3/8" diameter carbon-coated aluminum current collector (Exopac Z-Flo 2650), resulting in an average areal loading of 6 mg cm^{-2}.

Electrochemical Characterization in Solution: The compounds were cycled in 0.1 M tetrabutylammonium hexafluorophosphate in CH_2Cl_2. A platinum wire and platinum disk were used for working and counter electrodes, respectively, and the working potential was measured versus a Ag/AgCl reference electrode.[24]

Electrochemical Characterization in the Solid State: Electrodes were tested in a 2016 coin cell with 1M $LiClO_4$ in 1:1 vol/vol ethylene carbonate : dimethyl carbonate (EC:DMC) electrolyte, using lithium metal as counter electrode and Celgard ##3401 separator. Minimum electrolyte volume was used in order to moisten the separator. The cells were assembled in an Argon filled glove box containing less than 1 ppm water and oxygen. Electrochemical characterization was

performed using a Biologic VMP-3 system. Each cell was characterized by cyclic voltammetry (CV) at multiple sweep rates and galvanostatic cycling at a C/5 rate based on the theoretical two-electron capacity of the electroactive material.

2.5.2. Synthetic Procedures

All reactions were performed under an inert atmosphere of argon unless otherwise stated. Chemicals were purchased from commercially available sources and used without further purification unless otherwise noted. Nuclear magnetic resonance (NMR) spectra for ^{1}H were obtained at 300, 400 or 500 MHz as noted, for ^{13}C at 125 MHz and for ^{19}F at 376 MHz. All chemical shifts are reported in ppm on the δ-scale using the residual natural abundance isotopes of the solvents as references. CDCl$_3$ was calibrated at δ7.26 and δ77.16 for ^{1}H and ^{13}C, respectively. DMSO-d_6 was calibrated at δ2.50 and δ39.52 for ^{1}H and ^{13}C, respectively. TFA-d was calibrated at δ11.5 and δ164.2 for for ^{1}H and ^{13}C, respectively, and CD$_2$Cl$_2$ was calibrated at δ5.32 for [1]H (not used for carbon). Freon-11 (CFCl$_3$) was calibrated at δ0.0 for fluorine. IR spectral data was recorded in cm^{-1} using an Attenuated Total Reflectance (ATR)-IR Spectrometer. High resolution mass spectrometry was performed using electrospray ionization with a time of flight (ESI-TOF) mass spectrometer.
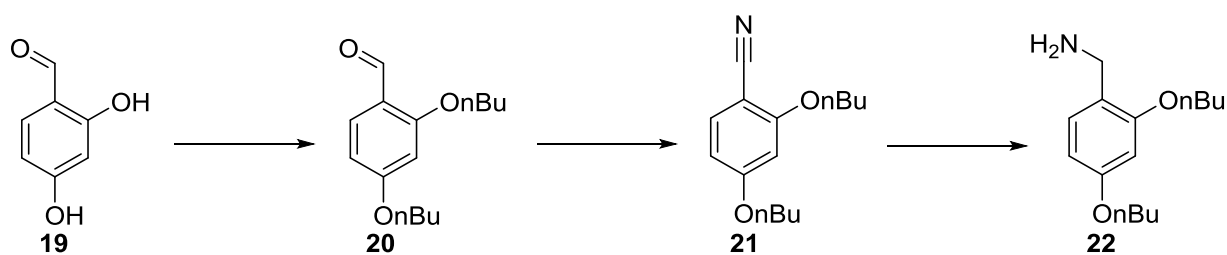
Synthesis of 2,4-dibutoxybenzaldehyde (20). Compound 20 was synthesized according to previously reported literature procedures.[25]

Synthesis of 2,4-dibutoxybenzonitrile (21)[26]. Compound 20 (220 mg, 0.879 mmol) and hydroxylamine hydrochloride (67 mg,0.967mmol) were dissolved in DMSO (2.5 mL). Reaction mixture was heated to 90°C for 1.5 hours. Solvent was removed under reduced pressure to yield yellow oil. Oil was diluted with diethyl ether (20 mL) and washed with brine (3x20 mL). Organics were dried with MgSO$_4$ and solvent was evaporated under reduced pressure. Crude product was purified by flash column chromatography (1:1 dichloromethane/ hexane) to yield compound 21 (202 mg, 93%) as clear oil. ^{1}H NMR (400 MHz, CDCl$_3$): δ = 7.42 (d, *J*= 8.6 Hz, 1H), 6.46 (dd, *J*= 8.6, 2.2 Hz, 1H), 6.42 (d, *J*=2.2 Hz, 1H), 4.02 (t, *J*=6.4 Hz, 2H), 3.98 (t, *J*=6.4 Hz, 2H), 1.78 (m, 4H), 1.49 (m, 4H), 0.97 (t, *J*= 7.4 Hz, 6H); ^{13}C NMR (125 MHz, CDCl$_3$): δ = 164.2, 162.6, 135.0, 117.2, 106.2, 99.7, 94.1, 68.8, 68.3, 31.2, 31.0, 19.30, 19.28, 13.9; IR (cm^{-1}): 2959, 2935, 2874, 2221, 1605, 1572, 1505, 1466, 1432, 1389, 1307, 1270, 1185, 1122, 1108, 1065, 1023, 835; HRMS (ESI) calcd for C$_{15}$H$_{21}$NO$_2$ [M+H]$^+$ 248.1651, found 248.1656.

Synthesis of 2,4-dibutoxybenzylamine (22). Compound 21 (1.06g, 4.3 mmol) was dissolved in anhydrous THF (47 mL) in flame dried round bottom and condenser system. Reaction was cooled to 0°C. Lithium aluminum hydride (488mg, 12.86 mmol) was added and reaction was heated to reflux for 3 hours. Reaction was cooled to 0°C. H$_2$O (2mL) was added slowly. A 15% NaOH solution (1mL) and H$_2$O (3mL) were added. Reaction was diluted with diethyl ether (50 mL) and washed with water (3x50mL). Organics were dried with Na$_2$SO$_4$. Solvent was evaporated under reduced pressure to yield compound 22 (1.018g, 95%) as pale yellow oil. Characterization matches previously reported literature data^i. Material was carried on without further purification.

Synthesis of 2,7-dihexanoylbenzo[lmn][3,8]phenanthroline-1,3,6,8(2H,7H)-tetraone (6). NTCDA (100 mg, 0.372 mmol) was suspended in pyridine (6 mL). Hexylamine (148 µL,

1.12 mmol) was added and reaction was heated to 120°C under reflux for 18 hours. Reaction was allowed to cool down to room temperature. HCl (0.6 mL) in MeOH (6 mL) was added and reaction was filtered and solid washed with MeOH (3 x 10 mL) to yield bright pink solid. Purification of the crude material by flash column chromatography (Dichloromethane/Hexane 7:3) yielded **6** (134 mg, 83%) as white solid. Characterization matches previously reported literature data.[27]

Synthesis of 4,9-dibromoisochromeno[6,5,4-def]isochromene-1,3,6,8-tetraone (15). Compound was synthesized according to previously reported literature procedures.[28] Synthesis was carried out with reagent dibromoisocyanuric acid, which was also synthesized according to previously reported literature procedures.[29] Product was isolated as bright yellow solid and contained a mixture of brominated products. Product was carried on without further purification.

Synthesis of 4,9-dibromo-2,7-dihexanoylbenzo[lmn][3,8]phenanthroline-1,3,6,8(2H, 7H)-tetraone (16). Compound **15** (500 mg) was suspended in acetic acid (15 mL). Hexylamine (1.524 mL, 11.54 mmol) was added and reaction mixture was heated to reflux for 30 minutes. Reaction mixture was allowed to cool down to room temperature. Reaction mixture was filtered and solid washed with acetic acid, water (2x10mL) and MeOH (2x10mL). Dark orange solid was purified by flash column chromatography on silica gel (3:2 dichloromethane/hexane) to yield 10 (271 mg, 40% over two steps) as pale yellow solid. ^{1}H NMR (400 MHz, CDCl$_3$): δ = 8.99 (s, 2H), 4.19 (t, J= 7.7 Hz, 4H), 1.74 (m, 4H), 1.40 (m, 4H), 1.35 (m, 8H), 0.90 (t, J=6.9 Hz, 6H); ^{13}C NMR (125 MHz, CDCl$_3$): δ = 160.90, 160.87, 139.2, 128.5, 127.9, 125.5, 124.2, 41.8, 31.6, 28.0, 26.9, 22.7, 13.2; IR (cm^{-1}): 3356, 3058, 2955, 2917, 2847, 1905, 1702, 1653, 1559, 1436, 1373, 1314, 1277, 1237, 1194, 1172, 1107, 957, 862, 787, 765, 723; HRMS (ESI) calcd for C$_{26}$H$_{28}$Br$_2$N$_2$O$_4$ [M]$^-$ 590.0416, found 590.0417.

Synthesis of 4,9-bis(dimethylamino)-2,7-dihexanoylbenzo[lmn][3,8]phenanthroline-1,3,6,8(2H,7H)-tetraone (7). Compound 16 (28 mg, 0.047 mmol) was suspended in dimethylamine in THF (2M, 4 mL) in a sealed tube. Reaction was heated to 80°C for 12 hours. Solvent was removed under reduced pressure. Product was purified by flash column chromatography to yield product (23 mg, 93%) as blue solid. ^{1}H NMR (500 MHz, CDCl$_3$): δ = 8.44 (s, 2H), 4.19 (t, *J*=7.6 Hz, 4H), 1.71 (m, 4H), 1.40 (m, 4H), 1.32 (m, 8H), 0.88 (t, *J*=7.0, 6H); ^{13}C NMR (125 MHz, CDCl$_3$): δ = 163.6, 162.0, 151.7, 125.3, 123.7, 123.4, 107.4, 44.3, 41.1, 31.7, 28.4, 27.0, 22.7, 14.2; IR (cm^{-1}): 2953, 2928, 2855, 2800, 1687, 1650, 1572, 1500, 1444, 1399, 1334, 1316, 1238, 1190, 1124, 1064, 947, 791; (HRMS (ESI) calcd for C$_{30}$H$_{40}$N$_4$O$_4$ [M+H]$^+$ 521.3128, found 521.3119.

Synthesis of 4,9-difluoro-2,7-dihexanoylbenzo[lmn][3,8]phenanthroline-1,3,6,8(2H, 7H)-tetraone (8). Compound 16 (110 mg, 0.186 mmol), 18-Crown-6 (25 mg, 0.093 mmol), and freshly dehydrated KF (75 mg, 1.30 mmol) were dissolved in anhydrous tetramethylene sulfone (1.5 mL) in a flame dried flask over 3 Å molecular sieves. Reaction was heated to 165°C and stirred for 45 minutes. Reaction was allowed to cool down to room temperature. H$_2$O (10 mL) was added and reaction was allowed to stir at room temperature for 20 mins, while a brown solid precipitated out. Reaction was filtered and crude product washed with water. Crude product was purified by flash column chromatography (1:1 dichloromethane/ hexane) and solvent was evaporated under reduced pressure to yield product (46 mg, 53%) as pale pink solid. ^{1}H NMR (400 MHz, CDCl$_3$): δ = 8.53 (dd, *J*= 8.0, 3.1 Hz, 2H), 4.17 (t, *J*= 7.6, 4H), 1.73 (m, 4H), 1.42 (m, 4H), 1.34 (m, 8H), 0.90 (t, *J*= 6.9, 6H); ^{19}F NMR (376 MHz, CDCl$_3$): δ = −101.62 (dd, *J*= 8.0, 3.2 Hz); ^{13}C NMR (125 MHz, CDCl$_3$): δ = 162.9 (d, *J*=275.8 Hz), 161.2, 159.8, 129.0, 125.1, 123.7 (d, *J*= 27.5 Hz), 112.4, 41.2, 31.6, 28.0, 26.8, 22.7, 14.2; IR (cm^{-1}): 3068, 3048, 2963,

2923, 2855, 1704, 1657, 1588, 1513, 1454, 1398, 1329, 1317, 1271, 1253, 1221, 1190, 1074, 947, 792; HRMS (ESI) calcd for $C_{26}H_{28}F_2N_2O_4$ [M]$^-$ 470.2017, found 470.2019

Synthesis of 2,7-dihexanoyl-1,3,6,8-tetraoxo-1,2,3,6,7,8-hexahydrobenzo[lmn][3,8] phenanthroline-4,9-dicarbonitrile (0). Compound 16 (37mg, 0.0624mmol) was dissolved in NMP (4mL). CuCN (56mg, 0.624mmol) was added and reaction heated to 100°C. Reaction was allowed to stir for 2 hours. Solvent was removed under reduced pressure to yield dark brown solid. Brown solid was suspended in dichloromethane and filtered. Solid was washed continuously with dichloromethane until filtrate no longer contained product by TLC. Filtrate was evaporated under reduced pressure to yield crude product as pale brown solid. Crude product was purified by flash column chromatography (DCM) to yield 4 (26mg, 87%) as off-white solid. ^{1}H NMR (400 MHz, CDCl$_3$): δ = 9.04 (s, 2H), 4.23 (t, *J*= 7.7 Hz, 4H), 1.76 (m, 4H), 1.43 (m, 4H), 1.35 (m, 8H), 0.90 (t, *J*=6.8 Hz, 6H); ^{13}C NMR (125 MHz, CDCl$_3$):δ = 160.2, 159.8, 136.1, 128.8, 127.6, 127.3, 117.0, 115.9, 42.0, 31.5, 28.0, 26.8, 22.7, 1 4.1; IR (cm^{-1}): 3068, 2952, 2922, 2856, 1708, 1655, 1588, 1452, 1379, 1345, 1323, 1281, 1255, 1238, 1199, 1144, 964, 794, 766, 727, 662; HRMS (ESI) calcd for $C_{28}H_{28}N_4O_4$ [M]$^-$ 484.2111, found 484.2108.
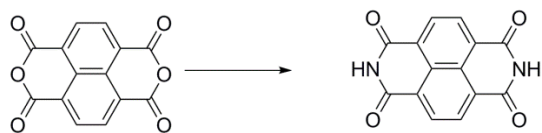
Synthesis of benzo[lmn][3,8]phenanthroline-1,3,6,8(2H,7H)-tetraone (10). Compound 10 was synthesized according to previously reported literature procedures.[30]

Synthesis of 4,9-dibromo-2,7-bis(2,4-dimethoxybenzyl)benzo[lmn][3,8] phenanthroline-1,3,6,8(2H,7H)-tetraone (16a). Compound 15 (200 mg) was suspended in acetic acid (6 mL). 2, 4-dimethoxybenzylamine (0.69 mL, 4.62 mmol) was added and reaction

was heated to reflux for 30 mins. Reaction was cooled to room temperature. Reaction mixture was filtered and solid was washed with acetic acid (2 mL), H_2O (2x5 mL) and MeOH (2x5mL) to yield crude product as orange solid. Product was carried on without further purification.

Synthesis of 2,7-bis(2,4-dimethoxybenzyl)-4,9-bis(dimethylamino)benzo[lmn][3,8] phenanthroline-1,3,6,8(2H,7H)-tetraone (18a). Compound 16a (44 mg) was added to a sealed tube under anhydrous conditions. Dimethylamine in THF (2M, 3mL) was added and reaction mixture was stirred at 95°C for 20 hours in a sealed tube. Solvent was evaporated under reduced pressure. Crude product was purified via flash column chromatography (100% CH_2Cl_2 to 49:1 CH_2Cl_2/Et_2O) to yield 13 (34 mg, 13% over three steps) as blue solid. ^{1}H NMR (400 MHz, $CDCl_3$): δ = 8.44 (s, 2H), 6.99 (d, *J*= 8.3 Hz, 2H), 6.46 (d, *J*= 2.4 Hz, 2H), 6.34 (d, *J*= 8.4, 2.4 Hz, 2H), 5.36 (s, 4H), 3.85 (s, 6H), 3.75 (s, 6H), 3.11 (s, 12H); ^{13}C NMR (125 MHz, $CDCl_3$): δ = 163.7, 162.0, 160.1, 158.3, 151.6, 128.3, 125.3, 123.8, 123.5, 117.9, 107.4, 104.1, 98.7, 55.7, 55.5, 44.2, 39.3; IR (cm^{-1}): 3079, 3000, 2937, 2838, 1682, 1645, 1618, 1571, 1499, 1439, 1399, 1304, 1261, 1237, 1206, 1155, 1123, 1029, 973, 918, 859,; (HRMS (ESI) calcd for $C_{36}H_{36}N_4O_8$ [M+H][+] 653.2611, found 653.2634.

Synthesis of 4,9-bis(dimethylamino)benzo[lmn][3,8]phenanthroline-1,3,6,8(2H,7H)-tetraone (11). Compound 118a (121 mg, 0.185 mmol) was dissolved in a biphasic reaction mixture of toluene (13 mL) and freshly distilled methanesulfonic acid (1.3 mL). Reaction was heated to 115°C for 3 hours. Reaction mixture was cooled to 0[0]C. Ammonium hydroxide was added slowly until reaction mixture was neutralized. Solvent was evaporated under reduced pressure. Solid was washed with H_2O, MeOH, CH_2Cl_2 and Et_2O sequentially until each wash was clear to yield product (51 mg, 79%) as blue/purple solid. ^{1}H NMR (400 MHz, TFA-d): δ = 9.48 (s, 2H), 3.73 (s, 2H); ^{13}C NMR (125 MHz, TFA-d): δ = 167.2, 163.2, 149.0, 132.7,

130.7, 128.2, 119.6 (overlaps with solvent satellite peak), 48.8; IR (cm^{-1}): 3171, 3105, 3047, 2842, 1698, 1657, 1567, 1500, 1430, 1406, 1314, 1270, 1208, 1150, 1128, 1059, 935, 900, 888, 829, 779, 762, 706; (HRMS (ESI) calcd for $C_{18}H_{16}N_4O_4$ [M+H]$^+$ 353.1250, found 353.1251.

Synthesis   4,9-dibromo-2,7-bis(2,4-dibutoxybenzyl)benzo[lmn][3,8]phenanthroline-1,3,6,8(2H,7H)-tetraone (16b). Compound 15 (242 mg) was suspended in acetic acid (17 mL). Compound 17 (600 mg, 2.387 mmol) was added and reaction was heated to reflux for 5 hours. Reaction was cooled to room temperature. H_2O (20 mL) was added and reaction mixture was filtered. Crude solid was washed with water (3x10mL)and MeOH (10 mL). Solid was purified by flash column chromatography to yield product (146 mg, 29% over two steps) as pale orange solid. ^{1}H NMR (500 MHz, CDCl$_3$): δ = 8.97 (s, 2H), 7.15 (d, *J*= 8.3 Hz, 2H), 6.39 (m, 4H), 5.36 (s, 2H), 3.91 (m, 8H), 1.72 (m, 8H), 1.44 (m, 8H), 0.94 (m, 12H); ^{13}C NMR (125 MHz, CDCl$_3$): δ = 160.9, 160.6, 160.1, 158.1, 139.2, 130.1, 128.4, 127.9, 125.6, 124.4, 116.2, 104.5, 99.8, 68.0, 67.8, 40.6, 31.48, 31.46, 19.5, 19.4, 14.1, 14.0; IR (cm^{-1}): HRMS (ESI) calcd for $C_{44}H_{48}Br_2N_2O_8$ [M]$^-$ 890.1777, found 890.1816.

Synthesis of 2,7-bis(2,4-dibutoxybenzyl)-1,3,6,8-tetraoxo-1,2,3,6,7,8-hexahydrobenzo [lmn][3,8]phenanthroline-4,9-dicarbonitrile (17b). Compound 16b (314 mg, 0.352 mmol) was suspended in NMP (20 mL). CuCN (314 mg, 3.516 mmol) was added and reaction was heated to 100°C for three hours. Solvent was removed under reduced pressure to yield dark brown solid. Brown solid was suspended in dichloromethane and filtered. Solid was washed continuously with dichloromethane until filtrate no longer contained product by TLC. Filtrate was evaporated under reduced pressure to yield crude product as pale brown solid. Crude product was purified by flash column chromatography (DCM) to yield 12 (193 mg, 70%) as brown solid. ^{1}H NMR (400 MHz, CD$_2$Cl$_2$): δ = 9.00 (s, 2H), 7.19 (d, *J* = 8.7 Hz, 2H), 6.41 (m, 4H), 5.36 (s, 4H), 3.92

(m, 8H), 1.70 (m, 8H), 1.44 (m, 8H), 0.94 (m, 12H); ^{13}C NMR (125 MHz, CDCl$_3$): δ = 160.5, 160.0, 159.6, 158.2, 136.0, 131.3, 128.9, 127.6, 127.5, 116.9, 115.9, 115.4, 104.6, 99.8, 68.1, 67.9, 40.9, 31.5, 31.4, 19.5, 19.4, 14.03, 13.97; IR (cm^{-1}): 2960, 2925, 2855, 1713, 1669, 1615 1587, 1511, 1446, 1384, 1309, 1286, 1260, 1185, 1092, 1024, 798; HRMS (ESI) calcd for C$_{46}$H$_{48}$N$_4$O$_8$ [M]$^-$ 784.3472, found 784.3426.

Synthesis of 1,3,6,8-tetraoxo-1,2,3,6,7,8-hexahydrobenzo[lmn][3,8]phenanthroline-4,9-dicarbonitrile (13). Compound 17b (92 mg, 0.117 mmol) was dissolved in toluene (8 mL). Freshly distilled methanesulfonic acid (0.8 mL) was added and reaction was heated to 110^{0}C for 4 hours. Reaction mixture was cooled down to 0^{0}C. Concentrated ammonium hydroxide was added dropwise until reaction mixture had been neutralized. Solvents were evaporated under reduced pressure and solid was washed and separated via centrifuge with H$_2$O, MeOH, CH$_2$Cl$_2$ and Et$_2$O until each solvent became clear to yield a grey solid. Grey solid was suspended in anhydrous DMF (6 mL). Thionyl chloride (60 μL) was added and reaction was allowed to stir for 1.5 hours. Solvent was evaporated under reduced pressure. Solid was washed with H$_2$O, aqueous sodium bicarbonate, MeOH, CH$_2$Cl$_2$ and Et$_2$O until each solvent ran clear to yield 6 (30 mg, 81%) as grey solid. ^{1}H NMR (400 MHz, DMSO): δ = 12.55 (s, 2H), 8.82 (s, 2H); ^{13}C NMR (125 MHz, DMSO): δ = 161.4, 161.1, 133.5, 130.0, 128.7, 127.6, 116.5, 113.7; IR (cm^{-1}): 3383, 3206, 3102, 3080, 2841, 2236, 1709, 1689, 1589, 1441, 1382, 1319, 1262, 1173, 1057, 939, 811, 780, 695;□□HRMS (ESI) calcd for C$_{18}$H$_4$N$_4$O$_4$.

2.6. Appendix: Compound characterization

Figure 2.6.1. ^{1}H NMR of compound 21 in CDCl$_3$ at 400 MHz
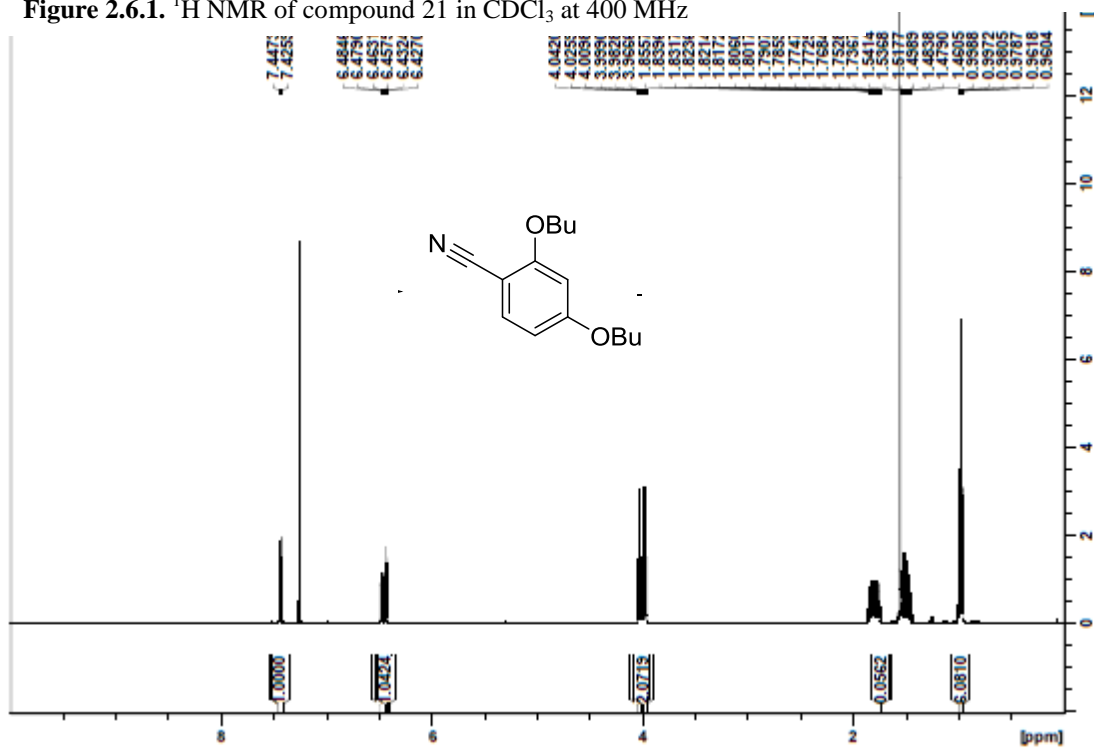
Figure 2.6.2. ^{13}C NMR of compound 21 in CDCl$_3$ at 125 MHz
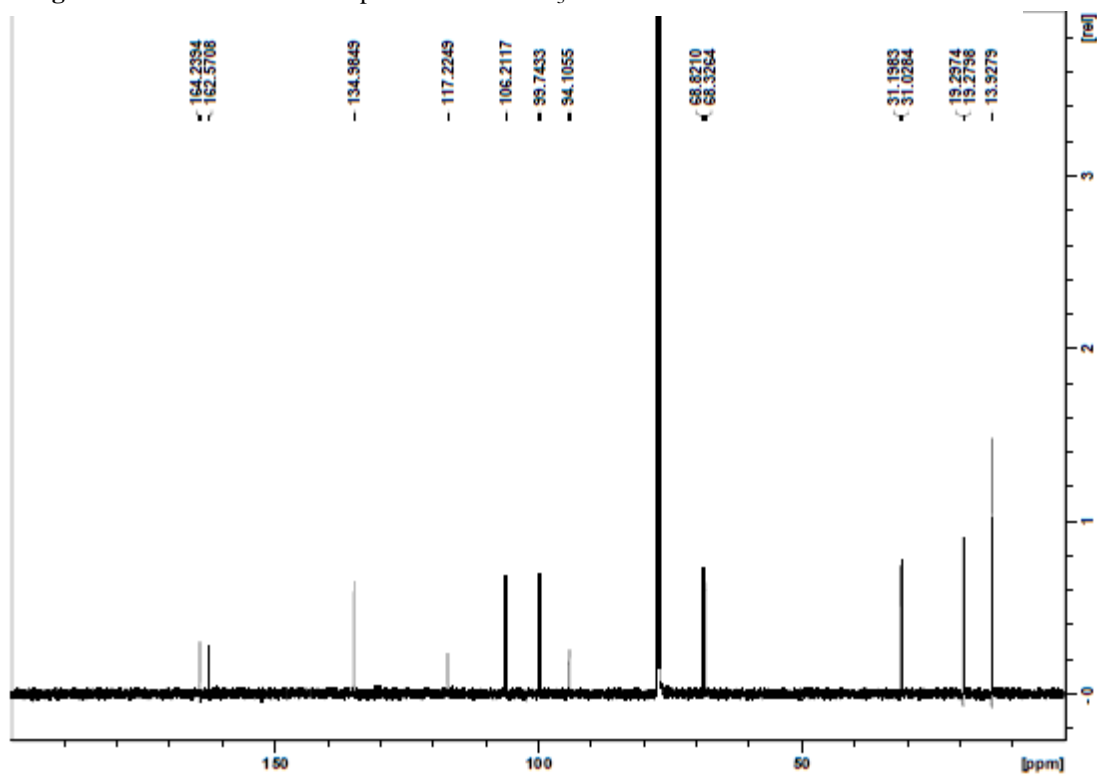
Figure 2.6.3. ^{1}H NMR of compound 16 in CDCl$_3$ at 400 MHz
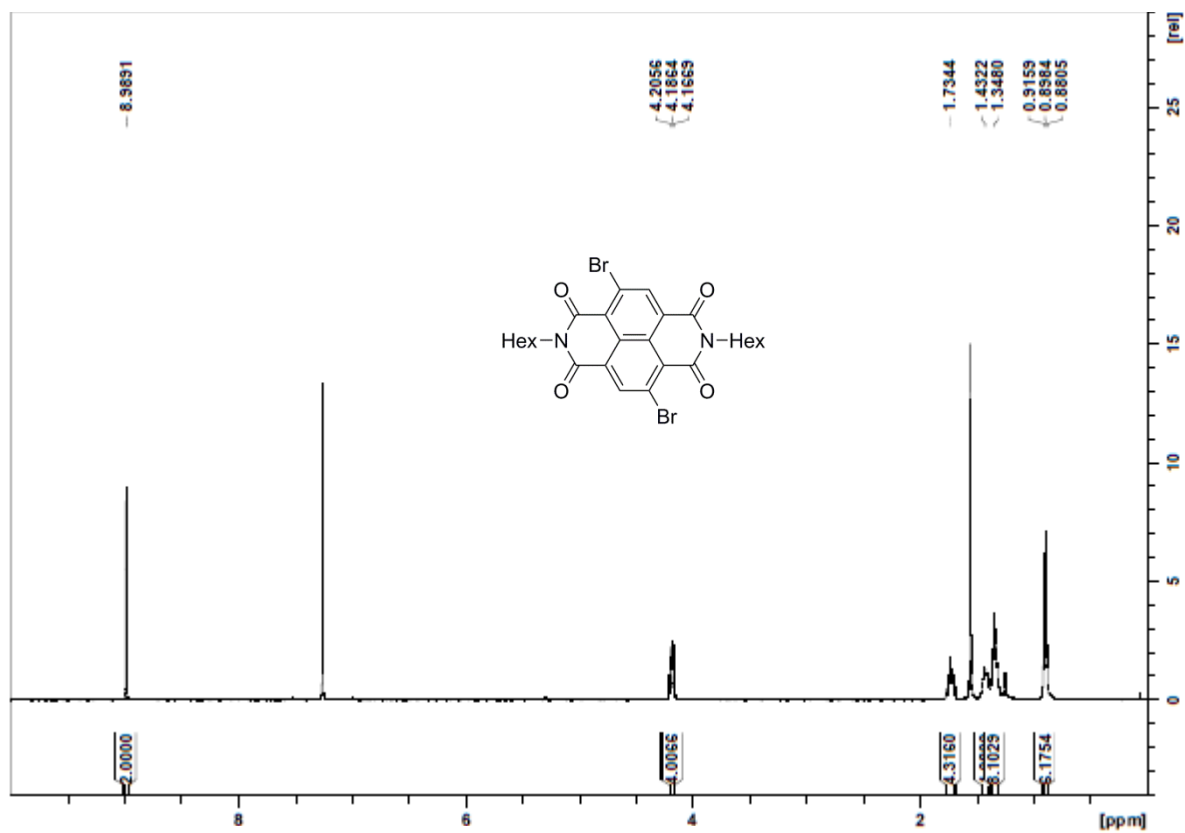
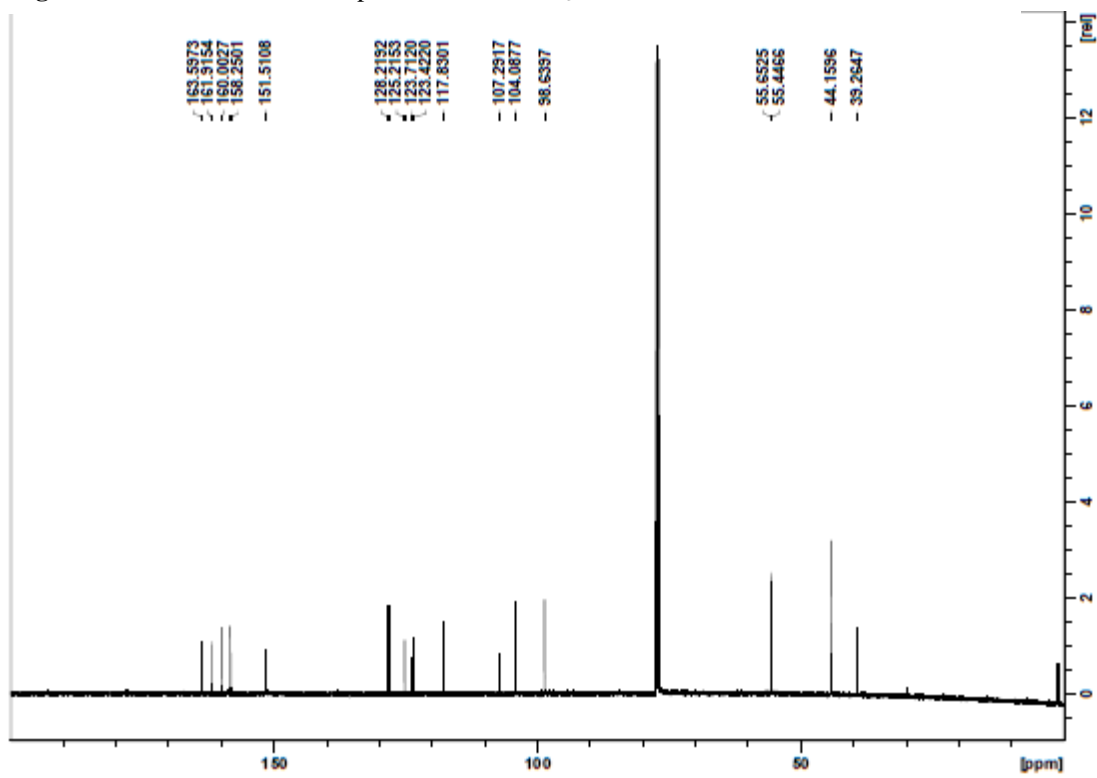**Figure 2.6.4.** ^{13}C NMR of compound 16 in CDCl$_3$ at 125 MHz
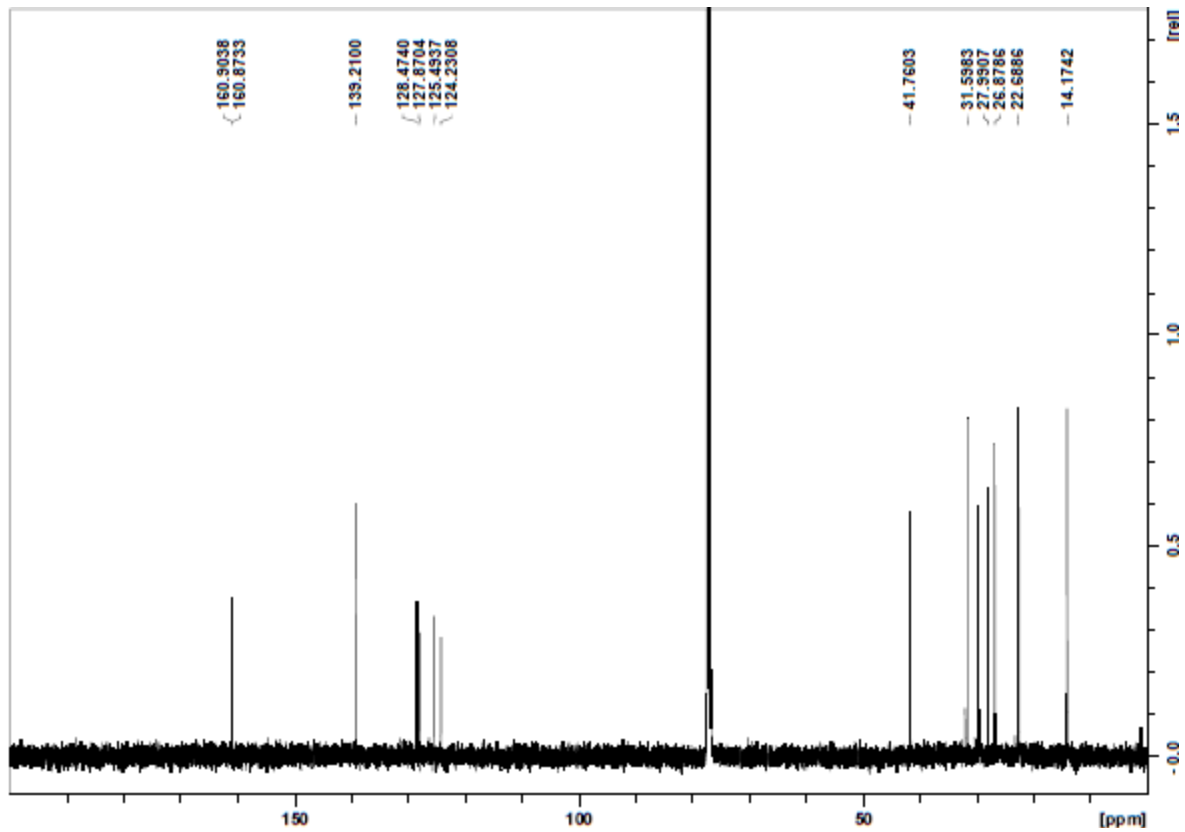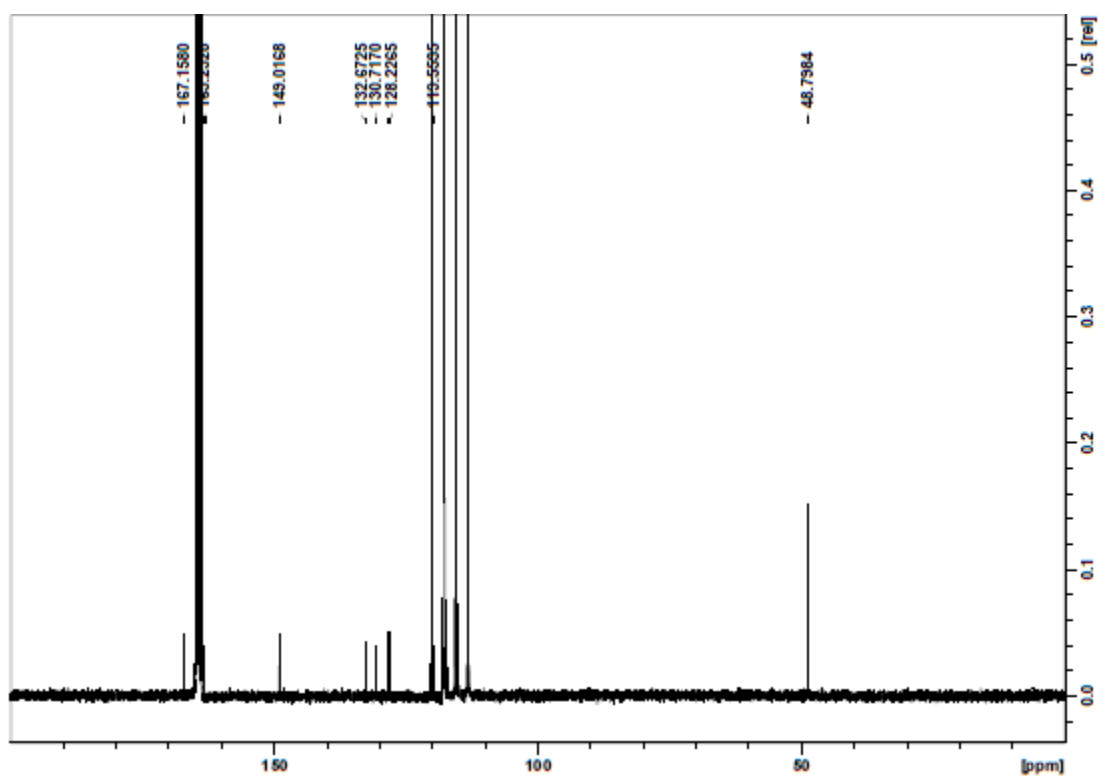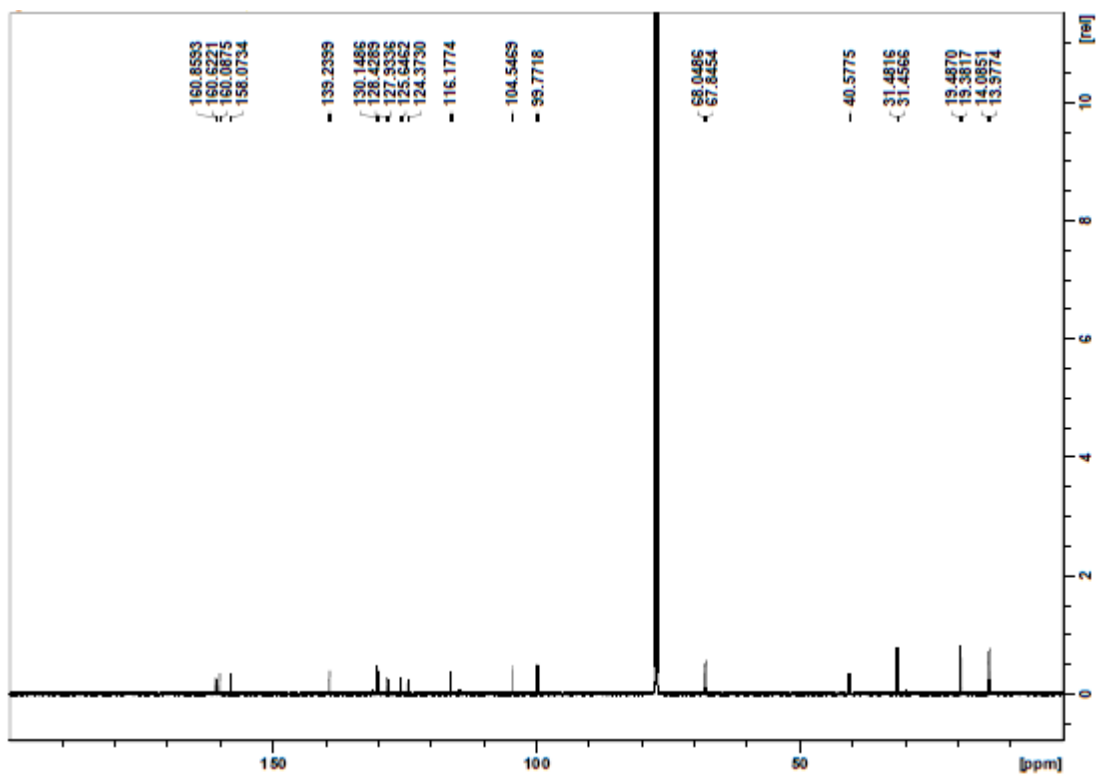
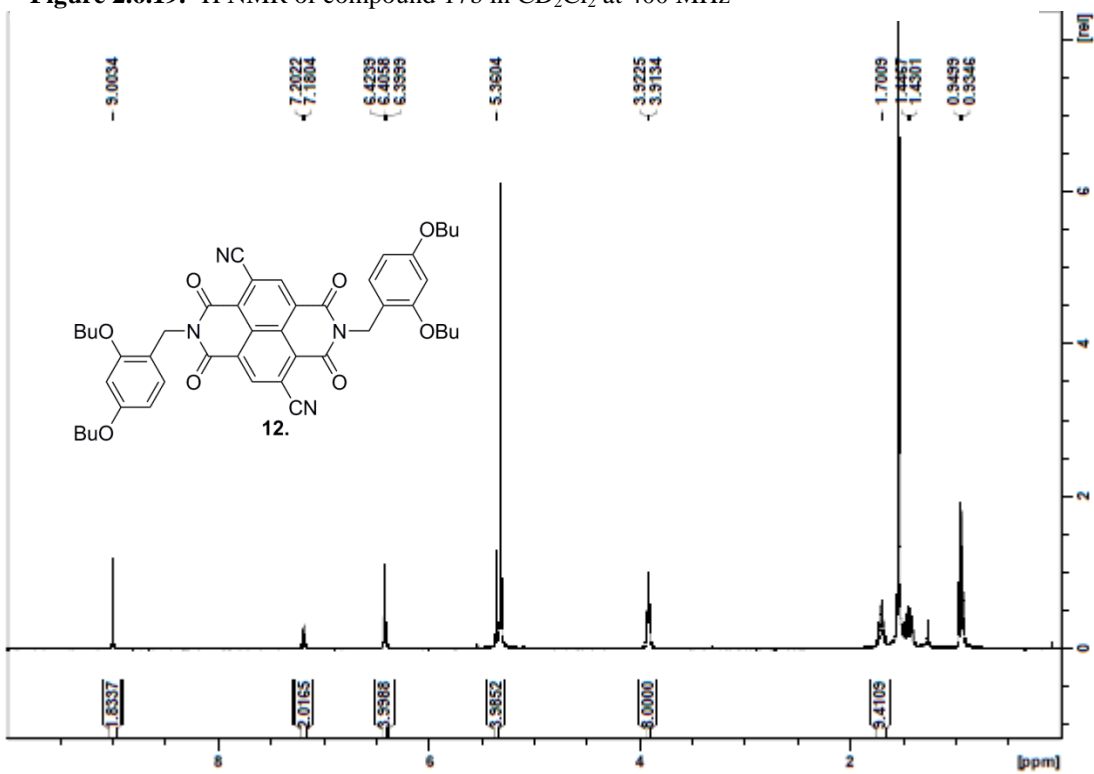**Figure 2.6.5.** ^{1}H NMR of compound 7 in CDCl$_3$ at 400 MHz
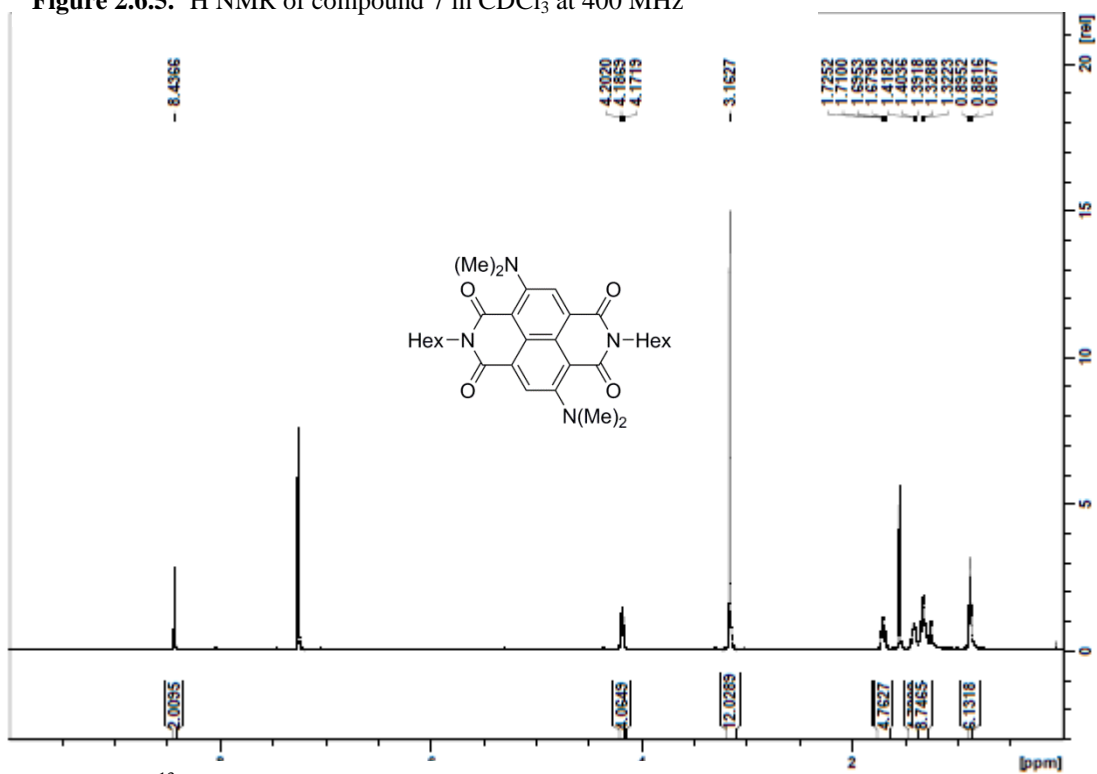
Figure 2.6.6. ^{13}C NMR of compound 7 in CDCl$_3$ at 125 MHz
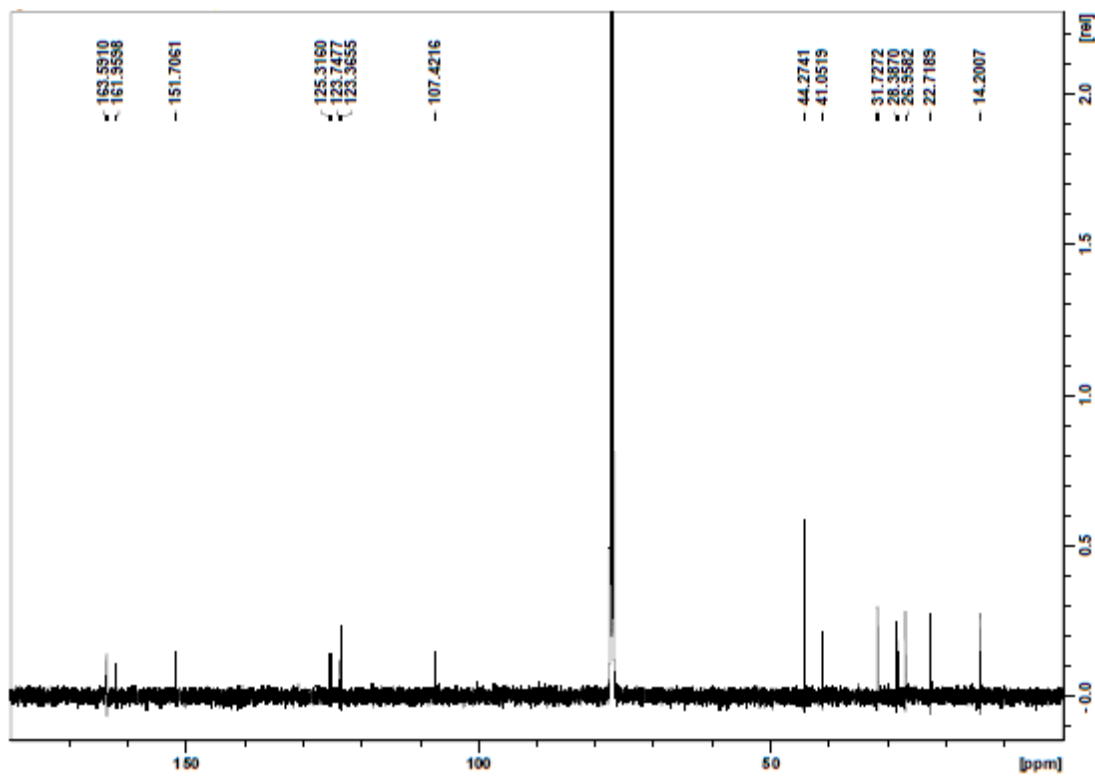
Figure 2.6.7. ^{1}H NMR of compound 8 in CDCl$_3$ at 400 MHz
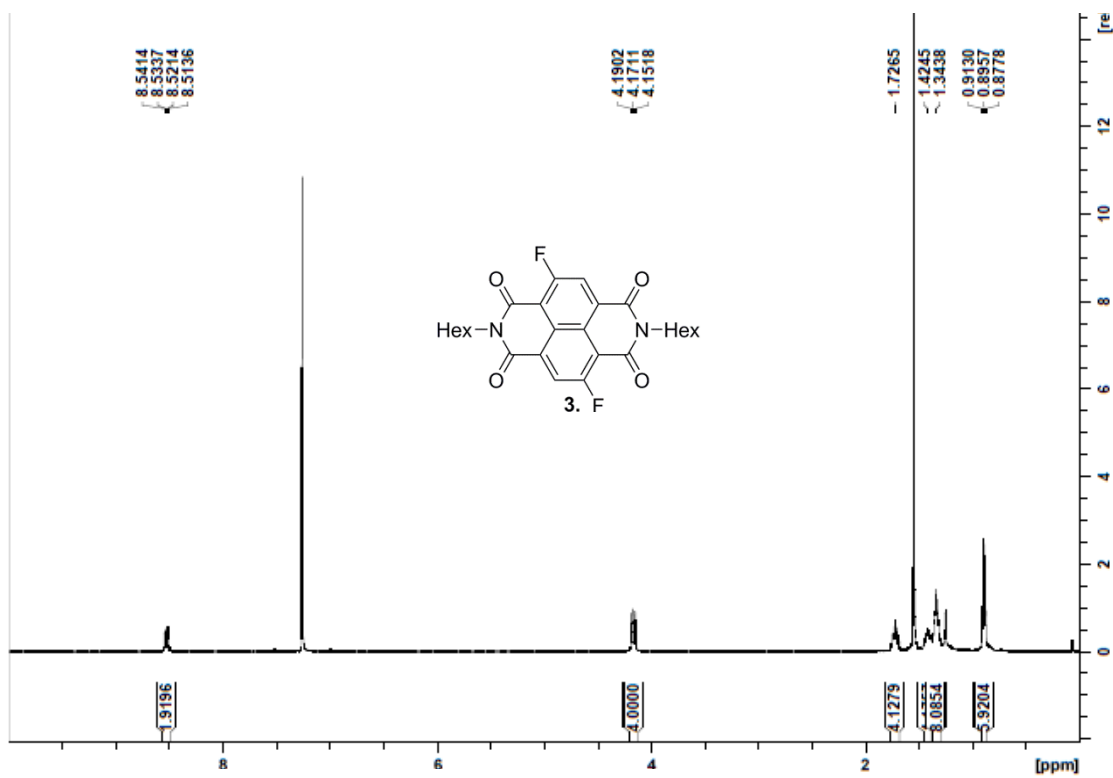
Figure 2.6.8. ^{13}C NMR of compound 8 in CDCl$_3$ at 125 MHz
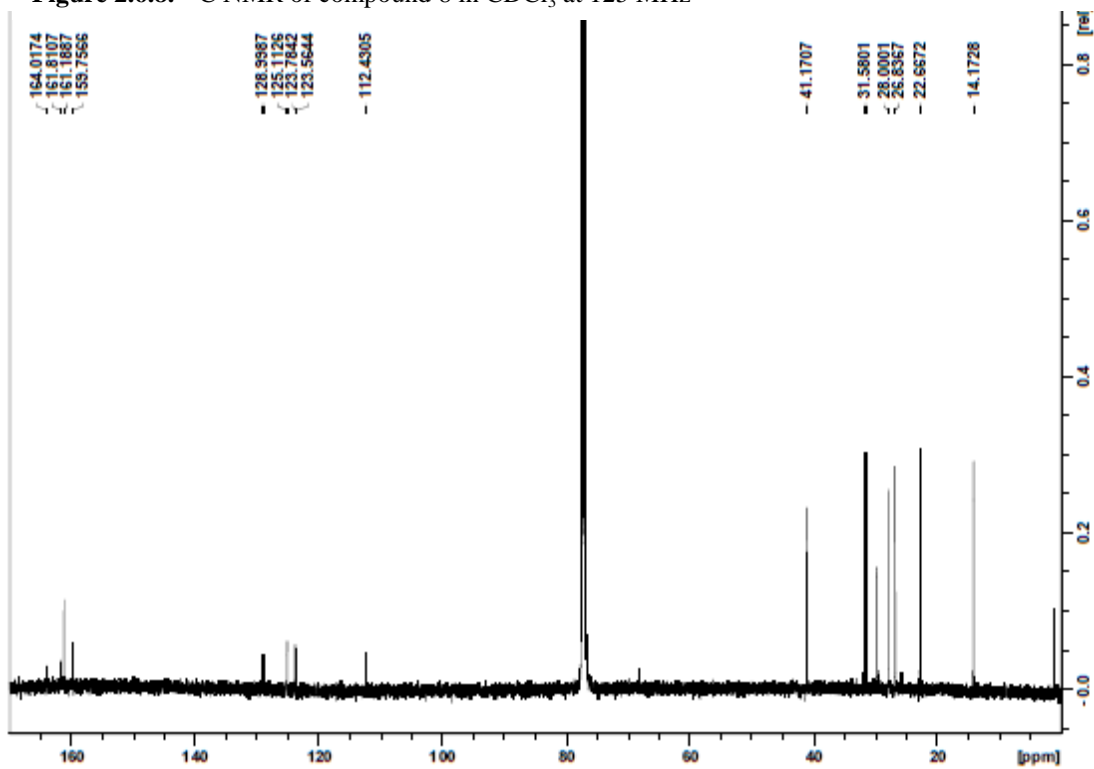
Figure 2.6.9. ^{19}F NMR of compound 8 in CDCl$_3$ at 376 MHz
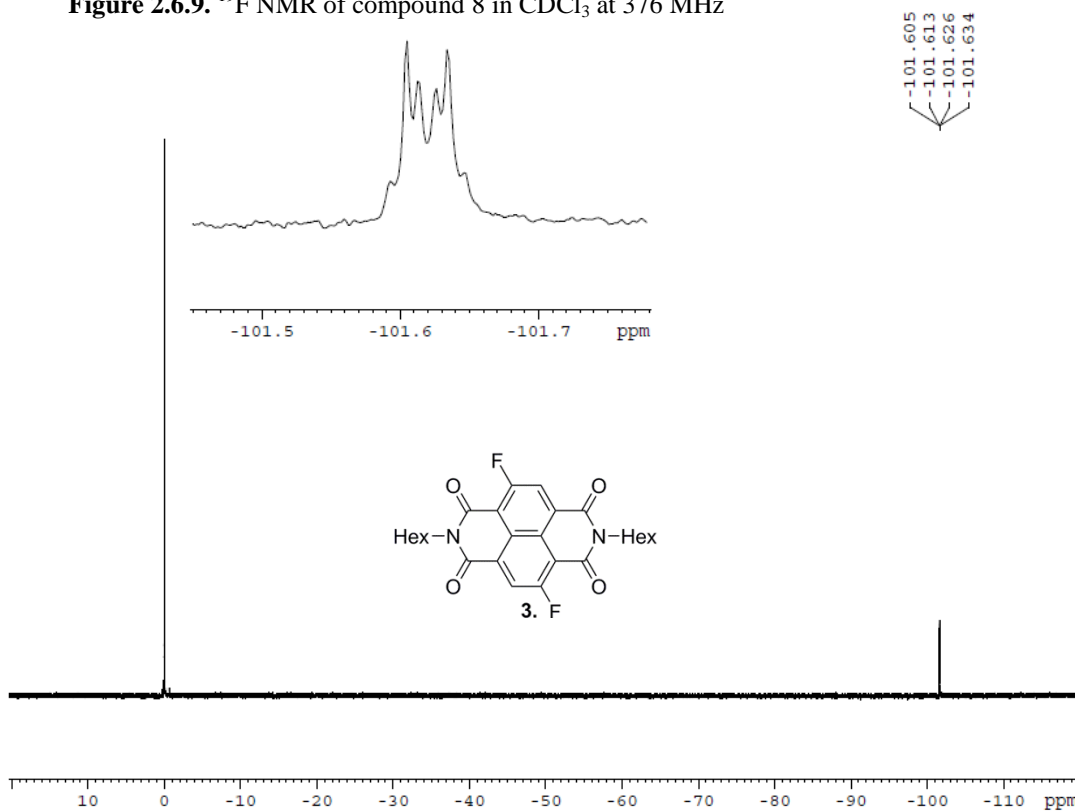
Figure 2.6.10. ^{19}F NMR of compound 8 in CDCl$_3$ at 376 MHz (Proton decoupled)
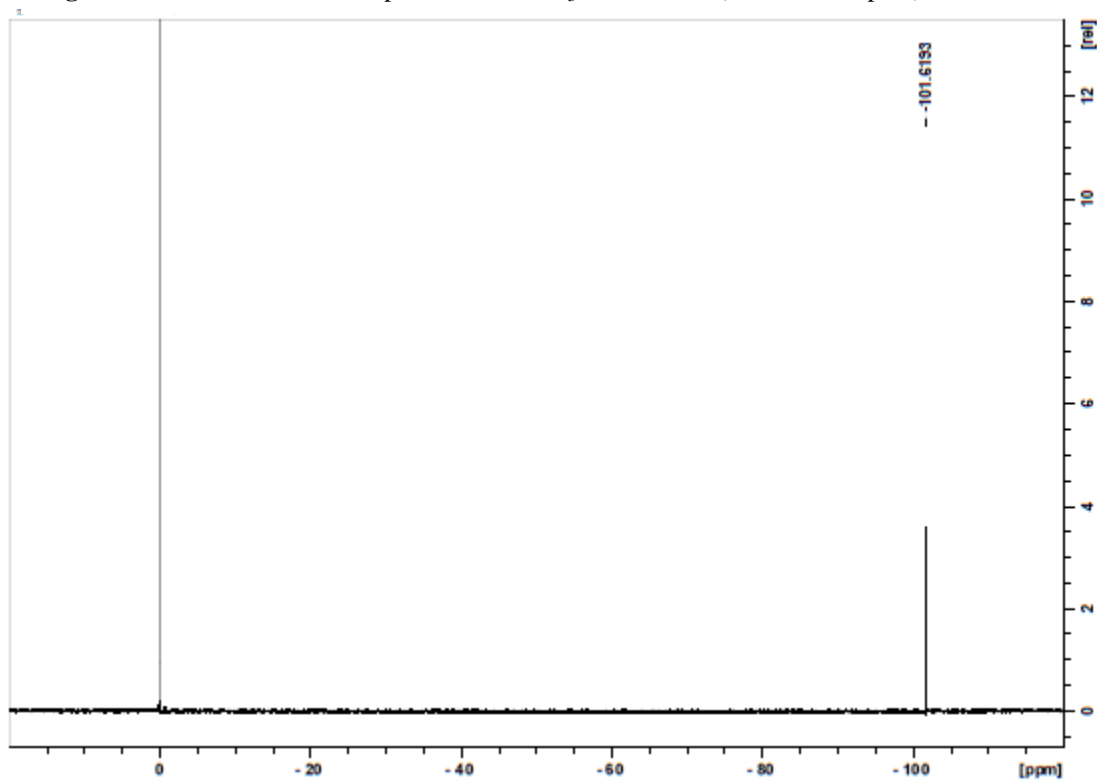
Figure 2.6.11. ^{1}H NMR of compound 9 in CDCl$_3$ at 300 MHz
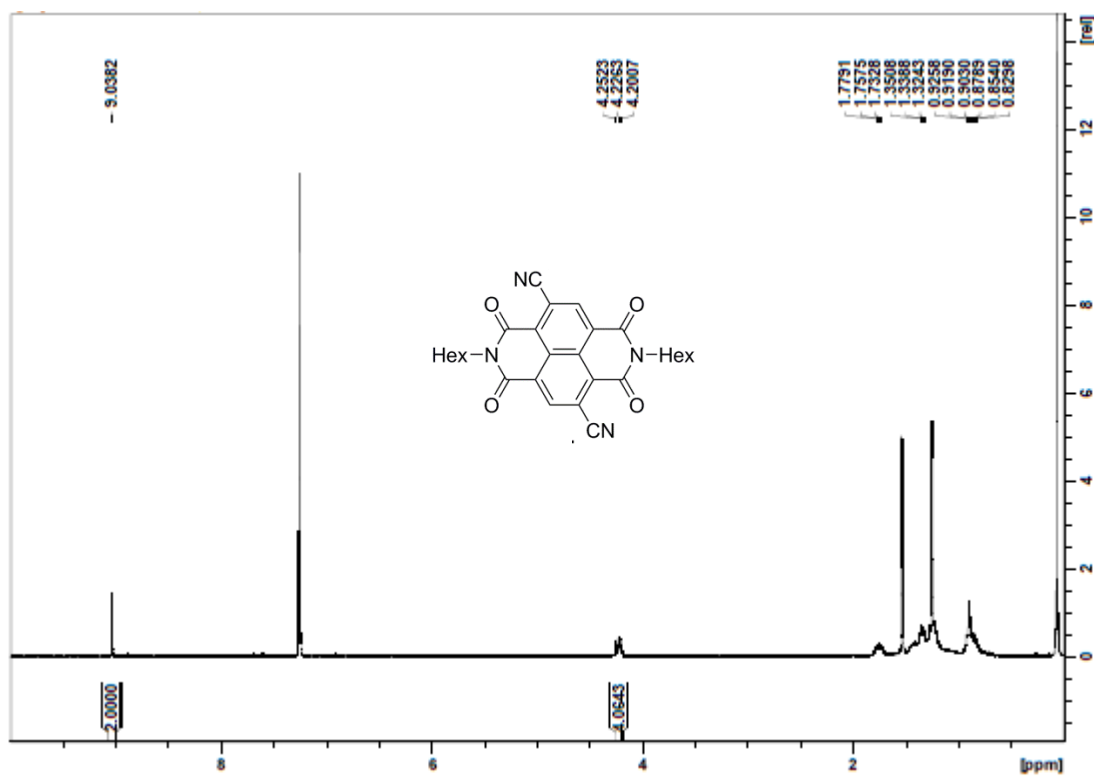
Figure 2.6.12. ^{13}C NMR of compound 9 in CDCl$_3$ at 125 MHz
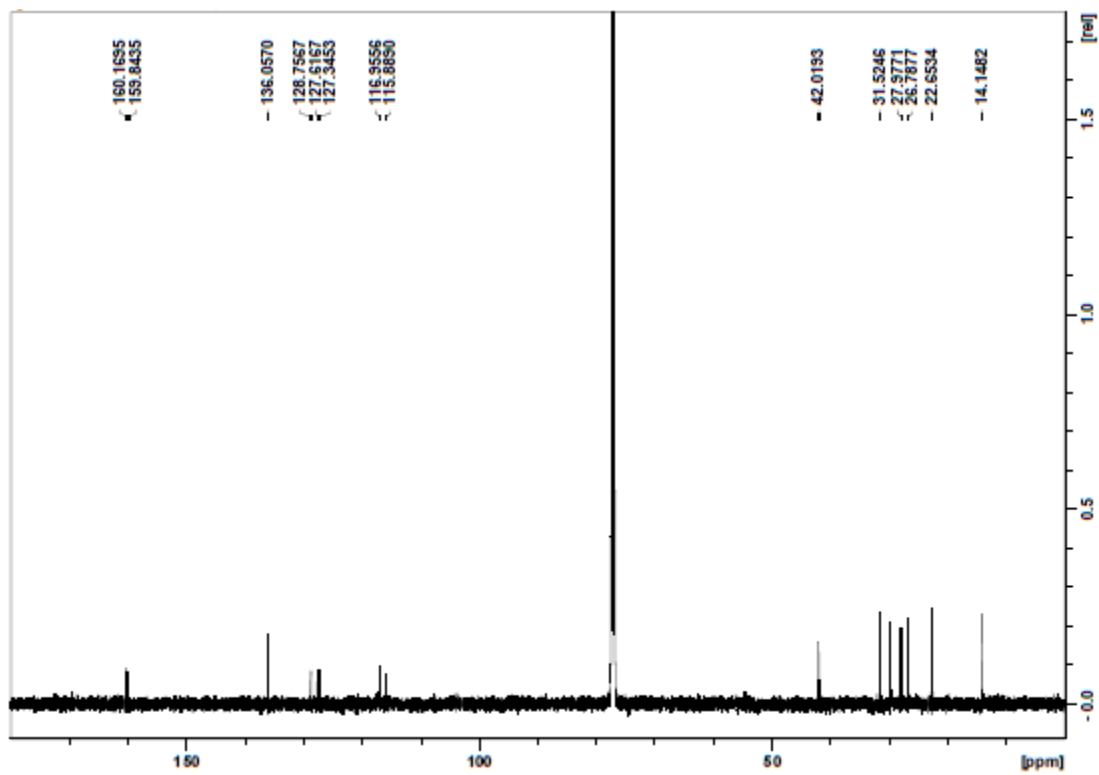
Figure 2.6.13. ^{1}H NMR of compound 18a in CDCl$_3$ at 400 MHz
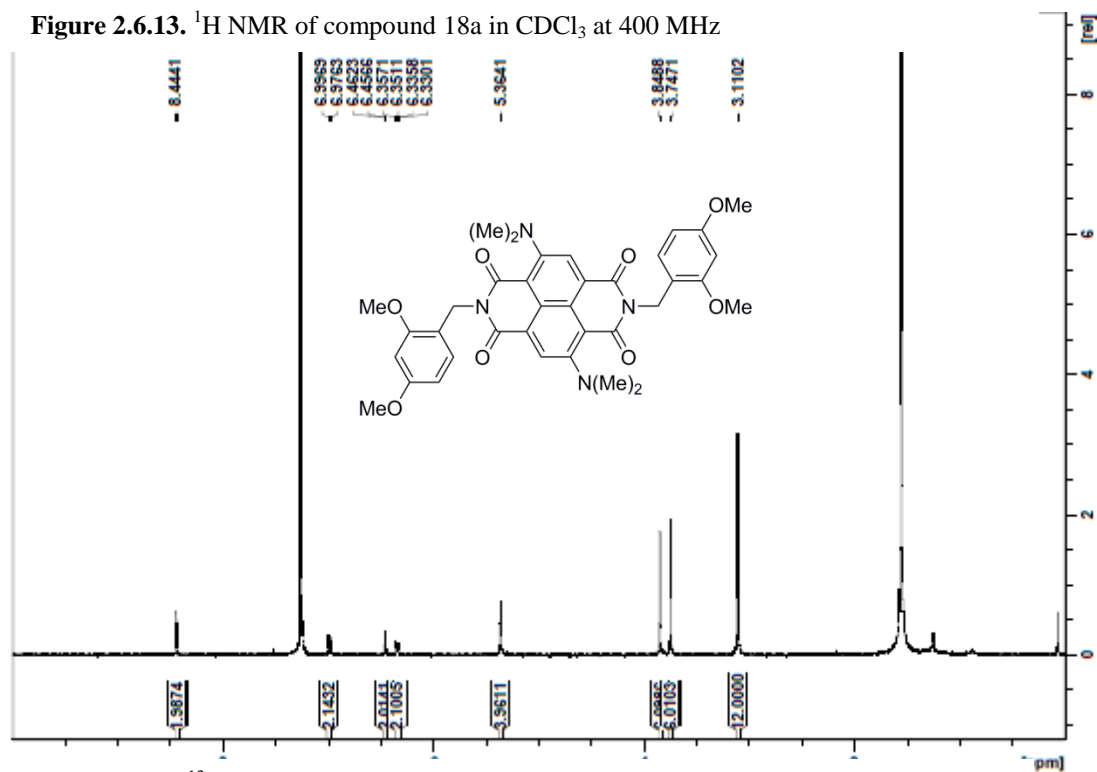
Figure 2.6.14. ^{13}C NMR of compound 18a in CDCl$_3$ at 125 MHz

Figure 2.6.15. ^{1}H NMR of compound 11 in TFA-*d* at 400 MHz
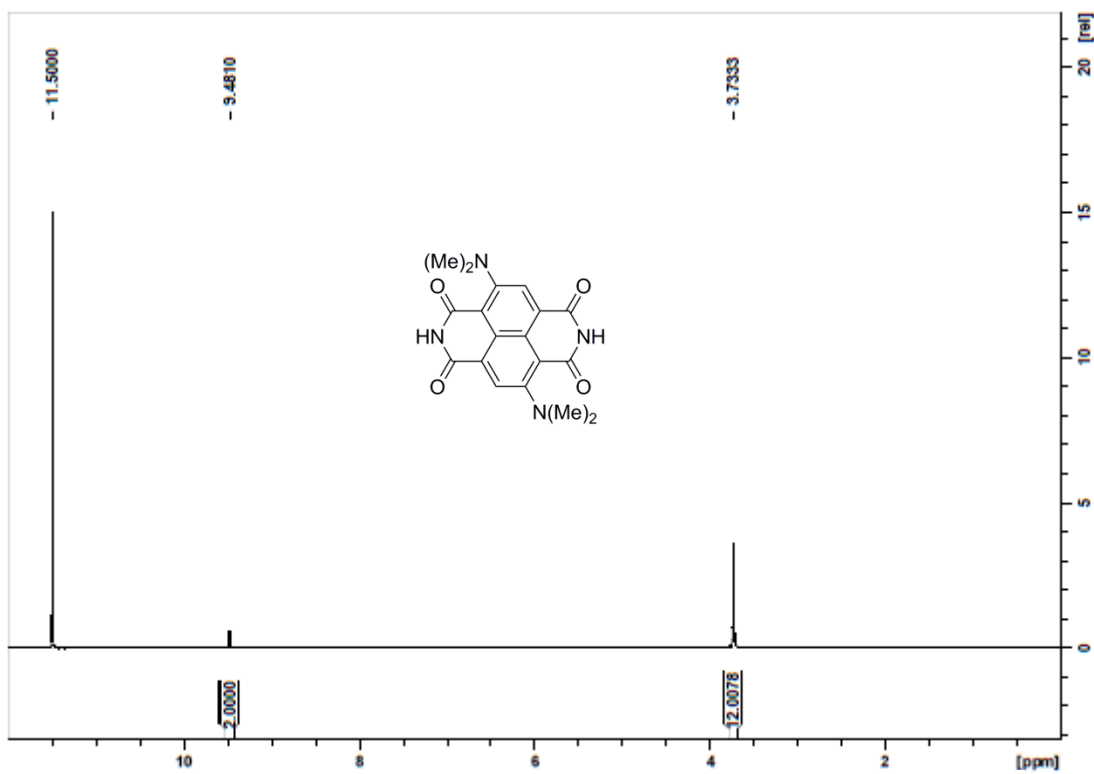
Figure 2.6.16. ^{13}C NMR of compound 11 in TFA-*d* at 125 MHz

Figure 2.6.17. ^{1}H NMR of compound 16b in CDCl$_3$ at 400 MHz
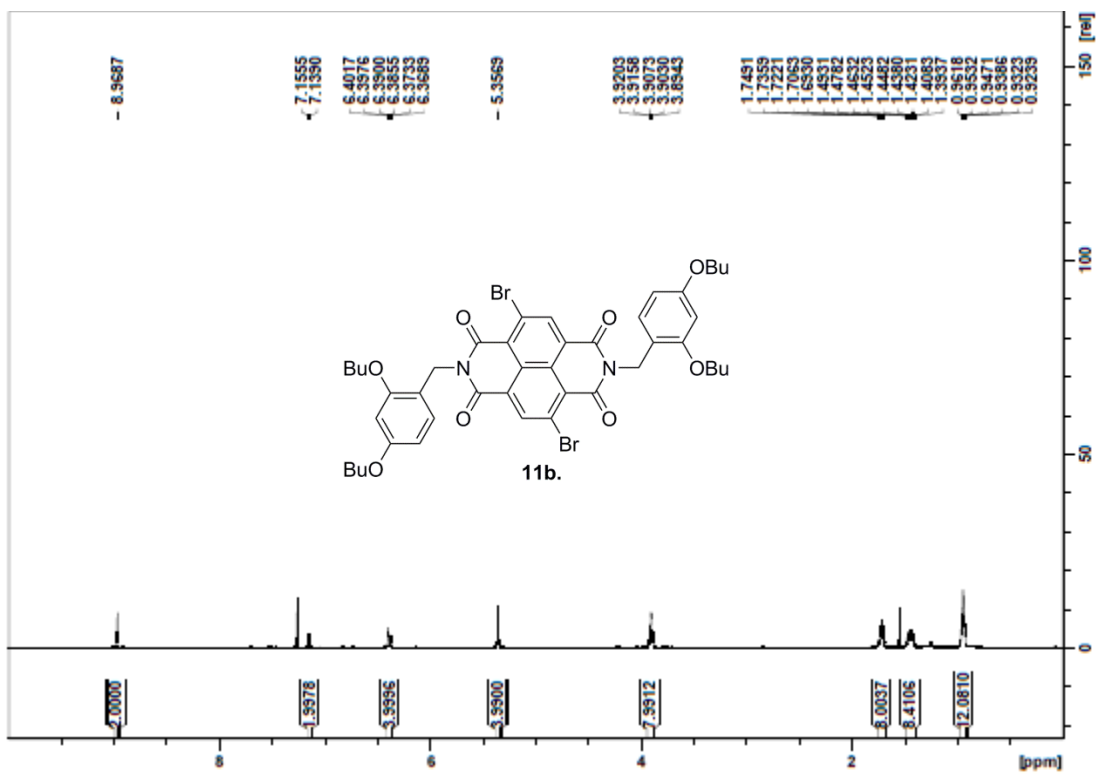
Figure 2.6.18. ^{13}C NMR of compound 16b in CDCl$_3$ at 125 MHz

Figure 2.6.19. ^{1}H NMR of compound 17b in CD_2Cl_2 at 400 MHz

Figure S20. ^{13}C NMR of compound 17b in $CDCl_3$ at 125 MHz
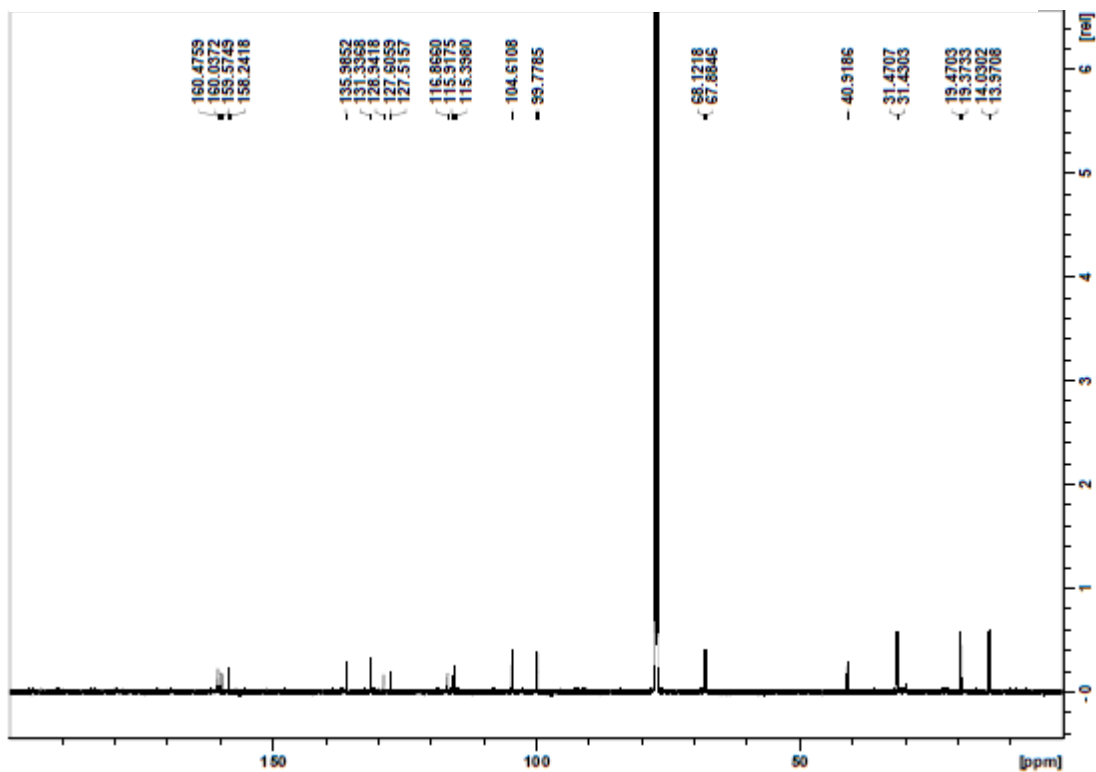
Figure 2.6.21. ^{1}H NMR of compound 13 in DMSO-d_6 at 500 MHz
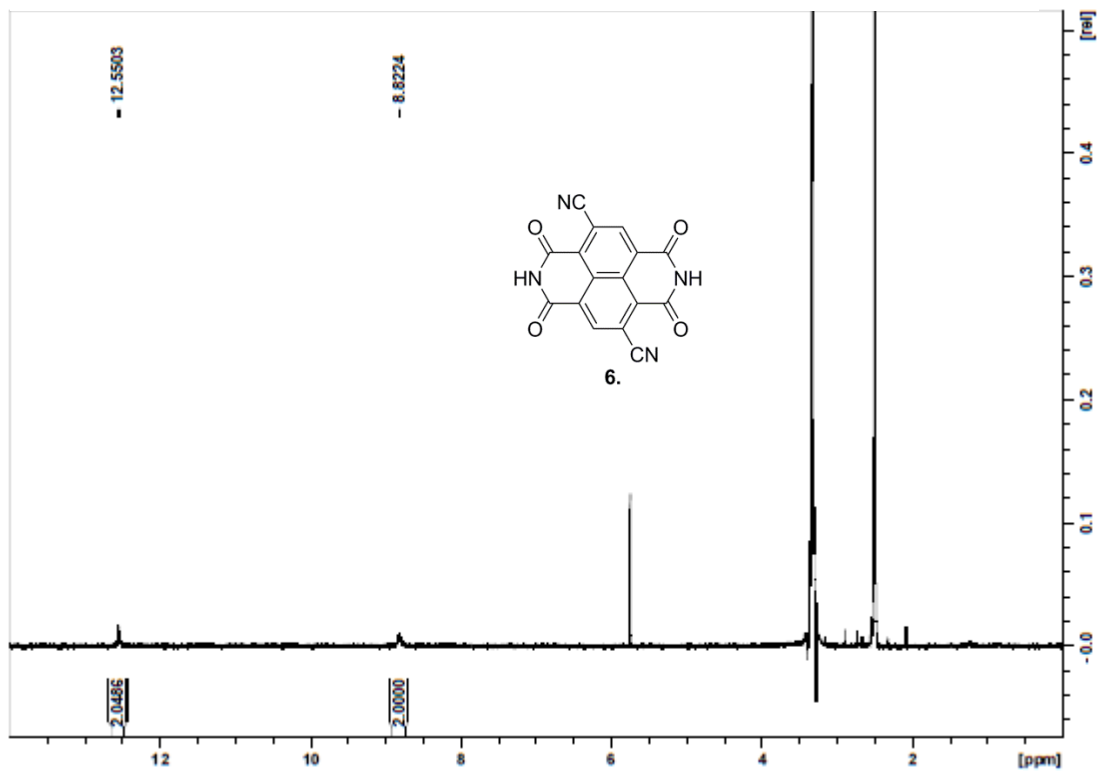
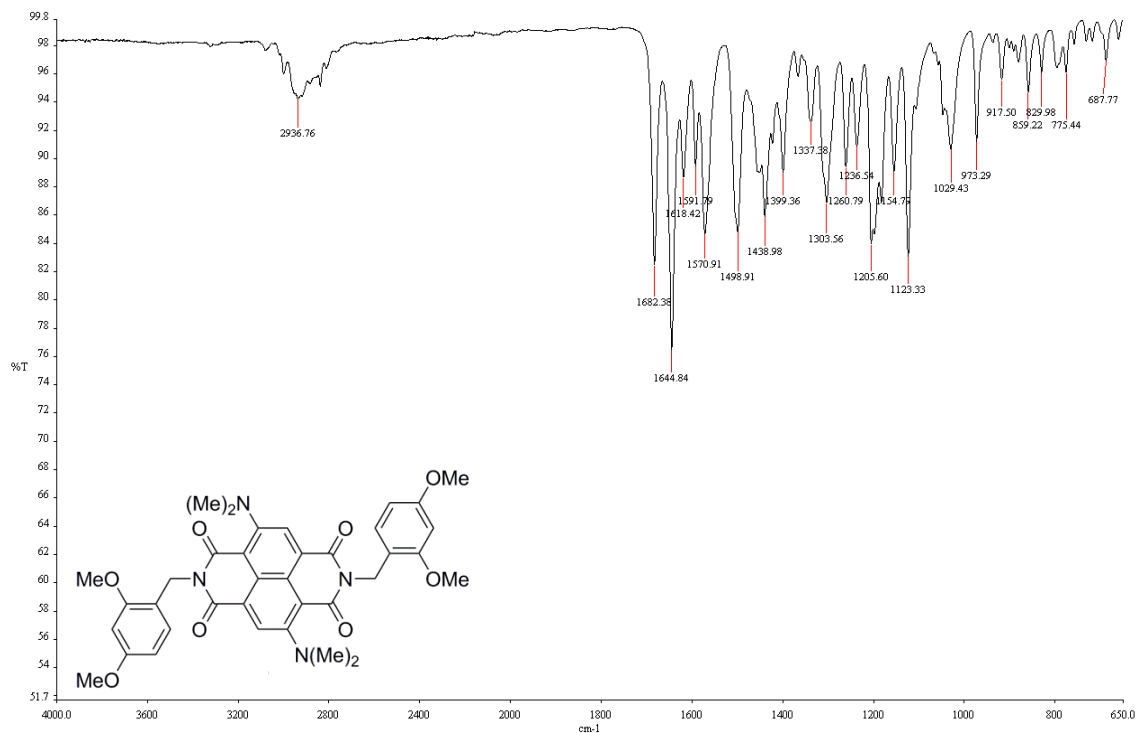**Figure 2.6.22.** ^{13}C NMR of compound 13 in DMSO-d_6 at 125 MHz
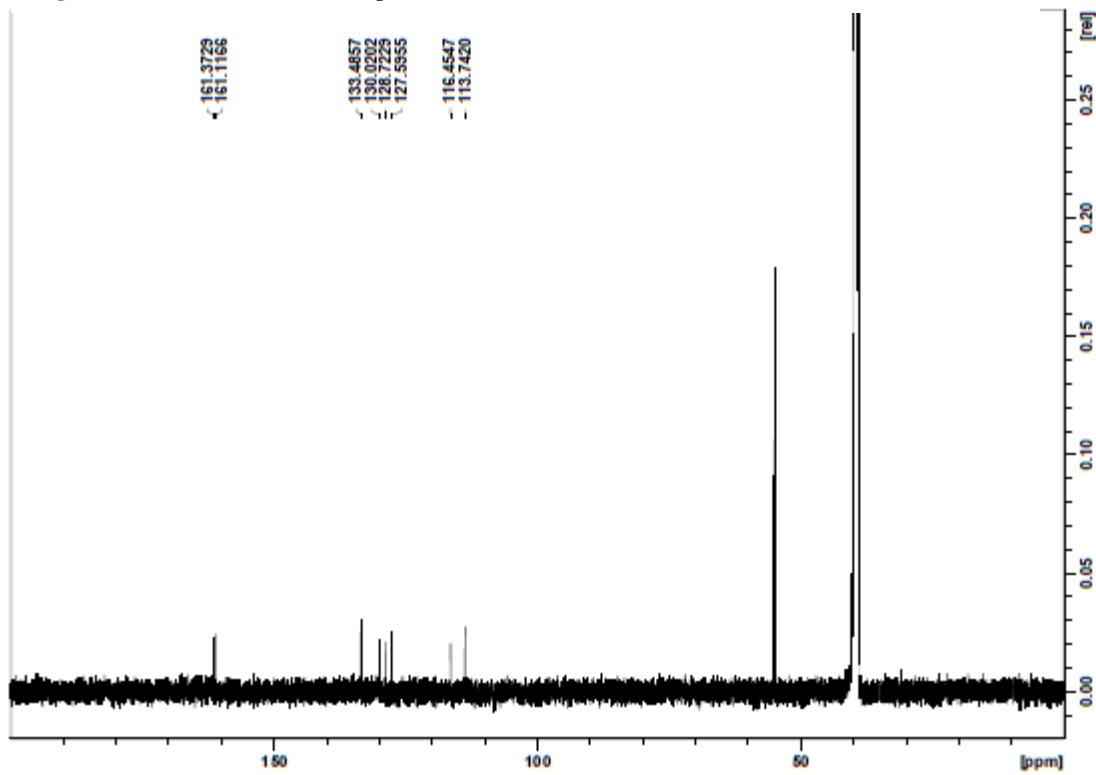
Figure 2.6.23. ATR IR of compound 21
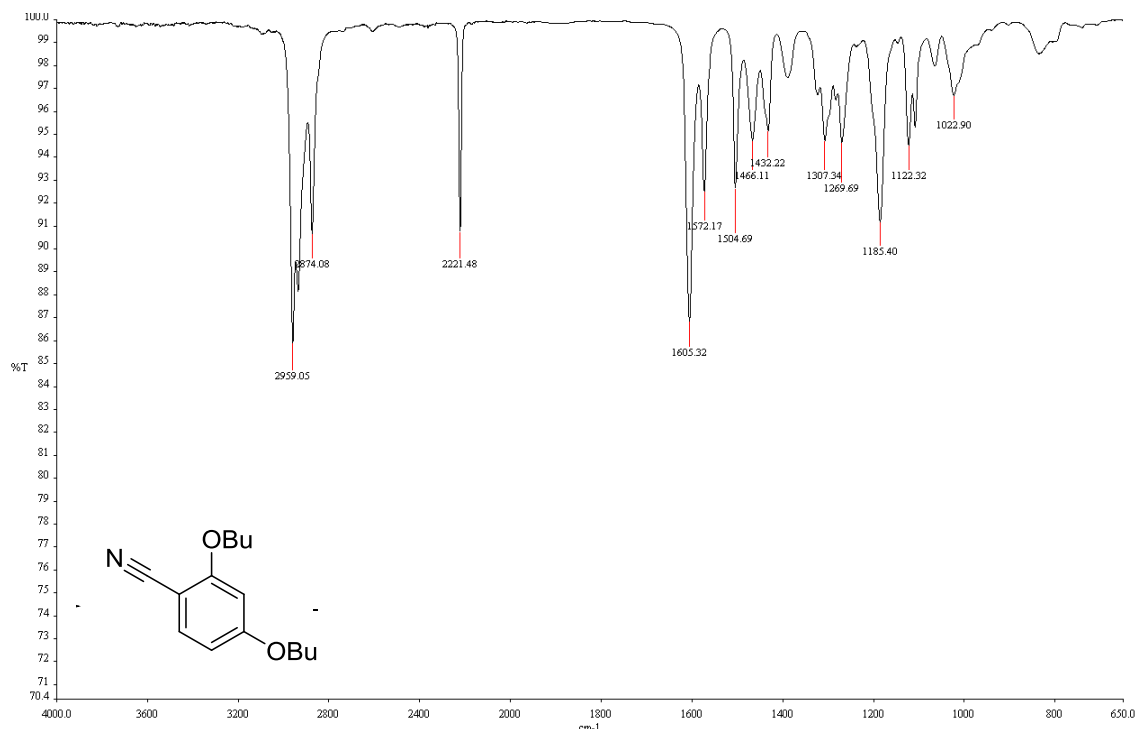
Figure 2.6.24. ATR IR of compound 16
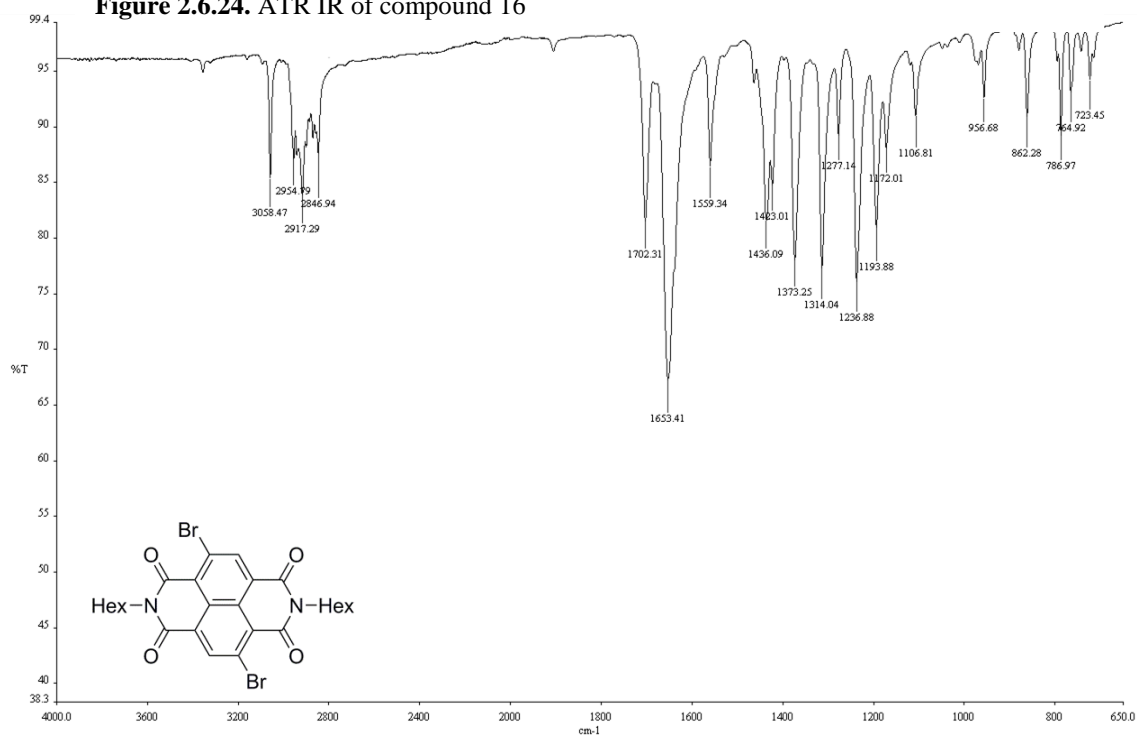
Figure 2.6.25. ATR IR of compound 7
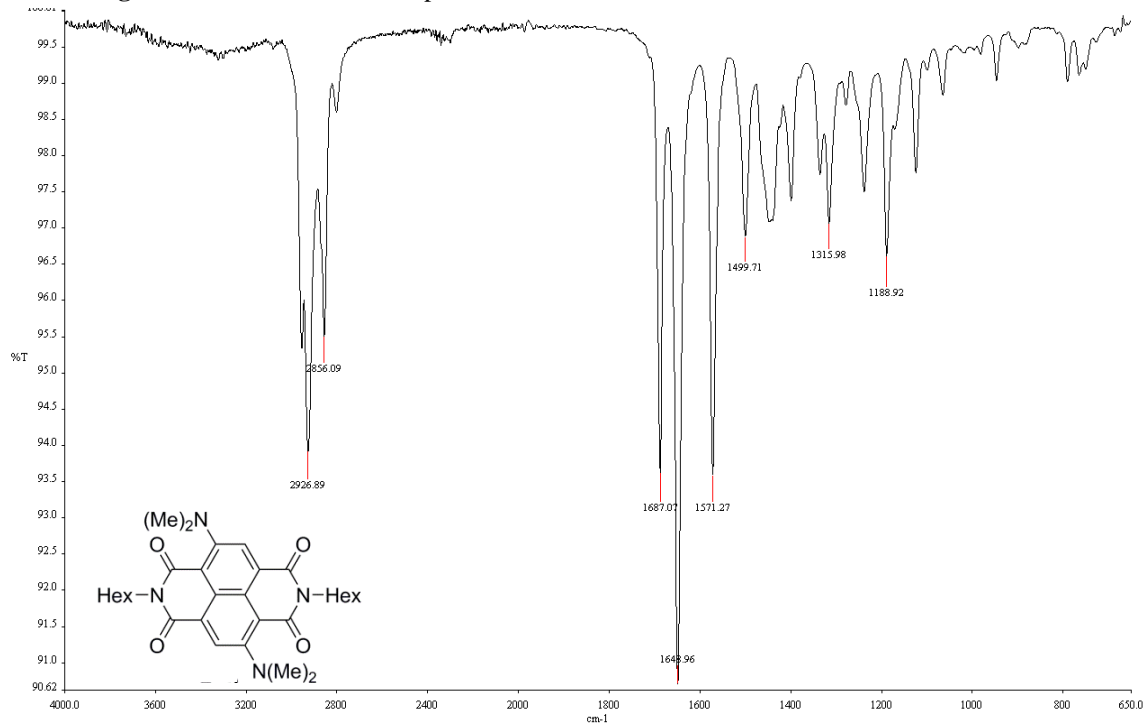
Figure 2.6.26. ATR IR of compound 8
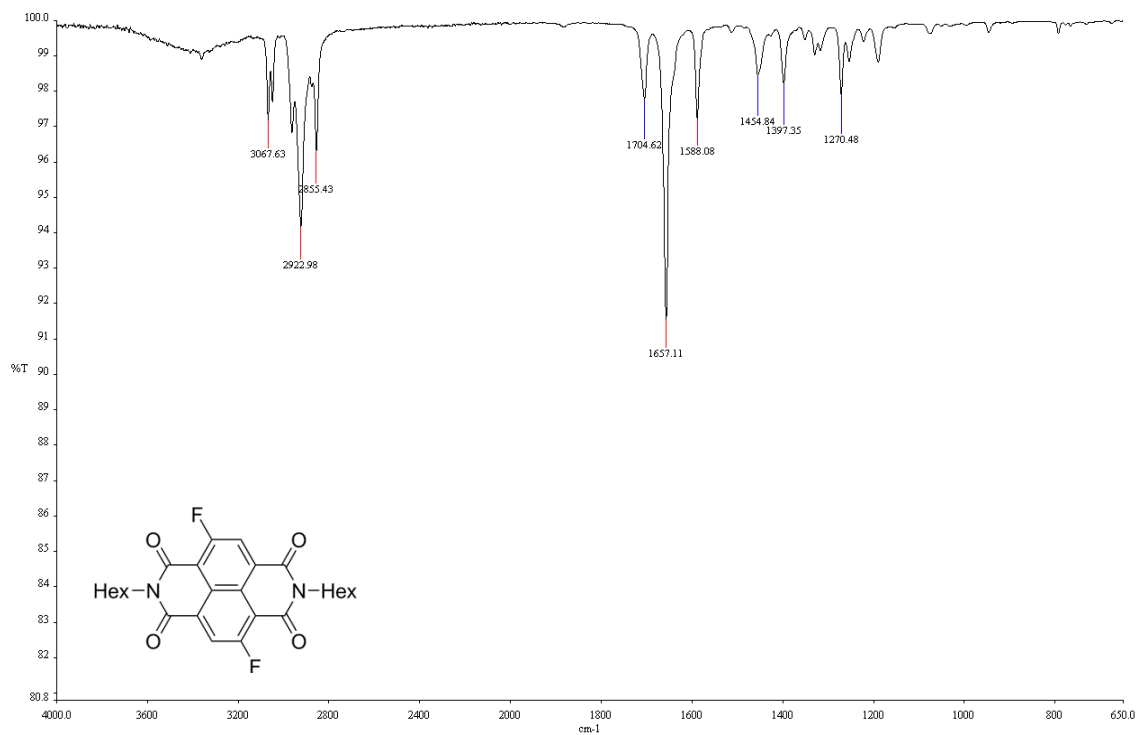
Figure 2.6.27. ATR IR of compound 9
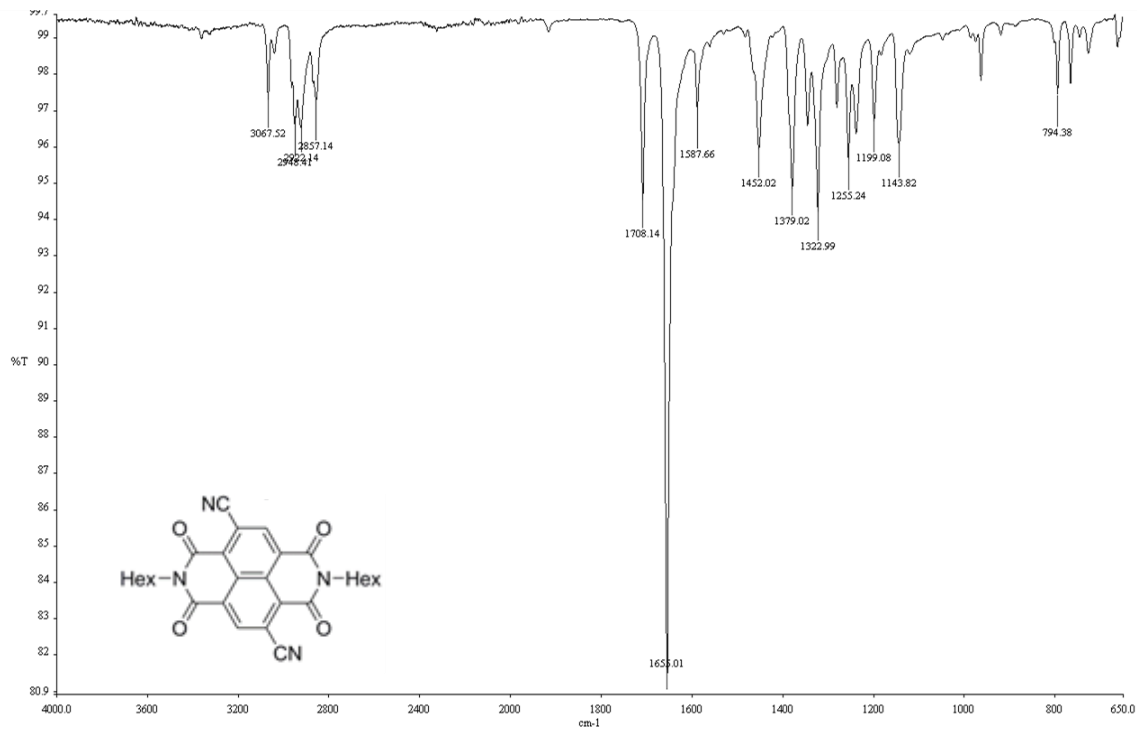
Figure 2.6.28. ATR IR of compound 18a

Figure 2.6.29. ATR IR of compound 11
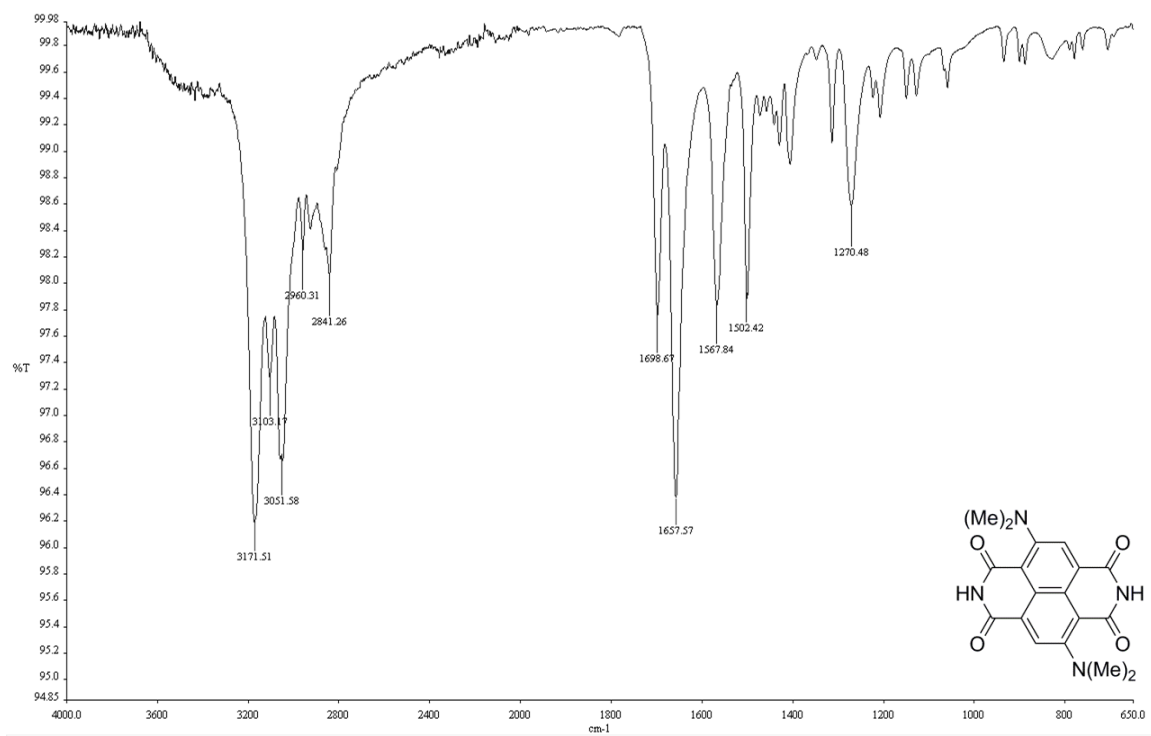
Figure 2.6.30. ATR IR of compound 17b
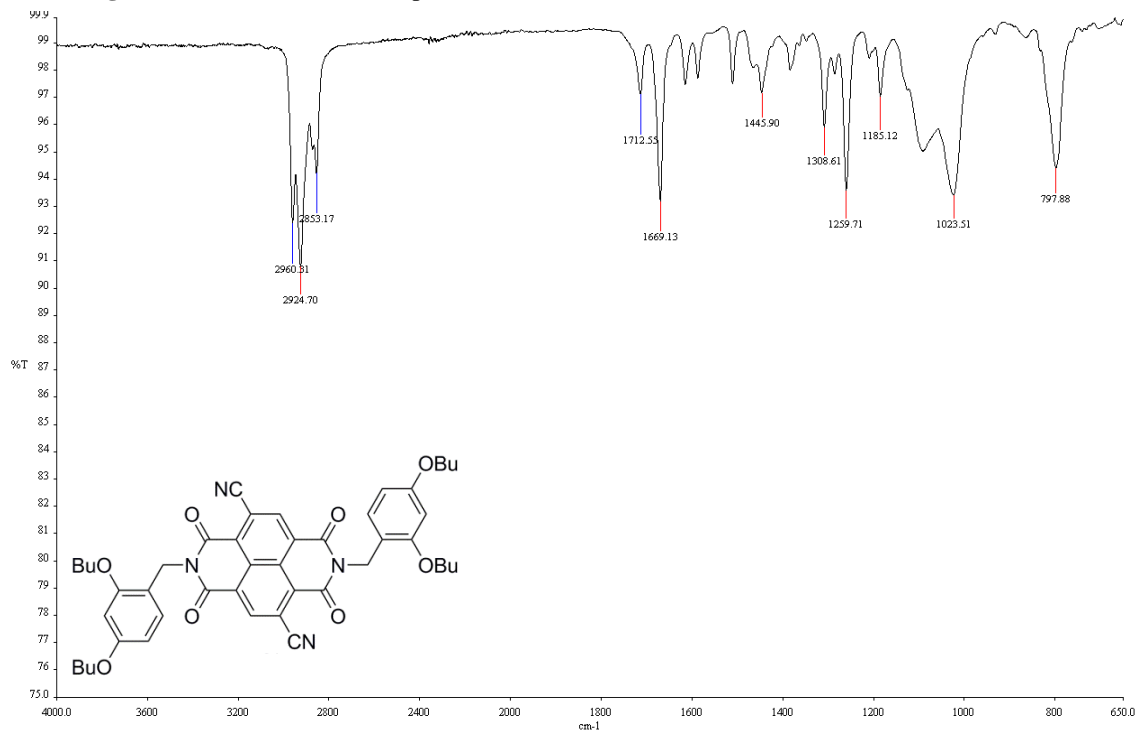
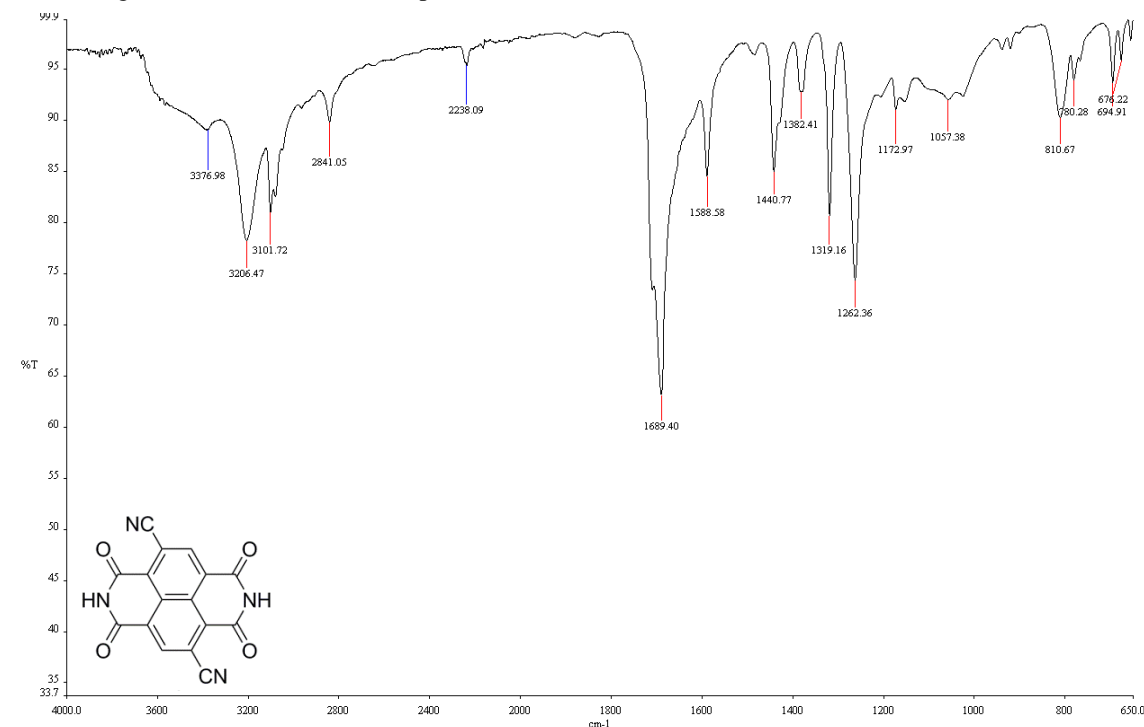Figure **2.6.31**. ATR IR of compound 13

2.7. References

[1] Manthiram, A. *J. Phys. Chem. Lett.*, **2011**, *2*, 176.

[2] Goodenough, J.B.; Kim, Y. *J. Power Sources*, **2011**, *196*, 6688.

[3] Poizot, P.; Dolhem, F. *Energy Environ. Sci.*, **2011**, *4*, 2003.

[4] B. Dunn , H. Kamath , J. M. Tarascon , *Science* **2011** , *334* , 928.

[5] Alt, H.; Binder, H.; Köhling, A.; Sandsteede, G. *Electrochim. Acta.,* **1972**, *17*, 873.

[6] Chen, H.; Armand, M.; Demailly, G.; Dolhem, F.; Poizot, P.; Tarascon, J. M. *ChemSusChem*, **2008**, *1*, 348.

[7] Liang, Y.; Tao, Z.; Chen, J. *Adv. Energy Mater.*, **2012**, *2*, 742.

[8] Walker, W.; Grudgeon, S.; Vezin, H.; Laruelle, S.; Armand, M.; Wudl, F.; Tarascon, J. M. *J. Mater.Chem.*, **2011**, *21*, 1615.

[9] Renault, S.; Geng, J.; Dolhem, F.; Poizot, P. *Chem. Commun.*, **2011**, *47*, 2414.

[10] Kim, D. J.; Je, S. H.; Sampath, S.; Choi, J. W.; Coskun, A. *RSC Adv.*, **2012**, *2*, 7968.

[11] Walker, W.; Grugeon, S.; Mentre, O.; Laruelle, S.; Tarascon, J. M.; Wudl, F. *J. Am. Chem. Soc.*, **2010**, *132*, 6517.

[12] Song, Z.; Zhou, H. *Energy, Environ. Sci.*, **2013**, *6*, 2280.

[13] Nakahara, K.; Iwasa, S.; Satoh, M.; Morioka, Y.; Iriyama, J.; Suguro, M.; Hasegawa, E. *Chem. Phys. Lett.*, **2002**, *359*, 351.

[14] Sarukawa, T.; Yamaguchi, S.; Oyama, N. *J. Electro.Soc*. **2010**, *12* 196.

[15] Inamasu, T.; Yoshitoku, D.; Sumi-otorii, Y.; Tani, H.; Ono, N. *J. Electrochem. Soc.*, **2003**, *150*, A128.

[16] Liang, Y.; Zhang, P.; Yang, S.; Tao, Z.; Chen, J. *Adv. Energy, Mater.*, **2013**, *3*, 600.

[17] Song, Z.; Zhan, H.; Zhou, Y. *Chem. Comm.*, **2009**, 448.

[18] Armand, M.; Grudgeon, S.; Vezin, H.; Laruelle, S. Ribiére, P.; Poizot, P.; Tarascon, J.M. *Nature Mat.*, **2009**, *8*, 120.

[19] Song, Z.; Zhan, H.; Zhou, Y. *Angew. Chem. Int. Ed.*, **2010**, *49*, 8444.

[20] Würthner, F.; Osswald, P.; Schmidt, R.; Kaiser, T.; Mansikkamaki, H.; Konemann, M. *Org. Lett.*, **2006**, *8*, 3765.

[21] Dawson, R.; Hennig, A.; Weimann, D.; Emery, D.; Ravikumar, V.; Montenegro, J.; Takeuchi, T.; Gabutti, S.; Mayor, M.; Mareda, J.; Schalley, C.; Matile, S. *Nature Chem.*, **2010**, *2*, 533.

[22] Röger, C. and Wurthner, F. *J. Org. Chem.*, **2007**, *72*, 8070.

[23] Sotiriou-Leventis, C.; Mao, Z. *J. Heterocyclic Chem.*, **2000**, *37*, 1665.

[24] Only the N-Hexyl compounds were tested in solution, due to the lack of solubility of the X=H compounds in dichloromethane.

[25] Pollard, A.; Perkins, E.; Smith, N.; Saywell, A.; Goretzki, G.; Phillips, A.; Argent, S.; Sachdev, H.; Müller, F.; Hüfner, S.; Gsell, S.; Fischer, M.; Schreck, M.; Osterwalder, J.; Greber, T.; Berner, S.; Champness, N.; Beton, P. *Angew. Chem. Int. Ed.* *2010*, 49, 1794.

[26] Adapted procedure from Augustine, J.K.; Bombrun, A.; Nath Atta, R. *Synlett.*, **2011**, *15*, 2223.

[27] Reczek, J.; Villazor, K.; Lynch, V.; Swager, T.; Iverson, B. *J. Am. Chem. Soc.* **2006**, 128, 7995.

[28] Chaignon, F.; Falkenström,M.; Karlsson, S.; Blart, E.; Odobel, F.; Hammarström, L. *Chem. Comm.*, **2007**, 1, 64.

[29] Gottardi, W. *Monatshefte fuer Chemie*, **1967**, 98, 507.

[30] Sotiriou-Leventis, C.; Mao, Z. *J. Heterocycl. Chem.* **2000**, 37, 1665.

CHAPTER 3

Furan Dicarbonyl: The Sustainable Design and Synthesis of a Low

Potential Redox-Active Moiety from Biomass

3.1. Abstract.

This chapter describes the sustainable design of a polymer containing a novel redox-active organic center—furan dicarbonyl and its derivatives—to be explored as a low potential electroactive material in lithium-ion batteries. These small organic groups can be easily incorporated into various polymeric materials with sufficient structural and thermal stability to withstand this application as well as being designed to optimize performance of the reactive center. They are preferable over other potential redox-active organic groups because they are highly environmentally friendly. The synthesis of the monomers can be envisioned in just two scalable steps from naturally occurring carbohydrates[1] and the polymer in four.

3.2 Background.

Numerous metal oxides have been explored as the positive electrode material. While, they have had a great deal of success, there exists a set of common roadblocks—namely, expense, toxicity and weight—in this research, that organic based materials have the potential ability to address, as more specifically discussed in the previous chapters.

Current negative electrode materials, on the other hand, face a different set of issues. The initial conception of the lithium ion battery envisioned the use of metallic lithium as the negative electrode material. Its extremely high theoretical gravimetric capacity due to its low atomic weight, in combination with its low density and electrochemical potential make it the obvious choice.[2] However, in practice, the metallic lithium negative electrode suffers from a set of problem. Apart from the obvious safety concerns of including metallic lithium, the metallic lithium negative electrode has two main problems limiting its performance. Firstly, it actually displays extremely poor coulombic efficiency and, secondly, the redox process causes metallic

lithium to form dendrites across the cell—a process known as lithium plating—eventually causing cell shortage.

With this in mind, the traditional negative electrode material of choice is graphite. Graphite, as a negative electrode material, has a high theoretical capacity, 372 mAh/g, relative to that of positive electrode materials. Due to its high conductivity, cyclability and cheap cost, it is the most prevalent negative electrode material. However, while graphite does not share many of the concerns of the current metal oxide positive electrodes, it does present its own drawbacks in terms of safety. Graphite's low intercalation potential of ca. 150 mV vs. Li/Li^+ gives it the obvious advantage of maximizing the energy density of the battery depending on the characteristics of the positive electrode material. However, due to the proximity of this value with that of the reduction of Li^+, graphite allows the reduction of the lithium ions from the electrolyte causing the lithium plating process described above. This leads to both the safety concerns associated with metallic lithium as well as battery failure due to shortage if sufficient metallic lithium builds up.[2,3] Furthermore, this value is outside the electrolyte stability window leading to partial break down of the electrolyte. As such, while the high energy density of current lithium ion technology, relative to the alternatives, has allowed for the cobalt-graphite lithium ion batteries to dominate the market of smaller electronics, the current commercially available models are not particularly practical for larger general applications.

3.3 Current Area of Exploration

3.3.1 Organic Redox-Active Polymers as Electrode Materials

Organic compounds are a promising alternative to traditional electrode materials in terms of circumventing their thematic problems. As there are many known organic redox processes that

can be exploited with a wide variety of factors contributing to the electronics of these processes, it follows, that we can access a similarly wide set of redox potentials through molecular design. Moreover, the low molecular weight of these redox-active centers means that extremely high theoretical capacities can be envisioned.[4] However, these compounds lack the structural stability of their inorganic counterparts and often suffer dissolution into the electrolyte upon cycling. This problem can be avoided by utilizing polymer counterparts of redox active monomers as polymers tend to be significantly more insoluble. However, the translation from redox active monomer to polymer is not so facile.

Strategies to utilize polymers for electrode applications can be separated into two categories: first, exploring semiconducting polymers in which the redox-active groups are conjugated (Figure 3.3.1.1a), and, second, exploring polymers in which the redox active groups are not conjugated—which can take on two different possible basic forms as can be seen in Figure 3.3.1.1b,c. In most of the latter models, these polymers are electronically insulating.[5] The ability of the former to be doped in combination with its electronic conductivity made semiconducting polymers a naturally attractive organic alternative and a popular area of research early on. Furthermore, some of these polymers were able to demonstrate potentials higher than those obtained by traditional cathode materials[5]. However, due the inherent doping limits of these polymers as well as the necessity for the involvement of the electrolyte anion in balancing the charge of the oxidized state, semiconducting polymers were unable to reach their theoretical capacities. Therefore, they were never able to produce capacities high enough to compete with metal oxides for practical application, and this area of research was largely abandoned.
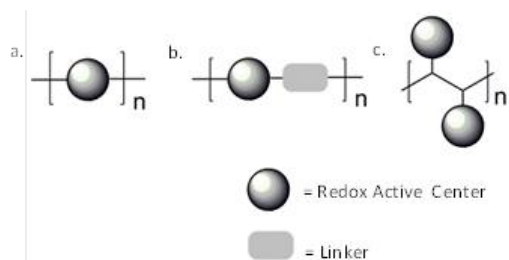
Figure 3.3.1.1. a.) Semiconducting polymer in which redox active, dopeable centers are conjugated (b.) Non-conjugated polymer in which redox active centers are separated by a linker. Also referred to as linker model (c.) Non-conjugated polymer in which the redox active centers are attached as pendants to a polymer backbone. Also referred to as pendant model

Polymers in which the redox-active groups are not conjugated, on the other hand, avoid issues with doping limits. As these polymers generally have insulating properties, however, they are a less obvious option. They also have traditionally been unable to reach their theoretical capacities due to the inability of ions to diffuse into the polymer layer. Unlike the issues associated with semiconducting polymers, however, in the past few years, various groups have had some success with developing strategies to work around the lack of overall conductivity that was initially the downfall of this strategy.

3.3.2 Poly(Ethylene Oxide) as Ion-Conducting Polymer

The poly alkyl back bone of many of these non- conjugated, pendant type polymers contributes to their ionophobic nature. Therefore, if groups that promote ionic conductivity could be added, this should increase the overall conductivity. Just in the past decade this strategy has begun to show success in improving the conductivity of polymers containing organic free radicals.
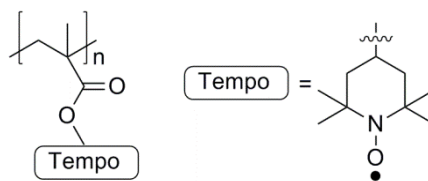
Figure 3.3.2.1. The polymer bearing a redox active center as a pendant on an alkyl polymer backbone proved too insulating for practical use.

In an attempt to take advantage of the reversible redox of 2,2,6,6-tetramethylpiperidine-1-oxyl, or TEMPO, a stable organic free radical molecule, Nakahara, *et al.* incorporated it into a polymer utilizing the pendant model as seen in Figure 3.3.2.1[6] While the simple TEMPO monomer as a small molecule would not be able to undergo cycling in itself, they believed that incorporating it into a polymer would give it sufficient structural stability. This strategy proved both successful and unsuccessful: the capacity remained essentially constant over 500 cycles indicating the success of the polymer strategy. However, as with most non-conducting polymers, the insulating nature of this polymer meant that a maximum of only 70% of its theoretical capacity was observed, even when the amount of carbon in the electrode was raised to amounts far too high to be practical—80 wt % carbon.

In order to work around the issue of the insulating nature of these polymers, more recent groups have borrowed an idea from the field of ionic conductivity in order to design a polymer in which ionic conductivity would be promoted. This original TEMPO-containing polymer had contained a hydrophobic alkane backbone. The ether linkages in combination with the flexibility of poly(ethylene oxide), on the other hand, is known to effectively solvate and conduct ions.[7] With this in mind, more recent publications have taken the idea of utilizing a polymer with pendant TEMPO groups, and combined that with the idea of incorporating it on to a more ion-conducting polymer by two different strategies: Oyaizu *et al.* utilized a poly(ethylene oxide)

backbone[8] (3.3,2,2b) and Suguro *et al.* incorporated a separate poly(ethylene oxide) pendant unit[9] (3.3.2.2c) as an improvement on the original alkyl linked backbone (3.3.2.2a).
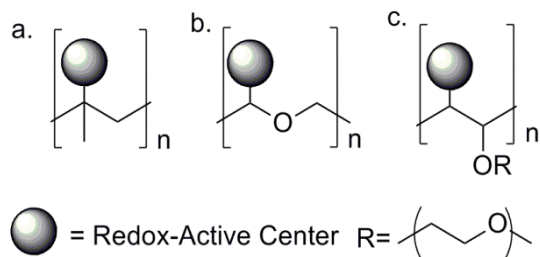

Figure 3.3.2.2. Pendant radical polymers (a.) Insulating alkyl backbone (b.) Ionophoric poly(ethylene oxide) backbone (c.) alkyl backbone with ionophoric side chains.

Both of these models proved successful to varying degrees. In both cases the excellent capacity retention of the original polymer was maintained, but with improved material utilization. Oyaizu's flexible and ionophoric polymer backbone (3.3.2.2b) was able to deliver up to twice as much capacity as the original polymer synthesized in the (3.2.2.2a) model. Suguro's polymer (3.2.2.2c) was synthesized in two forms: mono- and tri-ethylene glycol units as the ion-conducting pendants alternating with the redox-active TEMPO-bearing pendants. They established that the one with a monoethylene glycol unit was not significantly improved in comparison to its (3.2.2.2a) counterpart. However, the polymer (3.2.2.2c) synthesized with triethylene glycol units performed significantly better: at 20°C with 60% carbon, (3.2.2.2c) utilized 85% of its active material in contrast to its (3.2.2.2a) counterpart, which utilized less than 59%.

3.3.3. Conjugated Dicarbonyl Model

The free radical electrodes utilizing the TEMPO group show high potential redox—generally greater than 3.5V vs Li/Li$^+$. This value is slightly lower, but in the same general region, as current metal oxides, and, therefore, a cathode application. In fact, of the work in organic

compounds that discusses these values, most focus on achieving higher potentials for cathode applications. However, it should be noted that much of the work on organic compounds has demonstrated potentials between approximately 1.5 and 2.5 V vs. Li/Li$^+$, which is a grey region too high to be ideal for ideal anode applications and too low to be ideal for ideal cathode applications.

	Potential	Initial Capacity	Capacity Loss
	(V vs Li/Li+)	(mAh/g)	(ca. %)
a.	0.8	300	22
b.	1.4	150	17
c.	0.65	200	10

Figure 3.3.3.1. The expected two electron redox processes and performance of (a.) Di-lithium terephthalate and (b.) Di-lithium *trans-trans-* muconate (c.) 4,4'tolanedicarboxylate.

Only very recently has there been work in the area of low potential organic compounds. In 2009 Jean-Marie Tarascon *et al.* showed the applicability of a conjugated dicarboxylate model by utilizing lithium terephthalate and the analogous non-aromatic lithium *trans-trans*-muconate (Figure 3.3.3.1 a,b).[10] This recent publication is one of the few examples that specifically focuses on addressing the concerns of the mediocre potentials demonstrated by most organic compounds by designing carboxylate compounds with potentials low enough to be applicable for anode application. Both compounds showed reversible redox at low potentials. However, the loss of aromaticity in this case, resulted in lower potentials, therefore making the terephthalate the more successful compound. Furthermore, the non-aromatic muconate was unable to accommodate the desired two-electron process and so only underwent a reversible one-electron process. Unfortunately, however, while the low molecular weight of these compounds allowed for high

initial capacities, a substantial decrease of ca. 20% was observed over 50 cycles. In a later publication, Tarascon was able to decrease this value to only ca. 10% loss by increasing the size of the molecule by incorporating an analogous process into the tolane dicarboxylate (3.3.3.1c).[11] This increase in molecular weight, however, decreased the theoretical capacity.

3.3.4 Furan Model.

Given the success of modifying the polymer backbone in enhancing conductivity, as demonstrated in the examples of the free radical polymers, it follows that this strategy could be exploited to enhance the performance of other redox-active centers. With this in mind, we aimed to combine these three strategies by synthesizing a co-polymer of a redox-active dicarbonyl with an ion-conducting linker.

Motivated by the realization that furan derivatives could have applications in biofuel research, Mark Mascal *et al.* showed in 2008 that a stable furan backbone, 5-(chloromethyl)furfural (CMF), could be formed in one step from cellulose under biphasic conditions when treated with highly acidic conditions with a high chloride content (Figure 3.3.4.1a.)[1] Since then, many more publications have emerged showing various improvements and different applications of this reaction. It has now been shown that this reaction is not specific to cellulose starting material, but is actually general to many carbohydrates demonstrating yields up to 95%.[12,13] The LiCl and HCl can be replaced with LiBr and HBr to produce the brominated derivative, BMF,[12] and, more recently, this reaction was shown to be easily incorporated into a continuous flow reactor, therefore, demonstrating its large scale applicability.[13] CMF and BMF, can subsequently serve as a useful synthetic precursors to a wide variety of furan derivatives, which can undergo the desired redox process (Figure 3.3.4.1b).
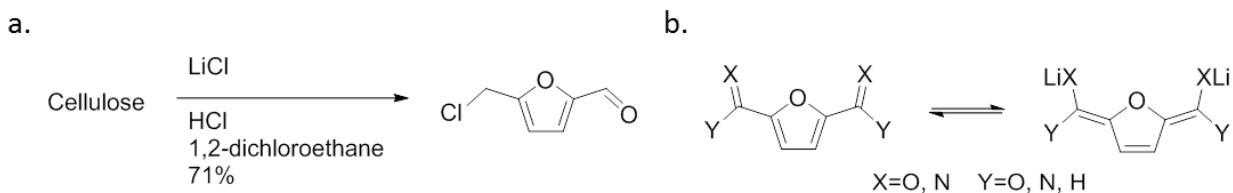
Figure 3.3.4.1. (a.) Mascal's formation of furan backbone from cellulose (b.) Redox process of furan dicarbonyls can be applied to a variety of different X and Y.

However, in contrast to utilizing the terephthalate demonstrated by Tarascon, the five-membered furan group seems preferable partially due to its lower molecular, but mainly due to its increased sustainability, to eventually synthesize poly(ethylene furandicarboxylate). This polyester has a molecular weight of 182.13 g/mol per monomer unit, which translates into a theoretical capacity of 295 mAh/g.

3.4 Results

Although our ultimate goal would be to take advantage of the low solubility of the polymer, we opted to begin our efforts with small molecule test cases in the hopes of demonstrating, which functionality would allow us to access the optimum electrochemical activity.

3.4.1 Synthesis.

The target functionalities are the amide, the ester and the imine (Figure 3.3.4.1 b). The amide and the ester can be accessed in two steps from CMF via furan dicarboxylic acid, FDCA Though it has been shown the CMF can be synthesized from any carbohydrate, the process has shown to be most efficient from fructose.[12] With this in mind, CMF was synthesized from fructose, and carried on to form FDCA in modified literature procedures.[13,14] The imine was accessed from the commercial available 2,5-diformyl furan (DFF) (Scheme 3.4.1.1)—although

the synthesis of this compound in one step from fructose—or two, via the same CMF intermediate—is well documented.[15]
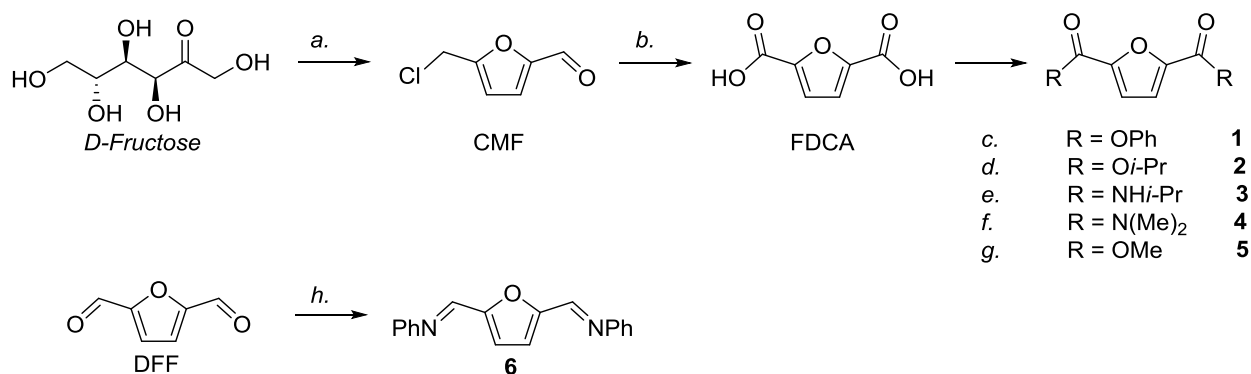
Scheme 3.4.1.1. (a.) *ref. 14* (b.) *ref 13* (c.) Phenol, TsCl, Methylimidazole (d.) TsCl, IPA, PhMe (e.) 1.(COCl)$_2$, THF; 2. Isopropyl amine, DMAP, TEA, THF (f.) SOCl$_2$, DMF (g.) TMS-CH$_2$N$_2$, Et$_2$O (h.) Aniline (*neat*).

Furans **1**-**5** were isolated as white solids, while the increased conjugation of imine **6** resulted in a yellow crystalline solid. The substitutions of the esters and amides were selected to optimize their properties with regard to their solubility, theoretical capacity and thermal properties. While the diamides are relatively robust, the diesters proved to have less forgiving thermal properties. When the size of the R group was decreased, as in the case of furan **5**, the boiling point becomes low. However, increasing the size of the substitution to a higher order alkane, in the hopes of circumventing this problem, tends to result depressed melting points. With this in mind, the isopropyl group was selected for diester **2**.

3.4.2 Electrochemistry in Solution

There has been relatively little mention of the electrochemical behavior of the furan dicarbonyl group in the literature. To our knowledge, the sole mention comes from a study of the electrochemical behavior of aromatic dicarbonyls at -78$^{\mathbf{o}}$C with the aim of establishing ammonia-free alternatives to the birch reduction.[16] With this in mind, our study began with
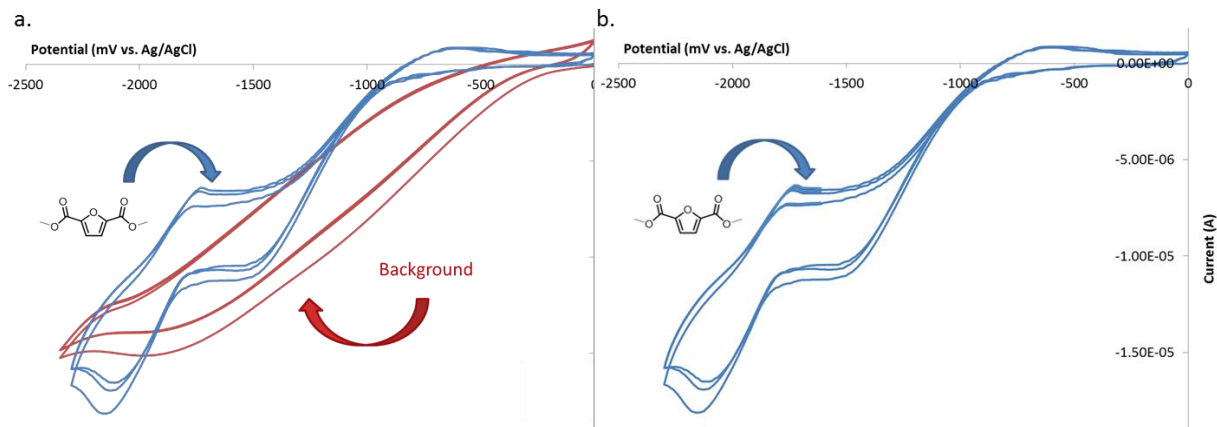
Figure 3.4.2.1. Electrochemistry of furan **5** at 0.1 M N(Bu)$_4$ClO$_4$ in THF at a scan rate of 100mV/sec (a.) compared against the supporting electrolyte and (b.) alone.

establishing the electrochemical activity in solution. Furan **5** was selected as our test system. To our satisfaction, we found that the material displayed the classical behavior for a two electron redox system displaying redox processes. The potentials that they displayed these processes, however, -1.1 V vs Ag/Ag$^+$ (2.1 V vs Li/Li$^+$) for X/X$^-$ and at -2.0 V vs Ag/Ag$^+$ (1.2 V vs Li/Li$^+$) for X$^-$/X^{2-}, were slightly higher than ideal.

3.4.3 Electrochemistry in Solid

Given our experience with translating the electrochemical measurements from solution to the solid (Chapter 2.3), however, we found that while the values found in solution would generally give a decent range to explore in the solid, the translation of media did cause a decent variation in results that was sample specific. The nitrile substituted NDI **9** displayed redox activity at -0.1 V vs Ag/Ag$^+$ (3.1 V vs Li/Li$^+$) for X/X$^-$ and at -0.4 V vs Ag/Ag$^+$ (2.6 V vs Li/Li$^+$) for X$^-$/X^{2-}, its first reduction potential in the solid, 2.8 V vs Li/Li$^+$, seemed to indicate a value near average of the two, though slightly closer to X$^-$/X^{2-} process. In contrast, however, dimethylamino substituted NDI **7** displayed redox activity at -0.97 V vs Ag/Ag$^+$ (2.27 V vs Li/Li$^+$) for X/X$^-$ and at -1.2 V vs Ag/Ag$^+$ (2.0 V vs Li/Li$^+$) for X$^-$/X^{2-}, its first reduction potential

in the solid, 2.3 V vs Li/Li$^+$, was even higher than that displayed in the X/X$^-$ process in solution (Table **2.3.1**, Figure **2.3.1**)

With this in mind, the furans were explored in the solid state over a variety of potential
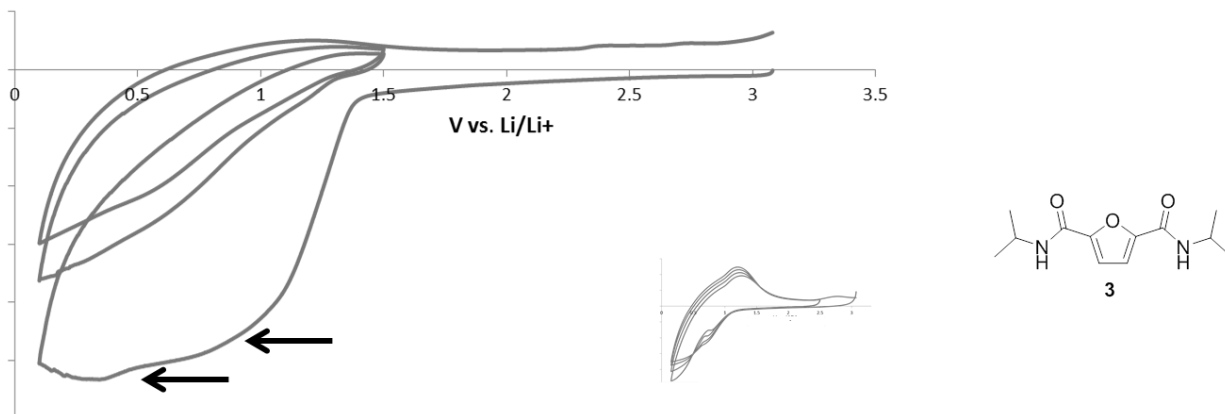
Figure 3.4.3.1. Cyclic voltametry of furan **3** in 2016 coin cell with 1M LiClO$_4$ in 1:1 vol/vol ethylene carbonate : dimethyl carbonate (EC:DMC) electrolyte, using lithium metal as counter electrode at a scan rate of 5 mV/sec with an electrode formulation composition of furan **3** and acetylene black in a 1:1 ratio. *Inset shows control experiment under similar conditions in the absence of furan.*

windows. Unfortunately, however, these results proved far less promising. All furans showed minimal to no electrochemical activity. Isopropylamide **3**, which showed the most promising result (Figure **3.4.3.1**) displayed a small reductions at ~1.0 V vs. Li/Li$^+$ and ~0.4 V vs. Li/Li$^+$, which would have been attractive values. However, these processes, unfortunately, seemed minimal and irreversible. Attempts to optimize these results by varying formulation and electrochemical experimental setup were unsuccessful.

3.5 Synthetic Procedures and Characterization

R = OPh	1
R = O*i*-Pr	2
R = NH*i*-Pr	3
R = N(Me)$_2$	4
R = OMe	5
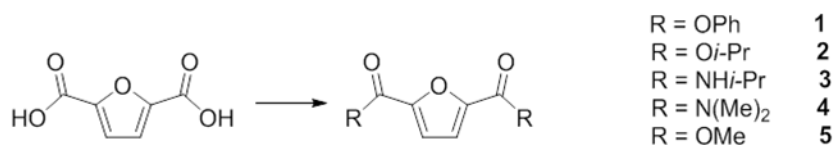
Scheme 3.5.1. Synthesis of furans **1-5**

72

Synthesis of 1.[17] To 2,5-furan dicarboxylic acid (150 mg, 0.96 mmol), toluenesulfonyl chloride (183 mg, 0.96 mmol) and phenol (181 mg, 1.92 mmol) were added together in a reflux system. 1-methylimidazole (230 µL, 2.88 mmol) was added and reaction was heated to 60°C for one hour. Mixture was cooled to room temperature. Water was added and mixture was extracted with dichloromethane. Crude mixture was purified by flash column chromatography to yield product as white fibrous solid (120 mg, 43%).

Synthesis of 2. To a dry reflux system under argon was added 2,5-furan dicarboxylic acid (100 mg, 0.64 mmol) and toluenesulfonic acid monohydrate (243 mg, 1.28 mmol). Solids were dehydrated under vacuum and backfilled. Anhydrous toluene (4 mL) and isopropyl alcohol (1.5 mL) were added and reaction was heated to reflux for 36 hours. Reaction was cooled to room temperature. Reaction was basified with saturated $NaHCO_3$, and organics were washed with $NaHCO_3$, dried with $MgSO_4$ and purified by flash column chromatography (20% DCM in hexane) to yield product as white solid (83 mg, 54%).

Synthesis of 3. To a roundbottom flask under argon was suspended 2,5-furan dicarboxylic acid (200 mg, 1.28 mmol) in tetrahydrofuran. Oxallyl chloride (275 µL, 3.2 mmol) was added. Triethylamine (611µL) was added followed by isopropylamine (263 µL). Reaction was stirred until reaction completed by TLC. Reaction was purified by aqueous workup followed by flash column chromatography to yield product as white solid.

Synthesis of 4.[18] To a dry reflux system under argon was added 2,5-furan dicarboxylic acid (200 mg, 1.28 mmol). Anhydrous dimethylformamide (13 mL) was added until starting material had fully dissolved. Thionyl Chloride (232 µL, 3.20 mmol) was added and reaction was heated to 150°C for 6 hours. Reaction was allowed to cool to 0°C and saturated $NaHCO_3$ (25 mL) was added. Diethyl ether was added. Aqueous layer was removed and organics were washed with

NaHCO$_3$ and Brine, dried with MgSO$_4$ and purified by flash column chromatography to yield product as white solid.

Synthesis of 5. With the exception of substituting diazomethane with the more stable TMS-diazomethane, synthesis and characterization were carried out according to previously reported literature procedures.[19]
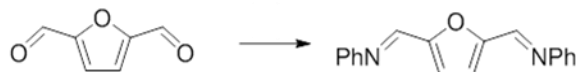
Scheme 3.5.2. Synthesis of furan **6**

Synthesis of 6. . To 2, 4-Diformylfuran (50 mg, 0.403 mmol) was added freshly distilled aniline (77 µL, 0.846 mmol) dropwise. Upon addition, reaction became yellow solid. Reaction was stirred for 15 minutes. Yellow solid was purified by recrystallized from a minimum amount of hot MeOH. Characterization matches previously reported literature data.[20]

Figure 3.5.1. ^{1}H NMR of compound **1** in CDCl$_3$ at 400 MHz
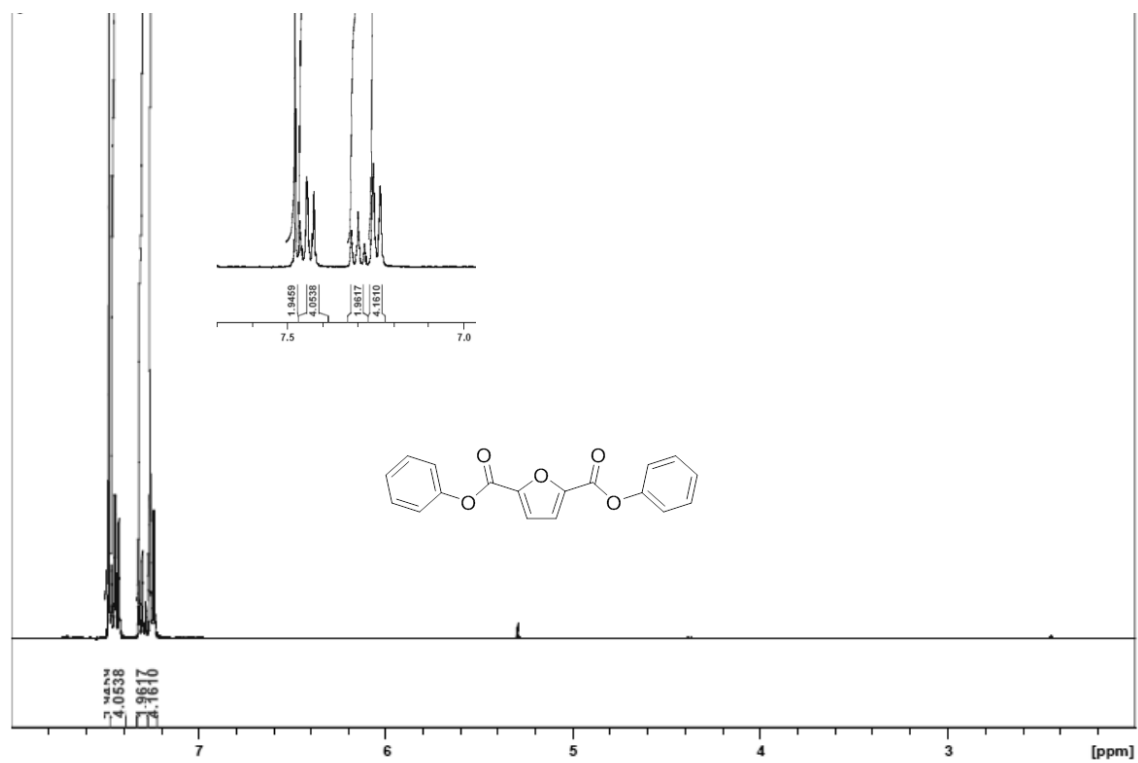
Figure 3.5.2. ^{13}C NMR of compound **1** in CDCl$_3$ at 125 MHz
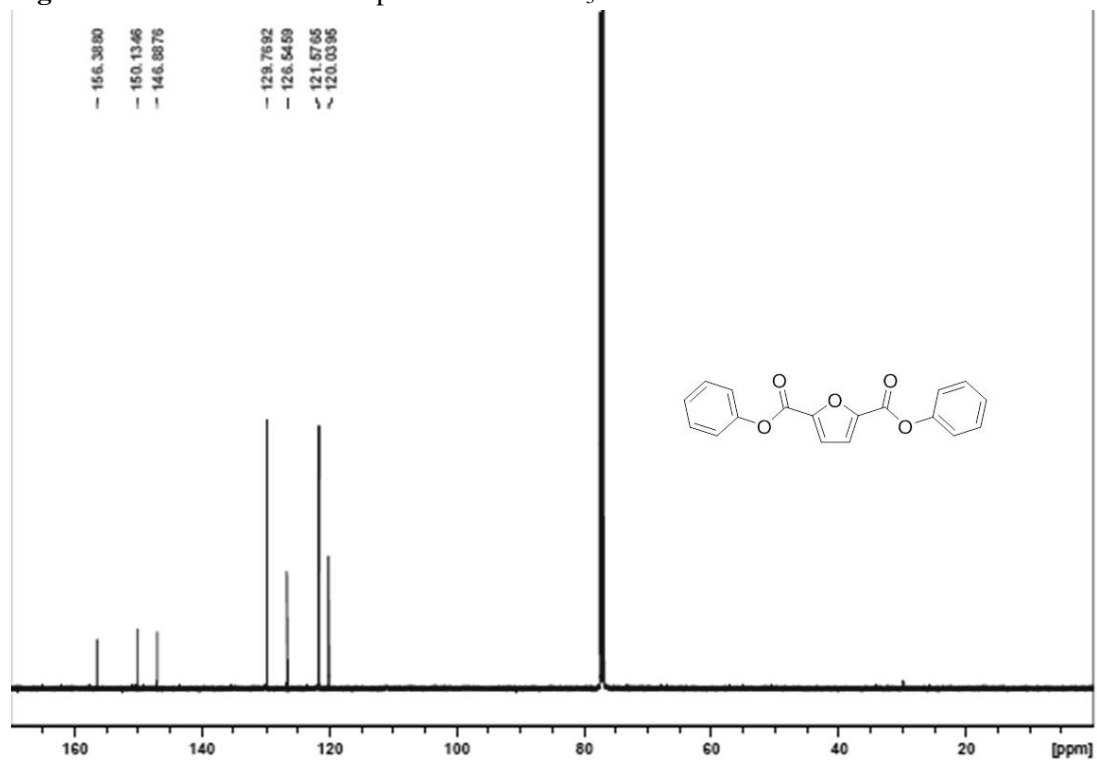
Figure 3.5.3. ^{1}H NMR of compound **2** in CDCl$_3$ at 400 MHz
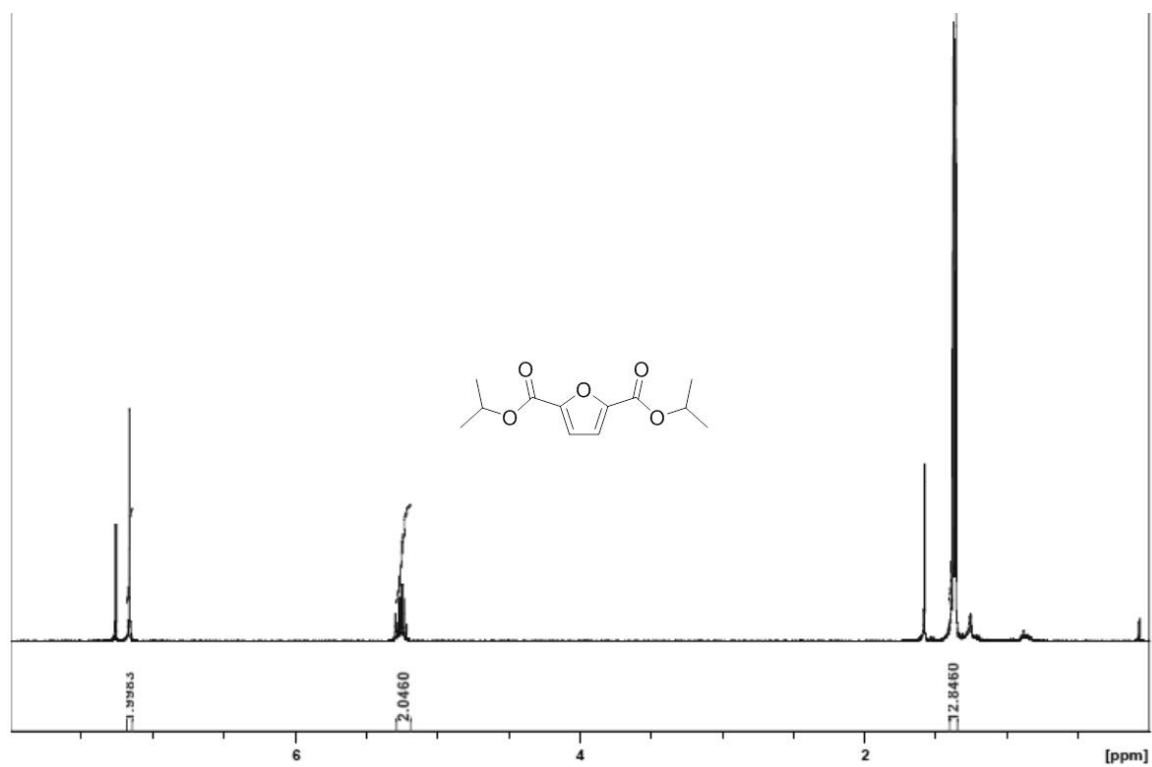
Figure 3.5.4. ^{13}C NMR of compound **2** in CDCl$_3$ at 125 MHz

76
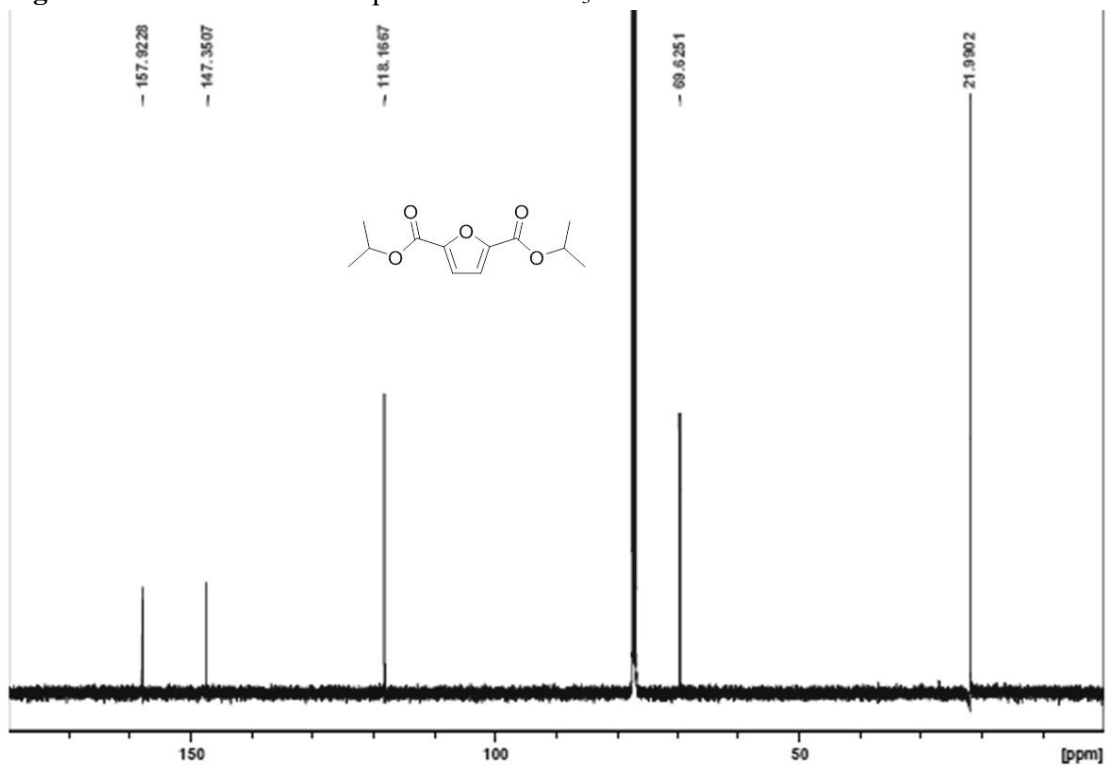
Figure 3.5.5. ^{1}H NMR of compound **3** in CDCl$_3$ at 400 MHz
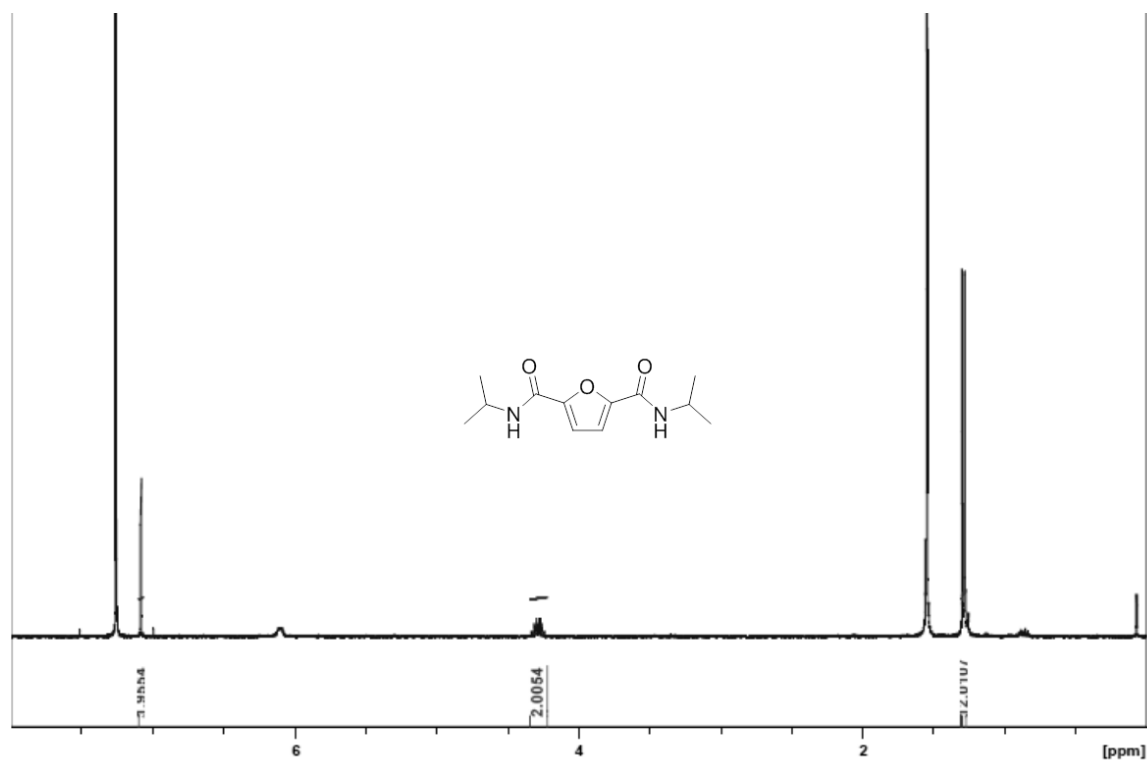
Figure 3.5.6. ^{13}C NMR of compound **3** in CDCl$_3$ at 125 MHz
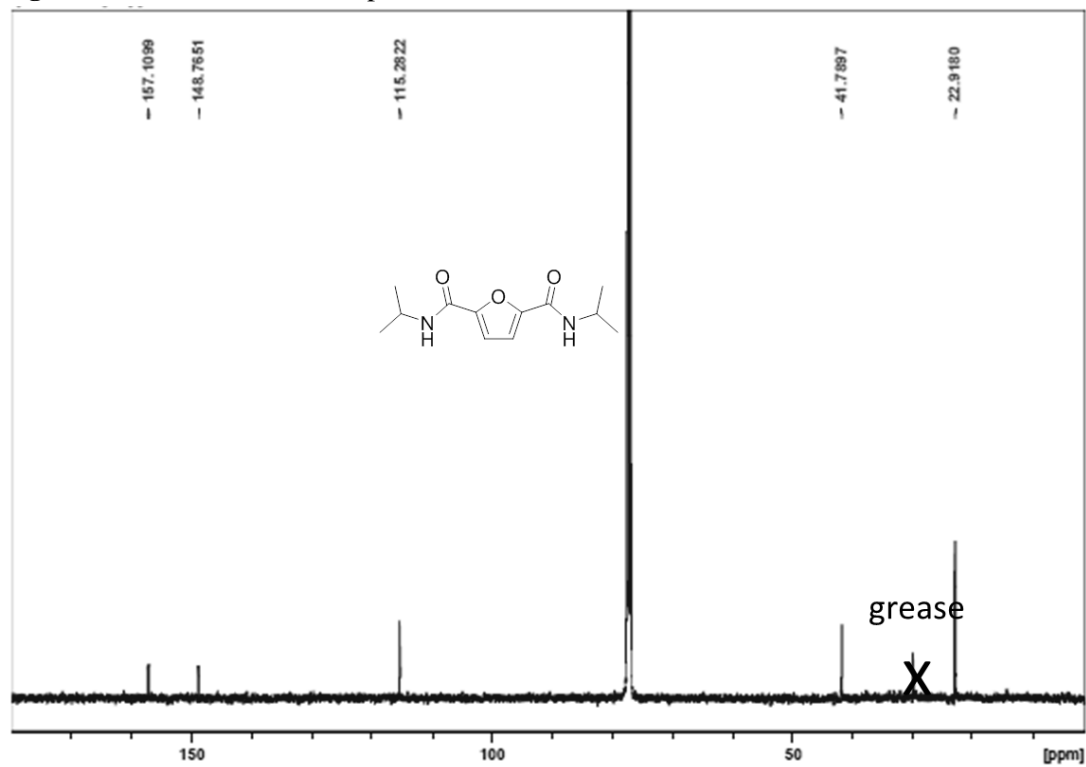
Figure 3.5.7. ^{1}H NMR of compound **4** in CDCl$_3$ at 400 MHz

2.0001

12.1408

7 6 5 4 3 [ppm]
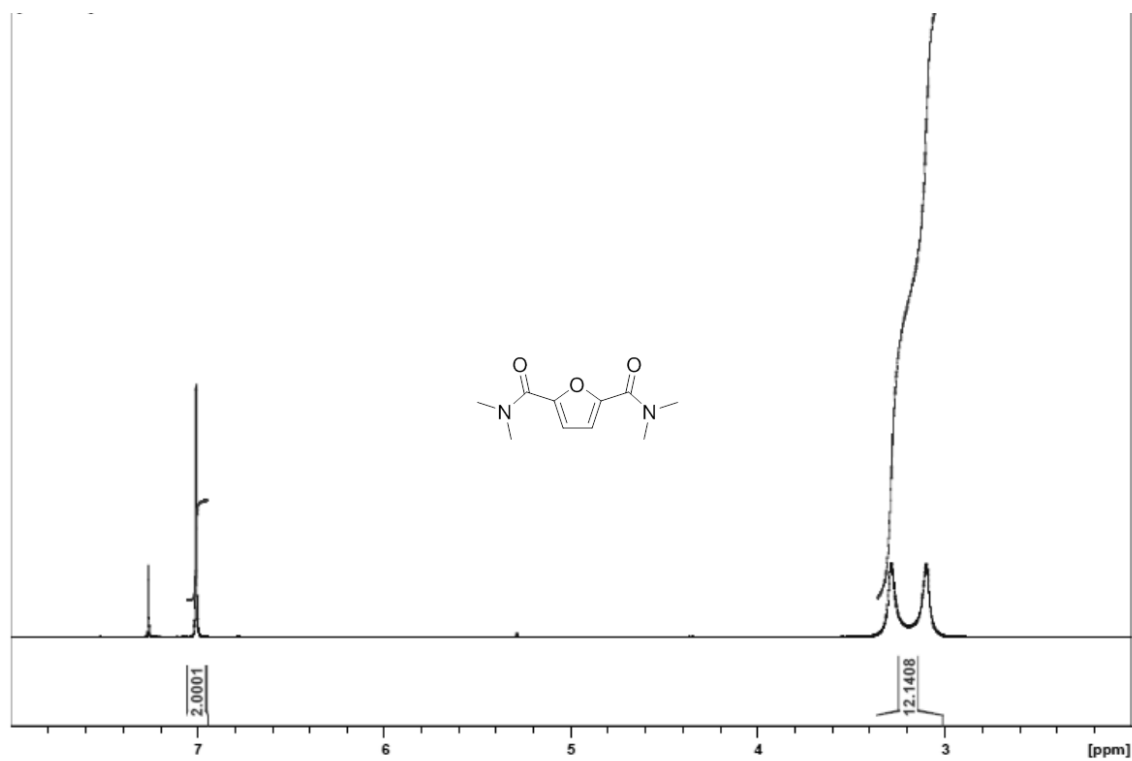
Figure 3.5.8. ^{13}C NMR of compound **4** in CDCl$_3$ at 125 MHz

159.9132
148.6651
116.6818
38.4752
36.5907

150 100 50 [ppm]
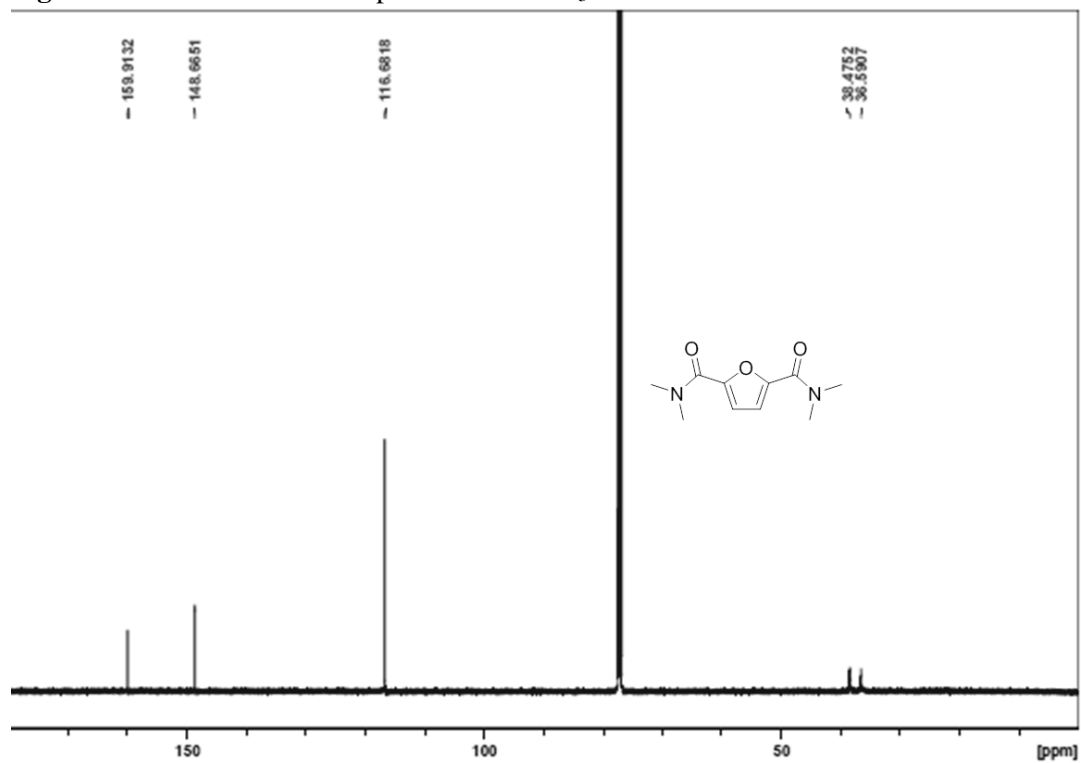
3.6. References

[1]Mascal, M.; Nikitin, E. B. *Angew.Chem. Int. Ed.* **2008**, *47*, 7924.

[2] (a.) Quian, J.; Henderson, W. A.; Xu, W.; Bhattacharya, P.; Engelhard, M.; Borodin, O.; Zhang, J.-G. *Nat. Commun.*, **2015**, *6*, 6362. (b.) Xu, W.; Wang, J.; Ding, F.; Chen, X.; Nasybulin, E.; Zhang, Y.; Zhang, J.-G. **2014**, *7*, 513. (c.) Takehara, Z.-I. *J. Power Sources*, **1997**, *68*, 82.

[3]Arrouvel, C.; Parker, S.; Islam, M. S. *Chem. Mater.*, **2009**, *21*, 4778.

[4]Lian, Y.; Tao, Z.; Chen, J. *Adv. Energy Mater*, **2012**, *2*, 742.

[5]Novák, P.; Müller, K.; Santhanam, K. S. V.; Haas, O. *Chem. Rev.*, **1997**, *97*, 207.

[6] Nakahara, K.; Iwasa, S.; Satoh, M.; Morioka, Y.; Iriyama, J.; Suguro, M.; Hasegawa, E. *Chem. Phys. Lett.*, **2002**, *359*, 351.

[7]Yoshizawa, M.; Ohno, H. *Chem. Lett.*, **1999**, 889.

[8]Oyaizu, K.; Suga, T.; Yoshimura, K.; Nishide, H. *Macromolecules*, **2008**, *41* 6646.

[9]Suguro, M.; Iwasa, S.; Nakahara, K. *Electrochem. Solid-State Lett.*,**2009**, *12* A194.

[10] Armand, M.; Grugeon, S.; Vezin, H.; Laruelle, S.; Ribiére, P.; Poizot, P.; Tarascon, J. M. *Nat. Mater.*, **2009**, *8*, 120.

[11]Walker, W.; Grugeon, S.; Vezin, H.; Laruelle, S.; Armand, M.; Wudl, F.; Tarascon, J.M. *J. Mater.Chem.*, **2011**, *21* 1615.

[12]Kumari, N.; Olesen, J.K.; Pedersen, C. M.; Bols, M. *Eur. J. Org. Chem.* **2011**, 1266.

[13]Brasholz, M.; von Kanel, K.; Hornung, C. H.; Saubern, S.; Tsanaktsidis, J. *Green Chem.*, **2011**, *13*, 1114.

[14] Synthesis of CMF from fructose: Quiroz-Florentino, H.; Hernandez-Benitez, R. I.; Aviña, J. A.; Bergueño-Tapia, E.; Tamariz, J. *Synthesis*, **2011**, *7*, 1106. Synthesis of FDCA from ref. 13

[15] (a.) Halliday, Gary A.; Young, R. J.; Grushin, V. V. *Org. Lett.*, **2003**, *5*, 2003. (b.) Laugel, C.; Estrine, B.; Le Bras, J.; Hoffman, N.; Marinkovic, S.; Muzart, J. *ChemCatChem*, **2014**, *6*, 1195.

[16] Donohoe, T.; Johnson, D.; Compton, R.; Wadhawan, J. *Tetrahedron*, **2004**, *60*, 5945.

[17] Procedure adapted from: Khalafi, Nezhad, A.; Parhami, A.; Zare, A.; Moosavi Zare, A. R. *J. Iran. Chem.Soc.*, **2008**, *5*, 413.

[18] Procedure adapted from Kumagai, T.; Anki, T.; Ebi, T.; Konishi, A.; Matsumoto, K.; Kurata, H.; Kubo, T.; Katsumoto, K.; Kitamura, C.; Kawase, T. *Tetrahedron*, **2010**, *66*, 8968.

[19] Citron, C. A.; Rabe, P.; Dickshat, J. S. *J. Nat. Prod.*, **2012**, *75*, 1765.

[20] Dominguez, C.; Escobar, G.; Plumet, J.; Gaset, A.; Rigal, L. *Anales de Quimica, Serie C: Quimica Organica y Bioquimica*, **1986**, *82*, 241.

CHAPTER 4

Correlated Motion Studies of a Molecular Rotor/ Solvent Co-Crystal

based on the Synthesis and Characterization of a Peripherally

Substituted Triptycene base Rotor

4.1. Abstract.

The development of machines on the molecular scale is a desirable yet challenging goal, that the Garcia-Garibay group has explored using the model of the molecular gyroscope (chapter 1.3.2).[1] Previous work has shown that peripherally hexamethylated triptycene stator based gyroscope **1** co-crystallized with bromobenzene leads to impressive rotational dynamics of the rotator despite the proximity of the rotator to the crystallographically defined solvent molecules. With this result in mind, this chapter focuses on the synthetic optimization of this rotor and its derivatives as well as preliminary studies—still in progress—towards demonstrating a correlated "gearing"-like motion between the rotator and the solvent molecules.

4.2. Introduction.

Mislow and Iwamura's 1988 study on triptycene based bevel gears[2] demonstrated correlated motion at the molecular level—an extremely attractive concept to translate to the solid state as it allows us to envision their behavior as analogous to that of gears in a machine. In the context of using the molecular gyroscope to achieve this, we now have two goals in our design: firstly a solid that will allow for unhindered rotation of the rotator, and, secondly, a partner that can undergo a motion correlated to the rotation of the rotator.

Previous work from the Garcia-Garibay group has shown that rotation in the solid state is determined by the hindrance imposed by presence of close neighbors to the rotator within the crystal.[3] As such, the stator portions are often designed to be sterically bulky in comparison to a smaller rotator with the hopes of creating enough free volume around the rotator in the crystallized structure to allow for its unobstructed motion. With this in mind, early work in the

group displayed a triptycene based stator combined with a phenylene rotator.[4] Perhaps, not altogether surprisingly, it was found that, in this case, the molecules tended to pack with adjacent
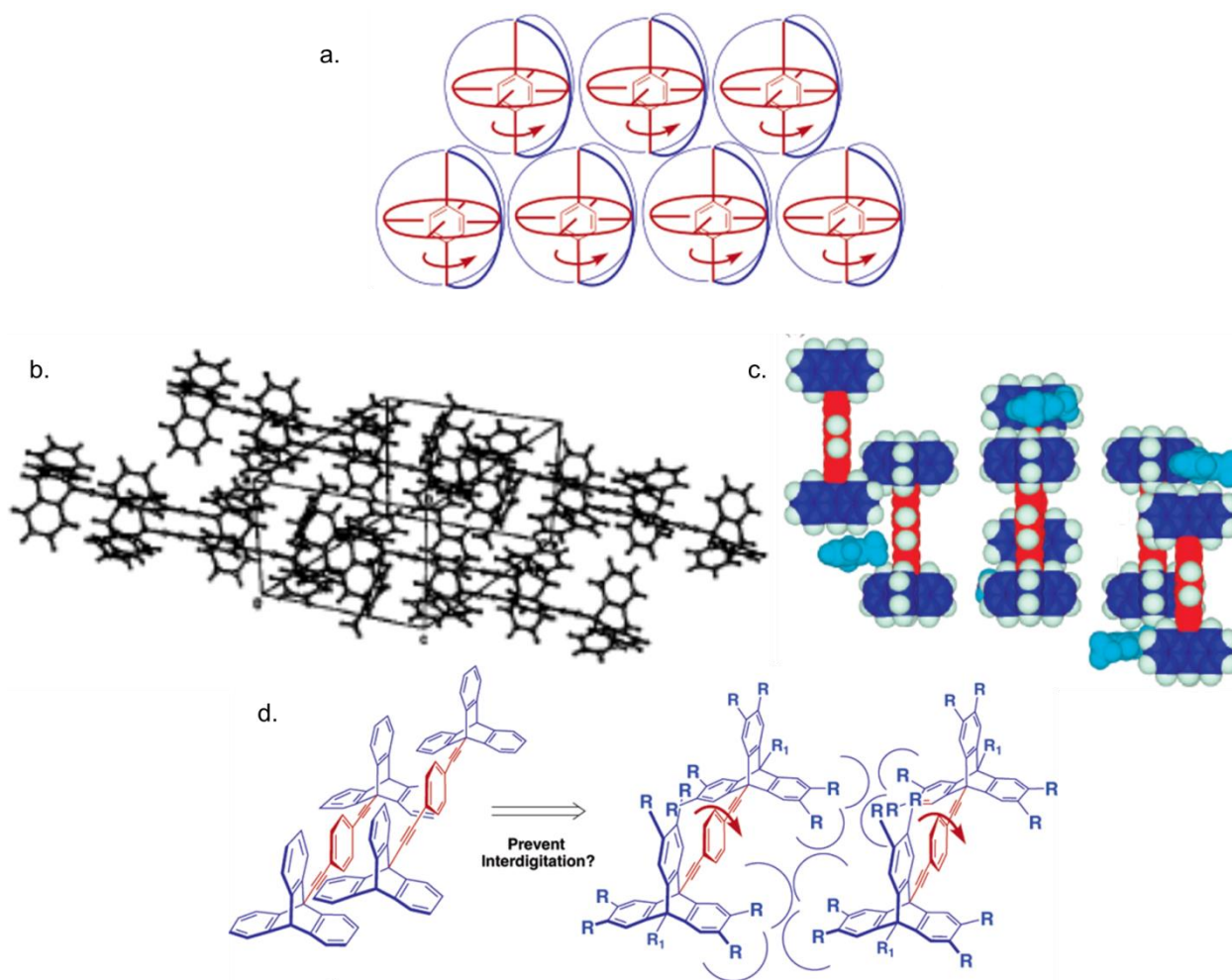

Figure 4.2.1. (a.) Optimal packing arrangement allows for sufficient free volume around the rotator to allow for unhindered rotation. (b.) Crystal structure and (c.) space-filling model of triptycene based rotor crystallized from m-xylene demonstrates absence of this free volume due to interdigitation and solvent molecules. (d.) As the triptycene did not provide sufficient bulk to create the desired cavity, the steric bulk was increased. *Reproduced from Godinez,* et al.[4,5]

molecules interdigitated and crystallographically defined solvent close to the rotator (Figure

4.2.1a-c). As a result, the rotator experienced aromatic π-π-stacking and edge-to-face interactions

with its neighbors leading to hindered rotation. In order to circumvent this problem, Godinez *et*

al.[5,6] reasoned that further increasing the steric bulk of the stator by peripherally substituting the

triptycene group would prevent this interdigitation, and allow for the desired cavity (Figure 4.2.1d). Their study documented the synthesis and crystallization of a series of five peripherally methylated triptycene stator based rotors in the hopes of preventing this interdigitation. Unfortunately, out of the five synthesized rotors—each with different bridgehead substitution— x-ray quality crystals could only be grown from two of them: the phenyl derivative and the propyl derivative. Inspection of the crystal structures, revealed that while, unfortunately, both structures contained neighbors in proximity to the rotator, the propyl derivative—rotor **1**—only contained solvent molecules (bromobenzene) in the desired cavity and not interdigitated

Figure 4.2.2. (a.) Crystallization of the phenyl substituted rotor from m-xylenes still displayed an interdigitated packing arrangement. (b.) Crystallizaiton of the propyl substituted rotor **1**, however, demonstrated desired packing, but with the presences of crystallographically defined bromobenzene in the voids (c.) space-filling model of rotor **1** with solvent molecules removed for clarity demonstrates desireable packing. (d.) Top-down view of rotator and solvent molecules demonstrates a ratchet like arrangement of solvent molecules suggesting a correlation between the motion of the rotator with the rotation of the sovent.

neighboring triptycenes. Given this, solid state ^{2}H NMR analysis of rotor **1** demonstrated that despite the presence of the solvent molecules in the desired cavity, the rotator still displayed impressive dynamics with a very low activation energy of the rotator at a 4.4 kcal/mol. Closer inspection of the arrangement of the solvent molecules about the rotator (Figure 4.2.2.d) reveals a "ratchet"-like arrangement of these solvent molecules. It follows, therefore, that, given the rotation of the rotator, the solvent molecules should display a correlated motion as a result of this rotation.

4.3. Results

4.3.1. Synthetic Strategies

Despite the promise of the hexamethylated triptycene stator, the general strategy taking advantage of peripherally substitute iptycenes has remained relatively unexplored due to the inefficiency of accessing these compounds via traditional synthetic strategies. Godinez *et al.* demonstrated impressive results with regard to the rotational dynamics,[6] but if we take a closer look at the synthetic efforts required to achieve this, we can appreciate how laborious this process was.[5] The model provides two main areas of substitution (Figure 4.3.1.1): the peripheral and the bridgehead. The original study demonstrated the synthesis of five stators, which varied only
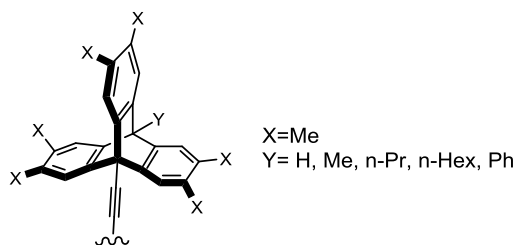
X=Me
Y= H, Me, n-Pr, n-Hex, Ph

Figure 4.3.1.1. The triptycene model has two main areas of substitution: the peripheral (X) and the bridgehead (Y).

the bridgehead substitution. Once synthesized, the crystal structure of these compounds revealed that four of the five could not be carried on. Scheme 4.3.1.1. displays the synthesis of the crystallographically promising n-propyl rotor **1**. This thirteen step synthesis has an overall yield of ~1%, and has two major problems: firstly, both the peripheral and the bridgehead substitution were installed extremely early—the methyl groups in the very first step—and, secondly, the lowest yielding step—the diels-alder to form the bicycle—is extremely late. As the substitutions are installed so early, each of the five synthesized rotors required its own synthesis. Moreover,

this tedious synthesis ending with a late-stage low yielding step, is to be expected as the 15%

yield reported for this step is not unexpected for this type of transformation.
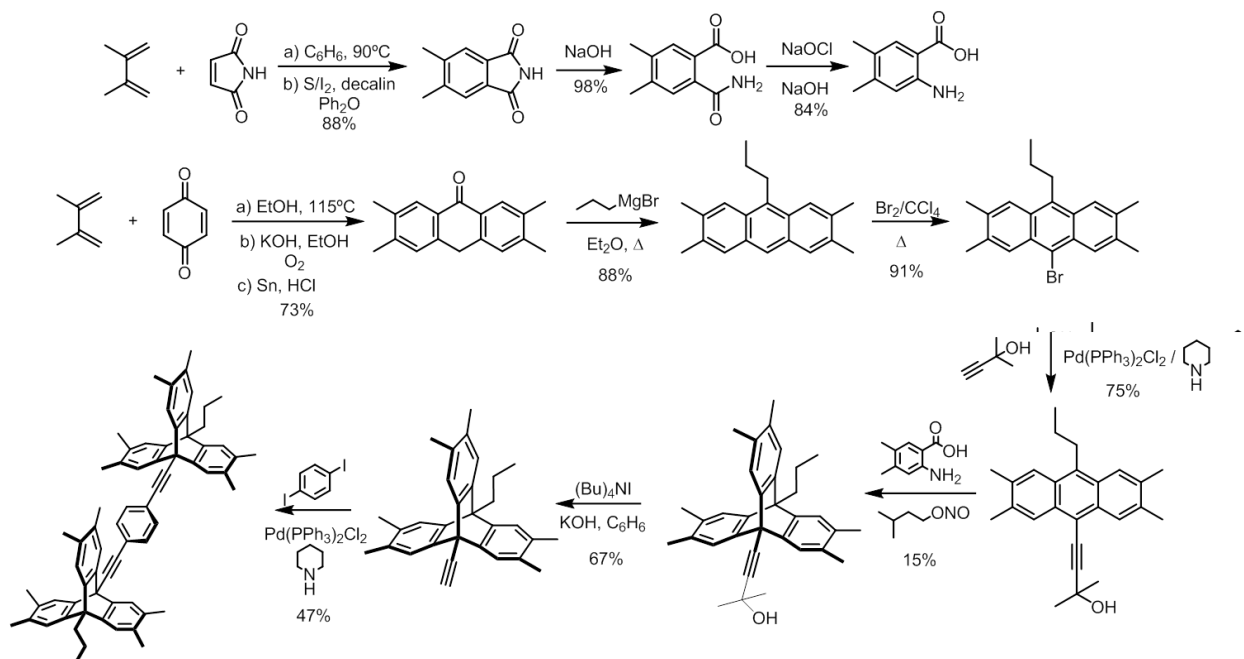
Scheme 4.3.1.1. Original synthetic route by *Godinez et al.* shows laborious synthesis to access
rotor.

With this in mind, we aimed to develop a new synthetic strategy in order to more

efficiently access this rotor as well as those with different peripheral substitution. To this end,

our retrosynthetic analysis would, ideally, display a more divergent approach (Scheme 4.3.1.2).

The peripheral substitution should be installed as late as possible such that each compound

would not require its own synthesis, and the low-yielding diels-alder as early as possible, to

minimize the wastefulness of the late stage, low-yielding step.
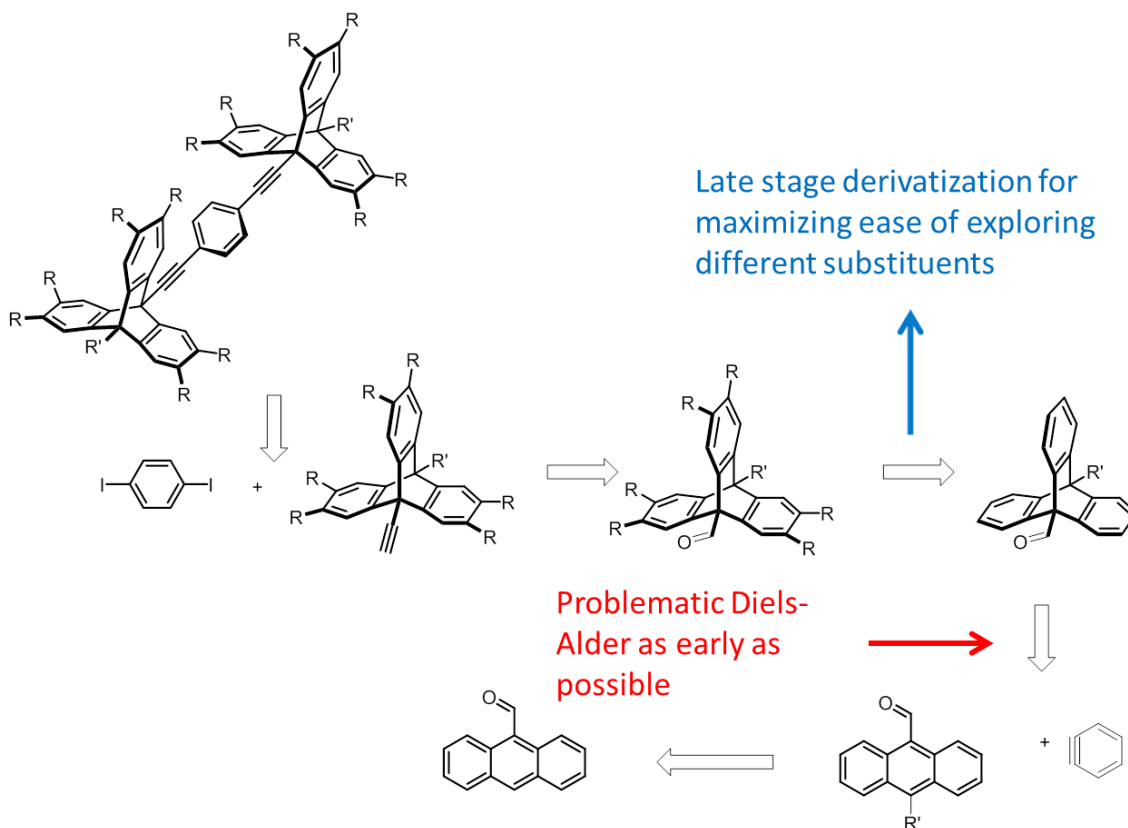
Scheme 4.3.1.2. Retrosynthetic analysis of divergent approach to access rotor.

4.3.1.1. Late Stage Peripheral Substitution

The key step in this synthesis would come from the late stage peripheral substitution installation. Our assumption was that the triptycene structure would make regioisomers partially substituted triptycenes challenging, if not impossible, to separate. With this in mind, it was crucial to be able to exhibit complete control over this reaction, and, therefore, was the first aspect to be explored.

Up until this point, the synthesis of peripherally substituted triptycenes was mainly achieved by synthesizing the substituted anthracene and benzyne precursor. However, within the last decade, people have begun to further explore late stage functionalization strategies.[7-9] In 2009 Hilton *et al.*[7] demonstrated that triptycene itself could be regioselectively hexabrominated

87

in one step using modified Friedel-Crafts conditions improving on the much longer scheme in the only prior synthesis of this compound.[10] Inspired by this method, dimethyl triptycene **3-Me** (Scheme 4.3.1.1.1) was used as a test system, and we found that optimized conditions yielded the desired hexbrominated **4-Me** in 98%. The desired hexamethylated substitution could then be
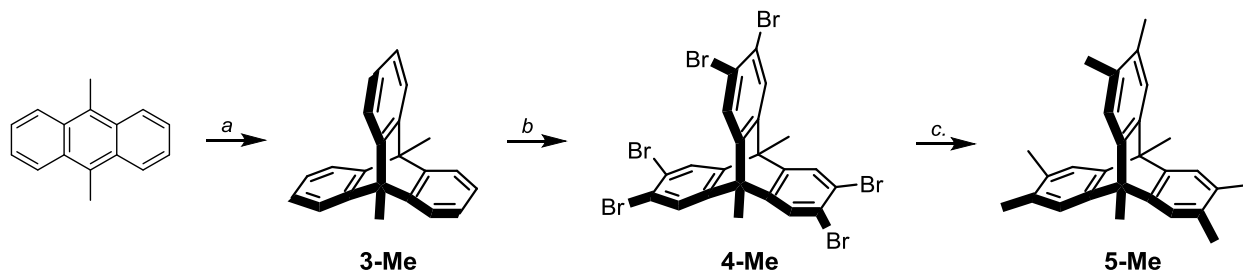
Scheme 4.3.1.1.1. (a.) *i.* Anthranilic acid, Isoamyl Nitrite, HCl, EtOH; *ii.* Propylene Oxide, PhMe 82% (b) Fe, Br_2, $CHCl_3$ 98% (c.) $Al(Me)_3$, $PdCl_2(PPh_3)_2$, THF 94%.

readily accessed via palladium cross-catalysis. To our satisfaction we found that palladium cross-coupling conditions would go to completion—leaving no unreacted bromine sites. While we found that hexamethylated **5-Me** could be accessed in high yields using the standard Suzuki coupling partner—methylboronic acid—we found the transformation to be cleanest when subjected to trimethylaluminum. We found the efficiency of this process to be especially impressive leading to yields well above 90% for each of the two steps despite that each step created six bonds.

4.3.1.2. Installing Bridgehead Substitution.

Having established the promise of the late stage substitution, the issue became incorporating these steps into the synthesis of the rotor. While efficient, neither the molecular bromine (Scheme 4.3.1.1.1a) nor trimethylaluminum (Scheme 4.3.1.1.1b) would be compatible with the internal alkyne of the desired rotor **1**.

Inspired by previous work demonstrating successful manipulation of the bridgehead by forming an organolithium species followed by quenching with a carbonyl based electrophile[11], our initial attempts started with brominated bridgehead positions. **5-Br** was synthesized from commercially available 9,10-dibromoanthracene using the same synthetic scheme as that used to access **5-Me**. With this material in hand, we attempted to perform a lithium halogen exchange using one equivalent of an organolithium source, followed by quenching with bromopropane. This, however, did not result in the desired substitution reaction. Strong lithiation conditions were needed to perform the lithium halogen exchange, but, even once the desired anion was accessed, it was too hindered to act as a nucleophile.

Given this failed result, it follows that the previously discussed success of the carbonyl based electrophile was likely via an electron transfer mechanism and not nucleophilic addition as initially proposed by Kawada *et al.*[11c] Though disappointing, this conclusion was not unexpected, as it is well documented that the bridgehead position of the iptycene group is notoriously unreactive.[12] Despite this, Harmata *et al.*[13] demonstrated that substitution at the inert bridgehead position, in some systems, can be can occur and actually be favored over other electrophilic sites
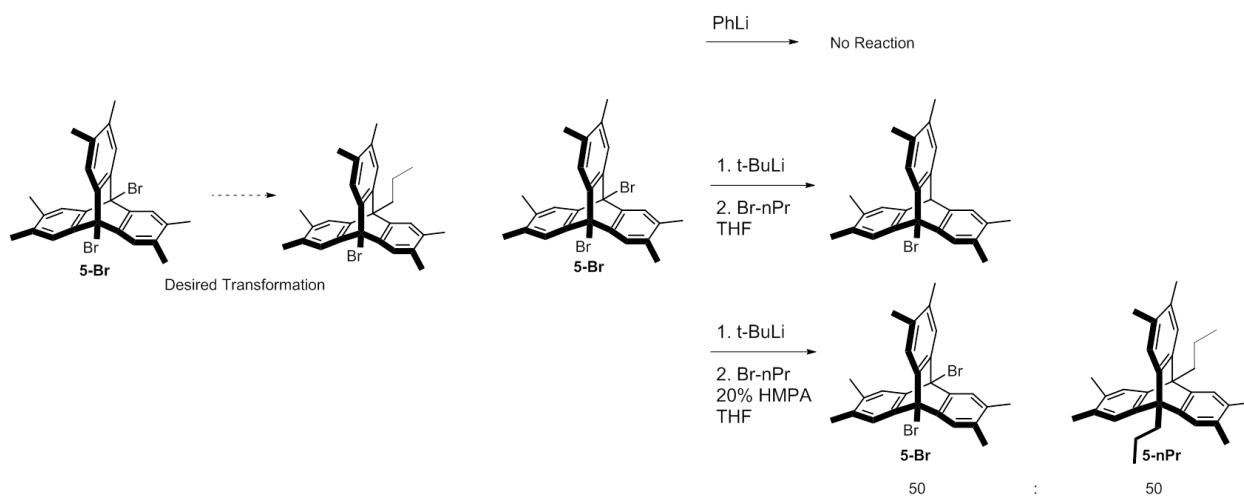
Scheme 4.3.1.2.1. Attempts to alkylate bridge head position.

when the solvent is changed from THF or diethyl ether to 20% HMPA in THF. When this solvent system was applied to **5-Br** in the presence of one equivalent of a lithium source, we found that the desired alkylation did occur. However, curiously, it seemed to occur selectively to the second brominated position on a single triptycene resulting in a 1:1 mixture of the starting material **5-Br** and the dialkylated **5-nPr**.

Given the challenge of alkylating the bridegehead substitution, in one more attempt, we opted to install the propyl group prior to the Diels-Alder and only attempt the better precedented formalation of the bridgehead position[11] later on. With this in mind, **5-nPr,Br** was lithiated followed by formalation taking advantage of the precedented conditions. While the reaction did yield the desired aldehyde, the formalation was was the minor product (<20%) in favor of the protonation when performed on the hexamethyl triptycene in place of the parent triptycene—a result consistent with an electron transfer mechanism (Scheme 4.3.1.2.2). It is also in agreement with a carboxylation of a hexamethyl triptycene that has since been reported to occur in 15% in contrast to the previously reported 85%[14] on the analogous non methylated compound.[11c]
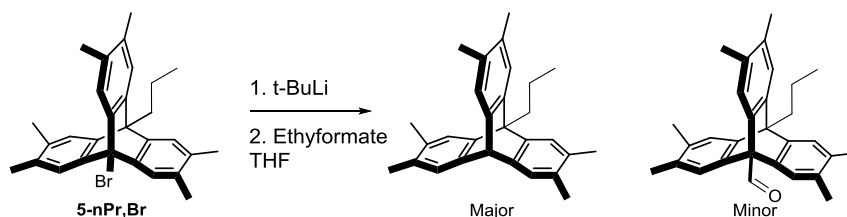
Scheme 4.3.1.2.2. Inefficient formalation of hexamethyl triptycene.

4.3.1.3. Installing 9,10-Anthracene Substitution.

Given the inert nature of the bridgehead position, synthetic efforts towards installing functionality to only these positions prior to forming the bicycle were explored simultaneously. As previously discussed, the alkyne group could not be installed prior to the peripheral substitution. Therefore, aldehyde **8** which could be synthesized in two simple steps from

commercially available 9-anthraldehyde[15] (Scheme 4.3.1.3.1), was selected, as numerous know synthetic conditions that allow us to access an alkyne from an aldehyde.[16] Modified Diels-Alders conditions allowed us to access the bicycle in triptycene **9** in the comparatively high yield of 62%. At this point, the peripheral substitution, as described above, was performed. The bromination proceeded as expected.
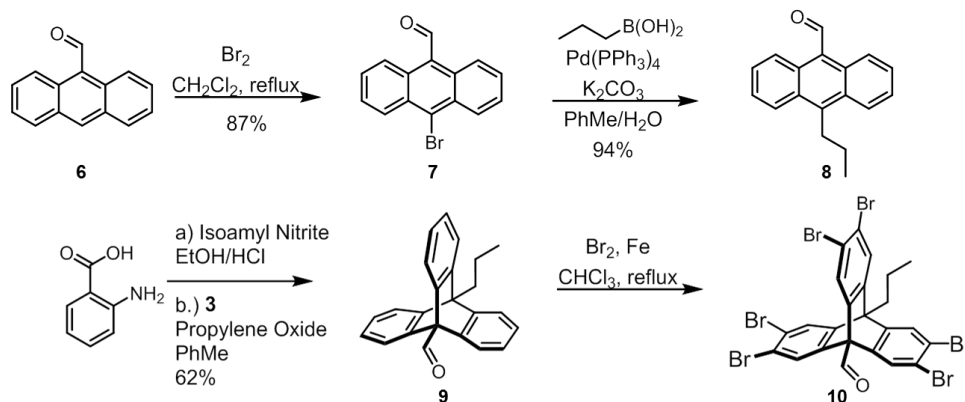
Scheme 4.3.1.3.1. Synthesis of peripherally brominated triptycene **10**.

Like the alkyne, the aldehyde is incompatible with trimethyl aluminum. Unlike the alkyne, however, the aldehyde could be protected via a number of protecting groups—here, we chose the thioacetal as it is less labile than the acetal, and, therefore, would be more likely to withstand the acidic trimethylaluminum (Scheme 4.3.1.3.2),. Once the thioacetal was installed, the transformation to access hexamethyl **11** occurred in extremely efficient 97% yield, and could then be cleanly removed access aldehyde **12**. Bestman-Ohira homologation followed by optimized sonogoshira coupling conditions[17] concluded the synthesis of desired rotor **1**.
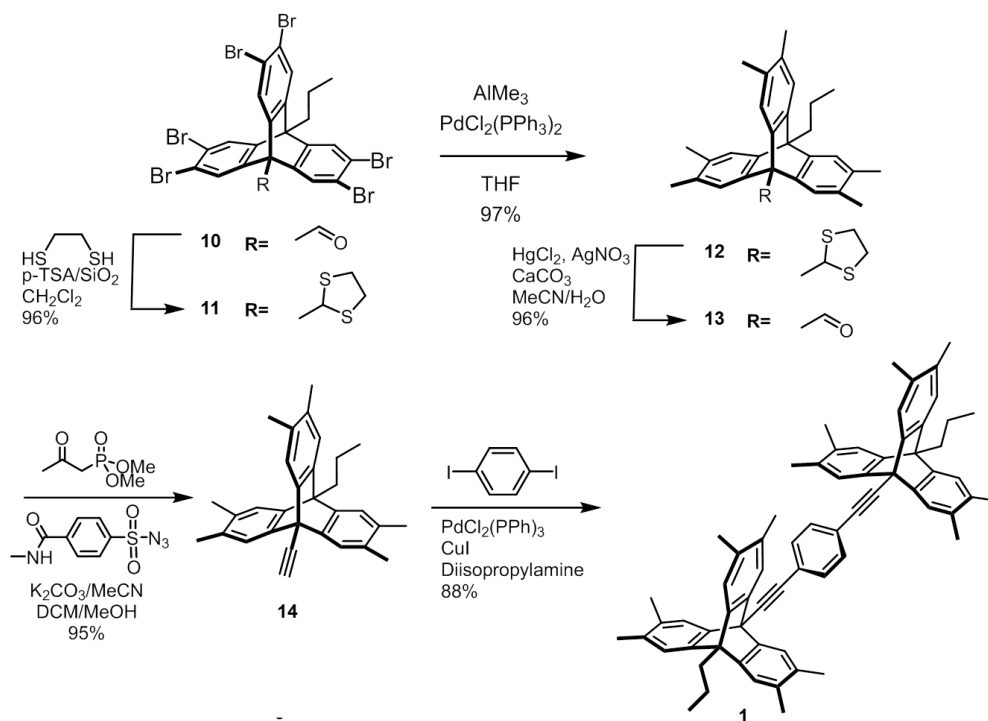
Scheme 4.3.1.3.2. Conclusion of synthesis of rotor **1**.

4.3.2. Solid State Results

With the natural abundance rotor in hand, the materials could then be crystallized from
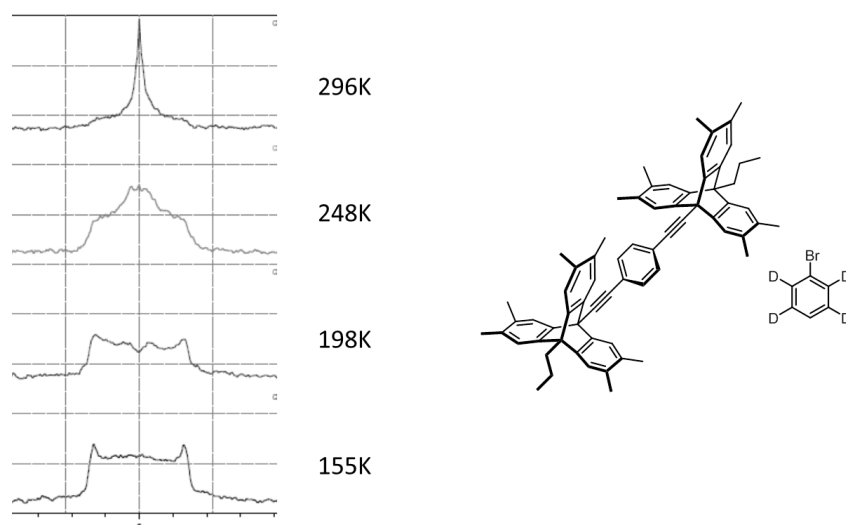
Figure 4.3.2.1. Preliminary **SS** ^{2}H NMR data of a rotor/ bromobenzene-d_4 co-crystal demonstrating temperature dependent rotation..

the deuterated bromobenzene and the dynamics measured. While some promising preliminary data has been demonstrated, these studies are ongoing.

4.4. Conclusions.

Given the known success of peripherally substituted triptycene rotor **1**,[5,6] two follow up studies can easily be envisioned taking advantage of this result: firstly, an exploration of the dynamics of the crystallographically defined bromobenzene molecules, and, secondly, an exploration of other, larger peripheral substitutions. However, given the challenge and wasteful nature of traditional methods to access these compounds, neither of these directions could be efficiently explored, and, as such, this strategy was largely abandoned. This chapter describes the development of a synthesis that allows us to efficiently access not only this compound but also any other peripheral substitution that can be accessed as via palladium cross coupling (Chapter 5) that one may want to explore, all coming from a common late stage intermediate. It should be noted that while the incompatibility of trimethylaluminum with the aldehyde led to the necessity of a protecting group in this case, it would not be the case in the vast majority of other coupling partners. As such, this synthesis, not only, provides a more convenient and efficient divergent strategy with no late-stage, bottleneck step, it has also shortened the synthesis from 13 steps to either seven or nine, depending on the coupling partner.

4.5. Experimental

All reactions were performed under an inert atmosphere of argon unless otherwise stated. Chemicals were purchased from commercially available sources and used without further purification unless otherwise noted. Nuclear magnetic resonance (NMR) spectra for ^{1}H were obtained at 300, 400 or 500 MHz as noted and 125 MHz for [13]C. All chemical shifts are

reported in ppm on the δ-scale using the residual natural abundance isotopes of the solvents as references. CDCl$_3$ was calibrated at δ7.26 and δ77.16 for ^{1}H and ^{13}C, respectively. It should be noted the the ^{13}C NMR spectra of the triptycene derivatives displayed a temperature dependence (Figure 4.5.1). With this in mind, these spectra were collected at elevated temperatures as noted.
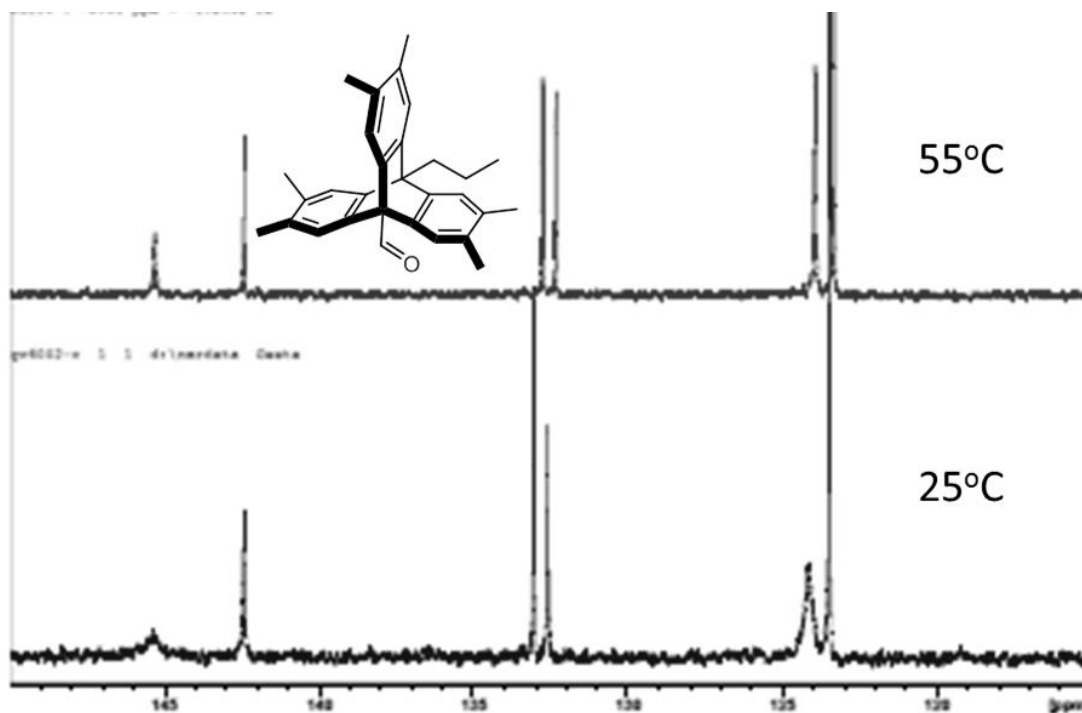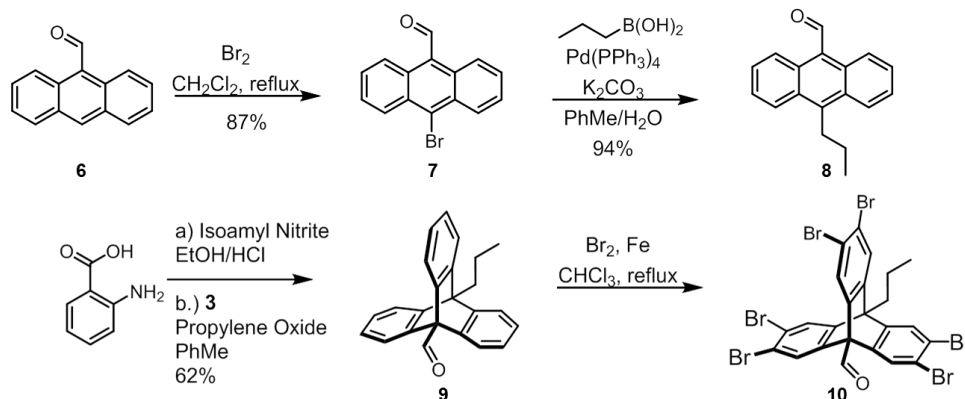

Figure 4.5.1. Representative data demonstrating temperature dependence on experimental ^{13}C NMR spectra: aromatic region of ^{13}C NMR spectrum of triptycene 13 shows broadening of signals at room temperature due to slowed rotation.

Synthesis of 10-bromoanthracene-9-carbaldehyde (7). Compound 7 was synthesized according to previously reported literature procedures.[18]

Synthesis of 10-propylanthracene-9-carbaldehyde (8). To a reflux system was added compound 7 (2g, 7.01 mmol), propylboronic acid (925 mg, 10.52 mmol) and K_2CO_3 (1.94g, 14.02 mmol). Solids were taken up in biphasic toluene (35 mL) : H_2O (35 mL) mixture and thoroughly degassed. $Pd(PPh_3)_4$ (40.4 mg, 0.035 mmol) was added and reaction was further degassed. Reaction was heated to reflux and allowed to proceed to completion via TLC (44 hours). Reaction was cooled to room temperature, and worked up with an aqueous workup followed by flash column chromatography 2:1 Hexane to DCM to yield product as yellow solid (1.634g, 94%).

Synthesis of aldehyde, propyl triptycene (9). Anthranilic acid (2.86 g, 20.05 mmol) was oxidized to corresponding diazonium-chloride salt via previously reported procedures and carried on as crude solid without further purification.[19] Anthracene **8** (940 mg, 3.79 mmol) was added to a flame dried reflux system. Anhydrous toluene (112 mL) was added. Crude diazonium salt was added under argon followed by propylene oxide (23.2 mL) and reaction was heated to reflux over night. Reaction was evaporated under reduced pressure to yield brown solid in brown oil. Mixture was diluted hexane and filtered. Solids were washed with hexane. Solids were dry loaded on to silica and added to column in hexane. Filtrate was loaded onto column and pushed through analogous to a longer plug to remove polymerized/aromatic baseline. Solvents were evaporated under reduced pressure. Crude product was taken up in dichloromethane and stirred with activated charcoal followed by filtering off activated charcoal. Solvents were evaporated. Finally, triptycene was purified via recrystallization from hexane to yield pure product as white solid. Mother liquor could be further purified by flash column chromatography from hexane if

necessary. If crystallized triptycene is colored (pale brown) this likely contains remaining baseline polymer, so can be removed by fast plug. Alternatively, can be purified without crystallization or activated charcoal via *very* slow/careful flash column chromatography. Product as white solid (764 mg, 62%).

Synthesis of brominated triptycene (10). Bromination of triptycene 9 was performed according to procedures outlined in chapter 5.
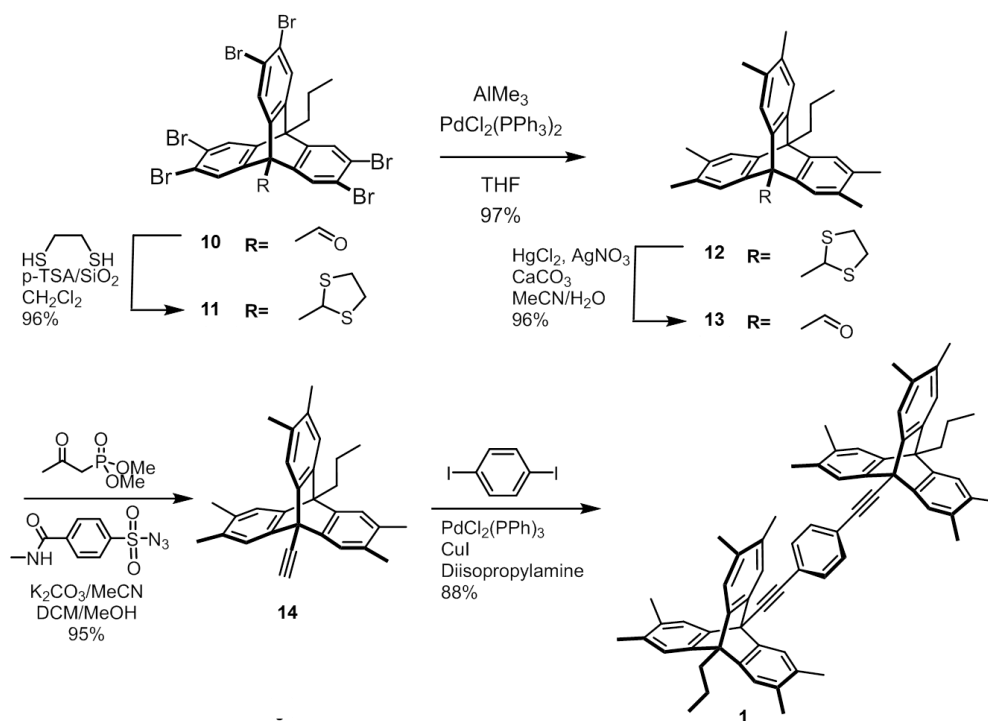
Synthesis of brominated triptycene (11). Triptycene 10 (700 mg, 0.877 mmol) was dissolved in dichloromethane (7.1 mL). Silica supported P_2O_5[20] and ethanedithiol (91 µL) was added and reaction was stirred until aldehyde was no longer present.

Synthesis of Methylated triptycene (12). Triptycene 11 (225 mg, 0.257 mmol) was taken up in anhydrous THF (21 mL) a flame-dried reflux system. Mixture was thoroughly degassed. $PdCl_2(PPh_3)_2$ (54 mg, 0.078 mmol) was added and mixture was further degassed. Reaction was heated to 50^0C for 30 minutes. $AlMe_3$ (2M in hexane, 1.55 mL, 3.09 mmol) was added and

reaction was heated to reflux overnight. Reaction was cooled to 0^0C. THF (not anhydrous) was added slowly followed by 2 M HCl. Aqueous workup followed by flash column chromatography 10% DCM in hexane to yield product as white solid (122 mg, 97%).

Synthesis of Methylated triptycene (13). Triptycene 12 (120 mg, 0.247 mmol) was taken up in acetonitrile (80 mL) and water (20 mL). $CaCO_3$ (50 mg, 0.495 mmol), $AgNO_3$ (353 mg, 2.08 mmol) and $HgCl_2$ (282 mg, 1.04 mmol) were added and reaction was heated to reflux for 48 hours until reaction had gone to completion by TLC. Product was filtered and purified by extraction with dichloromethane followed by flash column chromatography to yield product (96 mg, 96%).

Synthesis of Methylated triptycene (14). Dimethyl (2-oxopropyl) phosphonate (40μL, 0.278 mmol), 4-acetamidobenzenesulfonyl azide (67 mg, 0.278 mmol) and K_2CO_3 (114 mg, 0.8223) were suspended in acetonitrile (3.1 mL) and stirred for 2 hours. Triptycene 13 (84 mg, 0.206 mmol) was taken up in a minimal amount of CH_2Cl_2 and solution was added to acetonitrile solution, until reaction went to completion by TLC. Solution was filtered through celite pad, and solvents were evaporated. Crude material was taken up in biphasic water/diethyl ether. Aqueous later was removed and organics were washed with brine, dried with $MgSO_4$ and evaporated under reduced pressure to yield product as white solid (95%) (product was pure but could be chromatographed if desired. Characterization data matched previously reported.[5]

Rotor 1. Triptycene 14 (82 mg, 0.202 mmol) and diiodobenzene (32 mg, 0.0964) were suspended in freshly distilled diisopropylamine in reflux system. Suspension was thoroughly degassed. $PdCl_2(PPh_3)_2$ (1.35 mg) and CuI (0.8 mg) were added and reaction was heated to reflux until reaction had completed by TLC (reaction looked complete at 24 hours, but was allowed to proceed for 36 hours to ensure conversion as TLC spots were not extremely

fluorescent). After 24 hours, reaction was cooled to room temperature and solvents were removed under reduced pressure. Crude solid was taken up in chloroform and filtered through a celite pad. Filtrate was washed with water, dried with $MgSO_4$ and purified via flash column chromatography to yield product as white solid (71.8 mg, 83%). *Note: Product shows only sparing to no solubility in nearly every commonly used solvent including DCM. However, despite its low solubility in DCM, it actually shows comparatively high solubility in chloroform. .* Characterization data matched previously reported.[5]

4.6. Appendix

Figure 4.6.1. ^{1}H NMR of compound 8 in CDCl$_3$ at 400 MHz
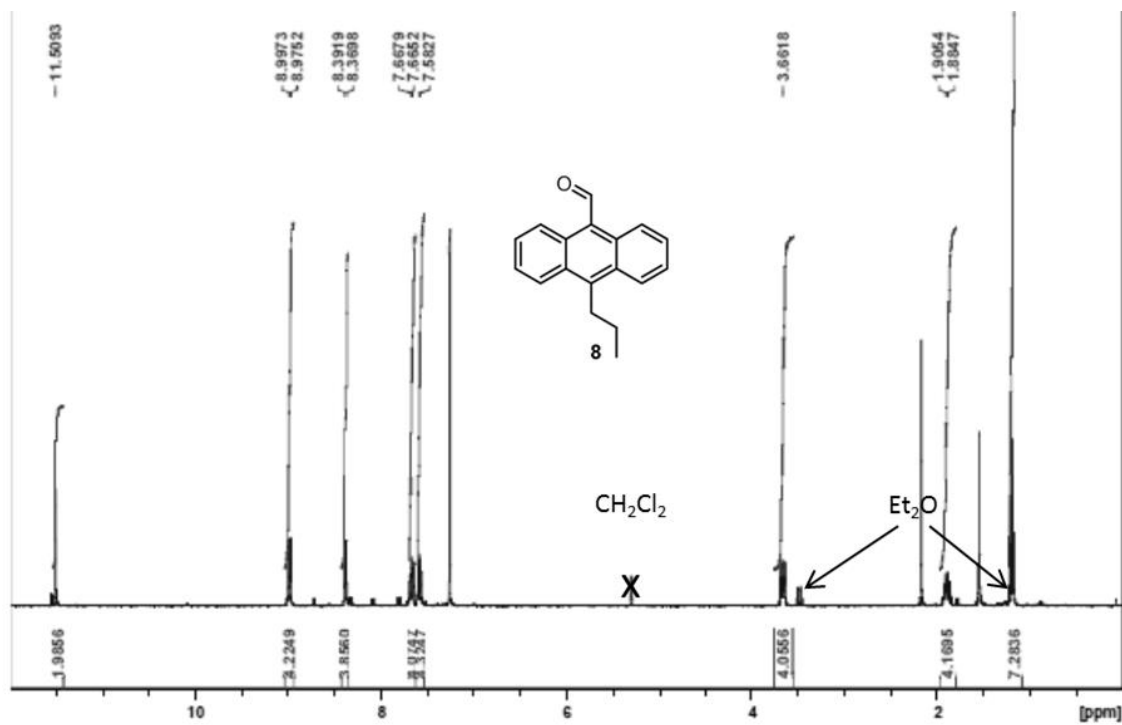
Figure 4.6.2. ^{13}C NMR of compound 8 in CDCl$_3$ at 125 MHz
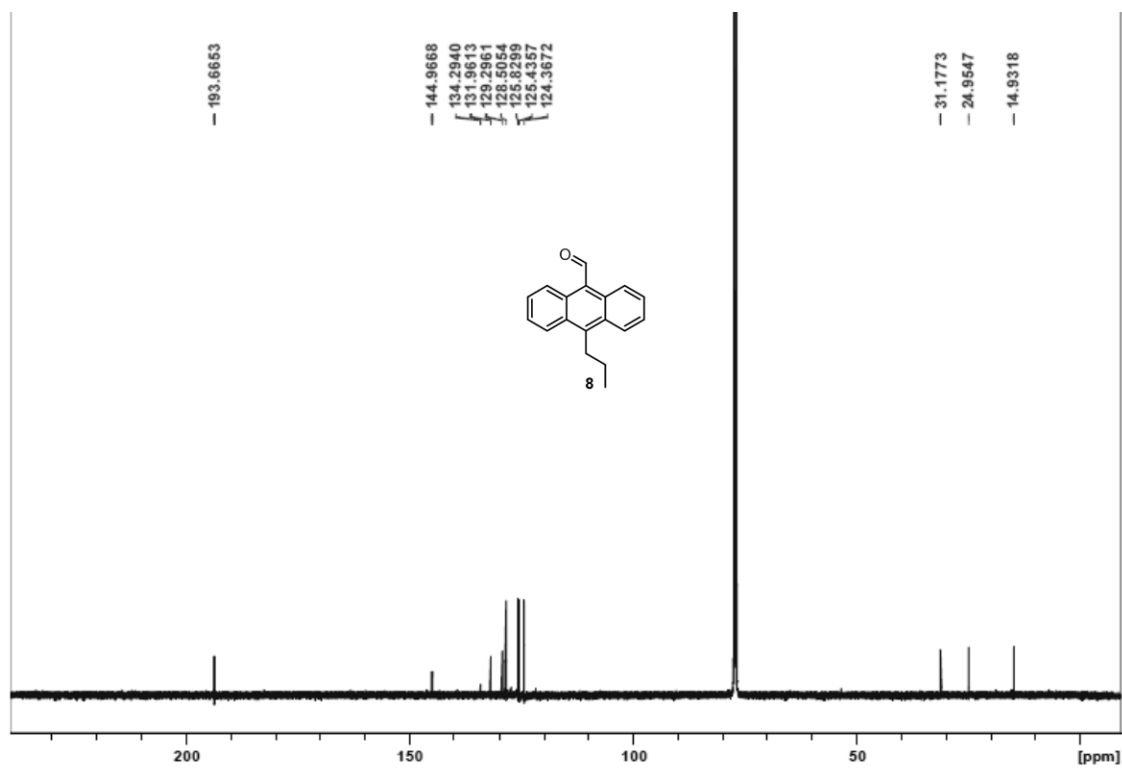
Figure 4.6.3. ^{1}H NMR of compound 9 in CDCl$_3$ at 400 MHz
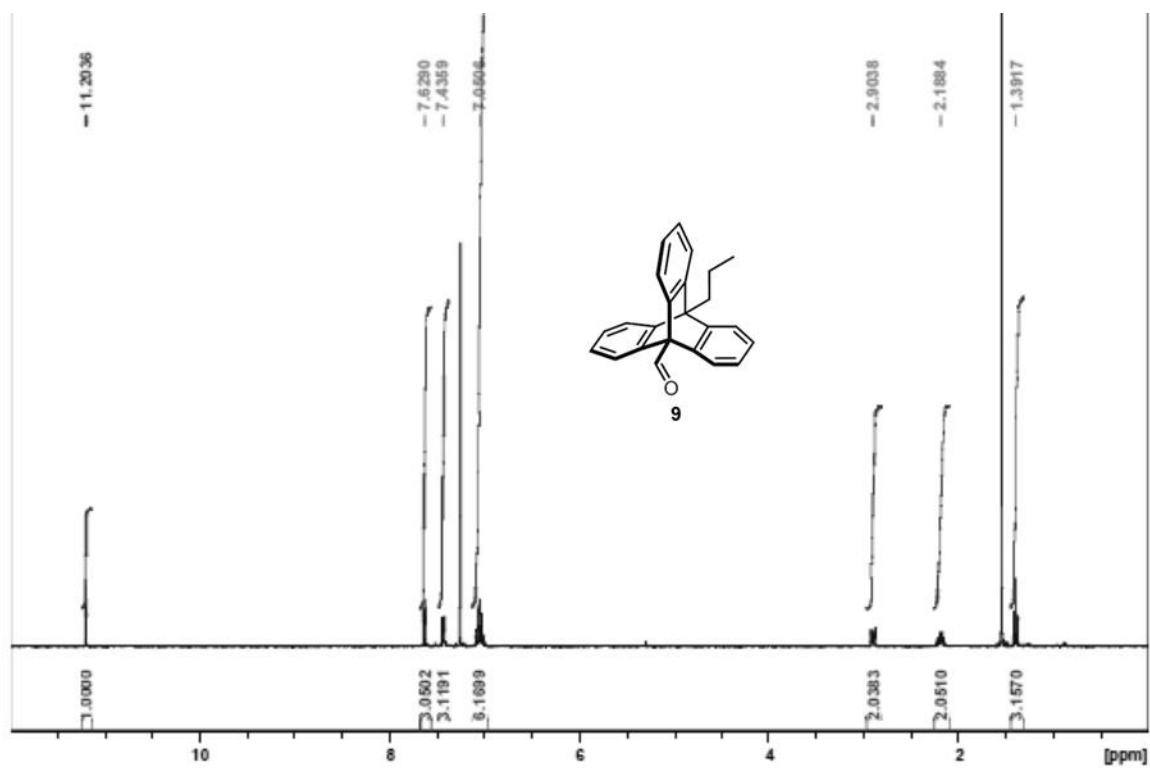
**Figure 4.6.4.** ^{13}C NMR of compound 9 in CDCl$_3$ at 125 MHz at room temperature.
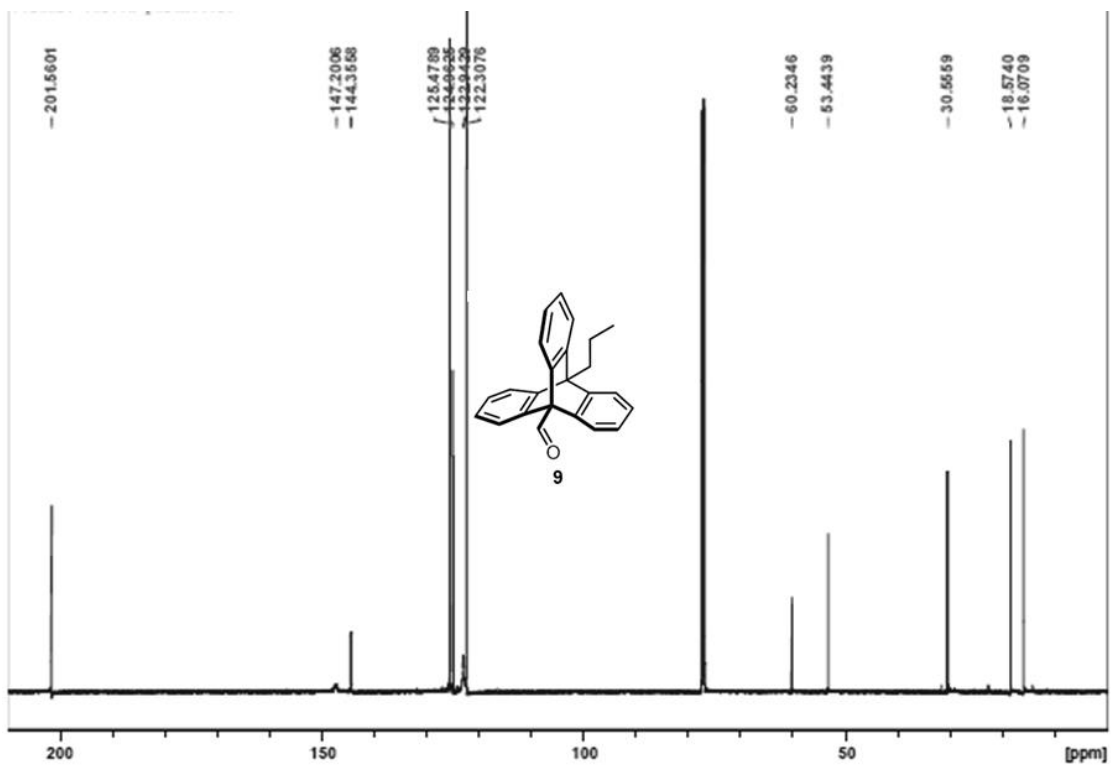
Figure 4.6.5. ^{1}H NMR of compound 10 in CDCl$_3$ at 300 MHz
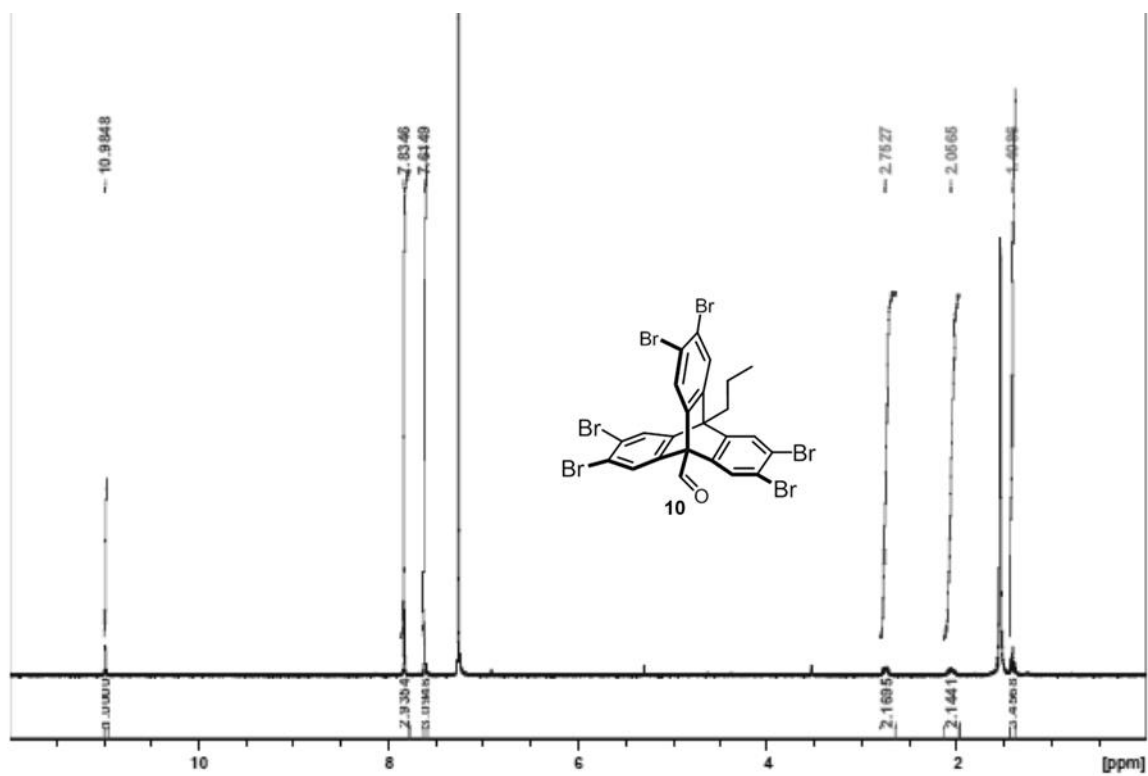
Figure 4.6.6. ^{13}C NMR of compound 10 in CDCl$_3$ at 125 MHz at 58^{0}C.
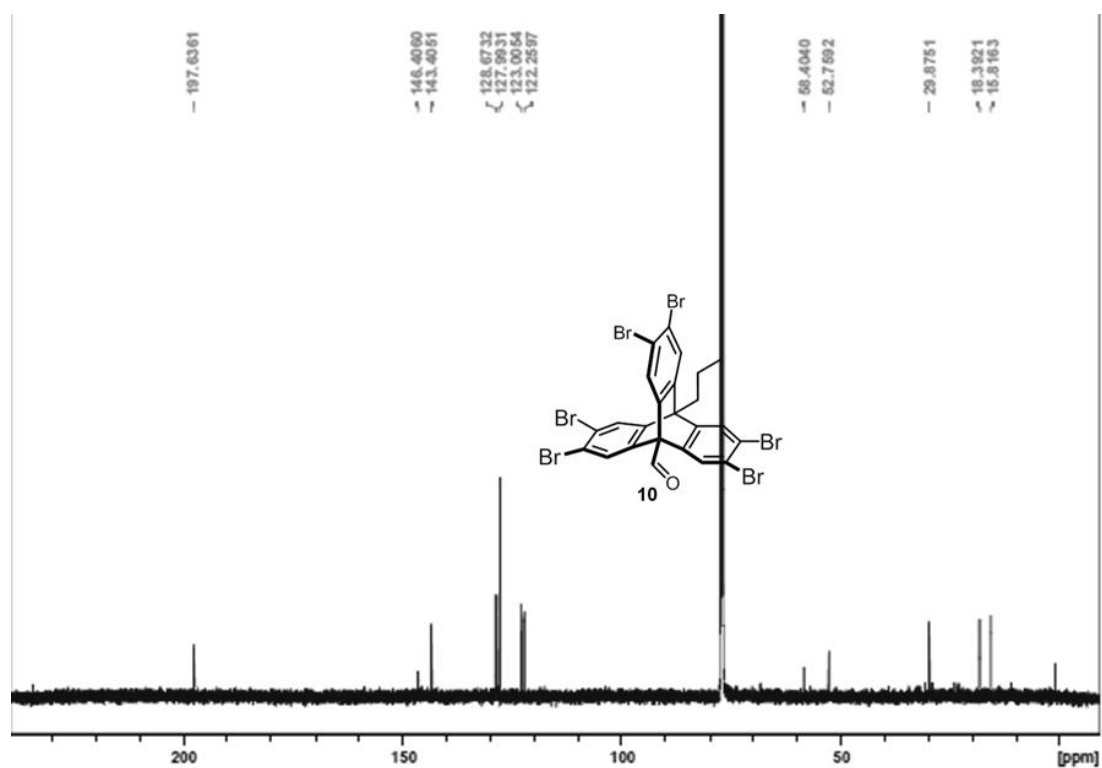
Figure 4.6.7. ^{1}H NMR of compound 11 in CDCl$_3$ at 500 MHz
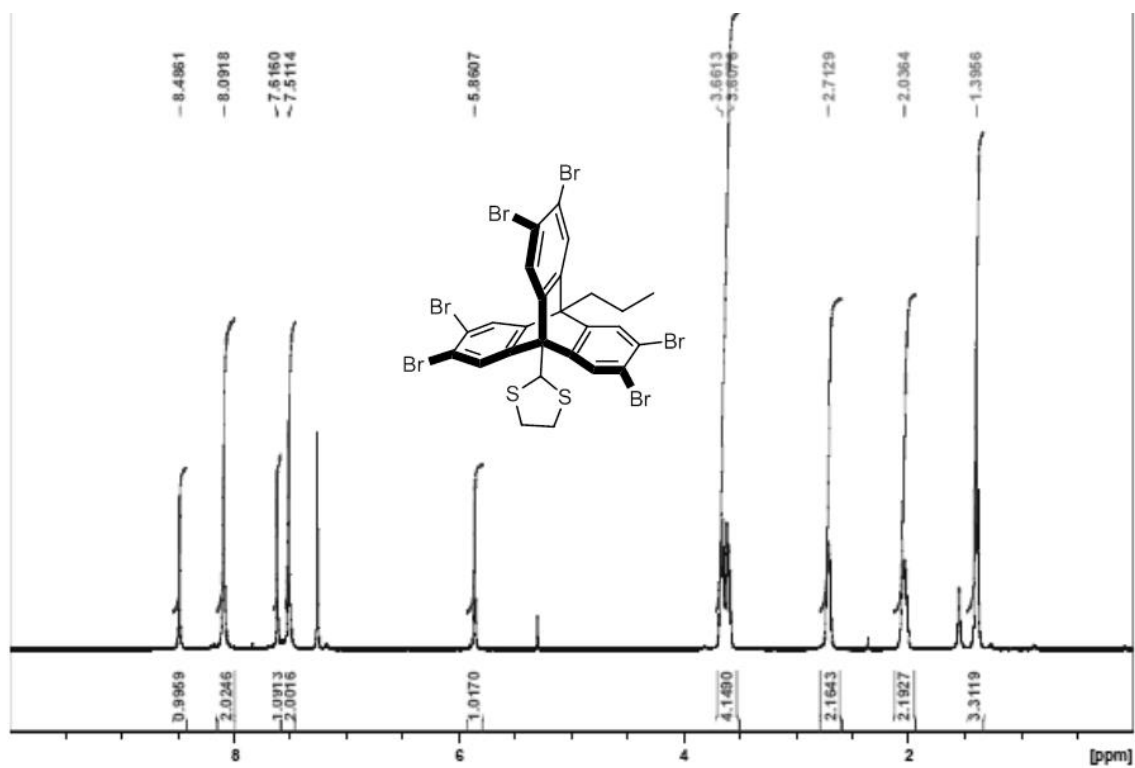
Figure 4.6.8. ^{1}H NMR of compound 12 in CDCl$_3$ at 400 MHz

102
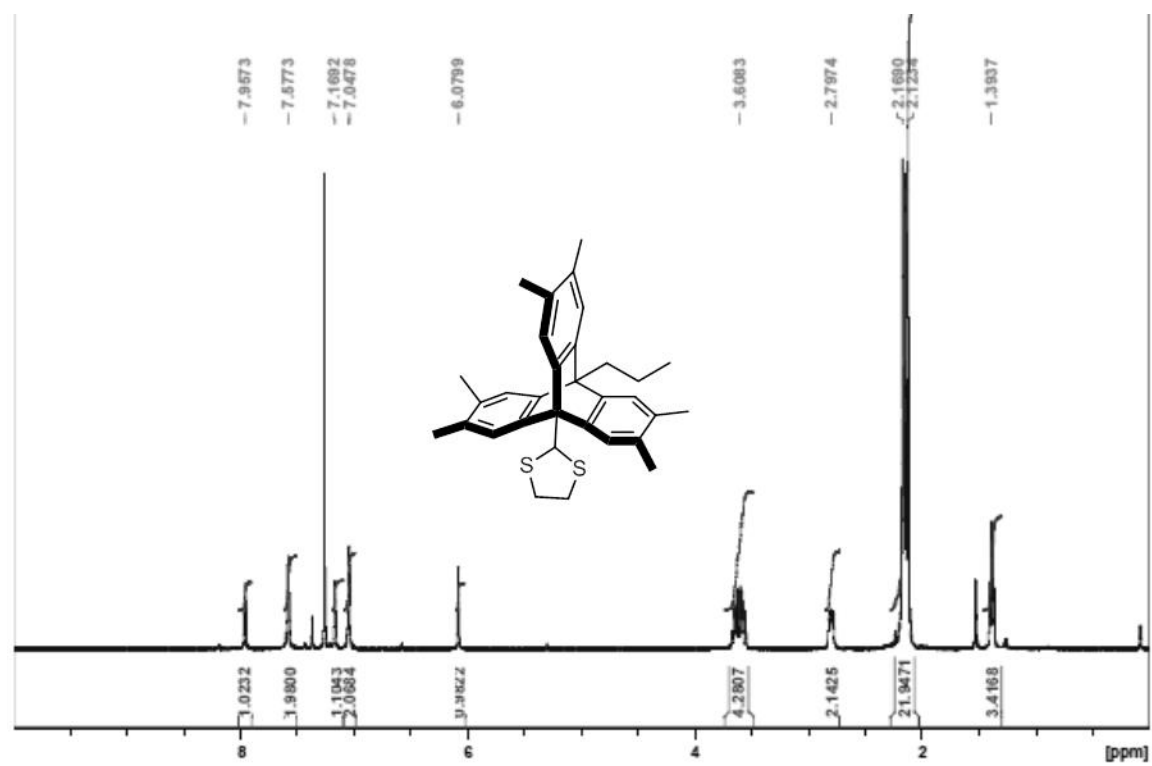
Figure 4.6.9. ^{1}H NMR of compound 13 in CDCl$_3$ at 400 MHz
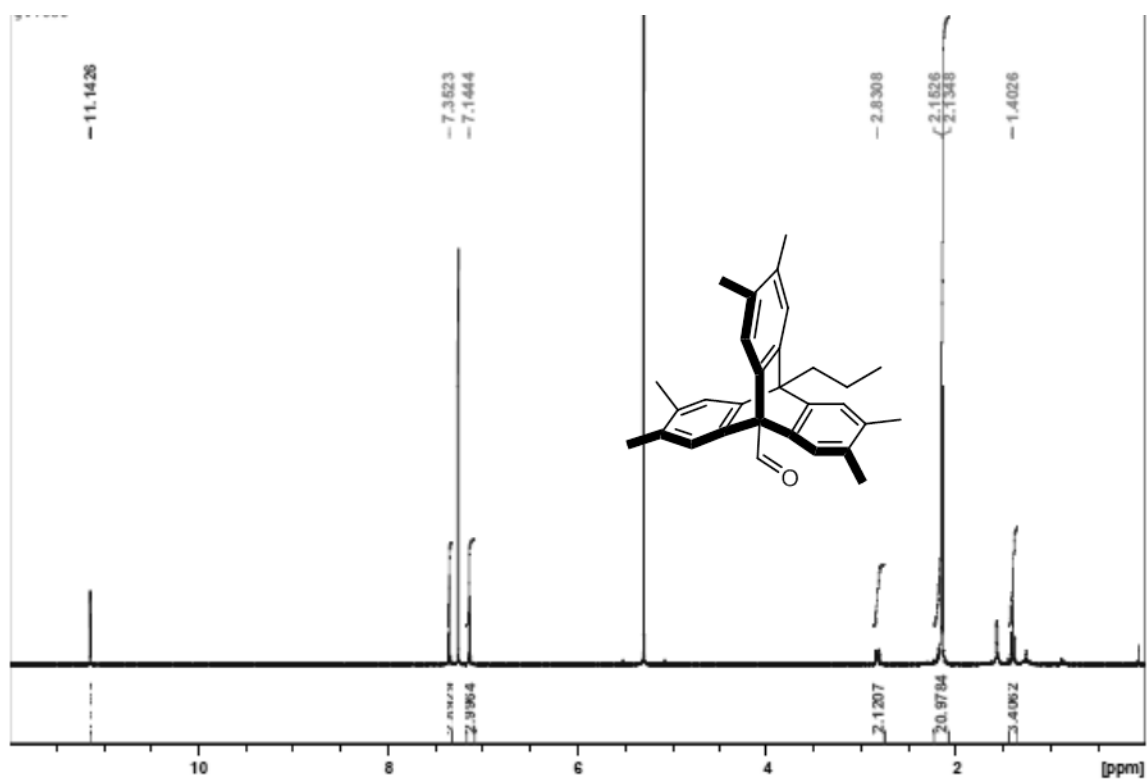
Figure 4.6.10. ^{13}C NMR of compound 13 in CDCl$_3$ at 125 MHz at room temperature
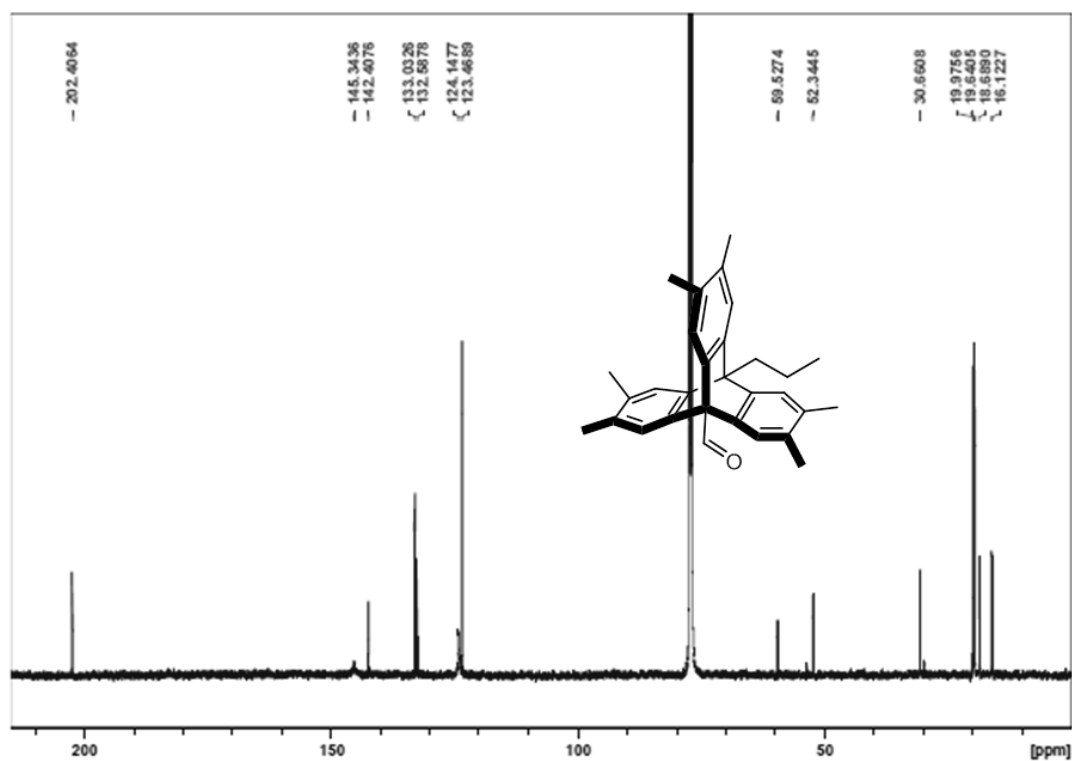
Figure 4.6.11. ^{13}C NMR of compound 13 in CDCl$_3$ at 125 MHz at 58^{0}C
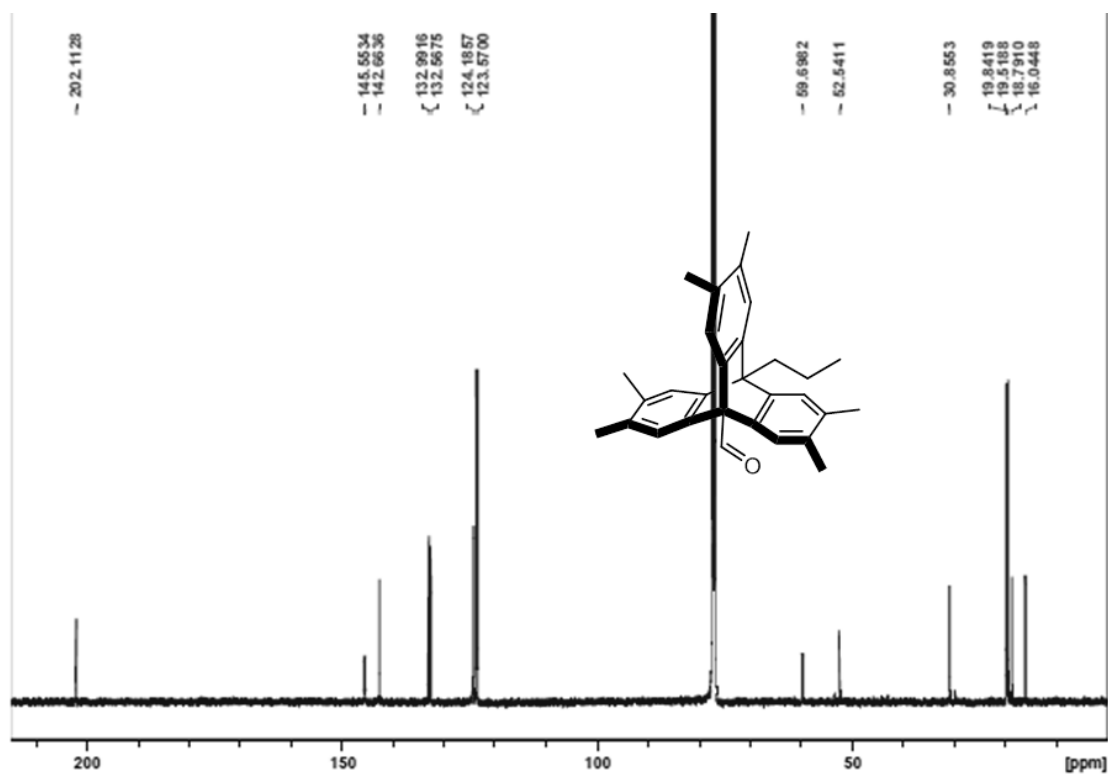
4.7. References

1 (a.) Coskun, A.; Banaszak, M.; Astumian, R. D.; Stoddart, J. F.; Grzybowski, B. A. *Chem. Soc. Rev.*, **2012**, *41*, 19. (b.) Karlen, S. D.; Garcia-Garibay, M. A. *Top Curr. Chem.,* **2005**, *262*, 179.

(c.) Vogelsberg, C. S.; Garcia-Garibay, M. A. *Chem. Soc. Rev.*, **2012**, *41*, 1892.

2 Iwamura, I.; Mislow, K. *Acc. Chem. Res.*, **1988**, *21*, 175

3 (a) Khuong, T.-A. V.; Nuñez, J. E.; Godinez, C.E.; Garcia-Garibay, M. A. *Acc. Chem. Res.* **2006**, *39*, 413. (b) Garcia-Garibay, M. A. *Proc. Natl. Acad. of Sci.* **2005**, *102*, 10793.

4 Godinez, C. E.; Zepeda, G.; Garcia-Garibay, G. A. *J. Am. Chem. Soc.*, **2002**, *124*, 4701.

5 Godinez, C.; Zepeda, G.; Mortko, C.; Dang, H.; Garcia-Garibay, M. *J. Org. Chem.*, **2004**, *69*, 1652.

6 Garcia-Garibay, M. A., Godinez, C. *Cryst. Growth Des.*, **2009**, *7*, 3124.

7 Hilton, C.; Jamison, C.; Zane, H.; King, B. *J. Org. Chem.*, **2009**, *74*, 405.

8 Bonaccorsi, P.; Di Gioia, M. L.; Leggio, A.; Minuti, L.; Papalia, T.; Siciliano, C.; Temperini, A.; Barattuci, A. *Beilstein J. Org. Chem.*, **2013**, *9*, 2410.

9 Mastalerz, M.; Sieste, S.; Cenic, M.; Oppel, I. M. *J. Org. Chem.*, **2011**, *76*, 6389.

10 Previous synthesis: A mixture of regioisomers of trinitrotriptycene was reduce to a corresponding mixture of triaminotriptycene regioisomers. This mixture was then brominated via electrophilic aromatic substitution to access a mixture of triamino, tribromo-triptycene isomers. This mixture was subjected to sandmeyer conditions to access the final hexabromotriptycene. Shalaev, V. K.; Getmanova, E. V.; Skvarchenko, V. R. *Zh. Org. Khim.*, **1976**, *12*, 191.

11 (a.) Molle, G.; Dubois, J-E.; Bauer, P. *Tet. Lett.*, **1978**, *34*, 3177. (b.) Molle, G.; Briand, S.; Bauer, P.; Dubois, J-E. *Tetrahedron*, **1984**, *40*, 5113. (c.) Kawada, Y.; Iwamura, H. *J. Org. Chem.*, **1981**, *46*, 3357.

12 Chen, C-F; Ma, Y-X (2013). *Iptycenes Chemistry: From Synthesis to Applications.* Heidelberg: Springer Science & Media.

13 (a.) Harmata, M. and Wacharsindhu. S. *Chem. Comm.*, **2003**, 2492. (b.) Harmata, M. and Wacharsindhu. S. *J. Org. Chem.*, **2005**, *70*, 725.

14 Sanada, K.; Ube, H.; Shionoya, M. *J. Am. Chem. Soc.*, **2016**, *138*, 2945.

15 Vellis, P.; Mikroyannidis, J. A.; Bagnis, D.; Valentini, L.; Kenny, J. *J. Appl. Polym. Sci.*, **2009**, *2*, 1173.

16 Habrant, D.; Rauhala, V.; Koskinen, A. M. P *Chem. Soc. Rev.*, **2010**, *39*, 2007.

17 Conditions adapted from recent literature provided improved yields from the original synthesis: Lledo, A.; Restorp, P.; Rebek, J. *J. Am. Chem. Soc.*, **2009**, *131*, 2440.

[18] Vellis, P.; Mikroyannidis, J. A.; Bagnis, D.; Valentini, L.; Kenny, J. *J. Appl. Polym. Sci.*, **2009**, *2*, 1173.

[19] Zhu, X.-Z. and Chen, C.-F. *J. Am. Chem. Soc.*, **2005**, *127*, 13158.

[20] Silica supported phosphorous pentoxide was prepared according to: Hasaninejad, A.R.; Zare, A.; Sharghi, H.; Shekouhy, M. *Arkivoc*. **2008**, *11*, 64.

CHAPTER 5

A Succinct, High Yielding and Divergent New Paradigm for the

Synthesis of D_{2h}-Symmetric Octakis-Substituted Pentiptycenequinones

And C_{3V}-Symmetric Hexakis-Substituted Triptycenes

5.1. Abstract.

With a rigid fused polyaromatic framework and a well-defined, highly symmetric molecular geometry, pentiptycenes are appealing building blocks for a variety of functional materials. Unfortunately, their use has been limited by the lengthy syntheses of their functionalized derivatives. In this communication we describe a highly efficient, brief, divergent new paradigm for the preparation of octakis-substituted pentiptycene derivatives that starts with the preparation of an octakis(bromo)-compound, which can be used as Pd(0)-catalyzed coupling partner with suitable organometallic compounds to install methyl, phenylethynyl, phenyl, vinyl and tetrephenylmethyl substituents in the peripheral 2,3,6,7,14,15,19,20 positions.
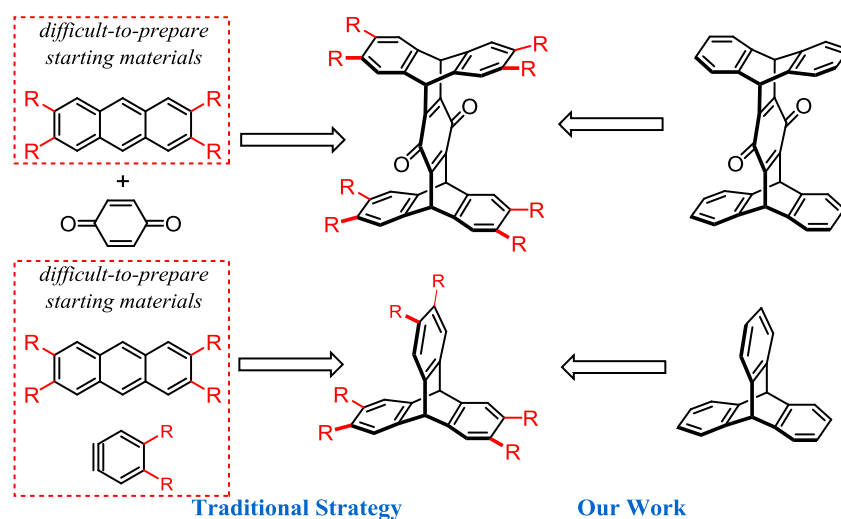
Figure 5.1.1. Traditional Strategies versus our strategy to access peripherally substituted iptycenes

5.2. Introduction.

Iptycenes, a family of compounds which incorporates aromatic moieties fused by a bicyclo[2.2.2]octatriene system, have received an increasing amount of attention due to their potential application in a vast number of fields. The rigid nature of these frameworks allows

them to adopt geometries which are both fixed and predictable, and, therefore, allow them to dictate the geometries of the systems that they are incorporated into. Moreover, as these geometries do not lend themselves to efficienctly tight packing, these compounds tend to give rise to higly porous structures. Trypticenes, the simplest of this class of molecules, have been the most widely explored up until this point. The triptycene framework is able to induce a 2-D architecture with a C_3 axis of symmetry into low density solids. These features have led to their application in such fields as catalysis[1], molecular machines, materials chemistry and supramolecular chemistry.

Pentiptycenes, the next of these compounds with five benzene rings fused to two bicyclo[2.2.2]octatrienes, which may be viewed as extended triptycenes.[2] Their rigid framework can be used to build geometrically regular structures with substituents attached along the central ring[3,4] or by taking advantage of the peripheral positions,[5] as illustrated by the R-groups in Scheme 1. With five non-coplanar aromatic rings creating protuberances and cavities of unequal size, it is difficult for pentiptycenes to form densely packed structures, which renders them useful for the design of low density materials[6] for applications in sensors,[3] molecular machines[7] and supramolecular chemistry.[8]

In general, the pentiptycene core is conveniently obtained by Diels-Alder reactions between p-benzoquinone with two equivalents of anthracene (Scheme 1). The resulting pentiptycenequinones are highly versatile intermediates for the synthesis of linearly conjugated polymers and other substituted analogs.[2] By contrast the preparation of peripherally substituted structures has been extremely challenging. The Diels-Alder reaction requires the use of substituted anthracenes,[9] which are not readily available and have a low solubility that makes them difficult to manipulate. To our knowledge, there is only one example of a peripherally

octakis(methoxy)-substituted pentypticene, which was prepared by this strategy (Scheme 1, R=OMe), and was obtained in low yield (16%).[3]

5.3. Results and Discussion

Considering the potential of the peripherally substituted structures for applications that rely on precise geometrical design, and aware of a highly improved selective multibromination[10] of triptycenes recently reported by Hilton et al.,[11] we set out to explore a three-step divergent functionalization strategy that starts from the readily available pentiptycene quinone 1.
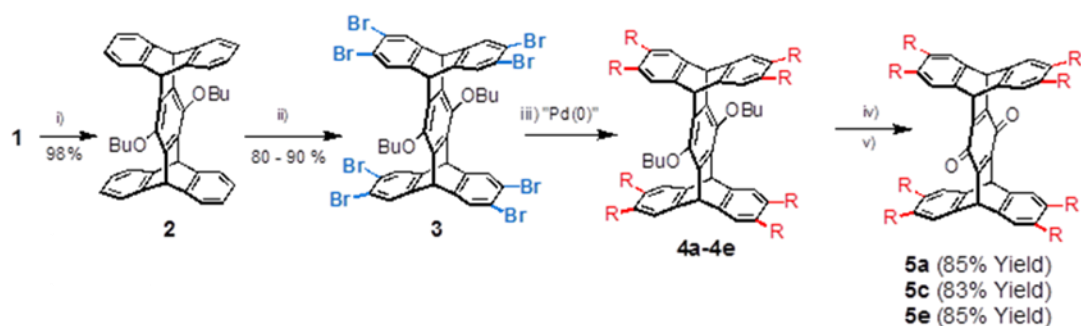
Scheme 5.3.1. (i) Na_2SO_4, $NaHCO_3$, n-BuBr, K_2CO_3, acetone; (ii) Br_2, Fe, $CHCl_3$, reflux; (iii) **Table 5.3.1.** Demonstrating yields of returning to quinone: (iv) BBr_3, DCM (v.) MeOH, DDQ.

Pentiptycene quinone 1 was obtained as reported in the literature in multigram reactions as a relatively insoluble crystalline solid in ca. 75% yield. Its reduction and alkylation were achieved in two steps in 98% yield overall to yield to obtain the significantly more tractable diether 2. The key eight-fold regioselective bromination was achieved using molecular bromine in the presence of iron filings in refluxing chloroform. This particular step could be thought of as a modified procedure of that to hexabrominate triptycene, which, after optimization, went cleanly. The ^{1}H NMR of the crude product mixture of pentiptycene 2 revealed the octabrominated product 3 with no side products in 79% isolated yield after a short silica plug; an average 97% yield per step

(Figure 5.3.1), in comparison to the similarly clean hexabromination of dimethyl triptycene under similar conditions.
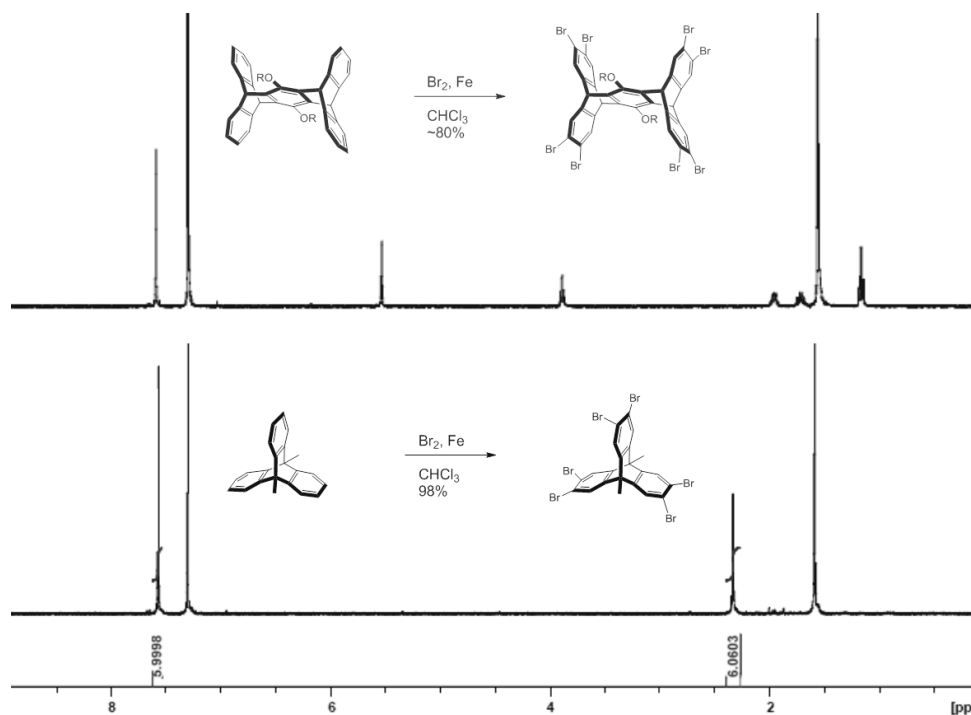
Figure 5.3.1. ^{1}H NMR of crude reaction mixture of pentiptycene 2 (above) and dimethyl triptycene (below) showing a clean and complete bromination of all eight and six sites, respectively. Key signals for the above include an aromatic singlet at 7.55 ppm, the bridgehead hydrogen at 4.8 ppm, and the four signals of the aliphatic butoxy groups.

Although the Lewis acid formed *in situ* leads to the cleavage of the ether linkage, this side reaction can be minimized by limiting the amount of FeBr$_3$ to ca. 8 equivalents. To our satisfaction, we were able to conduct the reactions to complete conversion of compound 3 to the octamethyl (4a), octaphenylethynyl (4b), octaphenyl (4c), octavinyl (4d) and even a relatively large and bulky octakis(tetraphenylmethyl) derivative (4e), by taking advantage, of Negishi (4a), Sonogashira (4b and 4e) and Suzuki (4c and 4d) conditions. Every eight-fold transformation occurred in yields that are >90%, indicating average individual steps of >99%. Reactions were easily monitored by following changes in the pentiptycene aromatic singlet in the ^{1}H NMR. While this peak appears at 7.55 ppm in brominated 3, as the reactions proceeds, the formation of

a final product can bes established with signals that appear at 7.04 ppm (4a), 7.53 ppm (4b), 7.45 ppm (4c), 7.40 ppm (4d) and 7.42 ppm (4e).

Product	—R	Reaction Conditions and Yield
4a	—Me	AlMe$_3$, PdCl$_2$(PPh$_3$)$_3$, THF, Reflux, 94%
4b	≡—Ph	PhCCH, Pd(PPh$_3$)$_4$, CuI, PPh$_3$, NEt$_3$, DMF, 70°C, 77%.
4c	—Ph	PhB(OH)$_2$, Pd(Pt-Bu)$_3$, K$_3$PO4, THF, 40°C, 93%.
4d	—CH=CH$_2$	C$_6$H$_9$B$_3$O$_2$, C$_5$H$_5$N, Pd(OAc)$_2$, PPh$_3$, K$_2$CO3, THF:DME:H$_2$O, 70°C, 91%.
4e	—p-(Ph$_3$C)C$_6$H$_4$	C$_6$H$_5$)$_3$CBpin, Pd(PPh$_3$)$_4$, K$_2$CO$_3$, THF:H$_2$O, 70°C, 85%.

Table 5.3.2. Conditions and yields of Pd-coupling reactions of octakis(bromo)pentiptycene 3 with various coupling partners

Having obtained the peripherally substituted dibutoxypentiptycenes we established their transformation back to the synthetically more versatile iptycenequinones. Knowing that conditions needed for the removal of the butoxy group and oxidation of the intermediate hydroquinone could compromise vinyl and phenylethynyl substituents in **4b** and **4d**, we selected the octamethyl, octaphenyl, and octakis[(*para*-triaphenylmethyl)phenyl] derivatives **4a**, **4c** and **4e** (Scheme 2). The reaction was achieved in ca. 85% isolated yields in one-pot procedures
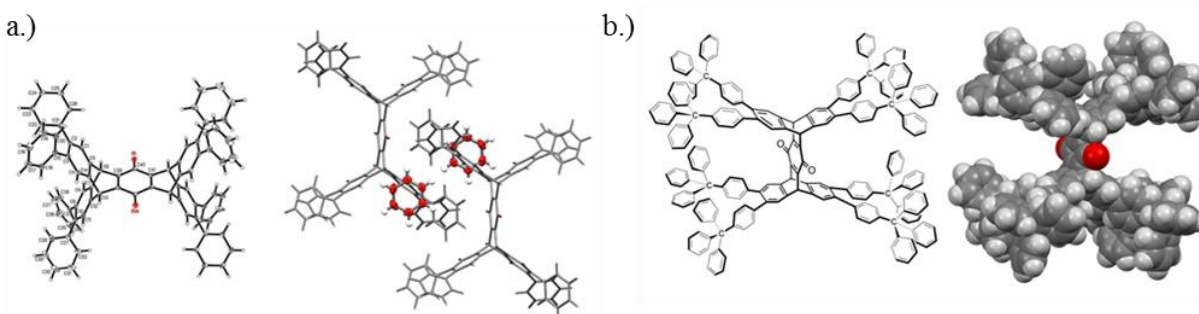
Figure 5.3.2. (a) (Left) ORTEP diagram of pentiptycene quinone 5c with ellipsoids shown at 50% (?) probability and (Right) packing interactions between adjacent molecules in the lattice. Benzene molecules shown in red. **(b)** Line structure and space-filling model of pentiptycene

quinone 5e with eight *para*-(triphenylmethyl)-phenyl groups in the periphery of the structure illustrating the power of the method.

consisting of BBr$_3$ deprotection followed by DDQ oxidation (Scheme 2). The corresponding methyl-, phenyl-, and octakis[(*para*-triaphenylmethyl)-phenyl]-pentitycenequinones **5a** and **5c** were sufficiently soluble for purification. All structures were confirmed by ^{1}H NMR, ^{13}C NMR and FTIR spectroscopic methods as well as by MALDI-TOF accurate mass measurements. Single crystal X-ray diffraction in the case of **5c** revealed packing in space group P$_1$ with two benzene molecules and one molecule of **5c** per unit cell. The phenyl groups rotate out of conjugation with the pentiptycene blade, forming dihedral angles that range from 45.8^o to 53.5^o. Molecules pack in layers orthogonal to the direction of the carbonyl axis, with the peripheral phenyl groups from one molecule projecting towards the groove of another and benzene located in the proximity of the quinone carbonyls, between the adjacent pentiptycene layers (Figure 1). The excellent overall yield for the formation of iptycenequinone **5e** with a molecular mass of 3005.3 amu and a severely sterically crowded structure (Figure 2) highlights the remarkable potential of this method.

5.4. Conclusion.

The new divergent strategy described in this communication is possible by the remarkably high efficiency of each the two key multiple steps, and will make it possible to prepare a wide range of peripherally substituted pentiptycene derivatives that will help explore and develop a wide range of chemical and materials science applications.

5.5. Experimental

All reactions were performed under an inert atmosphere of argon unless otherwise stated. Chemicals were purchased from commercially available sources and used without further purification unless otherwise noted. Nuclear magnetic resonance (NMR) spectra for [1] H were

obtained at 300, 400 or 500 MHz as noted using Bruker NMR spectrometers, for ^{13}C at 125 MHz. All chemical shifts are reported in ppm on the δ-scale using the residual natural abundance isotopes of the solvents as references. CDCl$_3$ was calibrated at δ7.26 and δ77.16 for ^{1}H and ^{13}C, respectively. IR spectral data was recorded in cm^{-1} using an Attenuated Total Reflectance (ATR)-IR Spectrometer. High resolution mass spectrometry was performed using electrospray ionization with a time of flight (ESI-TOF), DART or MALDI mass spectrometer, as noted. 2,4,6-trivinylcyclotriboroxane-pyridine complex **6** and 4-tetraphenyliodide **7** were prepared according to previously reported literature procedure.[12,13]

5.5.1. Synthetic Procedures

Synthesis of 2. **1** (800 mg, 1.74 mmol) was suspended in THF (8 mL). Sodium dithionite (2.6 g, 14.77 mmol) was dissolved in H$_2$O (12 mL). Aqueous solution was added to suspended starting material and the biphasic mixture was heated to 40°C while stirring vigorously for 1.5 hours—or until suspended solid in organic layer had completely dissolved and yellow color had paled. Reaction was cooled to room temperature and transferred to separatory funnel. Aqueous layer was removed and organic layer was washed with brine (3x25 mL) and dried with Na$_2$SO$_4$. Solvent was removed under reduced pressure to yield off-white solid. This solid, along with freshly dehydrated K$_2$CO$_3$ (1.2 g, 8.686 mmol) and a catalytic amount of 18-crown-6 (5 mg) was suspended in anhydrous acetone (75 mL) in a dry roundbottom. Bromobutane (940 µL, 8.68 mmol) was added and reaction was heated to reflux for 14 hours. Reaction was cooled to roomed temperature and solvent was removed under reduced pressure. CH$_2$Cl$_2$ (50 mL) was added and mixture was filtered. Solid was washed thoroughly with CH$_2$Cl$_2$ until filtrate no longer contained product by TLC analysis. Combined washes were washed with H$_2$O (3x50mL), dried with MgSO$_4$, and evaporated under reduced pressure to yield crude product. Crude product was

purified by flash column chromatography (25% DCM in hexane gradient to 50% DCM in hexane) to yield pure product as white powder (979 mg, 98%). ^{1}H NMR (400 MHz, CDCl$_3$): δ = 7.31 (dd, J= 5.3, 3.2 Hz, 8H), 6.93 (dd, J= 5.4, 3.2 Hz, 8H), 5.64 (s, 4H), 3.91 (t, J= 6.7 Hz, 4H), 1.99 (m, 4H), 1.72 (m, 4H), 1.14 (t, J= 7.4 Hz, 6H); ^{13}C NMR (125 MHz, CDCl$_3$): δ = 146.2, 145.5, 136.4, 125.2, 123.7, 76.1, 48.5, 32.8, 19.9, 14.3; IR (cm^{-1}): 3067, 3018, 2955, 1480, 1459, 1376, 1301, 1257, 1067, 1024, 751, 554; HRMS (ESI) calcd for C$_{42}$H$_{39}$O$_2$ [M+H]$^+$ 575.2950, found 575.2946.

Synthesis of 3. A flame dried 10 mL schlenck flask was charged with compound **2** (70 mg, 0.122 mmol) and a catalytic amount of iron filings (9 mg). The reaction flask was evacuated and backfilled with argon three times. Anhydrous dichloromethane (8 mL) was added and reaction was stirred for five minutes until starting material was fully dissolved. Freshly distilled Br$_2$ (55 μL, 1.06 mmol) was added, and reaction was heated to reflux under an argon atmosphere for 90 minutes. Reaction was cooled first to room temperature and then to 0°C. K$_2$CO$_3$ (~50 mg) was added and reaction was allowed to warm to room temperature and continue stirring for 10 hours. Solvent was removed under reduce pressure. Solid was taken up in hot chloroform (~75 mL) in order to dissolve the maximum amount of solid. Suspension was filtered through a sort silica pad. Solvent was removed under reduced pressure to yield crude product as pale yellow solid. Solid was then washed with acetone and a minimal amount of cold dichloromethane followed by collection by centrifugation to yield product as white powder (116 mg, 79%). ^{1}H NMR (400 MHz, CDCl$_3$): δ = 7.55 (s, 8H), 5.50 (s, 4H), 3.87 (t, J= 8.9 Hz, 4H), 1.94 (m, 4H), 1.70 (m, 4H), 1.15 (t, J= 9.7 Hz, 6H) ; ^{13}C NMR (125 MHz, CDCl$_3$): δ = 146.4, 145.0. 135.5, 128.9, 121.5, 76.6, 46.7, 32.8, 19.9, 14.3; IR (cm^{-1}): 2951, 2866, 1465, 1436,1359, 1266, 1065, 1028, 917, 858, 786, 532. MS (ESI) calcd for C$_{42}$H$_{30}$Br$_8$O$_2$ [M]$^+$ 1205.5631, found 1206.

Synthesis of 4c. A flame dried 50 mL schlenk flask was charged with phenylboronic acid (162 mg, 1.33 mmol) and K_3PO_4 (563 mg, 2.65 mmol). The flask was evacuated and backfilled with argon three times. Anhydrous THF (12 mL) was added and reaction was degassed with argon. $Pd(P^tBu_3)_2$ (17 mg, 0.033 mmol) was added and reaction was further degassed. **3** (100 mg, 0.083 mmol) was added and reaction was further degassed. Reaction mixture was heated to 40°C and stirred for 14 hours. Reaction was cooled to room temperature. Reaction mixture was washed with saturated NH_4Cl solution (3x20 mL), dried with $MgSO_4$ and concentrated under reduced pressure to yield crude product. Crude product was purified by flash column chromatography (30% DCM in Hexane gradient to 40% DCM in Hexane) to yield product as white solid (91 mg, 93%). ^{1}H NMR (400 MHz, $CDCl_3$): δ = 7.45 (s, 8H), 7.14 (m, 24H), 7.03 (m, 16H), 5.84, (s, 4H), 4.02 (t, J= 6.4 Hz, 4H), 2.01 (m, 4H), 1.76 (m, 4H), 1.09 (t, J= 7.3 Hz, 6H) ; ^{13}C NMR (125 MHz, $CDCl_3$): δ = 146.5, 144.6, 141.6, 137.8, 136.5, 130.1, 127.9, 126.4, 126.1, 76.3, 48.0, 32.9, 20.1, 14.3; IR (cm^{-1}): 3021, 2923, 2855, 1600, 1464, 1276, 1248, 1072, 763, 700, 574; HRMS (ESI) calcd for $C_{90}H_{74}NO_2$ $[M+NH_4]^+$ 1200.5714, found 1200.5734.

Synthesis of 4a. A flame dried 50 mL schlenck flask and condenser system was charged with **3** (150 mg, 0.124 mmol). The flask was evacuated and backfilled with argon three times. Anhydrous THF (24 mL) was added and suspension was thoroughly degassed. $PdCl_2(PPh_3)_2$ (35 mg, 0.0498 mmol) was added and mixture was further degassed. Reaction was heated to 60°C and allowe to stir for 30mins. 2 M $AlMe_3$ in hexanes (1 mL, 1.99 mmol) was added and reaction was heated to reflux for 12 hours. Reaction was cooled down to 0°C and 2 M HCl was added dropwise until bubbling ceased. Organics were washed with Brine 3x, dried over $MgSO_4$ and evaporated under reduced pressure. Product was purified by flash column chromatography (15% DCM in Hexane) to yield product as white solid (80 mg, 94%).^{1}H NMR (400 MHz, $CDCl_3$):

δ = 7.04 (s, 8H), 5.47 (s, 4H), 3.88 (t, J= 6.7 Hz, 4H), 2.07 (s, 24H), 1.98 (m, 4H), 1.71 (m, 4H), 1.14 (t, J= 7.3 Hz, 6H); ^{13}C NMR (125 MHz, CDCl$_3$): δ = 145.8, 143.4, 136.8, 132.7, 125.0, 75.9, 47.6, 32.9, 19.9, 19.5, 14.4; IR (cm^{-1}): 2959, 2918, 2852, 1463, 1261, 1068, 1026, 860, 799, 556; HRMS (ESI) calcd for C$_{50}$H$_{55}$O$_2$ [M+H]$^+$ 687.4202, found 687.4228.

Synthesis of 4d. **3** (70 mg, 0.058 mmol), 2,4,6-trivinylcyclotriboroxane-pyridine (84 mg, 0.348 mmolo) and K$_2$CO$_3$ (64 mg, 0.464 mmol) were suspended in a biphasic mixture of THF (3 mL), dimethoxyethane (1.5 mL) and H$_2$O (0.75 mL) in a 10 mL sealed tube. Mixture was thoroughly degassed with argon. PPh$_3$ (15 mg, 0.058 mmol) and Pd(OAc)$_2$ (5.2 mg, 0.023 mmol) was added and reaction was further degassed. Sealed tube was closed and stirred in sand bath at 70°C for 4 hours. Reaction could be visually monitored as was completed once all solids had gone into solution and reaction resembled a biphasic solvent system. At this point, reaction was cooled to room temperature. Aqueous layer was removed and organics were evaporated under reduced pressure. Residue was dissolved in biphasic mixture of ethyl acetate (40 mL) and brine (30 mL). Aqueous layer was removed and organics were washed with brine two more times before being dried with Na$_2$SO$_4$ and concentrated under reduced pressure. Residue was taken up in a 1:1 mixture of DCM and hexanes and *quickly* flushed through a silica plug.[14] Solvent was then concentrated under reduced pressure to yield pale yellow solid as crude product. Crude material could then be recrystallized from hexanes to yield pure product as white solid (41.2 mg, 91%). ^{1}H NMR (400 MHz, CDCl$_3$): δ = 7.40 (s, 8H), 6.87 (dd, J= 17.4, 11.0 Hz, 8H), 5.64 (s, 4H), 5.50 (dd, J= 17.4, 1.2 Hz, 8H), 5.21 (dd, J= 11.0, 1.2 Hz, 8H), 3.96 (t, J= 6.8 Hz, 4H), 2.02 (m, 4H), 1.71 (m, 4H), 1.14 (t, J= 7.4 Hz, 6H); ^{13}C NMR (125 MHz, CDCl$_3$): δ = 146.0, 144.5, 136.1, 134.8, 133.4, 121.5, 115.9, 76.3, 48.0, 32.8, 19.8, 14.3; IR (cm^{-1}): 2954, 2927, 2867, 1624, 1463,

1425, 1271, 1247, 1067, 1029, 986, 903, 750, 555; HRMS (ESI) calcd for $C_{58}H_{55}O_2$ $[M+H]^+$ 783.4202, found 783.4224.

Synthesis of 4b. . To a 100 mL round bottom flask were added anhydrous DMF (5 mL), NEt$_3$ (1 mL), **3** (120.6 mg, 0.100 mmol), and PPh$_3$ (15.7 mg, 0.060 mmol). The resulting mixture was cooled down to -78 °C before it was connected to vacuum for 30 min. It was then allowed to warm up to room temperature under Argon atmosphere. Phenylacetylene (490 mg, 4.80 mmol), Pd(PPh$_3$)$_4$ (34.7 mg, 0.030 mmol), and CuI (5.7 mg, 0.030 mmol) were added into the reaction flask, and the reaction mixture was cooled down in a dry ice-acetone bath before it was connected to vacuum again for 5 min. The flask was then gradually heated up and the reaction was stirred at 65 °C under argon for 48 hours. A 1:1 water-acetone mixture (20 mL) was added in to quench the reaction and the crude product was collected by filtration. The obtained solids were further washed with excess of water and acetone, and they were proved to be pure by ^{1}H NMR (106 mg, 77 %) after solvent removal. ^{1}H NMR (400 MHz, CDCl$_3$): □□□□7.53 (s, 8H), 7.50 (m, 16H), 7.30 (m, 24H), 5.67 (s, 4H), 3.99 (t, J= 6.4 Hz, 4H), 2.03 (m, 4H), 1.83 (m, 4H), 1.23 (t, J= 7.3 Hz, 6H); ^{13}C NMR (125 MHz, CDCl$_3$): □□= 146.4, 144.3, 135.6, 131.8, 128.45, 128.43, 127.0, 123.5, 123.4, 93.2, 88.6, 76.5, 47.8, 33.0, 20.1, 14.4; IR (cm^{-1}): 2936, 2860, 1596, 1493, 1460, 1255, 1060, 1027, 912, 752, 688, 564, 529, 456; HRMS (ESI) calcd for $C_{106}H_{70}O_2Na$ $[M+Na]^+$ 1397.5268, found 1397.5284.
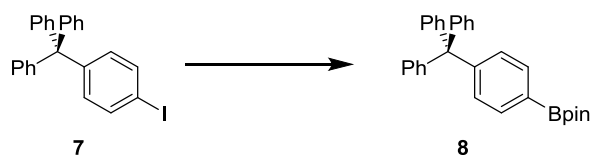
Synthesis of TetraphenylBpin 8.[15] To a 25 mL round bottom flask was added tetraphenylmethyl iodide **7** (300mg, 0.672mmol), B$_2$Pin$_2$ (295mg, 1.16 mmol) and KOAc (198

mg, 2.016 mmol) were taken up in DMF (16mL). Suspension was deoxygenated by freeze-pump-thaw method. $Pd(OAc)_2$ (7.5 mg, 0.0336 mmol) was added, and solution was further deoxygenated. Reaction was heated to 100°C for 12 hours. Reaction mixture was filtered through celite pad. Solvent was removed under reduce pressure. Solid was taken up in ether/water mixture. Aqueous layer was removed and organics were washed with aqueous NH_4Cl (3x). Organics were dried over $MgSO_4$ and concentrated under reduced pressure to yield pale brown solid as crude product. Crude product was purified by flash column chromatography (20% DCM in hexane) to yield white solid. Solid was triturated with MeOH to remove remaining B_2Pin_2 reagent to yield pure product as white solid (202mg, 67%). m.241-243°C; ^{1}H NMR (400 MHz, $CDCl_3$): δ = 7.69 (d, J= 8.4 Hz, 2H), 7.19 (m, 17H), 1.33 (s, 12H); ^{13}C NMR (125 MHz, $CDCl_3$): δ = 150.1, 146.8, 134.1, 131.3, 130.7, 127.6, 126.0, 83.9, 65.3, 25.0; IR (cm^{-1}): 3083, 2976, 1609, 1492, 1397, 1381, 1144, 750, 701; HRMS (DART) calcd for $C_{31}H_{32}BO_2$ [M+H]$^+$ 447.2495, found 447.24787.

Synthesis of 4e. To a 20 mL sealed tube was added THF (9mL), H_2O (3mL), **3** (65 mg, 0.054 mmol), **8** (289 mg, 0.647 mmol) and K_2CO_3 (298 mg, 2.156 mmol). Suspension was thoroughly degassed with Argon. $Pd(PPh_3)_4$ (25 mg, 0.0216) was added and reaction was further degassed, before being sealed under argon. Reaction was stirred in sealed tube at 95°C for 13 hours. Reaction became a solution that stayed in solution upon cooling to room temperature. Aqueous layer was removed, and organics were dried over $MgSO_4$ and evaporated under reduced pressure. Solid was then taken up in biphasic DCM/ H_2O mixture. Organic layer was washed with H_2O (3x), dried—once again—over $MgSO_4$, and concentrated under reduced pressure. Crude brown solid was purified by flash column chromatography (20% DCM in Hexanes) to yield white solid, which contained a mixture of desired product **4e** and **8**. Bpin **8** could then be

removed by triturating solid with hexanes and filtered until filtrate, was clean by TLC to yield pure **4e** as white solid. (143 mg, 85%). ^{1}H NMR (400 MHz, CDCl$_3$): δ = 7.42 (s, 8H), 7.09-7.16 (m, 120H), 6.94 (d, *J*= 8.6 Hz, 16H), 6.84 (d, *J*= 8.5 Hz, 16H), 5.77 (s, 4H), 3.99 (t, *J*= 6.3 Hz, 4H), 1.98 (m, 4H), 1.74 (m, 4H), 1.06 (t, *J*= 7.4 Hz, 6H); ^{13}C NMR (125 MHz, CDCl$_3$): δ = 146.8, 146.4, 144.9, 144.5, 139.1, 137.5, 136.4, 131.3, 130.6, 129.2, 127.5, 126.0, 125.7, 76.2, 64.8, 48.0, 32.9, 20.1, 14.3; IR (cm^{-1}): 3056, 3028, 2927, 1597, 1491, 1446, 1034, 830, 748, 699; HRMS (MALDI-TOF) calcd for C$_{242}$H$_{182}$O$_2$ [M]$^+$ 3119.4140 , found 3119.464.

Synthesis of 5a. A flame dried 25mL round bottom was charged with pentiptycene **4a** (50mg, 0.073), dissolved in anhydrous DCM (19mL). Solution was cooled to -78°C. BBr$_3$ (510 µL, 0.51 mmol, 1M in DCM) was added dropwise. Upon completion of addition dry ice bath was removed and reaction was allowed to gradually warm to room temperature and stir until TLC showed complete dealkylation (45 minutes). Reaction was then cooled to 0°C. MeOH (100 µL) was added dropwise. DDQ (41 mg, 0.18 mmol). Reaction was allowed towarm to room temperature, and stir for a further 20 minutes. Aqueous sodium bicarbonate was added and stirred. Sufficient DCM was added to fully dissolve all solids. Biphasic mixture was extracted with DCM. Organics were dried over MgSO$_4$. Crude product was purified by flash column chromatograph (35% DCM in Hexane) to yield product as orange solid (35 mg, 85%) . ^{1}H NMR (400 MHz, CDCl$_3$): δ = 7.10 (s, 8H), 5.57 (s, 4H), 2.09 (s, 24H); ^{13}C NMR (125 MHz, CDCl$_3$): δ = 180.4, 151.6, 141.7, 133.3, 125.6, 46.6, 19.5; IR (cm^{-1}): 2965, 1644, 1594, 1471, 1457, 1301, 1199, 902, 750, 728, 570; HRMS (DART) calcd for C$_{42}$H$_{37}$O$_2$ [M+H]$^+$ 573.2794, found 573.2758.

Synthesis of 5c. A flame dried 15mL round bottom was charged with pentiptycene **4c** (32mg, 0.027), dissolved in anhydrous DCM (7mL). Solution was cooled to -78°C. BBr_3 (190 µL, 0.190 mmol, 1M in DCM) was added dropwise. Upon completion of addition dry ice bath was removed and reaction was allowed to gradually warm to room temperature and stir until TLC showed complete dealkylation (65 minutes). Reaction was then cooled to 0°C. MeOH (100 µL) was added dropwise. DDQ (12.3 mg, 0.054 mmol). Reaction was allowed towarm to room temperature, and stir for a further 20 minutes. Aqueous sodium bicarbonate was added and stirred. Sufficient DCM was added to fully dissolve all solids. Biphasic mixture was extracted with DCM. Organics were dried over $MgSO_4$. Crude product was purified by flash column chromatograph (40% DCM in Hexane) to yield product as orange solid (24 mg, 83%). ^{1}H NMR (400 MHz, $CDCl_3$): δ = 7.50 (s, 8H), 7.15 (m, 24H), 7.03 (m, 16H), 5.94 (s, 4H); ^{13}C NMR (125 MHz, $CDCl_3$): δ = 180.0, 151.2, 142.8, 141.1, 138.2, 130.0, 128.0, 126.8, 126.7, 47.0; IR (cm^{-1}): 2920, 2851, 1641, 1592, 1463, 1129, 910, 758, 698, 584, 565, 525; HRMS (DART) calcd for $C_{82}H_{53}O_2$ $[M+H]^+$ 1069.4046, found 1069.39539.

Synthesis of 5e. A flame dried 10mL schlenk flask was charged with pentiptycene **4e** (45mg, 0.0144), orange solid (37 mg, 84%).. ^{1}H NMR (400 MHz, $CDCl_3$): δ = 7.48 (s, 8H), 7.16-7.08 (m, 120H), 6.94 (d, J= 8.6 Hz, 16H), 6.83 (d, J= 8.6 Hz, 16H), 5.87 (s, 4H) ^{13}C NMR (125 MHz, $CDCl_3$): δ = 180.0, 151.1, 146.8, 145.2, 142.7, 138.7, 137.9, 131.3, 130.7, 129.1, 127.5, 126.4, 126.0, 64.8, 47.0; IR (cm^{-1}): 2921, 2851, 1648, 1594, 1491, 1403, 1371, 1181, 1083, 831, 735, 700; HRMS (MALDI-TOF) calcd for $C_{2342}H_{164}O_2$ $[M]^+$ 3005. 2731, found 3005.277.

5.6. Appendix: Compound characterization

Figure 5.6.1. ^{1}H NMR of compound 2 in CDCl$_3$ at 400 MHz
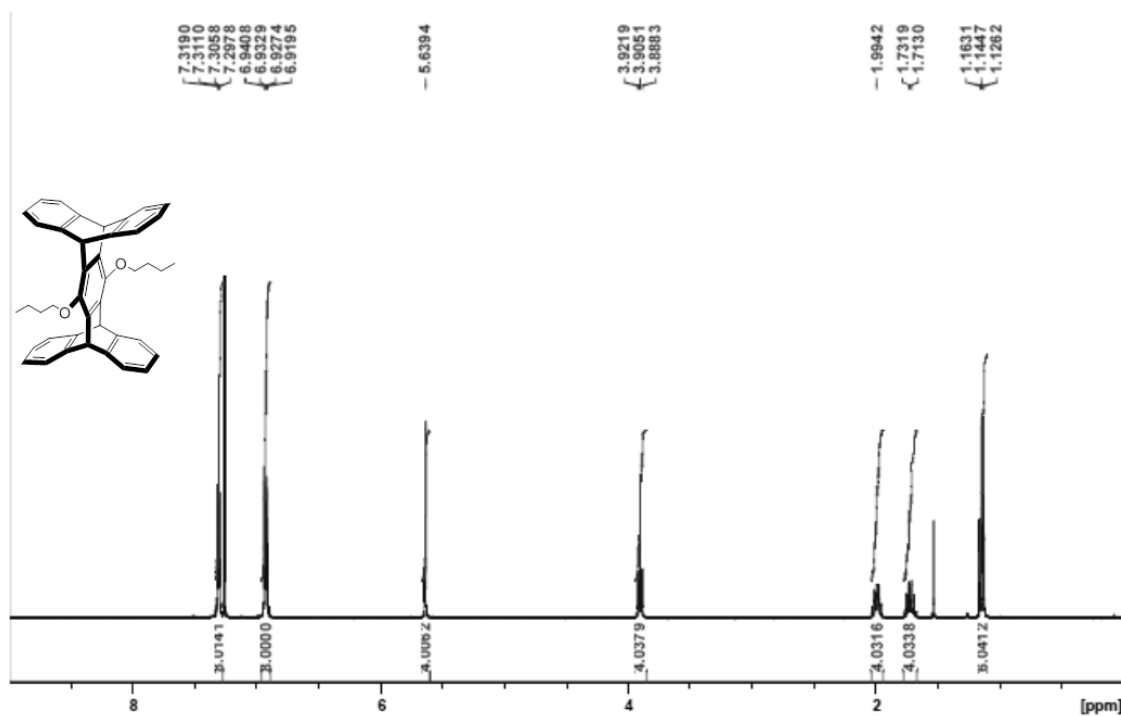
Figure 5.6.2. ^{13}C NMR of compound 2 in CDCl$_3$ at 125 MHz
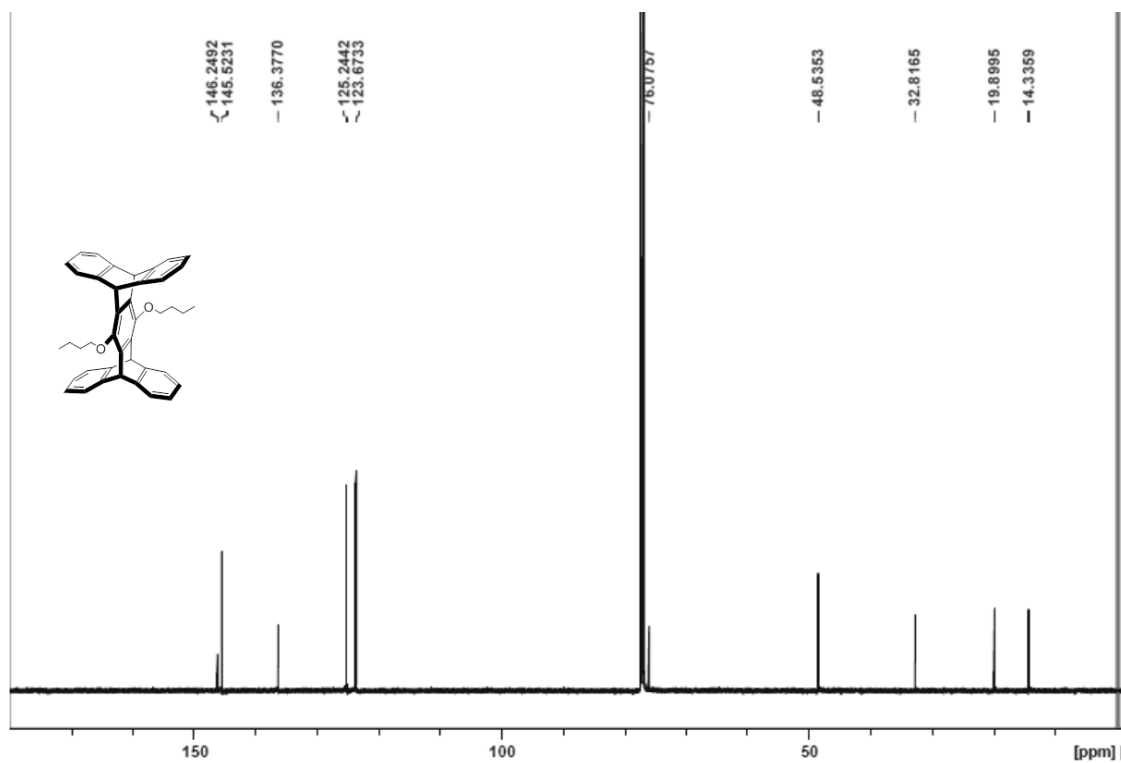
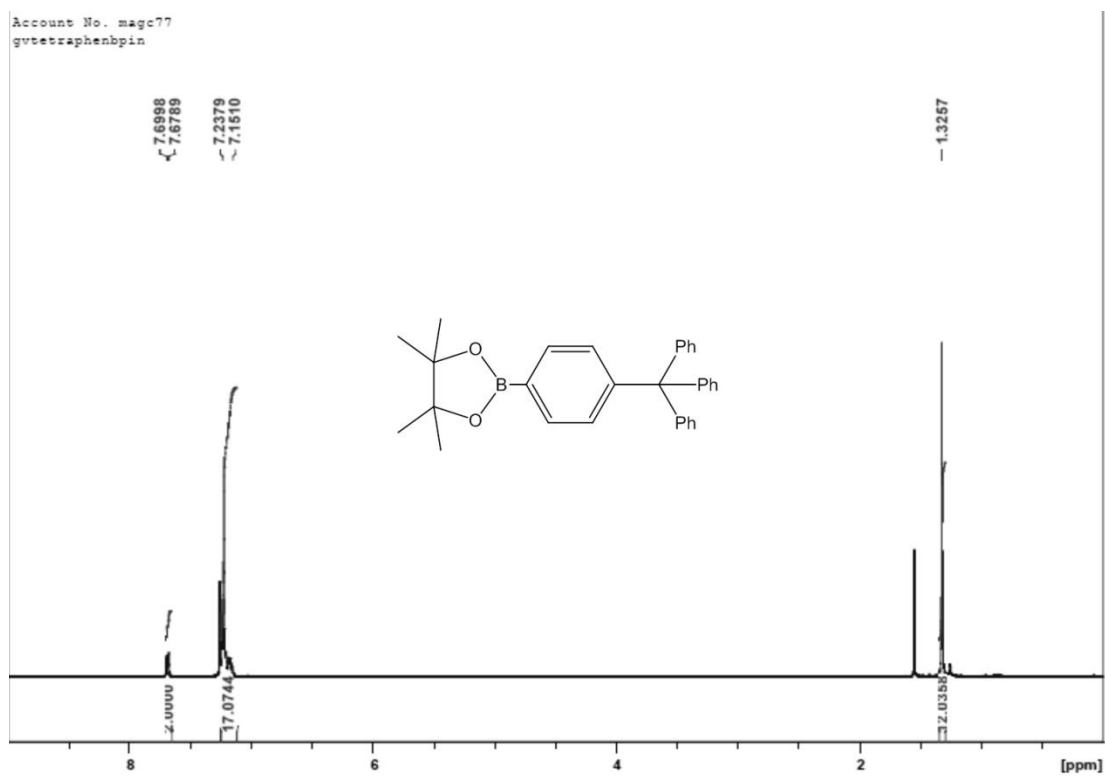**Figure 5.6.3.** ^{1}H NMR of compound 3 in CDCl$_3$ at 400 MHz
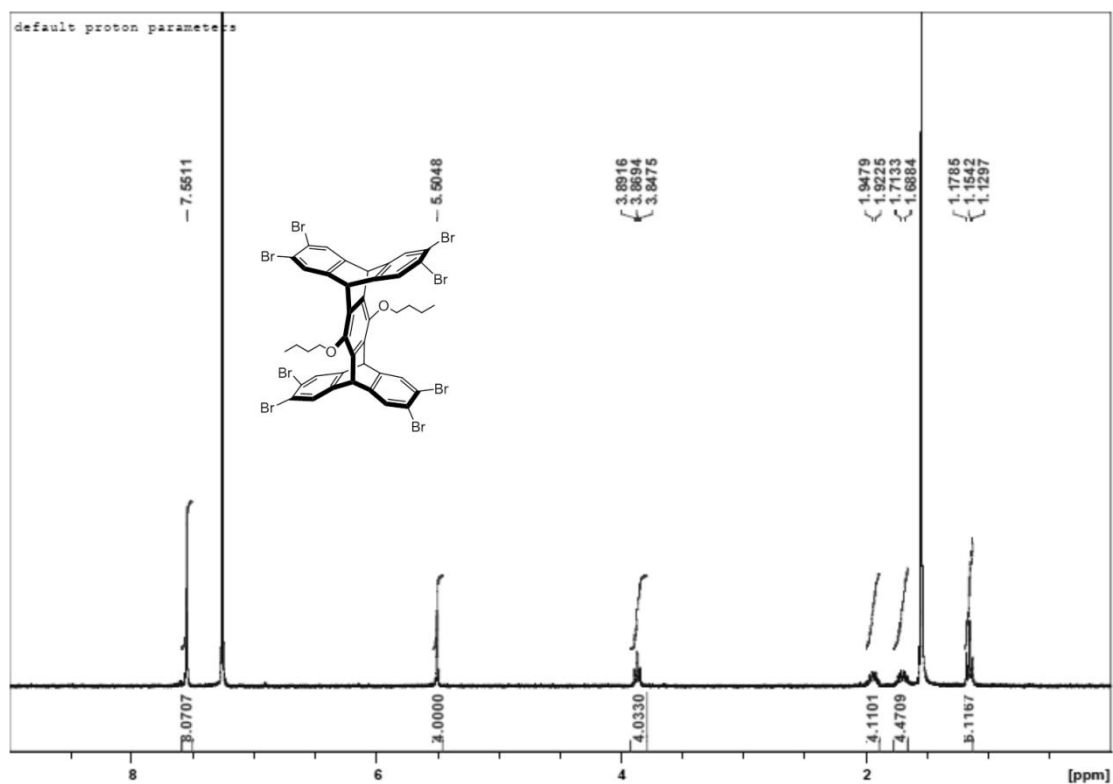
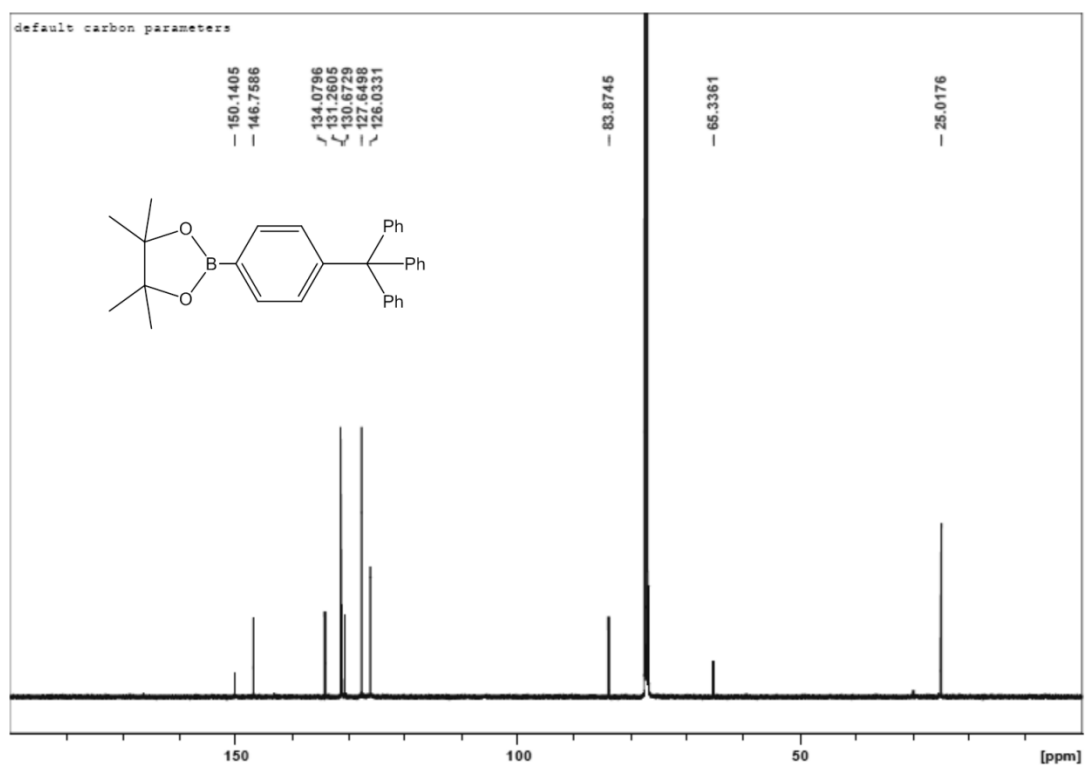**Figure 5.6.4.** ^{13}C NMR of compound 3 in CDCl$_3$ at 125 MHz
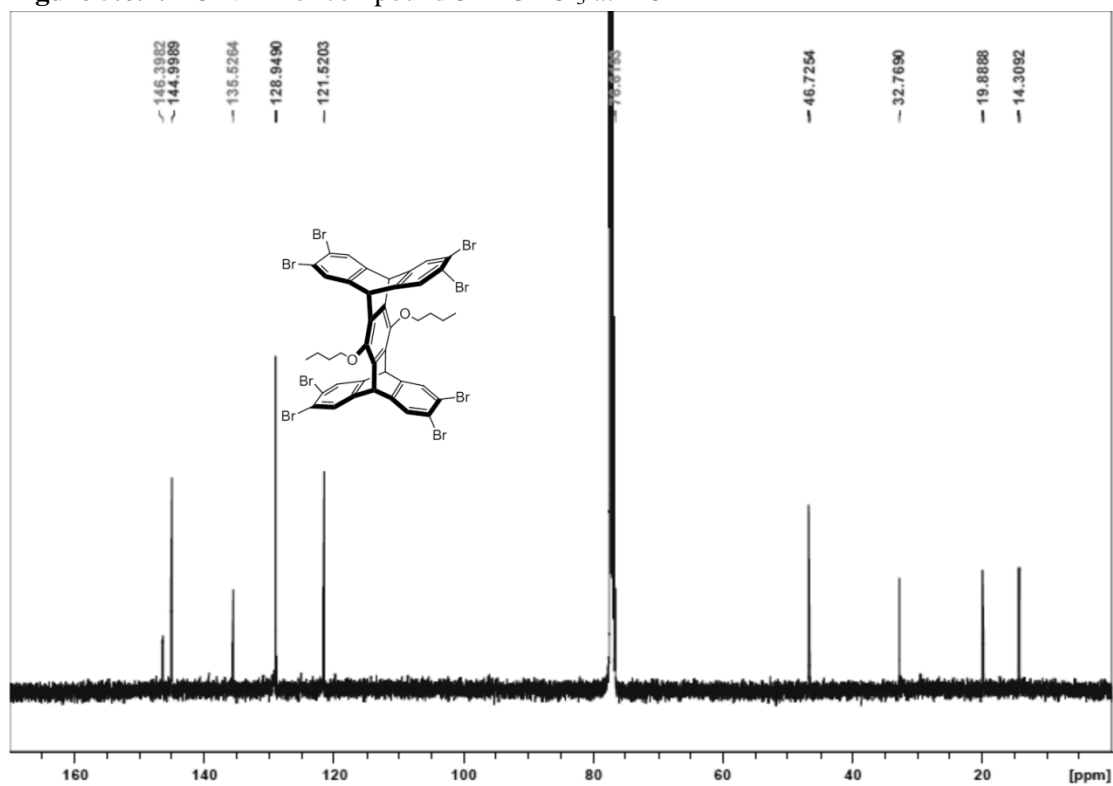
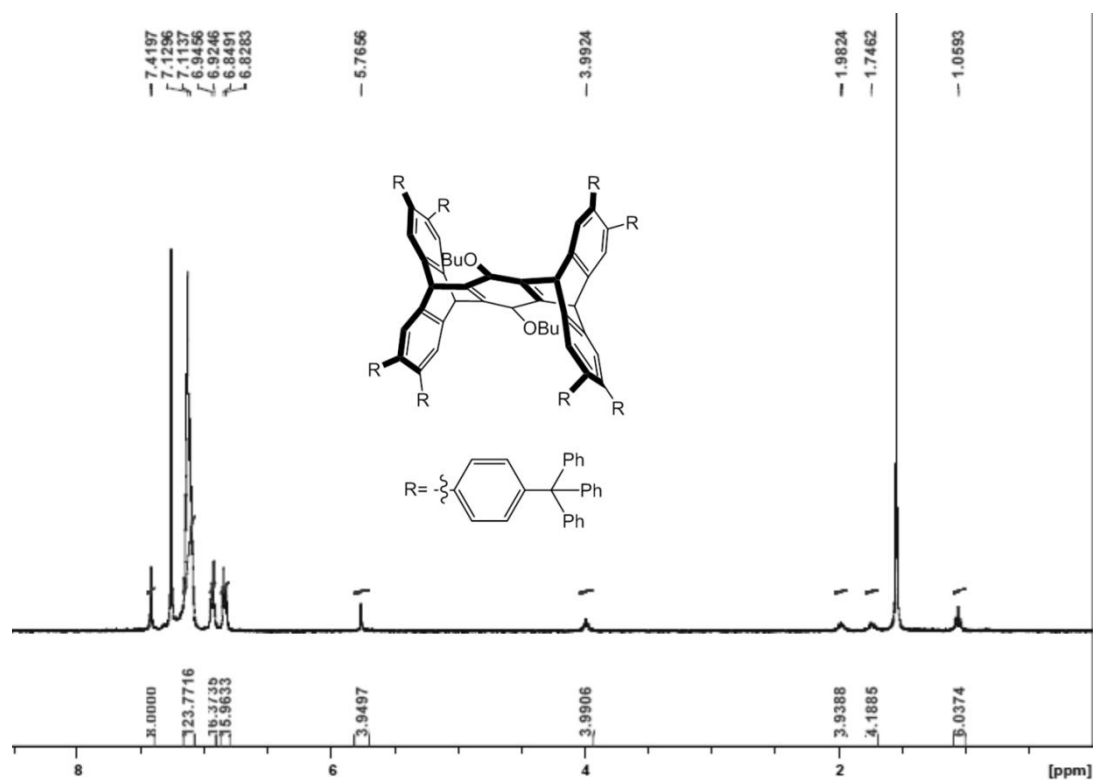**Figure 5.6.5.** ^{1}H NMR of compound 4a in CDCl$_3$ at 400 MHz
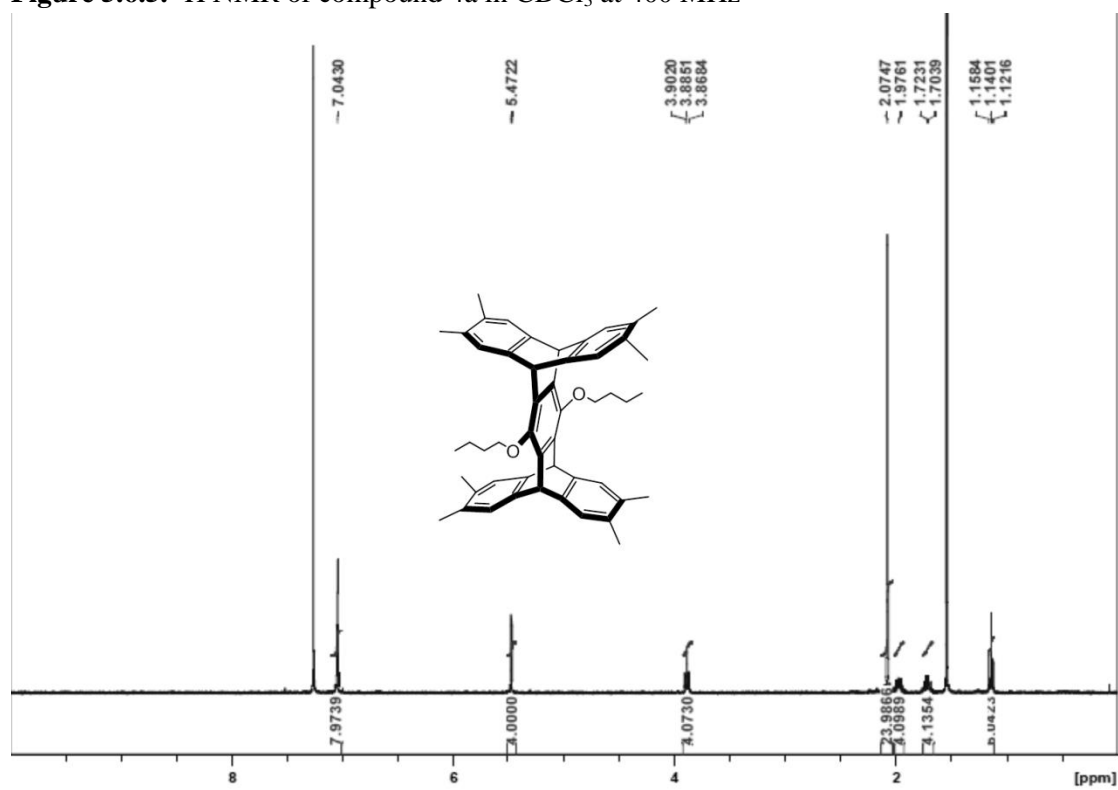
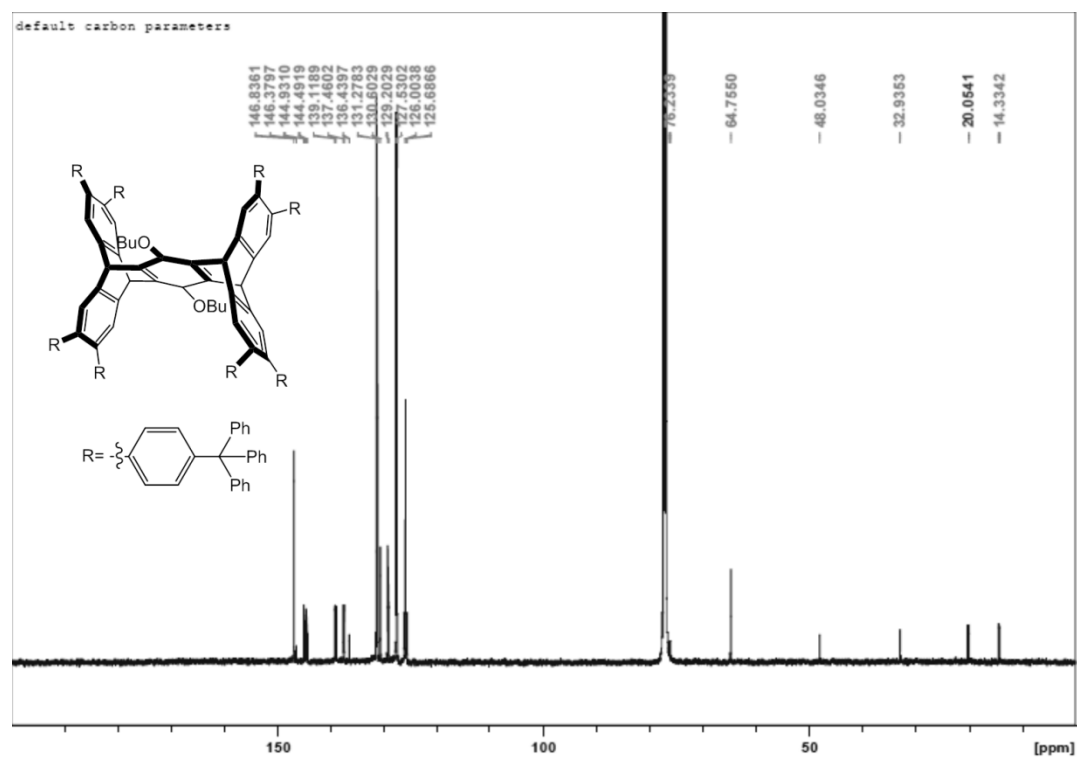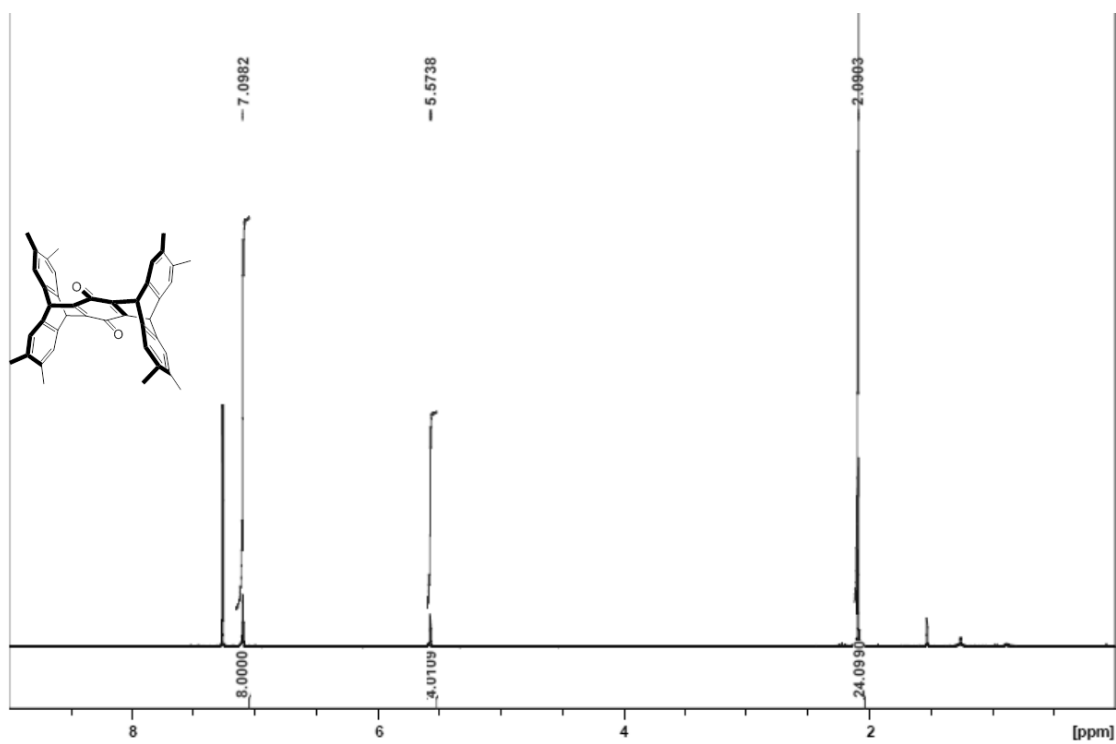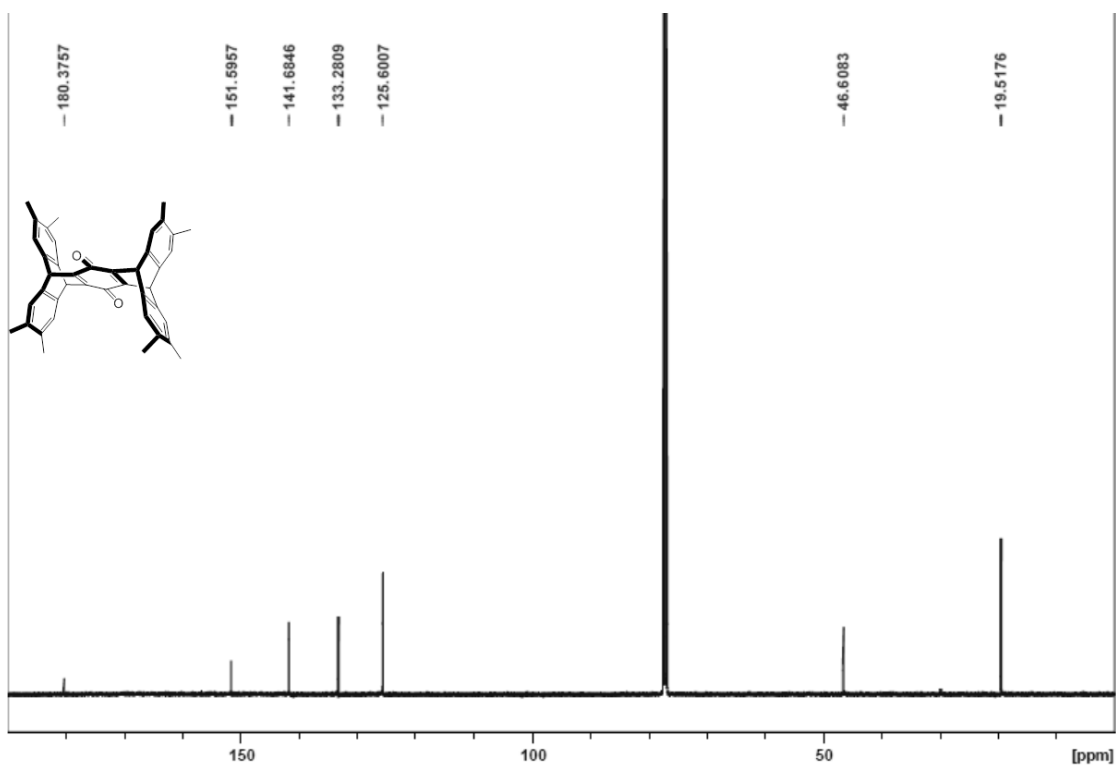**Figure 5.6.6.** ^{13}C NMR of compound 4a in CDCl$_3$ at 125 MHz
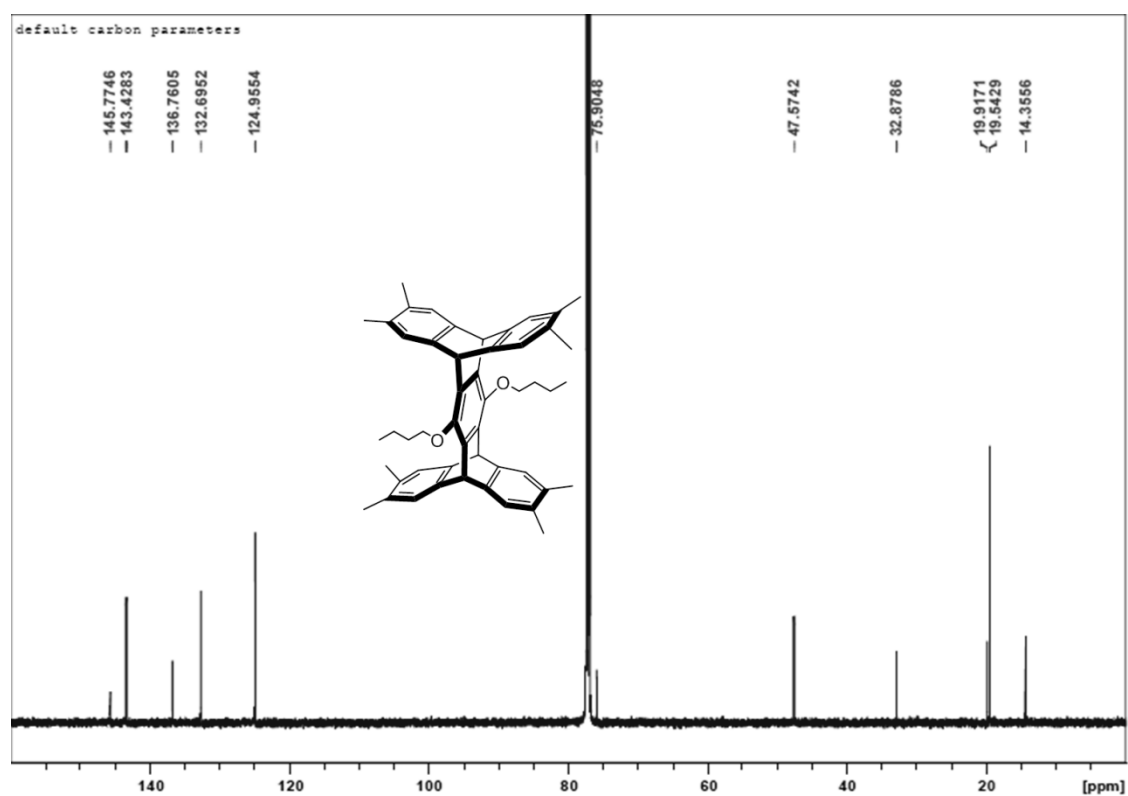
Figure 5.6.7. ^{1}H NMR of compound 4c in CDCl$_3$ at 400 MHz
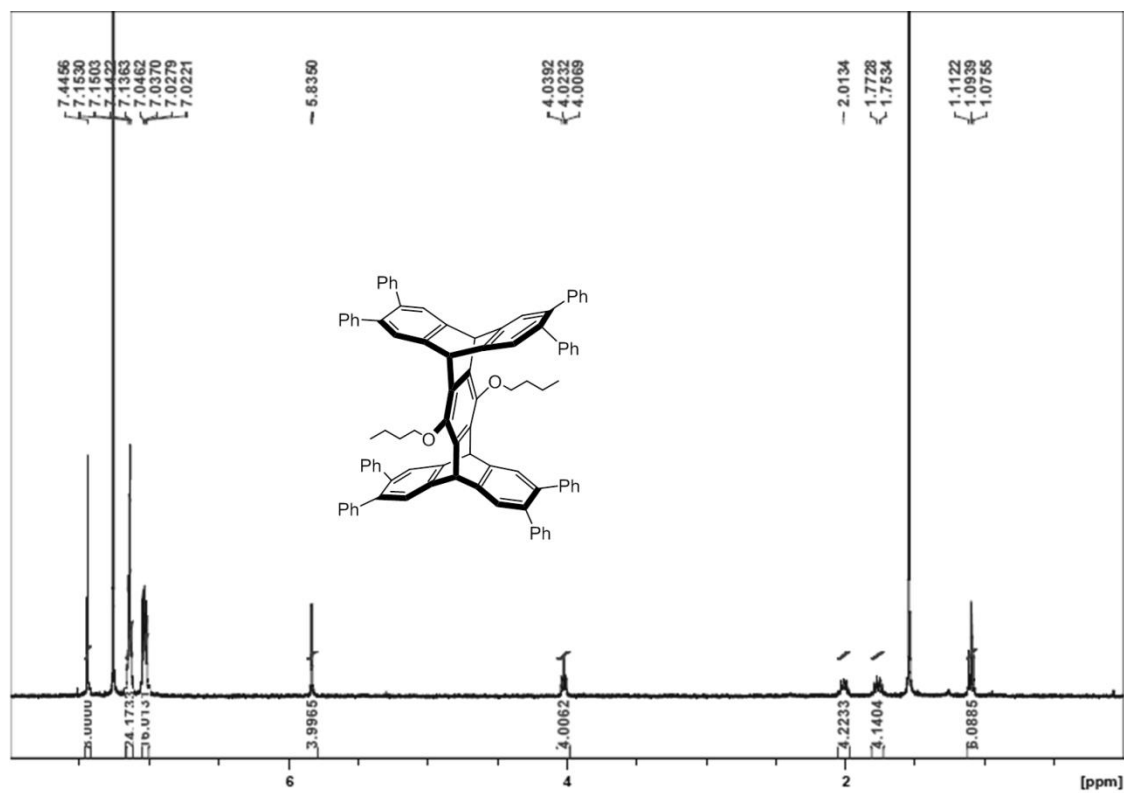
Figure 5.6.8. ^{13}C NMR of compound 4c in CDCl$_3$ at 125 MHz
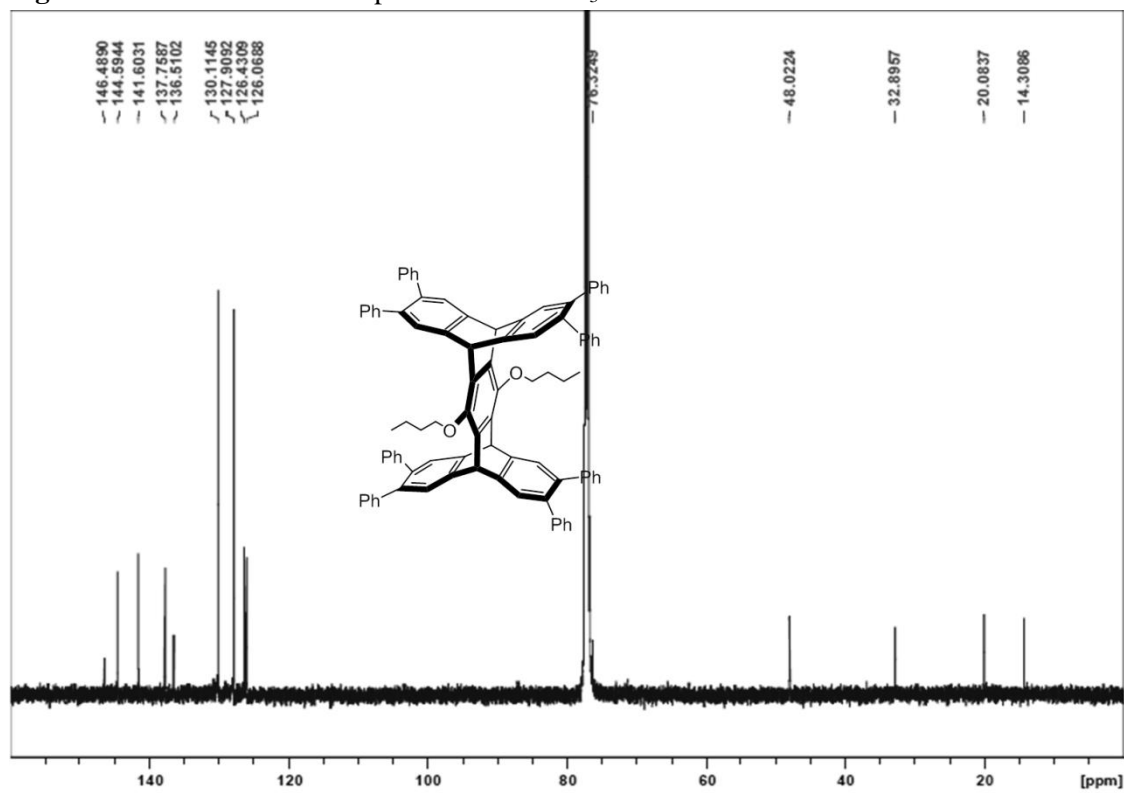
Figure 5.6.9. ^{1}H NMR of compound 4d in CDCl$_3$ at 400 MHz
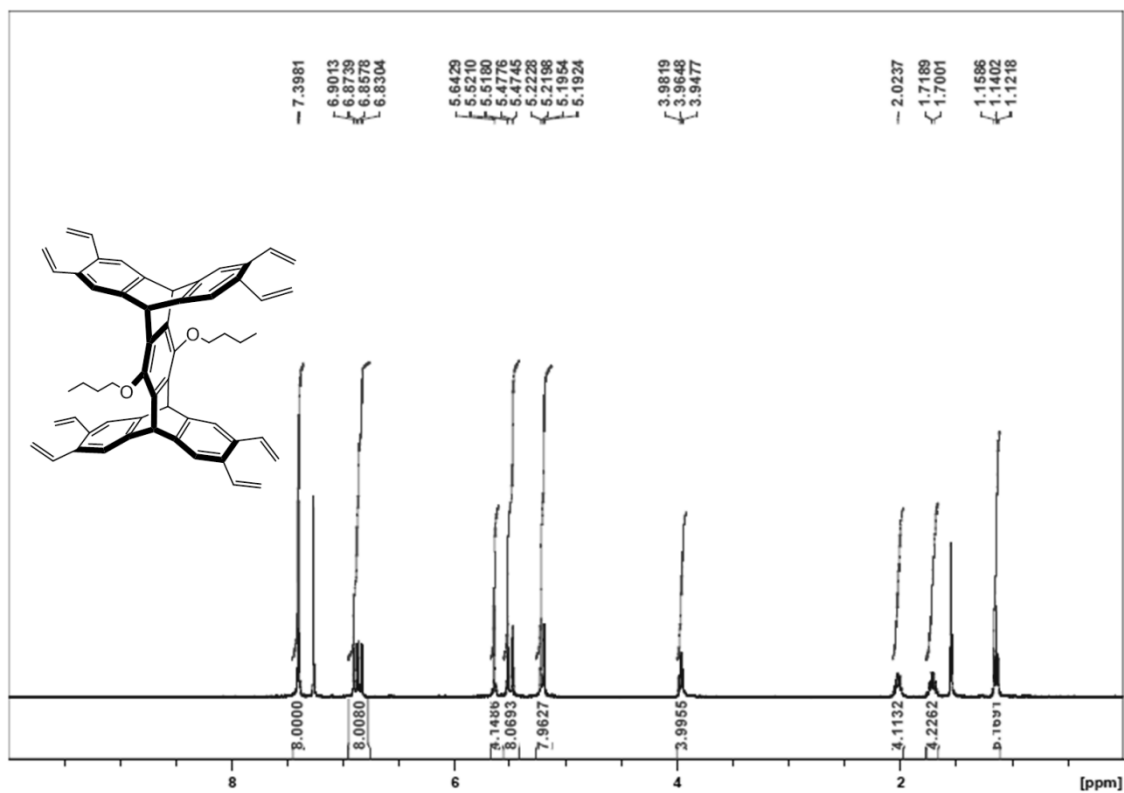
Figure 5.6.10. ^{13}C NMR of compound 4d in CDCl$_3$ at 125 MHz

126
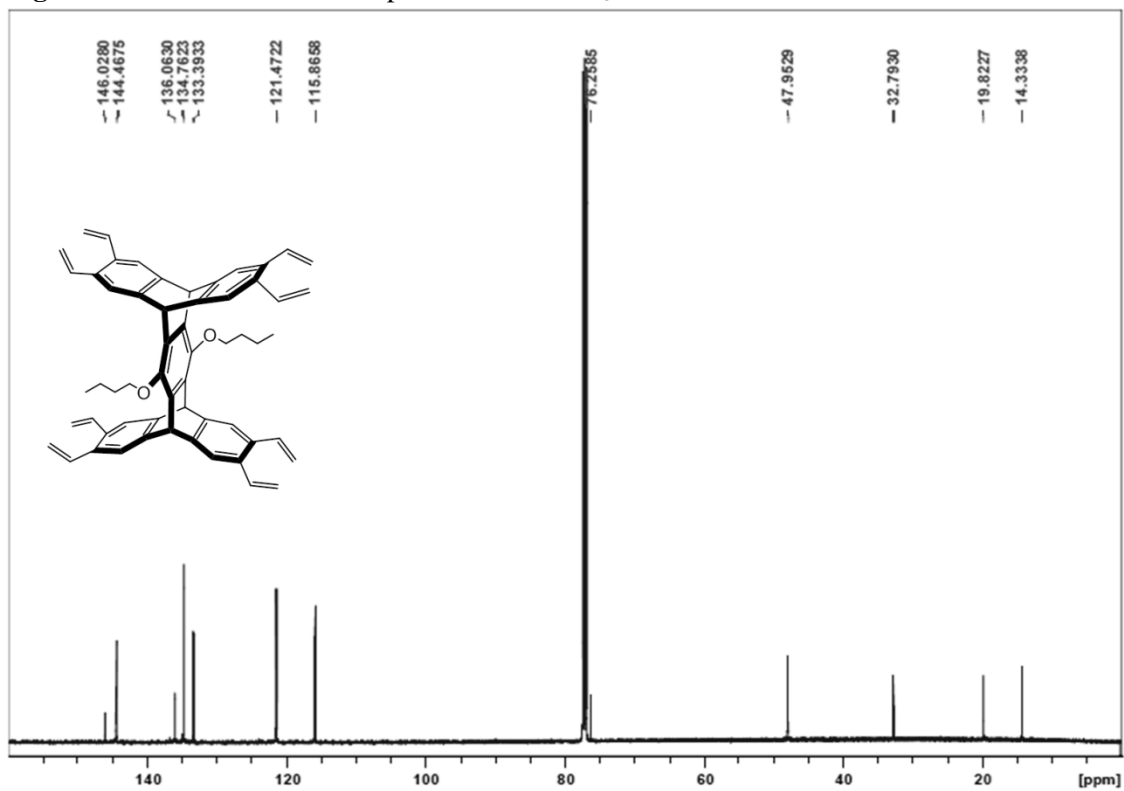
Figure 5.6.11. ^{1}H NMR of compound 4b in CDCl$_3$ at 400 MHz
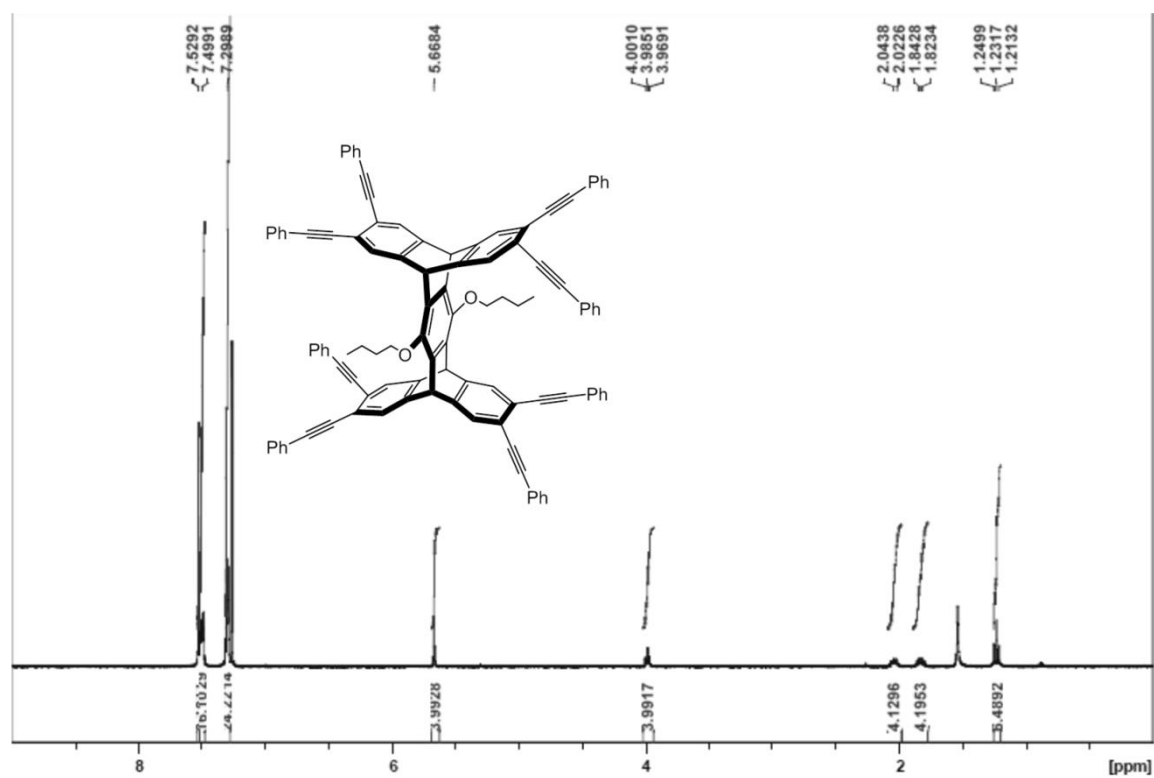
Figure 5.6.12. ^{13}C NMR of compound 4b in CDCl$_3$ at 125 MHz
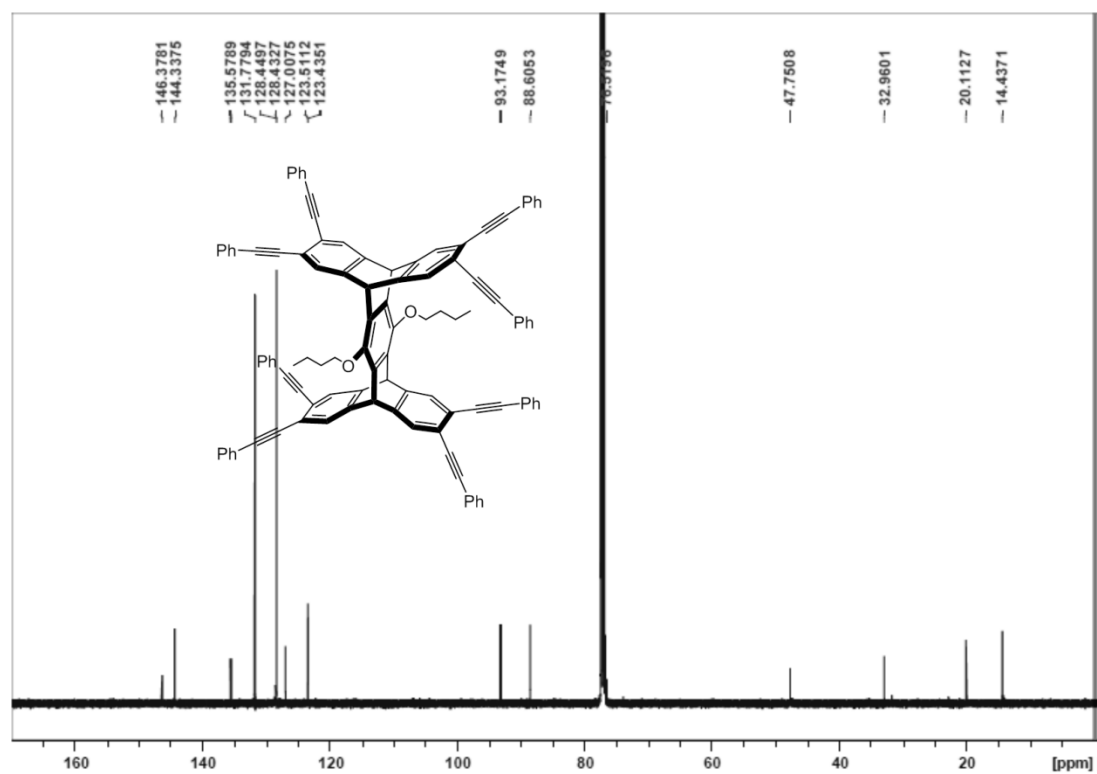
Figure 5.6.13. ^{1}H NMR of compound **8** in CDCl$_3$ at 400 MHz

Account No. magc77
gvtetraphenbpin

Figure 5.6.14. ^{13}C NMR of compound **8** in CDCl$_3$ at 125 MHz

default carbon parameters

Figure 5.6.15. ^{1}H NMR of compound 4e in CDCl$_3$ at 400 MHz

Figure 5.6.16. ^{13}C NMR of compound 4e in CDCl$_3$ at 125 MHz

Figure 5.6.17. ^{1}H NMR of compound 5a in CDCl$_3$ at 400 MHz

Figure 5.6.18. ^{13}C NMR of compound 5a in CDCl$_3$ at 125 MHz

Figure 5.6.19. ^{1}H NMR of compound 5c in CDCl₃ at 400 MHz
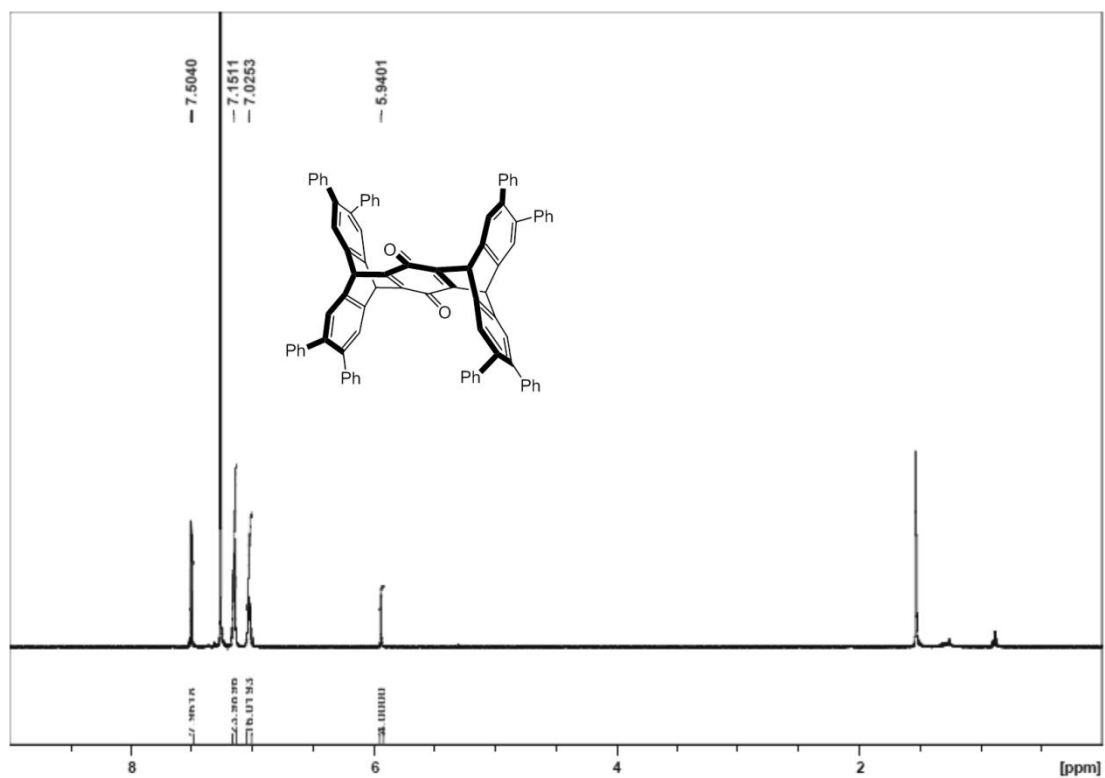
Figure 5.6.20. ^{13}C NMR of compound 5c in CDCl₃ at 125 MHz
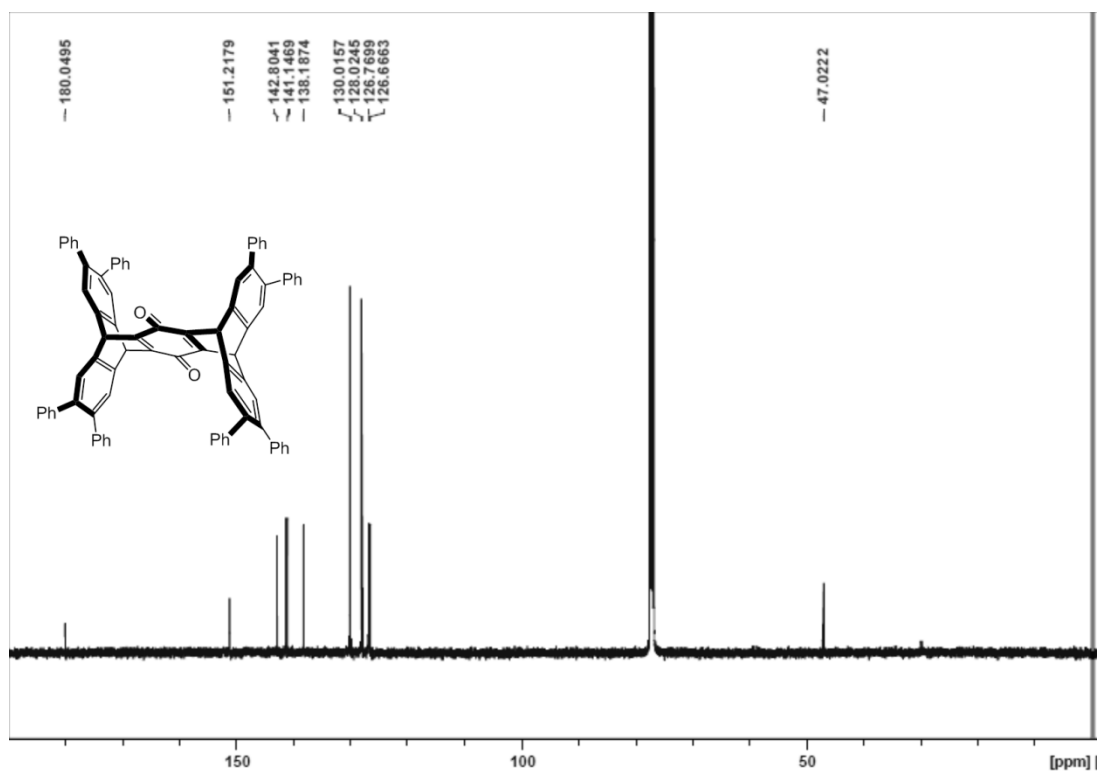
Figure 5.6.21. ^{1}H NMR of compound 5e in CDCl$_3$ at 500 MHz
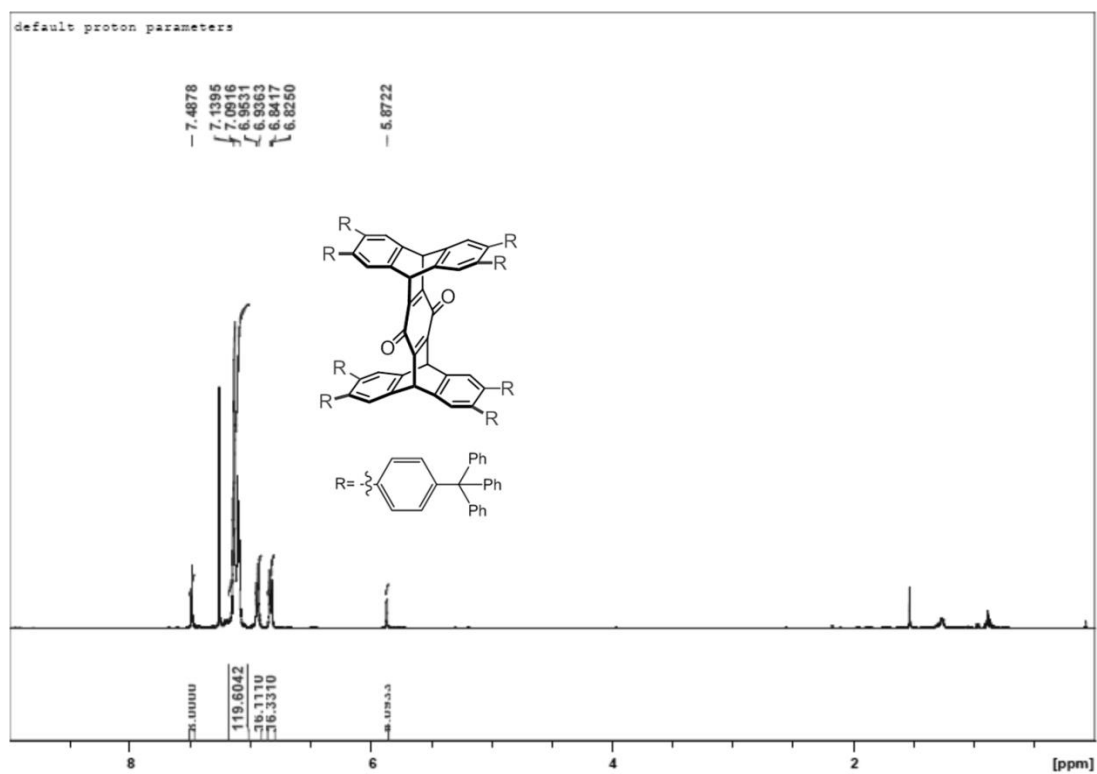
Figure 5.6.22. ^{13}C NMR of compound 5c in CDCl$_3$ at 125 MHz
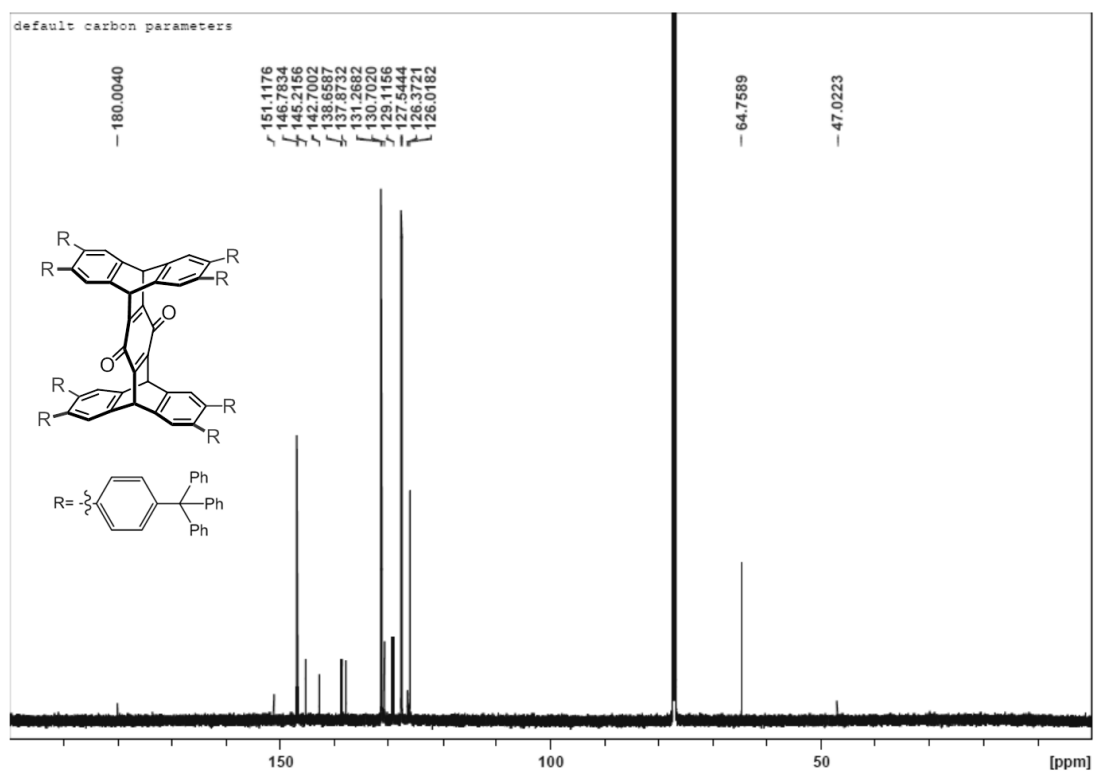
Figure 5.6.23. ATR IR of Compound 2
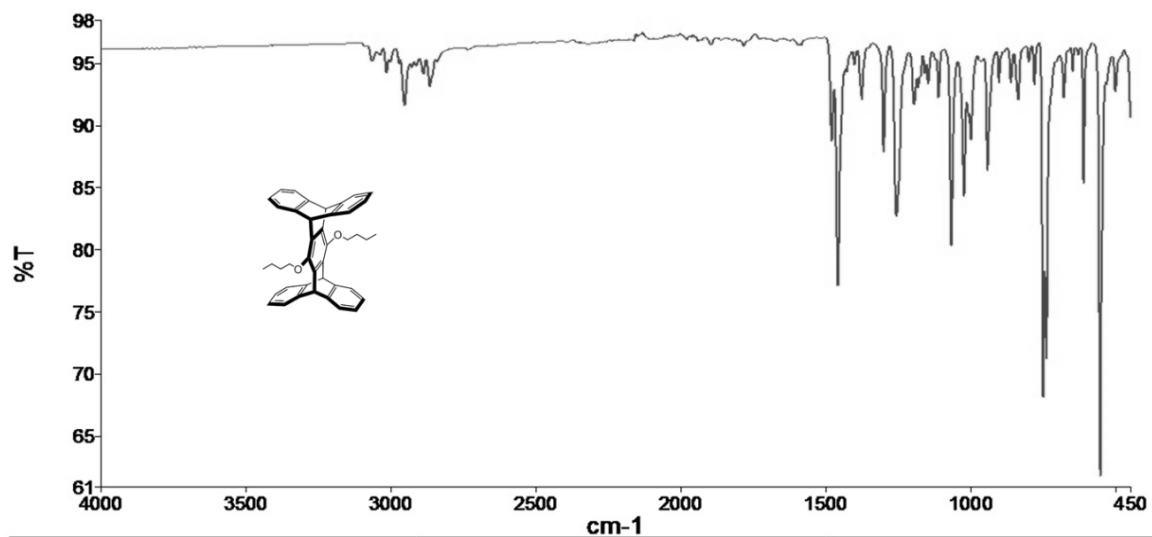
Figure 5.6.24. ATR IR of Compound 3
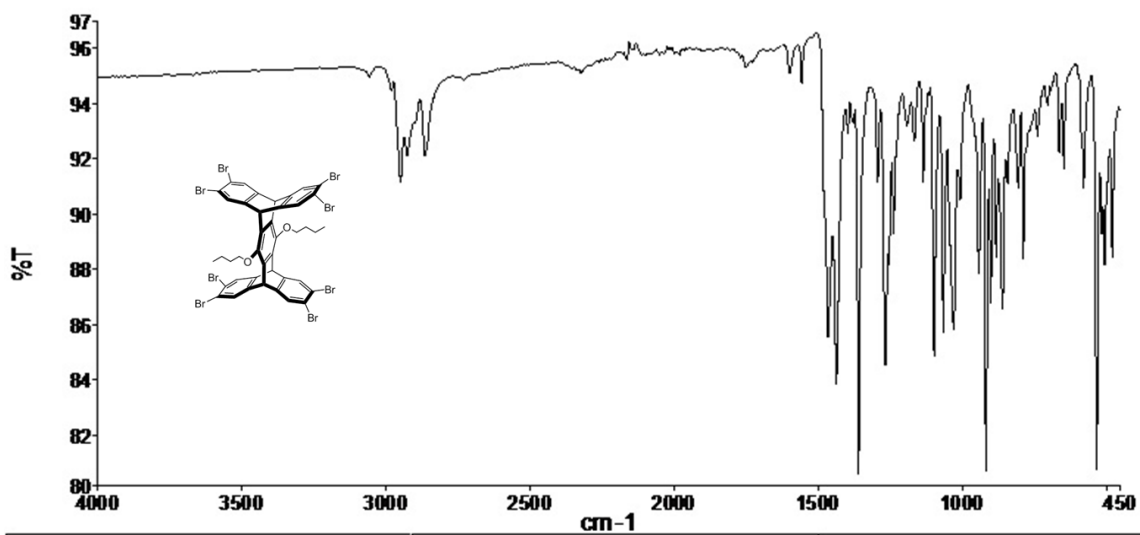
Figure 5.6.25. ATR IR of Compound 4c
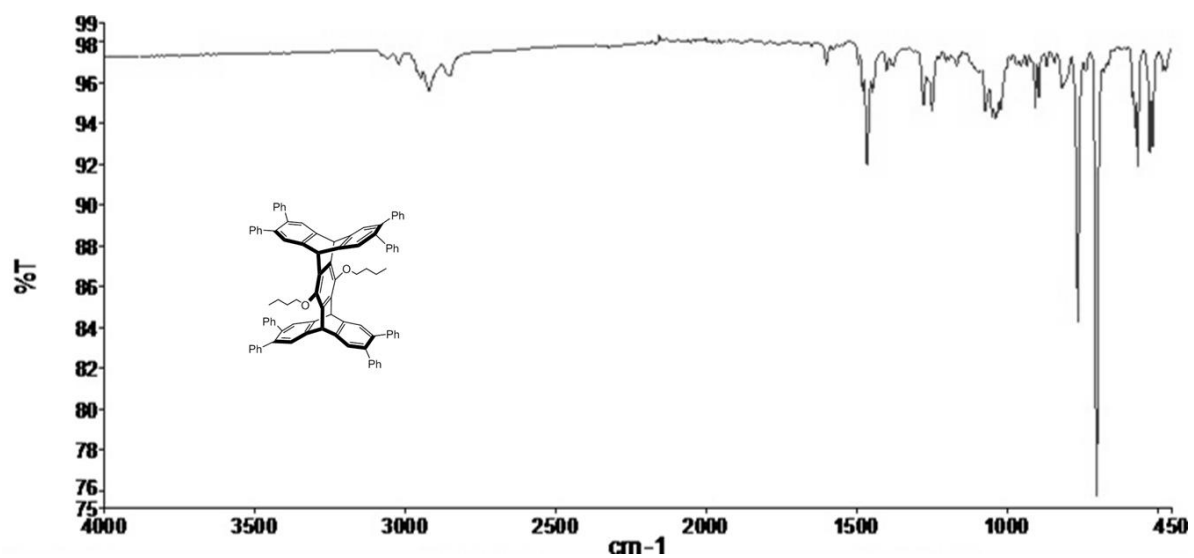
Figure 5.6.26. ATR IR of Compound 4a
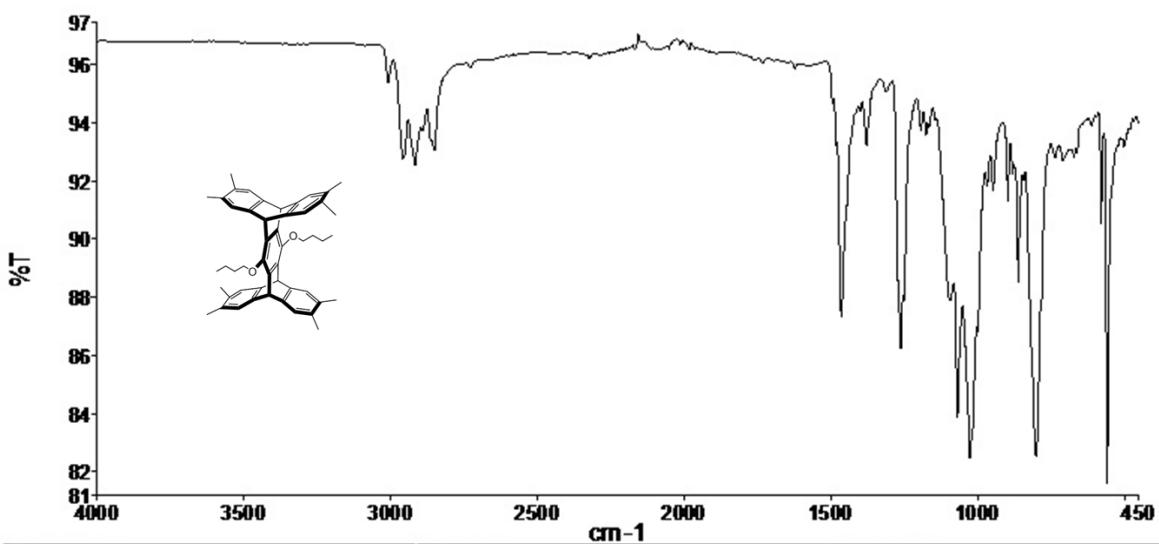
Figure 5.6.27. ATR IR of Compound 4d
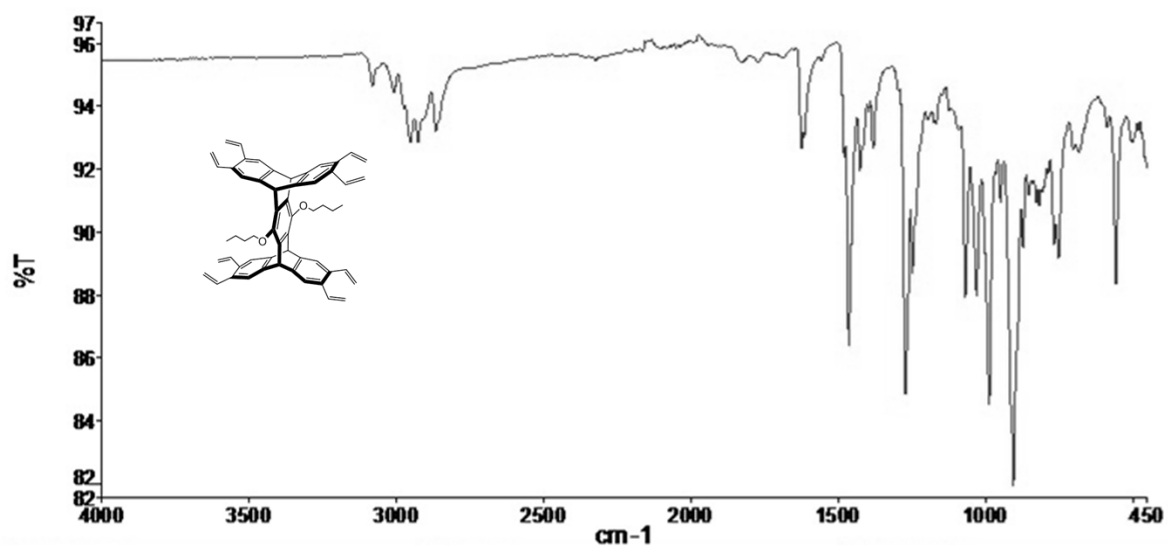
Figure 5.6.28. ATR IR of Compound 4b
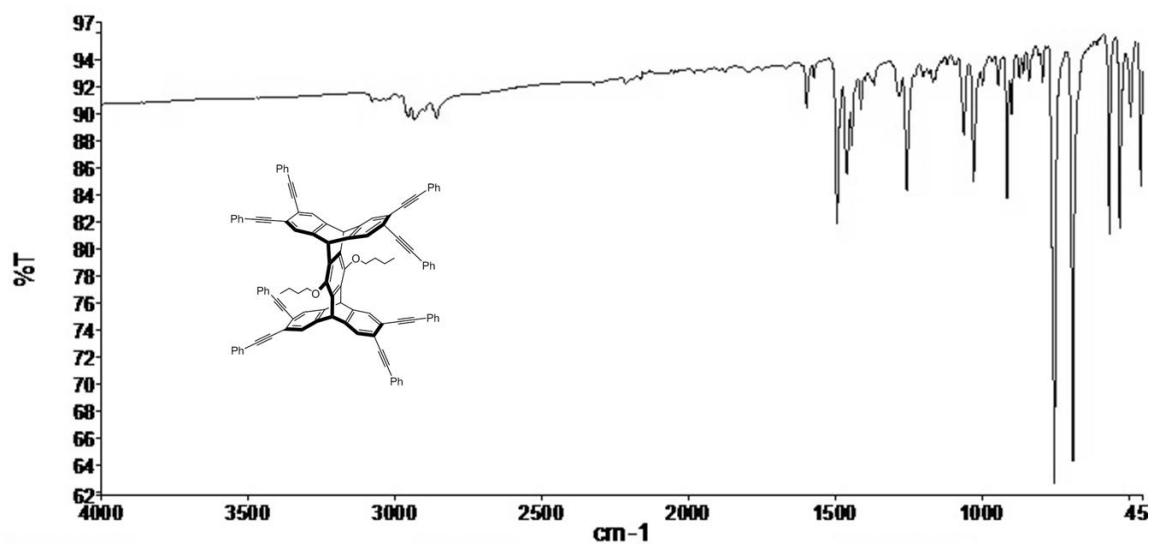
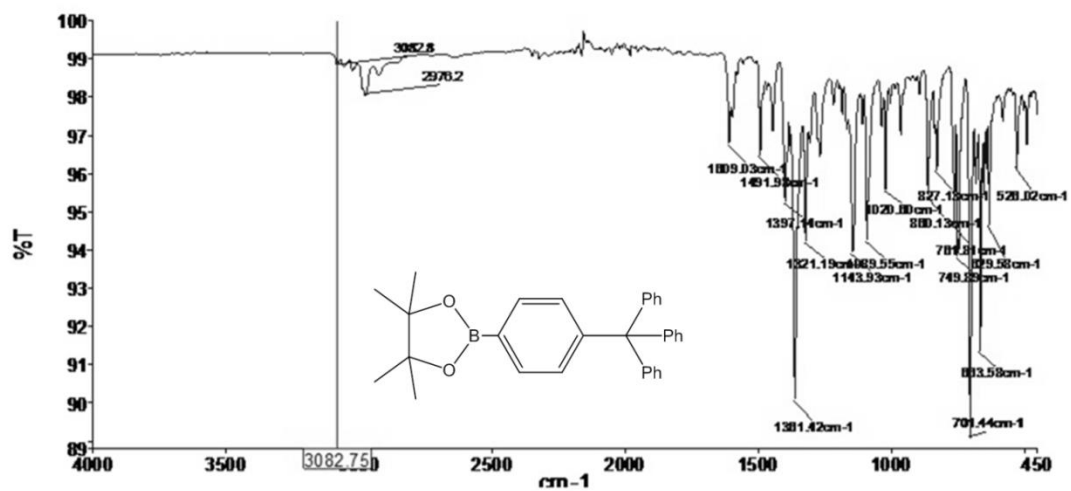**Figure 5.6.29.** ATR IR of Compound 8

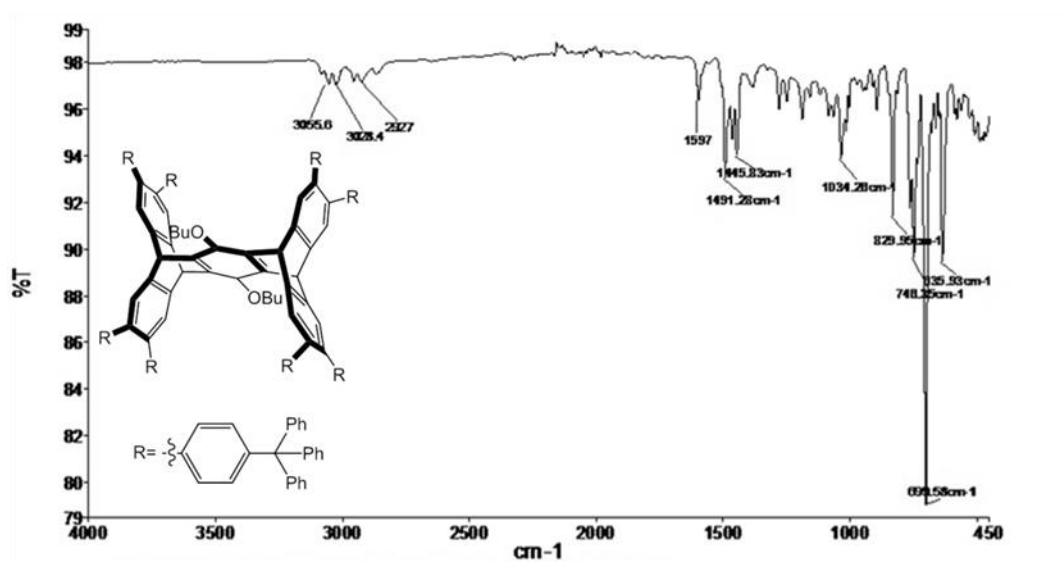**Figure 5.6.30.** ATR IR of Compound 4e
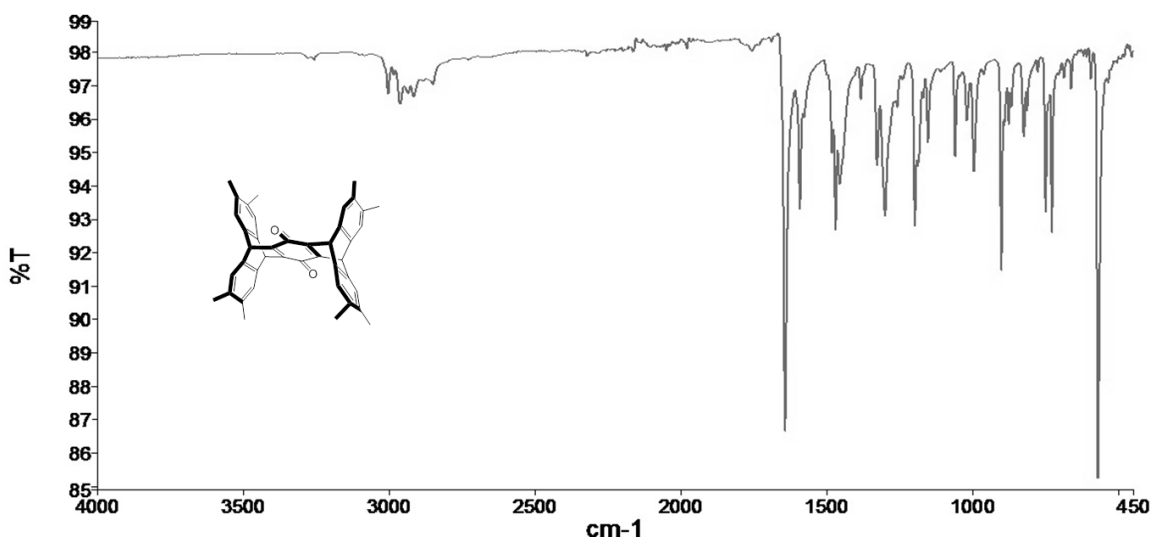
Figure 5.6.31. ATR IR of Compound 5a

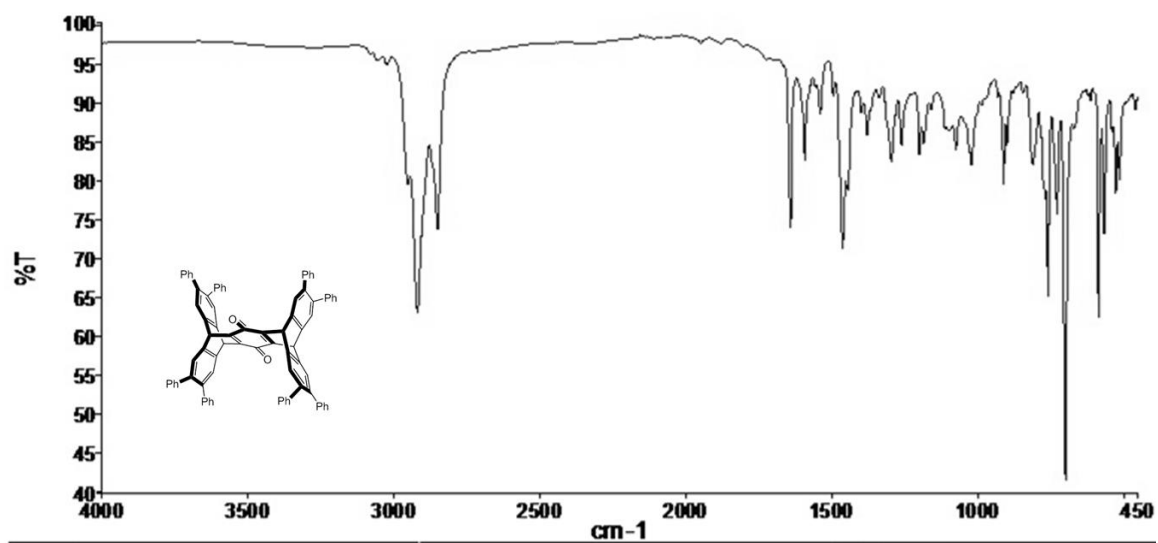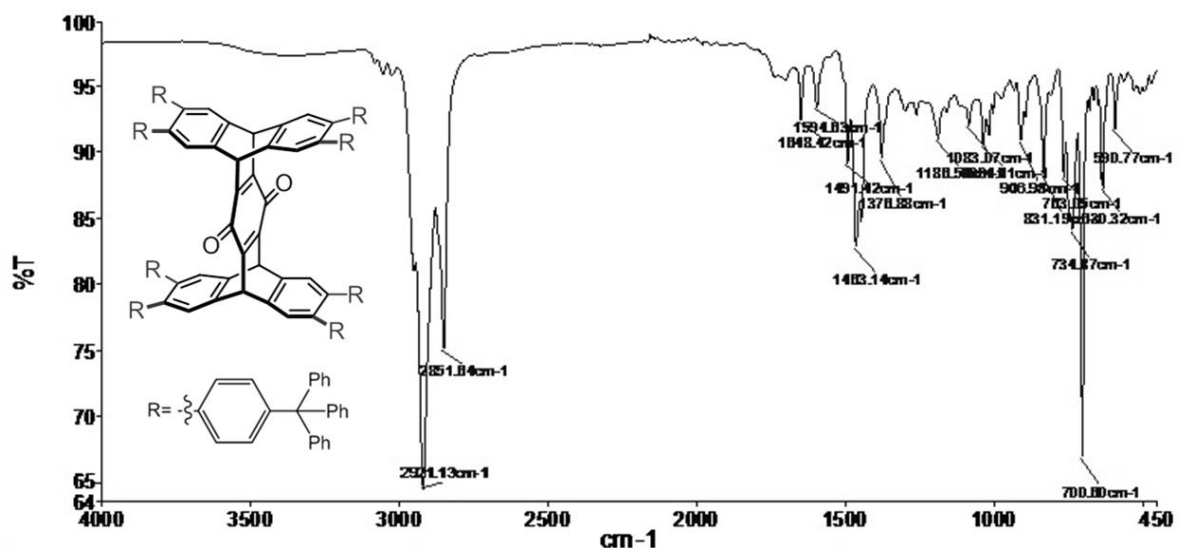**Figure 5.6.32.** ATR IR of Compound 5c

Figure 5.6.33. ATR IR of Compound 5e

5.7. References

[1] Gelman, D.; Grossman, O.; Azerraf, C. *Organometallics* **2006**, *25*, 375.

[2]   Hart, H.; Bashir-Hashemi, A.; Luo, J,; Meador, M.A. *Tetrahedron*, **1986**, *42*, 1641-1654.

[3]   (a) Breen, C.; Rifai, S.; Bulovic, V.; Swager, T. *NanoLett.*, **2005**, *5*, 1597. (b) Yang, J-S.; Yan. J.-L. *Chem. Commun.*, **2008**, *13*, 1501.

[4]   (a) Thomas, S. W., III.; Joly, G. D.; Swager, T. M. *Chem. Rev*. **2007**,*107*, 1339. (b) Yang, J.-S.; Swager, T. M. *J. Am. Chem. Soc*. **1998**, *120*, 5321. (c) Yang, J.-S.; Swager, T. M. *J. Am. Chem. Soc*. **1998**, *120*, 11864.

[5]   Cao, J.; Lu, H.; Chen, C. *Tetrahedron*, **2009**, *65*, 8104.

[6]   Crane, A.; White, N.; MacLachlan, M. *CrystEngComm*, **2015**, *17*, 4912.

[7]   (a) Hughs, M.; Jimenez, M.; Khan, S.I.; Garcia-Garibay, M. A. *J. Org. Chem.*, **2013**, *78*, 5293. (b) Sun, W.-T; Huang, Y.T.; Huang, G.-J.; Lu, H.-F.; Chao, I.; Huang, S.L.; Huang, S.-J.;

Lin, Y.-C.; Ho, J.-H.; Yang, J.S., *Chem. Eur. J.* **2010**, *16*, 11594. (c) Kao, C.-Y.; Lu, H.-F.; Chao, I.; Yang, J.-S. *Org. Lett.*, **2014**, *16*, 6100

8   (a) Supur, M.; Kawashima,Y.; Ma, Y.-X.; Ohkubo, K.; Chen, C.F.; Fukuzumi, S. *Chem.Commun.*, **2014**, *50*, 5796. (b) Jiang, Y.; Chen, C.-F. *Eur. J. Org. Chem.* **2011**, *6377.* (c) Mosca, L.; Koutník, P.; Lynch, V.M.; Zyryanov, G.V.; Esipenko, N.A.; Anzenbacher, P. *Cryst. Growth. Des.* **2012**, *12*, 6104. (d) Cao, J.; Guo, J.-B.; Li, P.-F. Chen, C.-F. *J. Org. Chem.*, **2011**, *76*, 1644.

9   Ma, Y-X.; Meng, Z.; Chen, C-G. *Synlett*, **2015**, *26*, 6.

10   Shalaev, V. K.; Getmanova, E. V.; Skvarchenko, V. R. *Zh. Org. Khim.* **1976**, *12*, 191.

11   Hilton, C. L.; Jamison, C. R.; Zane, H. K.; King, B. T. *J. Org. Chem.* **2009**, *74*, 405.

12 Kerins, F.; O'Shea, D. *J. Org. Chem.*, **2002**, *67*, 4968.

13 Li, Q.; Rukavishnikov, A.; Petukhov, P.; Zaikov, T.; Keana, J. *Org. Lett.*, **2002**, *21*, 3631.

14 It should be noted that the octavinyl derivative proved to be slightly sensitive to a variety of conditions including high heat, light and and SiO_2. As a result, attempts to completely purify the product by traditional column chromatography resulted in drastically depressed yields due to decomposition of the material from prolonged exposure to SiO_2.

15 Kamkaew, A.; Barhoumi, R.; Burghardt, R., Burgess, K. *Org. Biomol. Chem.*, **2011**, *9*, 6513.